



Injector linac optimizations for FCC-ee and applications for PRAE

Bowen Bai

► To cite this version:

Bowen Bai. Injector linac optimizations for FCC-ee and applications for PRAE. Accelerator Physics [physics.acc-ph]. Université Paris-Saclay; University of Chinese academy of sciences, 2021. English. NNT : 2021UPASP038 . tel-03276721

HAL Id: tel-03276721

<https://theses.hal.science/tel-03276721>

Submitted on 2 Jul 2021

HAL is a multi-disciplinary open access archive for the deposit and dissemination of scientific research documents, whether they are published or not. The documents may come from teaching and research institutions in France or abroad, or from public or private research centers.

L'archive ouverte pluridisciplinaire **HAL**, est destinée au dépôt et à la diffusion de documents scientifiques de niveau recherche, publiés ou non, émanant des établissements d'enseignement et de recherche français ou étrangers, des laboratoires publics ou privés.



Injector linac optimizations for FCC-ee and applications for PRAE *Optimisations des injecteurs linacs pour FCC-ee et applications pour PRAE*

Thèse de doctorat de l'University of Chinese academy of sciences et de l'université Paris-Saclay

École doctorale n°576 : particules hadrons énergie et noyau : instrumentation, image, cosmos et simulation (Pheniics)

Spécialité de doctorat : physique des accélérateurs

Unité de recherche : Université Paris-Saclay, CNRS, IJCLab, 91405, Orsay, France

Référent : Faculté des sciences d'Orsay

Thèse présentée et soutenue à Paris-Saclay, le 20/05/2021, par

Bowen BAI

Composition du Jury

Guoxi PEI

Professeur, IHEP, CAS

Président

Kazuro FURUKAWA

Professeur, KEK

Rapporteur & Examinateur

Jiaru SHI

Professeur agrégé, Tsinghua University

Rapporteur & Examinateur

Iryna CHAIKOVSKA

Chargée de Recherche, IJCLab

Examinateuse

Frank ZIMMERMANN

Directeur de Recherche, CERN

Examinateur

Direction de la thèse

Angeles FAUS-GOLFE

Directrice de Recherche, IJCLab

Directrice de thèse

Yunlong CHI

Professeur, IHEP, CAS

Co-Directeur de thèse

I would like to dedicate this thesis to my loving family ...

Acknowledgements

Words could not fully express my appreciations to those who offered any help and assistance to me in the process of my PhD study and in the completion of this thesis. But I will still try my best to deliver my sincere gratitude to everybody accompanied in this short journey.

I would like firstly to extend my thanks to *Institute of High Energy Physics, Chinese Academy of Sciences* (IHEP, CAS) and *Laboratoire de Physique des 2 Infinis Irène Joliot-Curie* (IJCLab, previous *Laboratoire de l'Accélérateur Linéaire*), CNRS, *Université Paris-Saclay* where I finished my PhD study as an international joint student and to *China Scholarship Council* for the grant to my study in France. I'm grateful to those staff who works in these establishments to provide me with the administrative services. Meanwhile, thanks to the Educational Office of *Ambassade de la République Populaire de Chine en République Française* for the timely and warm anti-epidemic supplies in the pandemic of COVID-19.

It has been an honor for me to study under the supervision of Dr. Angeles Faus-Golfe and Prof. Yunlong Chi during the three-year PhD period on the field of accelerator physics. This thesis could not be finished without their devotedly guidance and suggestions. Their rich experience not only helped me to develop the ability to solve problems, but also provided me with a chance to expand my horizon to learn more of the whole field. Their enthusiasm and dedication to research work always inspired me to face and overcome any difficulties without fear. The opportunities they have offered to me to work in the domestic and international projects with experts in different areas promoted my growth in scientific research as well. Especially thank Angeles for the daily discussions no matter in academic research or non-academic activities, it benefited me and helped me to adapt to the different cultures in Paris quickly from the very beginning when I just came to France.

The two projects (PRAE and FCC-ee) I have been engaged in gave me a great opportunity to know plenty of colleagues and friends. I first would like to give my thanks to Prof. Qing Qin from ESRF, France, who offered me much help to build the connection between me and Angeles. I also want to thank Dr. Yanliang Han (Now an associate professor in CSNS, China) for the two years' cooperation and help both in work and daily life in Paris. His attitude towards scientific research deeply affected me and made me treat any work more rigorously than before. I would like to convey my thanks to Dr. Zusheng Zhou for his kind help in daily life and nice

instructions in academic activites when I became a graduate student of IHEP, China. I am grateful as well to Dr. Iryna Chaikovska, Dr. Robert Chehab (IJCLab, France) for the great collaboration and unforgettable experience in the study of FCC-ee positron source. I also would like to give my thanks to Dr. Luc Perrot for his kind help in the French résumé correction. Special thanks to Prof. Kazuro Furukawa, Dr. Naoko Iida, Dr. Yoshinori Enomoto from KEK, Japan; Dr. Salim Ogur, Dr. Andrea Latina, Prof. Katsunobu Oide and Dr. Frank Zimmermann from CERN, Switzerland for the technological support, valuable comments and consistent assistance during my PhD study. Many thanks to other group members and colleagues for any tiny help in my study too.

Many thanks as well to every person of IJCLab (previous LAL) DEPACC group and Linac group of IHEP Accelerator Division, especially PhD students Ke, Huan, Chengguo, Kunlin, Jianbin, Banjamin, Ezgi and Muath, for the joyful relationships during my PhD study. I could not forget the meaningful discussions during lunchtime and coffee break. It has been a happy experience to learn from and work together with them. Thanks to my roommates, Jijiang and Yi, for the arranged travels, parties, and even food and videos sharing. Also, thanks to all my dearest friends for the listening, talk and companion during my stressful periods over the years!

In the end, I would like to give my deepest gratitude to my loving family and my girlfriend Rong'er for all the years' support, encouragement and love! I could not go this far without them always standing by my side.

Résumé

Au cours des dernières années, un développement intense d'accélérateurs d'électrons linéaires a été conduit par différentes communautés comme la communauté X-FEL, la communauté des collisionneurs linéaires de la physique des hautes énergies (HEP) : ILC et CLIC ainsi que la communauté des collisionneurs circulaires : FCC-ee et CEPC. En outre, il existe également de nombreuses autres applications de la science médicale à l'industrie qui utiliseront un tel LINAC comme accélérateur principal. Dans toutes ces études, un e-linac à haut rendement avec des énergies de 10 MeV à plus de 1 TeV est nécessaire comme conducteur ou injecteur. Même si la technologie LINAC pour faire face aux performances recherchées est très connue, un effort de R&D important proposant des solutions plus compactes, plus simples, plus rentables, efficaces, robustes et fiables est en cours. Dans ce contexte, cette thèse optimisera le LINAC et ses lignes de transfert associées dans deux cas :

1. L'injecteur LINAC pour FCC-ee (Future Circular électron-positon Collider), en particulier celui à positons.
2. Le LINAC pour une plate-forme d'application connue sous le nom de projet PRAE (Platform for Research and Applications with Electrons).

Le Future Circular Collider (FCC) hébergé par le CERN, est une collaboration internationale visant à explorer la faisabilité de différents scénarios de collisionneurs de particules dans le but d'augmenter considérablement l'énergie et la luminosité par rapport aux collisionneurs existants, dans la recherche de nouvelle physique. Dans le cas de FCC-ee, le rapport de conception conceptuelle (CDR) montre que $2,13 \times 10^{10}$ (3,2 nC) particules d'électrons et de positons par paquet sont nécessaires pour le remplissage complet le plus exigeant du mode de fonctionnement Z. La sélection de base pour l'injecteur LINAC FCC-ee est basée sur celle de SuperKEKB, qui nous donne un rendement en positons de $0,33 N_{e^+}/N_{e^-}$ contre $0,4 N_{e^+}/N_{e^-}$ obtenue dans une expérience récente. L'objectif principal de cette thèse est de réaliser la conception et l'optimisation de bout en bout pour la production de faisceau, l'accélération et le transport de la source d'électrons d'alimentation à l'anneau d'amortissement de positons. Il s'agit également d'augmenter l'efficacité et la flexibilité de la production de positons (le

rendement en positons doit être supérieur à $0,7 N_{e^+}/N_{e^-}$) pour l'injecteur LINAC de FCC-ee. Une étude complémentaire pour l'optimisation de la cible de positons utilisant une cible conventionnelle ou une cible hybride est également brièvement résumée. Compte tenu des inconvénients du schéma d'injecteur de SuperKEKB actuel, trois nouveaux modèles de schémas de dérivation différents ont été finis pour transférer les particules d'électrons et de positons séparément pour une meilleure transmission et une flexibilité améliorée de l'ensemble du système. Cela pourrait finalement nous donner un rendement en positons d'environ $1,2 N_{e^+}/N_{e^-}$ dans l'anneau d'amortissement du positon dans les simulations théoriques. En conclusion, ce travail est une première étape dans l'optimisation du système d'injecteur de FCC-ee du point de vue de l'efficacité du transport et de la conception optique. Les différents schémas proposés sont basés sur des technologies établies. Les différents chemins pour les électrons et les positons sont utilisés afin d'améliorer l'efficacité de transport du point de vue des pertes et du coût.

Dans la deuxième partie de cette thèse, la conception d'une plateforme d'application de radiobiologie et de physique nucléaire PRAE (Platform for Research and Applications with Electrons) LINAC basée sur un faisceau d'électrons pulsé de haute qualité d'énergie jusqu'à 70 MeV en phase 1 et 140 MeV en phase 2 a été réalisé. Deux paquets d'électrons d'intensité de l'ordre du nanoCoulomb dans l'accélérateur PRAE pour la phase 1 sont produits dans un canon RF à une fréquence de 50 Hz, post- accélérés par un LINAC en bande S jusqu'à 50-70 MeV et injectés dans la ligne directe du faisceau plus une ligne déviée. La conception optique des lignes de faisceau doit être aussi flexible que possible pour répondre aux différents types de caractéristiques de faisceau (taille du faisceau, énergie, dispersion, courant. . .) et modes de fonctionnement en fonction de l'application. L'étude des différentes options optiques et la mise en œuvre de ces deux lignes de faisceau ainsi que l'interaction faisceau-eau pour les études précliniques pour le cas des expériences de radiobiologie ont également été réalisées et présentées dans cette thèse.

Ce manuscrit comporte principalement quatre chapitres.

Dans le premier chapitre, nous donnons une introduction aux LINACs électroniques RF et leurs applications dans la société moderne. Nous présentons tout d'abord les principes de fonctionnement des LINAC, leurs compositions ainsi que leurs paramètres essentiels permettant de déterminer leurs qualités et leurs performances. Nous présentons ensuite les problèmes généralement rencontrés dans la conception optique des LINACs électroniques RF et des systèmes de transport de faisceau, incluant l'effet de la charge d'espace, l'effet de champ de sillage, le rayonnement synchrotron incohérent (CSR), le rayonnement synchrotron cohérent (CSR) . . . De ces instabilités collectives, nous introduisons en détail les problèmes physiques et les analyses mathématiques correspondantes ainsi que les outils de simulation employés pour

étudier leurs effets. Les codes de simulation incluent le code MADX, le code SAD (pouvant être utilisé pour l'étude de l'effet de charge d'espace, de l'effet de champ de sillage, du rayonnement synchrotron et des désalignements) et le code PLACET (utilisé pour l'étude de la RSE dans les aimants dipôles et les désalignements). Enfin, nous présentons les applications des LINACs électroniques RF. Selon la gamme d'énergie du faisceau d'électrons, les applications peuvent être divisées en trois catégories.

1. Elles peuvent fonctionner comme des injecteurs pour des collisionneurs de physique des hautes énergies (HEP) ou des sources lumineuses. L'énergie du faisceau est de plusieurs centaines de MeV à plusieurs GeV, voir des centaines de GeV).
2. Les LINACs d'électrons de moyenne énergie avec une gamme d'énergie de 50 MeV à environ 300 MeV sont généralement envisagés pour les installations ou les plates-formes de R&D pour des études multidisciplinaires de nouvelles technologies d'accélérateur.
3. Les LINACs à basse énergie (de plusieurs MeV à 30 MeV) sont les machines les plus couramment utilisées dans les applications médicales (traitement des cancers), industrielles (traitement des matériaux, stérilisation) et de sécurité (criblage aux rayons X de la cargaison) dans nos sociétés modernes.

Pour les trois applications, nous présentons respectivement les projets suivants à titre d'exemples : (1) FCC-ee, CEPC, ILC et CLIC; (2) installations de R&D comme CLEAR et CLARA; (3) LINAC d'électrons de basse énergie pour les installations de radiothérapie à rayons X et les machines de contrôle de sécurité des passeports.

Depuis la découverte du boson de Higgs au LHC en 2012, il y a un intérêt croissant pour les mesures de précision de la physique des EW, y compris les propriétés du boson de Higgs. Cela pousse à des études de collisionneur électron-positon de haute luminosité et de haute précision. Jusqu'à présent, CLIC, ILC, CEPC, FCC-ee ont été proposés comme les futures installations possibles pour explorer la frontière HEP.

Le deuxième chapitre présente les études d'optique et les optimisations pour le système d'injecteur FCC-ee. Ce chapitre est le cœur de cette thèse. Nous introduisons d'abord le schéma de base du système d'injecteur FCC-ee. Il est composé de deux sources d'électrons (un canon RF de 6,5 nC et un canon thermionique de 10 nC), un LINAC électrons/positons (pour les énergies jusqu'à 6 GeV) et un 1,54 GeV bague d'amortissement. La structure initiale est basée sur le LINAC d'injecteur de SuperKEKB. Mais le schéma de SuperKEKB présente l'inconvénient que les électrons à faible émittance et les positons à plus grande émittance partagent les mêmes LINACs avec une configuration de cible à positons fixe. Cela peut entraîner une faible efficacité de production de positons et une mauvaise flexibilité du système.

Une mesure expérimentale récente nous donne un rendement en positons de $0,33 N_{e^+}/N_{e^-}$ contre $0,4 N_{e^+}/N_{e^-}$ conçu à la sortie de l'injecteur LINAC pour un faisceau incident d'électrons d'énergie 3,5 GeV et d'intensité de 10 nC. Pour éviter un tel problème potentiel dans l'injecteur FCC-ee, nous avons proposé trois schémas d'injection différents utilisant une structure de contournement pour l'accélération et la transmission séparées des électrons et des positons. Nous présentons chaque composant du système d'injection : les sources d'électrons (canon RF de 6,5 nC et canon thermionique de 10 nC), la section d'accélération (structures d'accélération en bande S conductrices normales et structures d'accélération en bande S à grande ouverture), trois structures optiques de bypass (dérivation de type Dogleg, dérivation de type chicane et schéma d'arc), des moyens de production de positons, un nouveau LINAC de positons de 1,54 GeV conçu pour accélérer les positons capturés et une structure en boucle de retournement pour transférer les positons vers l'anneau d'amortissement des positons. La difficulté de conception est de garder une bonne transmission. Par conséquent, les problèmes physiques mentionnés dans le premier chapitre doivent être bien pris en compte. Pour les conceptions de dérivation, la dynamique du faisceau concernant la dispersion et la chromaticité doit également être prise en considération pour un système achromatique et isochrone. Les différents modes de production de positons utilisant différentes cibles de positons et différents modes d'accélération (mode d'accélération et mode de décélération dans la première structure RF du LINAC de capture) sont également étudiés pour capturer plus de positons. Enfin, nous montrons que le rendement en positons avant l'anneau d'amortissement des positons dans la conception des trois schémas d'injecteurs est de $1,2 N N_{e^+}/N_{e^-}$ dans la simulation. Cela peut répondre ainsi à l'exigence du FCC-ee CDR avec $0,7 N_{e^+}/N_{e^-}$. Du point de vue des coûts, d'autres schémas d'injection envisageables ont également été proposés. Ils pourraient être étudiés en détail à l'avenir pour une machine potentielle aussi grande et complexe.

Le chapitre 3 présente la conception optique pour le LINAC et les lignes de faisceau d'une plate-forme multidisciplinaire R&D nommée PRAE. Cette plateforme vise à rassembler la physique subatomique, l'instrumentation, la radiobiologie et la recherche clinique autour d'un accélérateur pulsé à 50 Hz de haute performance délivrant le faisceau d'électrons à deux lignes de faisceau dans la gamme d'énergie de 50 à 70 MeV dans la première étape, et évolutif à 140 MeV dans la deuxième étape. La construction était prévue à Orsay, en France. La gamme d'énergie des électrons de 50 à 140 MeV sera adaptée pour effectuer une série de nouvelles études de faisabilité et de radiobiologie prometteuses pour les traitements de radiothérapie moins destructifs reposant sur des faisceaux de crayons submillimétriques fractionnés dans l'espace et d'autres techniques nouvelles (mini-faisceau de grille et faisceau FLASH). Dans le domaine de la physique subatomique, ils visent une contribution significative à l'effort mondial de la compréhension de l'éigme du rayon de charge protonique. L'expérience ProRad (Proton-

Radius) étudiera la diffusion élastique du proton électronique pour mesurer avec précision le facteur de forme électrique du proton dans une plage quadratique ultra-faible à quatre impulsions et encore inexplorée. En outre, une plate-forme d'instrumentation entièrement équipée fournira les outils nécessaires pour développer une prochaine génération de détecteurs utilisés dans de nombreux domaines de recherche tels que l'imagerie médicale, la physique subatomique et des particules, la technologie spatiale et l'astrophysique.

Les études de conception de la plate-forme sont divisées en deux parties: les simulations du LINAC et la conception optique des deux lignes de faisceau. Le LINAC d'électrons RF de 70 MeV est composé de structures d'accélération en bande S conductrices normales (identiques à celles utilisées dans FCC-ee) avec un gradient d'accélération d'environ 22 MV/m. Les deux lignes de faisceau ont été conçues en utilisant les mêmes codes (MADX et PLACET) que nous utilisé dans FCC-ee. La ligne de faisceau VHEE sera utilisée pour l'étude préclinique de radiothérapie.. La ligne de faisceau ProRad sera dédiée à l'expérience de mesure du rayon de proton. La ligne de faisceau VHEE est une structure en Dogleg composée de deux dipôles et de plusieurs quadripôles. Le faisceau sortant de cette ligne de faisceau est utilisé pour deux types de modalités de radiothérapie : mini-faisceau de grille et faisceau FLASH. Dans les deux modalités, la simulation de l'interaction faisceau-eau a également été présentée pour étudier l'effet potentiel du traitement. La ligne de faisceau ProRad est une structure en chicane, composée de 4 dipôles, avec un collimateur au milieu de la structure pour obtenir une petite diffusion d'énergie.

La conception de l'optique et les technologies d'accélération appliquées sont présentées dans le manuscrit, dans le cadre des développements actuels et les applications des LINACs d'électrons RF dans la société moderne et de présenter une perspective pour l'exploitation future.

Mots-clés: Physique des accélérateurs, injecteur FCC-ee, projet PRAE, conception optique, optimisation, suivi de faisceau, rendement en positons

Abstract

In the last years there has been intense linear electron-accelerator development driven by different communities as the X-FEL community, the High Energy Physics (HEP) linear-collider community: ILC and CLIC as well as HEP circular-collider community: FCC-ee and CEPC. Furthermore, there are also many other applications from medical science to industry that will use such a linac as main accelerator. In all these studies, a high-efficient e-linac with energies from about 10 to over 1000 MeV is needed as driver or injector. Even if the linac technology to cope with the performances needed is very well known, an important R&D effort on more compact, simpler, cost-effective, efficient, robust and reliable designs is in progress. In this frame, this thesis will optimize the linac and its associated transfer lines in two cases:

1. The injector linac for FCC-ee (Future Circular electron-positron Collider), in particular the positron one.
2. The linac for an application platform known as PRAE project (Platform for Research and Applications with Electrons).

The Future Circular Collider (FCC) hosted by CERN, is an international collaboration to explore the feasibility of different particle collider scenarios with the aim of significantly increasing the energy and luminosity compared to existing colliders, in the search for new physics. In the case of FCC-ee, 2.13×10^{10} (3.2 nC) electron and positron particles per bunch are needed for the most demanding full filling of Z running mode in the conceptual design report (CDR). The baseline selection for FCC-ee injector linac is based on the SuperKEKB one, which gives us a positron yield of $0.2 N_{e^+}/N_{e^-}$ against $0.4 N_{e^+}/N_{e^-}$ design in recent experiment (After the replacement of the new Flux Concentrator since 2020, the latest measured positron yield reaches $0.33 N_{e^+}/N_{e^-}$). The main objective of this thesis is to perform the start-to-end design and optimization for beam production, acceleration and transport from the feeding electron source to the positron damping ring as well as to increase the efficiency and the flexibility of the positron production (the positron yield needs to be larger than $0.7 N_{e^+}/N_{e^-}$) for FCC-ee injector linac. A complementary study for positron target optimization using conventional target or hybrid target is also shortly summarized. Considered the drawbacks of the current

SuperKEKB injector scheme, three new different bypass scheme designs have been finished to transfer electron and positron particles separately for a better transmission and improved flexibility of the whole system, which finally could give us a positron yield of around $1.2 N_{e^+}/N_{e^-}$ at the positron damping ring in theoretical simulations. In conclusion, this work is a first step in the optimization of the FCC-ee injector system from the point of view of the efficiency of the transport and optics design. The various schemes proposed are based on established technologies and different paths for electrons and positrons are used in order to improve the efficiency of the transport from the point of view of losses and cost.

In the second part of this thesis, the design for a radiobiology and nuclear physics application linac platform PRAE (Platform for Research and Applications with Electrons) based on a high-quality pulsed electron beam of energy up to 70 MeV in phase 1 and 140 MeV in phase 2 has been realized. 2 nC electron bunches in the PRAE accelerator phase 1 are produced in a RF gun at 50 Hz frequency, post-accelerated by an S-band linac to 50-70 MeV and injected into the direct beam line plus a deviated line. The optics design of the beam lines has to be as flexible as possible to cope with different kinds of beam characteristics (beam size, energy, dispersion, current...) and operation modes depending on the application. The study of the different optics options and the implementation of these two beam lines as well as the beam-water interaction for pre-clinical studies for the case of the radiobiology experiments has also been done and presented in this thesis.

Keywords: Accelerator physics, FCC-ee injector, PRAE project, optics design, optimization, beam tracking, positron yield

Table of contents

List of figures	xv
List of tables	xxi
Symbols	xxiii
1 Introduction to RF electron linear accelerators and their applications	1
1.1 General concepts in RF electron linacs design	2
1.1.1 Beam acceleration in RF electron linacs	2
1.1.2 RF accelerating structures & essential parameters	6
1.2 Issues in optics design of RF electron linacs and beam transport systems	11
1.2.1 Space charge effect	11
1.2.2 Wakefields	12
1.2.3 Incoherent and coherent synchrotron radiation	15
1.2.4 Misalignments and corrections	17
1.3 Applications of RF electron linacs	19
1.3.1 Injector linacs for HEP Lepton Colliders	19
1.3.2 Multidisciplinary R&D facilities based on medium-energy RF electron linacs	25
1.3.3 Low-energy RF electron linacs	27
2 Optics studies and optimizations for FCC-ee injector system	29
2.1 Baseline injection scheme for FCC-ee	32
2.2 Electron source and positron production	40
2.2.1 Electron sources	40
2.2.2 Positron production	42
2.3 Linacs in the FCC-ee injector system	47
2.4 New injection schemes for FCC-ee injector linac	49
2.4.1 Dogleg scheme	49

2.4.2	Chicane scheme	74
2.4.3	Arc scheme	80
2.4.4	Comparisons and conclusions	84
3	Optics design for the linac and the beam lines of a multidisciplinary R&D platform PRAE	87
3.1	The linac simulation	90
3.1.1	The RF gun	90
3.1.2	The linac section	92
3.2	Two beam lines simulation	95
3.2.1	The VHEE Radiobiology beam line	96
3.2.2	The ProRad beam line	107
3.3	Conclusion	113
4	Summary and Conclusions	115
4.1	FCC-ee injector system	115
4.2	The PRAE platform	116
References		117
Appendix A Different accelerator simulation programs		127
A.1	SAD	127
A.2	MAD-X	127
A.3	PLACET	128

List of figures

1.1	Cylindrical pillbox cavities (disk-loaded waveguide)	2
1.2	TE and TM modes in rectangular and circular waveguides	3
1.3	EM field pattern of TM_{01} mode in a uniform cylindrical waveguide	3
1.4	Dispersion curve for a uniform waveguide (Brillouin diagram)[112]	4
1.5	Schematic drawing of a disk-loaded traveling wave structure [28]	5
1.6	Typical Brillouin diagram for a disk-loaded waveguide, showing fundamental accelerating mode operating at $2\pi/3$ phase shift per cell, and one branch of a higher-order HEM_{11} (HEM: Longitudinal Electric Mode) deflecting mode. [112]	5
1.7	(a) TW structure with matching input iris and matched load at output; (b) SW structure with total reflection at output end and matching input iris (steady state) [28]	6
1.8	Operation modes	9
1.9	Power and electric field change along a constant impedance structure	10
1.10	Space charge force	12
1.11	Schematic diagram of wakefield generation. (a) Before the beam passes through the discontinuity of the vacuum chamber; (b) The beam is passing through the discontinuity; (c) After the beam passes through the discontinuity. "e" represents the test charge that follows the beam and moves at the same speed, and "q" represents the beam charge [113]	12
1.12	Transverse wakefield effects. The upper figure represents single bunch effect and the lower figure represents the multi-bunch effect [112]	13
1.13	Synchrotron radiation (ISR and CSR) flux spectral distribution [114]	16
1.14	Model for the analytical treatment of one to one correction [105]	17
1.15	Schematic layout of the FCC-ee complex [36]	21
1.16	Schematic layout of the CEPC complex [59]	22
1.17	Schematic layout of the CEPC injector [79]	22
1.18	Schematic layout of the ILC in the 250 GeV staged configuration [20]	23

1.19 Schematic layout of the CLIC complex at 380 GeV [97]	24
1.20 The CLEAR facility for VHEE testing [27]	25
1.21 The CLARA facility [78]	26
1.22 Low-energy electron linac applications. Left: an electron medical linear accelerator (Photo: Varian Medical Systems) [108]; Right: Electron beam technology for sterilising medical products [5]	28
1.23 X-ray data from Passport Systems scanning technology, which can detect a wide variety of materials (Photo from MIT News [2])	28
2.1 The conventional positron production chain	31
2.2 Schematic layout of the FCC-ee injector complex	32
2.3 The SuperKEKB injector linac [67]	33
2.4 The SuperKEKB positron target [116]	34
2.5 Beam sizes, orbits and phase space plots before the positron target for the SuperKEKB injector calculated with SAD (for electron beam not serving for positron production). Top: transverse betatron function, beam envelope and the position deviation; Bottom: six dimensional phase space of ideal beam	35
2.6 Beam sizes, orbits and phase space plots of the produced positron beam after the positron target for the SuperKEKB injector calculated with SAD. Top: transverse betatron function, beam envelope and the position deviation; Bottom: six dimensional phase space of ideal beam	36
2.7 Parameters of the electron/positron beam before/after the positron target in SuperKEKB	37
2.8 The FCC-ee injector linac baseline	37
2.9 The 1.54 GeV (section 1) electron linac design in the FCC-ee injector system baseline calculated with SAD code [86]	38
2.10 The 1.54-6 GeV (section 2 + section 3) electron linac design calculated by SAD [86]	39
2.11 Schematic drawing of the S-band RF gun with parallel coupling accelerating structures of the FCC-ee baseline injector system [36]	40
2.12 Sketch layout of the 10 nC thermionic gun and pre-injector system for FCC-ee baseline inspired by the SuperKEKB injector. Others are beam monitors (screen monitor: PRM, and current monitor: WCM) and components of the beam transport system (magnetic lens: ML, focusing coil: FC, and quadrupole magnet: QM) [87]	41
2.13 Positron production process	43

2.14 Two different positron systems considered for positron production in the FCC-ee injector system. Top: hybrid target scheme; bottom: conventional target scheme	45
2.15 Model of the flux concentrator at the FCC-ee positron source [36]	45
2.16 Normal conducting S-band periodic accelerating structures in BEPCII [73] . .	47
2.17 Large aperture S-band (LAS) accelerating structure in SuperKEKB [106] . .	48
2.18 Dogleg scheme for the FCC-ee injector linac	50
2.19 The SLC positron system [32]	51
2.20 Overall SLC layout [46]	52
2.21 The electron injection chain of the dogleg scheme for the FCC-ee injector system	53
2.22 Beam optics of the 6 GeV electron linac for the dogleg scheme calculated with SAD	53
2.23 Phase space of 3.5 nC electron beam at the end of the 6 GeV electron linac for the dogleg scheme calculated with SAD	54
2.24 The positron production chain of dogleg scheme	54
2.25 Optics design of the 4.46 GeV electron linac in the dogleg scheme. Top: The 4.46 GeV electron injector linac twiss function with the 6.5 nC RF feeding electron source calculated by SAD; Bottom: The 4.46 GeV electron injector linac twiss function with the 10 nC thermionic electron feeding source calculated by SAD	55
2.26 Phase space at the 4.46 GeV electron linac exit in the dogleg scheme. Top: Phase space at the 4.46 GeV electron linac exit using the 6.5 nC RF feeding electron source calculated by SAD; Bottom: Phase space at the 4.46 GeV electron linac exit using the 10 nC thermionic gun calculated by SAD	56
2.27 Optics design of the dogleg bypass in the dogleg scheme calculated with MADX	58
2.28 Phase spaces before the positron target in the dogleg scheme (bunch head are in opposite directions in longitudinal phase for SAD and PLACET)	59
2.29 Misalignments impact study and CSR study before the positron target in the dogleg scheme	61
2.30 Positron source: Longitudinal phase space for different cases of positron production in the end of capture linac	63
2.31 Positron source: Phase space of case 3 at the end of the positron capture linac	64
2.32 The electron/positron separator chicane of SuperKEKB [66]	65
2.33 The schematic layout of the electron/positron separator chicane for FCC-ee positron system	65
2.34 Optics of the electron/positron separator chicane calculated with MADX . . .	66

2.35 Phase space at the end of the electron/positron separator chicane calculated with PLACET	66
2.36 Schematic drawing of the three FODO lattices in the 1.54 GeV (section 4) positron linac design for the dogleg scheme	68
2.37 Optics of the 1.54 GeV (section 4) positron linac in the dogleg scheme calculated with MADX. Top: betatron function; Bottom: beam envelope	69
2.38 The positron beam energy change along the 1.54 GeV (section 4) positron linac in the dogleg scheme	70
2.39 Phase space at the end of the 1.54 GeV (section 4) positron linac in the dogleg scheme calculated with PLACET	70
2.40 Optics of the turnaround loop in the dogleg scheme	71
2.41 R_{56} change along the turnaround loop	72
2.42 Optics design after the positron target in the dogleg scheme calculated with MADX and PLACET: Top plot: betatron function; Bottom plot: beam envelope evolution (This is the 10 nC thermionic feeding e^- gun case; the result is similar for the 6.5 nC RF feeding e^- gun)	73
2.43 Phase space at the end of the turnaround loop in the dogleg scheme	74
2.44 The Chicane scheme for the FCC-ee injector linac	75
2.45 The CEPC injector system and details of the positron production on the top (black color: electron beams; red color: positron beams) [79]	75
2.46 The electron injection chain of the chicane scheme for the FCC-ee injector system	76
2.47 Optics design of the 4.46 GeV electron linac in the chicane scheme calculated with SAD	76
2.48 Phase space of 3.5 nC electron beam at the end of the 4.46 GeV electron linac in the chicane scheme calculated with SAD	77
2.49 Optics design of the chicane bypass in the chicane scheme calculated with MADX	78
2.50 Phase space of the 4.46 GeV 3.5 nC electron beam at the chicane bypass exit calculated by PLACET	78
2.51 The CSR study of the chicane bypass calculated with PLACET	79
2.52 Phase space of 3.5 nC electron beam before injection into the PBR calculated by PLACET	79
2.53 Positron production chain of chicane scheme	80
2.54 Arc scheme for FCC-ee injector linac	81
2.55 The electron injection chain of arc scheme	81
2.56 The positron injection chain of arc scheme	82

2.57	Optics design of the before-target part in the arc scheme using the 10 nC thermionic electron gun calculated by SAD	83
2.58	Phase space of electron beam at the arc bypass exit using the 10 nC thermionic gun in the arc scheme calculated by SAD	83
2.59	Potential recommended modified schemes	86
3.1	Infrastructure and implantation of the PRAE accelerator	88
3.2	PRAE phase A	88
3.3	PRAE phase B	89
3.4	PRAE RF gun 3D design with solenoids [110]	91
3.5	Schematic drawing of the PRAE injector	92
3.6	PRAE HG accelerating structure 3D design calculated with CST [110]	93
3.7	A SLAC-type TW S-band periodic accelerating structure made by RI [95]	94
3.8	Normalized transverse emittances along the PRAE injector calculated with ASTRA (black vertical dashed lines indicate the boundary between each segment; the blue one corresponding ε_x is the same as the orange one (ε_y))	95
3.9	Beam size along the PRAE injector calculated with ASTRA [110]	96
3.10	Transverse phase space at the end of the PRAE injector calculated with RF-Track [110]	96
3.11	Sketch of PRAE phase A	97
3.12	Mechanical drawing of the PRAE platform	98
3.13	Beam optics design of the Radiobiology beam line for the 70 MeV Grid mini-beam calculated with MADX	99
3.14	Phase space at the end of the Radiobiology beam line for the 70 MeV Grid mini-beam calculated with PLACET	99
3.15	Sketch of the Grid mini-beam experiment	100
3.16	Horizontal beam profile along the longitudinal direction (left plot) and energy deposition on the x-z plane (right plot) in the 30-cm-length water box for 70 MeV Grid mini-beam calculated with Geant4	100
3.17	Beam optics and phase space at the end of the Radiobiology beam line, for 140 MeV Grid mini-beam	101
3.18	Beam optics and phase space at the end of the Radiobiology beam line, for 300 MeV Grid mini-beam	102
3.19	Beam-water interaction simulation in Grid mini-beam experiment calculated with Geant4	103
3.20	Optics designs for the FLASH beam in the Radiobiology beam line using Method 1 (top) and Method 2 (bottom)	105

3.21 Sketch of the FLASH beam experiment	106
3.22 Beam-water interaction simulation in FLASH beam experiment calculated with Geant4	106
3.23 Sketch of the ProRad beam line	108
3.24 Sketch of Energy Compressor System (ECS)	108
3.25 Optics design for the ProRad beam line of PRAE calculated with MADX	110
3.26 Phase space at the end of the ProRad beam line of PRAE calculated with PLACET	110
3.27 The comparison of the beam energy distribution in the ProRad beam line between with and without collimator	111
3.28 The comparison of transverse distribution in the ProRad beam line between with and without collimator. Left: the horizontal beam size (x) distribution; Right: the vertical beam size (y)	111
3.29 The beam distributions for 100 machines of the ProRad beam line with the element imperfection level of $100 \mu\text{m}$ and $100 \mu\text{rad}$. Left: the energy spread distribution for machines with surviving particle percentage larger than 20%; Right: the number of surviving particle distribution of the 100 machines (initial particle: 10,000)	112
3.30 The machine distributions for the imperfection of $500 \mu\text{m}$ and $500 \mu\text{rad}$ for the 100 simulated machines of the ProRad beam line after the one-to-one beam-based alignment correction	113

List of tables

2.1	Positron production in different colliders	30
2.2	FCC-ee injector parameters [88]	33
2.3	Parameters of the 1.54 GeV (section 1) linac	38
2.4	Parameters of the 1.54-6 GeV (section 2 + section 3) linac	39
2.5	Main parameters of the 6.5 nC RF gun [15]	41
2.6	Main parameters of the 10 nC thermionic gun [14]	42
2.7	Flux concentrator (FC) parameters for the FCC-ee injection system [36]	46
2.8	Normal conducting S-band accelerating structures parameters for the FCC-ee injector system	47
2.9	Large aperture S-band accelerating structures parameters	48
2.10	Main performance parameters for the 6 GeV electron injection chain in the dogleg scheme	51
2.11	Misalignments for the before-target elements in the dogleg scheme of the FCC-ee injector linac	60
2.12	Performances of the two feeding electron beams before the positron target in the dogleg scheme from tracking simulation with SAD code and PLACET code	62
2.13	Main parameters of the two accelerating structures used in the 1.54 GeV (section 4) positron linac for the dogleg scheme	67
2.14	Parameters of the three different FODO cells for the 1.54 GeV (section 4) positron linac design in the dogleg scheme	68
2.15	Main parameters of the 1.54 GeV (section 4) positron linac in the dogleg scheme	68
2.16	Summaries of the three new schemes injector linac as well as the baseline	85
3.1	Design performances of the beam at the end of the accelerating section in PRAE	91
3.2	The RF gun characteristics of PRAE	92
3.3	A SLAC-type TW S-Band accelerating structure parameters	93
3.4	Beam parameters at the exit of the PRAE injector	95

3.5 Beam performances in interactions with different materials for the Grid mini-beam and the FLASH beam experiments in the VHEE Radiobiology beam line	107
3.6 Misalignments for elements (bends, quads and the collimator) in the ProRad beam line of PRAE	112

Symbols

Acronyms / Abbreviations

AMD	Adiabatic Matching Device
ASTRA	A Space Charge Tracking Algorithm
BBA	Beam-Based Alignment
BBU	Beam-Breakup instability
BEPC	Beijing Electron-Positron Collider
BPM	Beam Position Monitor
BR	Booster Ring
CDR	Conceptual Design Report
CEPC	Circular Electron-Positron Collider
CERN	Conseil Européenn pour la Recherche Nucléaire; European Organization for Nuclear Research
CI	Constant Impedance
CLIC	Compact Linear Collider
CSR	Coherent Synchrotron Radiation
CST	Computer Simulation Technology
CTF	CLIC Test Facility
DC	Direct-Current
DFS	Dispersion-Free Steering

DR	Damping Ring
ECS	Energy Compressor System
eHGRT	electron High-energy Grid Radiation Therapy
EM	Electromagnetic
ESPP	European Strategy for Particle Physics
FCC-ee	Future Circular electron-positron Collider
FCC	Future Circular Collider
FC	Flux Concentrator
FEL	Free-Electron Laser
Geant4	GEometry ANd Tracking
HEM	Longitudinal Electric Mode
HEP	High Energy Physics
HFSS	High Frequency Structure Simulator
HG	High Gradient
HOM	Higher Order Modes
IHEP	Institute of High Energy Physics
IJCLab	Laboratoire de Physique des 2 Infinis Irène Joliot-Curie
ILC	International Linear Collider
IMNC	Imagerie et Modélisation en Neurobiologie et Cancérologie
IPNO	Institut de physique nucléaire d'Orsay
ISR	Incoherent Synchrotron Radiation
LAL	Laboratoire de l'accélérateur linéaire
LAS	Large aperture S-band
LEP	Large Electron-Positron Collider

LHC	Large Hadron Collider
Linac	Linear accelerator
MADX	Methodical Accelerator Design - X
NC	Normal Conducting
OTO	One-To-One steering
PBR	Pre-Booster Ring
PLACET	Program for Linear Accelerator Correction Efficiency Tests
PRAE	Platform for Research and Applications with Electrons
ProRad	Proton-Radius
PWFA	Plasma WakeField Acceleration
QWT	Quarter Wave Transformer
R&D	Research and Design
RF	Radio-Frequency
RMS	Root Mean Square
RT	Radiotherapy
SAD	Strategic Accelerator Design
SC	Super Conducting
SLC	Stanford Linear Collider
SR	Synchrotron Radiation
SW	Standing Wave
TBA	Triple Bend Achromat
TE	Transverse Electric mode
TM	Transverse Magnetic mode
TW	Traveling Wave

VHEE Very High Energy Electron

WFS Wakefield-Free steering

Chapter 1

Introduction to RF electron linear accelerators and their applications

In the last years there has been intense linear electron-accelerator development driven by different communities as the X-FEL community, the High Energy Physics (HEP) linear-collider community: ILC and CLIC as well as HEP circular-collider community: FCC-ee and CEPC. Furthermore, there are also many other applications from medical science to industry that will use such a linac as main accelerator. In all these studies, a high-efficient e-linac with energies from about 10 to over 1000 MeV is needed as driver or injector. Even if the linac technology to cope with the performances needed is very well known, an important R&D effort on more compact, simpler, cost-effective, efficient, robust and reliable designs is in progress.

Radio-Frequency (RF) electron linear accelerators (linacs) are a type of particle accelerators that accelerate electrons to a certain energy by subjecting them to RF electromagnetic (EM) fields along a linear path [70, 112, 111]. The RF accelerating field is either a traveling wave provided by the loaded waveguides, or a standing wave by the loaded cavities. Particles in linacs travel on a straight line and pass only once through the accelerating structures.

Compared with other accelerator types, RF linacs have the following features:

1. The beam injection (into the linacs) and extraction (from the linacs) are easier in RF linacs, compared to circular accelerators;
2. Charged particles can be boosted to very high-energies in RF linacs, while Direct-Current (DC) high-voltage accelerators usually have a DC voltage breakdown limitation and electron circular accelerators have a limitation of beam loss caused by the Synchrotron Radiation (SR).

3. They are mostly equipped by RF accelerating structures, not easy to be operated/maintained with high stability/reliability, and the construction/operation costs per unit beam power are expensive compared with circular accelerators.

There are many applications of RF electron linacs: (1) Injectors for High Energy Physics (HEP) colliders, including electron-positron circular and linear colliders; (2) Injectors for synchrotrons and SR light sources; (3) Radiotherapy (RT) accelerators for producing low-energy electrons for X-rays and high-energy electrons for direct RT or for producing medical radioisotopes; (4) Industrial irradiation facilities for various materials and products; (5) Linac-based Free Electron Laser (FEL), and so on. In this chapter, the beam dynamics and the design of such RF electron linacs including the downstream beam lines as well as the main applications nowadays will be introduced. In particular more detailed descriptions for two applications: (i) the injector linac optimization for FCC-ee (Future Circular electron-positron Collider), (ii) a linac platform for medical, industrial and instrumental applications - PRAE (Platform for Research and Application with Electrons), will be presented in the next chapters.

1.1 General concepts in RF electron linacs design

1.1.1 Beam acceleration in RF electron linacs

Most of the accelerating structures used in RF linacs are axisymmetric, periodic or quasi-periodic in their cell geometries. A pillbox-type cavity (disk-loaded waveguide) of such an accelerating structure is shown in Fig. 1.1. Different modes (TE and TM modes) of the EM wave in rectangular and circular waveguides are presented in Fig. 1.2. The longitudinal (axial) component (E_z) of the EM field in a waveguide is usually used to accelerate charged particles, so the TM (Transverse Magnetic) mode should be chosen.



Fig. 1.1 Cylindrical pillbox cavities (disk-loaded waveguide)

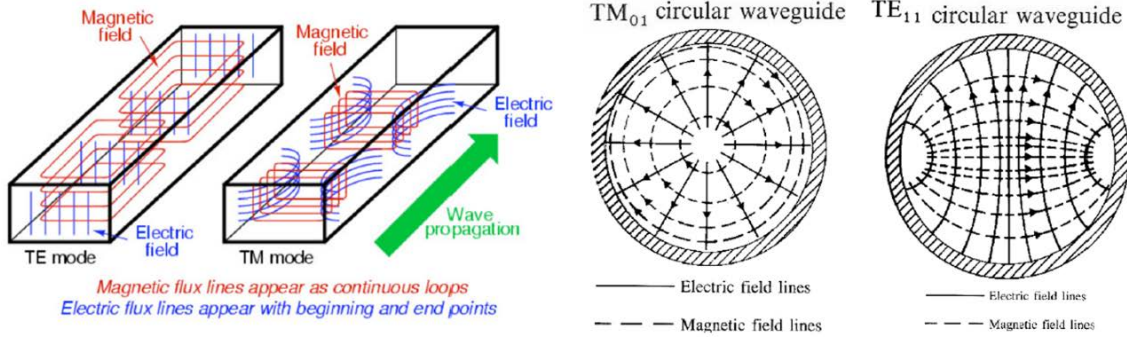
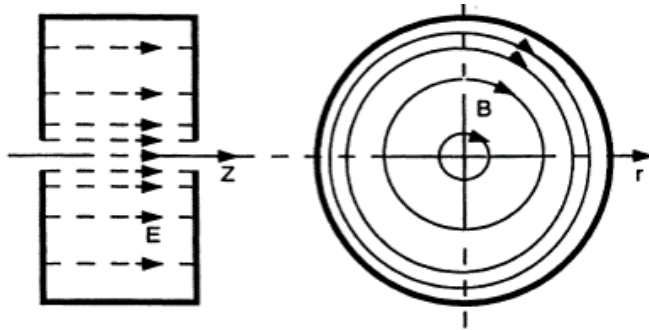


Fig. 1.2 TE and TM modes in rectangular and circular waveguides

Assuming an EM field travelling in a uniform cylindrical waveguide, its fundamental mode TM_{01} has the longitudinal component of the electric field E and the transverse component of the magnetic field B , as depicted in Fig. 1.3. Their distributions, which can be obtained by solving the well-known Maxwell and Helmholtz equations (wave equation) [96], are analytically described in the following expressions 1.1:

Fig. 1.3 EM field pattern of TM_{01} mode in a uniform cylindrical waveguide

$$\begin{aligned}
 E_z(r, z, t) &= E_0 J_0(k_c r) e^{j(\omega t - k_z z)} \\
 E_r(r, z, t) &= j E_0 \left[1 - \left(\frac{\omega_{cr}}{\omega} \right)^2 \right]^{1/2} J_1(k_c r) e^{j(\omega t - k_z z)} \\
 E_\theta &= 0 \\
 B_\theta(r, z, t) &= j \mu_0 E_0 J_1(k_c r) e^{j(\omega t - k_z z)} \\
 B_r &= B_z = 0
 \end{aligned} \tag{1.1}$$

where J_0 and J_1 are zero-order and first-order Bessel functions [10], respectively; $k_c = \omega_{cr}/c$, its frequency is the waveguide cutoff frequency ($\omega = \omega_{cr}$) and its corresponding phase velocity is the velocity of light ($v = c$).

According to the dispersion relation and wave number definition ($k^2 = k_c^2 + k_z^2$), we can obtain the propagation property as follow:

$$k_z^2 = \left(\frac{\omega}{c}\right)^2 - k_c^2 = \left(\frac{\omega}{c}\right)^2 - \left(\frac{\omega_{cr}}{c}\right)^2 \quad (1.2)$$

The Brillouin diagram [25] in Fig. 1.4 shows the relations among ω , k_z , and k_c .

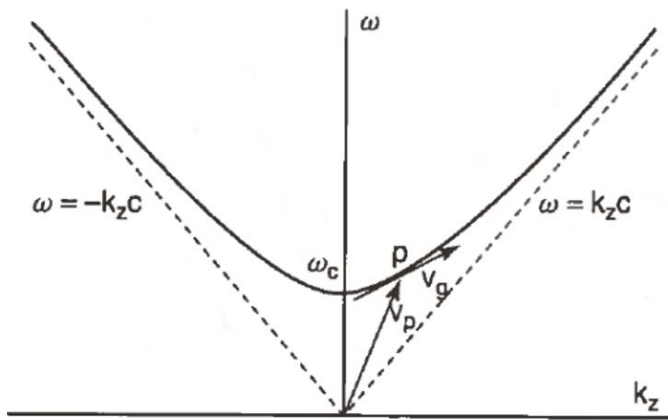


Fig. 1.4 Dispersion curve for a uniform waveguide (Brillouin diagram)[112]

According to equation (1.2), if TM₀₁ mode exists in the waveguide, k_z will be a real number. Then we can get $\omega > \omega_{cr}$. But in this situation, as depicted in the figure above, the wave phase velocity (v_p) will be larger than the velocity of light:

$$v_p = \frac{\omega}{k_z} = \frac{c}{\sqrt{1 - (\omega_{cr}/\omega)^2}} \geq c \quad (1.3)$$

Thus making it impossible to accelerate electrons. In order to make the phase velocity of the propagated waves in the accelerating structure $v_p < c$, we need to modify the structure to slow down the v_{phase} , for example, by introducing a periodic disk-loaded structure (traveling accelerating structure) [112, 70], as shown in Fig. 1.5.

Then according to Floquet theory [54] the wave amplitude can be periodically modulated:

$$\begin{aligned} E_z(r, z, t) &= E_L(r, z)e^{j(\omega t - k_0 z)}, \\ E_z(r, z + L, t) &= E_z(r, z, t)e^{-jk_0 L} \end{aligned} \quad (1.4)$$

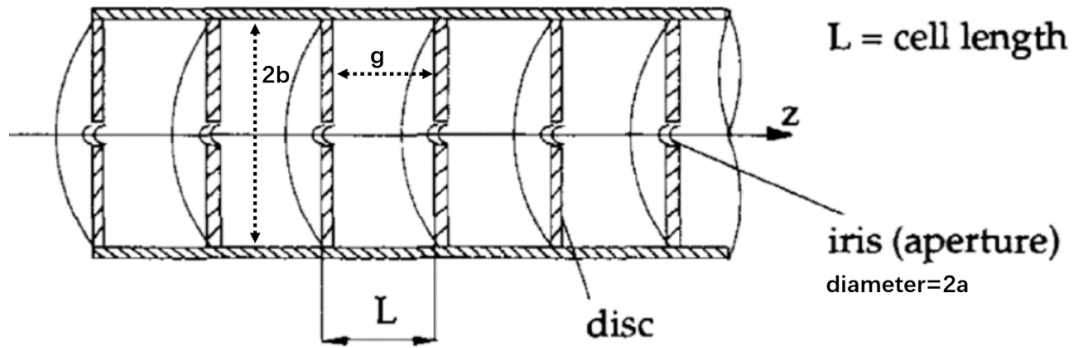


Fig. 1.5 Schematic drawing of a disk-loaded traveling wave structure [28]

where $E_L(r, z)$ is a periodic function with period L . After the expansion in Fourier series [107] of $F(r, z) = \sum a_n(r) e^{-j(2\pi n/L)z}$, we can get:

$$E_z(r, z, t) = \sum_n E_n J_0(k_n r) e^{j(\omega t - k_n z)} \quad (1.5)$$

where $k_n = k_0 + 2\pi n/L$, is the n^{th} space harmonic wave number, whose phase velocity can be expressed:

$$v_{p,n} = \frac{\omega}{k_n} = \frac{\omega}{k_0(1 + 2\pi n/k_0 L)} \leq c, \quad \text{if } n \text{ is big enough} \quad (1.6)$$

The Brillouin diagram for such a periodically disk-loaded structure consisting of infinite space harmonic waves is shown in Fig. 1.6.

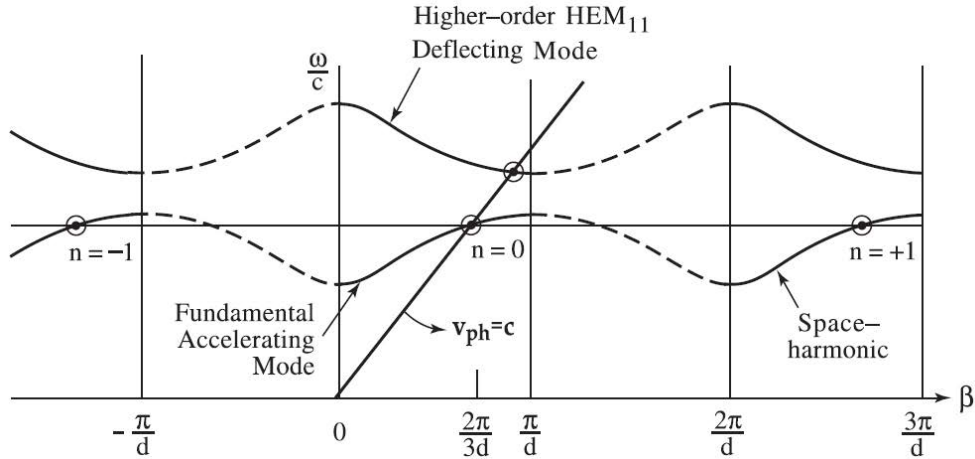


Fig. 1.6 Typical Brillouin diagram for a disk-loaded waveguide, showing fundamental accelerating mode operating at $2\pi/3$ phase shift per cell, and one branch of a higher-order HEM₁₁ (HEM: Longitudinal Electric Mode) deflecting mode. [112]

1.1.2 RF accelerating structures & essential parameters

TW and SW structures

There are many types of accelerating structures according to different applications [57]. Here two common types of structures used in RF linacs, namely **traveling wave (TW) structure** and **standing wave (SW) structure** [81, 4], as shown in Fig. 1.7, will be introduced.

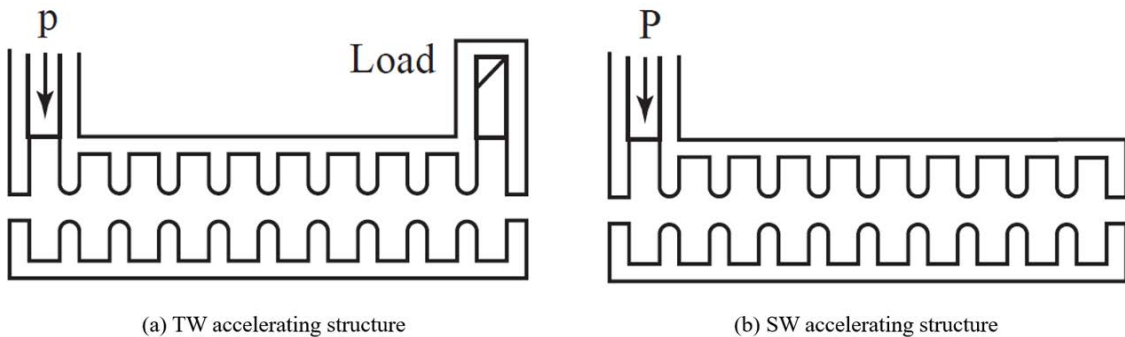


Fig. 1.7 (a) TW structure with matching input iris and matched load at output; (b) SW structure with total reflection at output end and matching input iris (steady state) [28]

The principal difference between TW and SW structures is how and how fast the structures are filled with RF power. TW structures are filled ‘in space’, which means that basically cell after cell is filled with power. SW structures on the other hand are filled ‘in time’: the EM waves are reflected at the end-walls of the structures and slowly build up a standing wave pattern at the desired amplitude. In applications that require very short beam pulses ($< 1 \mu\text{s}$), TW structures are much more power-efficient. For longer pulses ($> n \times 10 \mu\text{s}$) SW structures are usually preferred. Since the RF pulse in the TW structure can be very short, a higher peak field can be obtained compared to the SW structure. TW structures can theoretically be designed for non-relativistic particles, however, they are mostly used for relativistic particles in existing accelerators. Low-beta acceleration is typically performed with SW structures.

Essential parameters of a TW structure

As TW electron linacs are the main focus of this thesis, the essential parameters of a TW structure are introduced in the following.

Shunt-Impedance Z_s The shunt-impedance per unit length of the structure is defined as:

$$Z_s = \frac{E_a^2}{-dP_w/dz} (\text{M}\Omega/\text{m}) \quad (1.7)$$

It expresses, given the RF power loss per unit length ($-dP_w/dz$), how high an electric field E_a can be established on the axis.

Quality Factor Q The unloaded quality factor of an accelerating structure is defined as:

$$Q = \frac{\omega U}{-dP_w/dz} \quad (1.8)$$

It describes the efficiency of the structure. Given the stored energy (U is the stored energy per unit length of structure), the higher the Q , the less the RF loss; or given RF loss, the higher the Q , the higher the E_a (since $U \propto E_a^2$).

Z_s/Q With the definitions of Z_s and Q , we can get

$$Z_s/Q = E_a^2/\omega U \quad (1.9)$$

It means, for establishing a required electric field E_a in a structure, the stored energy U required. Obviously Z_s/Q is independent of power loss in the structure.

Group Velocity v_g Group velocity is the velocity at which the field energy travels along the waveguide:

$$v_g = P_w/U \quad (1.10)$$

where P_w is the power flow, defined by integrating the Poynting vector ($\vec{S} = \vec{E} \times \vec{H}$) [90] over a transverse plane. For TM₀₁ mode,

$$P_w = \int_0^a E_r H_\theta 2\pi r dr \quad (1.11)$$

here a is the iris radius, and for this mode, $E_r \propto r$, $H_\theta \propto r$, $v_g \propto a^4$.

Attenuation Constant

$$\left. \begin{array}{l} Q = \frac{\omega U}{-dP_w/dz} \\ v_g = \frac{P_w}{U} \end{array} \right\} \rightarrow \frac{dP_w}{dz} = -\frac{\omega U}{Q} = -\frac{\omega P_w}{Q v_g} = -2\alpha_0 P_w$$

$$\frac{1}{P_w} \frac{dP_w}{dz} = -2\alpha_0 \quad P_w = P_0 e^{-2 \int_0^L \alpha_0(z) dz} \quad (1.12)$$

where $\alpha_0 = \frac{\omega}{2Qv_g}$ is the attenuation per unit length of the structure.

We define

$$\tau_0 = \int_0^{L_s} \alpha(z) dz \quad (1.13)$$

as the ratio of output power to input power for an accelerating section of length L_s , and determines the power loss per unit length:

$$\begin{aligned} P_{out} &= P_{in} e^{-2\tau_0} \\ \frac{dP_w}{dz} &= \frac{P_{in}}{L_s} (1 - e^{-2\tau_0}) \end{aligned} \quad (1.14)$$

We can see that, the larger the τ_0 , the smaller the output power, and hence the higher the rate of power use. The output power is usually absorbed by a load installed at the end of the section, as shown in Fig. 1.7(a).

For a constant impedance structure (discussed later), α_0 is a constant, therefore,

$$\begin{aligned} \tau_0 &= \alpha_0 L_s = \frac{\omega L_s}{2Qv_g} = \frac{\omega t_f}{2Q} \\ t_f &= \frac{L_s}{v_g}, \quad \text{the power filling time} \end{aligned} \quad (1.15)$$

Working Frequency f_0 The parameters mentioned above all have a connection with f_0 as follows:

$$\begin{array}{ll} \text{Shunt-impedance } Z_s \propto f_0^{1/2} & \text{Quality Factor } Q \propto f_0^{-1/2} \\ \text{Total RF peak power } P_{tot} \propto f_0^{-1/2} & \text{Minimum energy stored } Z_s/Q \propto f_0 \\ \text{RF energy stored } U \propto f_0^{-2} & \text{Power filling time } t_f \propto f_0^{-3/2} \end{array}$$

The final choice of f_0 is usually made as a compromise of all the above factors and by considering the available RF source as well.

Operation Mode The operation mode is specified by the RF phase difference between two adjacent accelerating cells. Some typical operation modes are shown in Fig. 1.8.

Cell length: $L_c = \lambda$ (0-mode); $L_c = \lambda/4$ ($\pi/2$ -mode); $L_c = \lambda/3$ ($2\pi/3$ -mode); $L_c = \lambda/2$ (π -mode). For a disk-loaded TW structure the optimum operation mode is the $2\pi/3$ -mode ($v=c$), in that it has the highest shunt-impedance.

Constant Impedance TW Structure

Each cell in the constant impedance TW structure has the same geometric sizes as well as Q , v_g , Z_s and α . According to equations (1.7) and (1.12), we can get

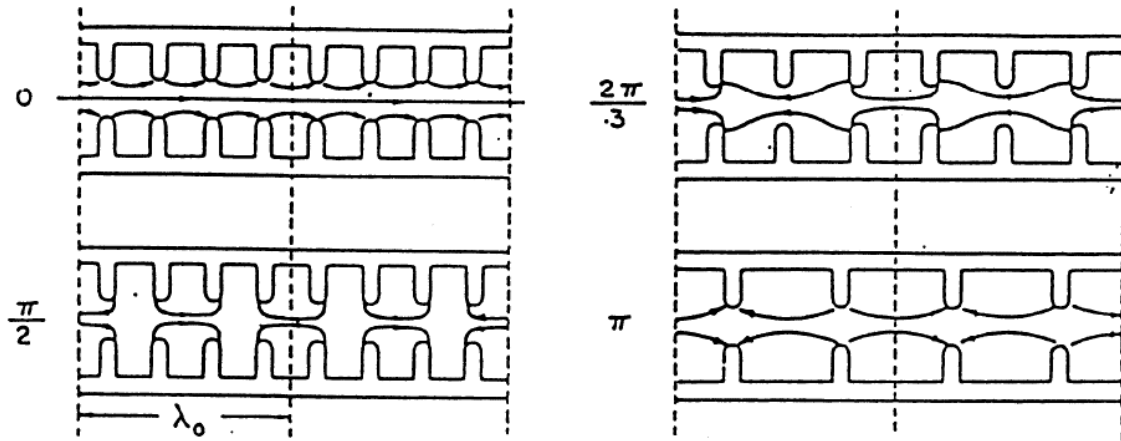


Fig. 1.8 Operation modes

$$\begin{aligned} E_a^2 &= 2\alpha_0 Z_s P_w \\ \frac{dE_a}{dz} &= -\alpha_0 E_a \end{aligned} \quad (1.16)$$

thereby getting

$$\begin{cases} P_w(z) = P_0 e^{-2\alpha_0 z} \\ E_a(z) = E_0 e^{-\alpha_0 z} \end{cases} \quad (1.17)$$

Thus in a constant impedance structure, $E_a(z)$ and $P_w(z)$ decrease along the z axis in a section, as described in Fig. 1.9. At the end of such a structure with length of L_s ,

$$\begin{cases} E_a(L_s) = E_0 e^{-\tau_0} \\ P_w(L_s) = P_0 e^{-2\tau_0} \end{cases} \quad (1.18)$$

Then the energy gain of an electron that “rides” on the crest of the accelerating wave and moves to the end of the structure is

$$\begin{aligned} \Delta W &= e \int_0^{L_s} E_a(z) dz = e E_0 L_s \frac{1 - e^{-\tau_0}}{\tau_0} \\ &= e \sqrt{2Z_s P_{in} L_s} \cdot \left(\frac{1 - e^{-\tau_0}}{\sqrt{\tau_0}} \right) \end{aligned} \quad (1.19)$$

To get the maximum ΔW , the two conditions need to be met: (1) Maximum Z_s ; (2) Maximum $(1 - e^{-\tau_0})/\sqrt{\tau_0} \rightarrow \tau_0 = 1.26$. We hope to decrease the power filling time $t_f = L_s/v_g = 2Q\tau_0/\omega$, so τ_0 should be less than 1.26.

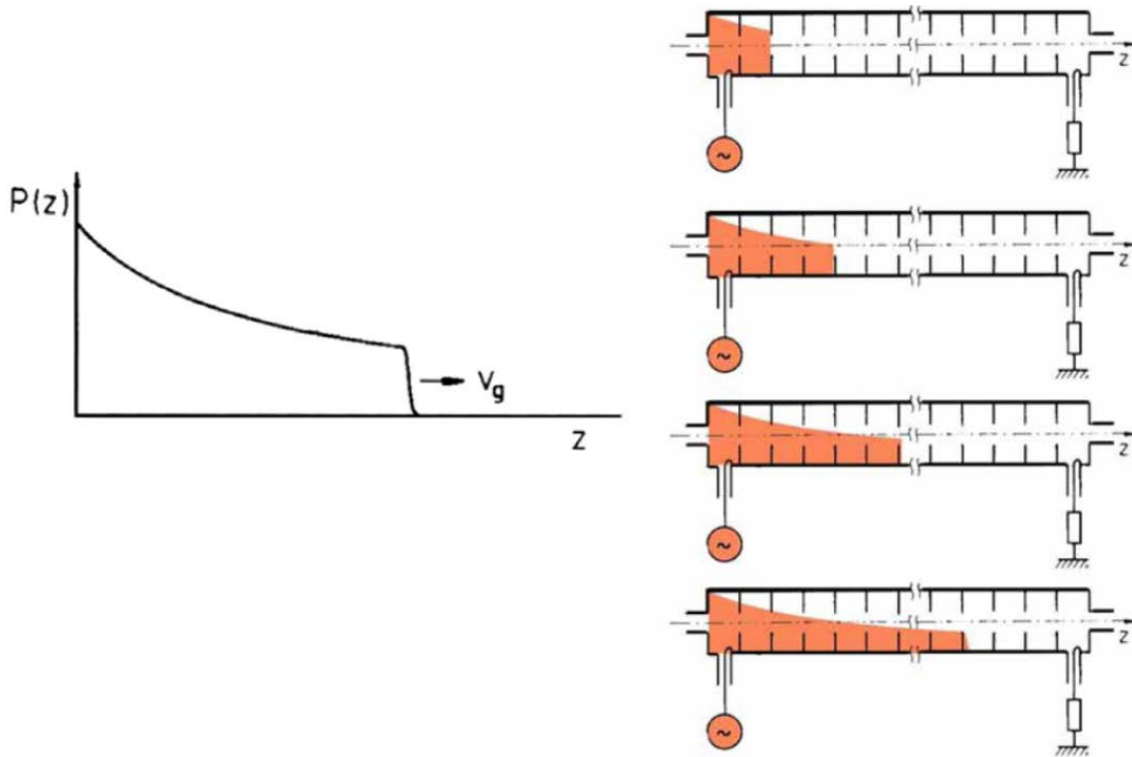


Fig. 1.9 Power and electric field change along a constant impedance structure

Constant Gradient TW Structure

In a constant gradient TW structure, $E_a = E_0$ is a constant along the structure (by changing its radii a and b), and we can further get $dP_w/dz = \text{const} \rightarrow \alpha_0(z) \neq \text{const}$. P_w can be written as follows:

$$P_w(z) = P_0 + \frac{P_{L_s} - P_0}{L_s} z = P_0 \left[1 - \frac{1 - e^{-2\tau_0}}{L_s} z \right] \quad (1.20)$$

Thus in a constant gradient structure, P_w should be linearly decreased along the structure. We can further get

$$\alpha_0(z) = \frac{1}{2L_s} \cdot \frac{1 - e^{-2\tau_0}}{1 - \frac{z}{L_s} (1 - e^{-2\tau_0})} \quad \text{and} \quad v_g(z) = \frac{\omega L_s}{Q} \cdot \frac{1 - \frac{z}{L_s} (1 - e^{-2\tau_0})}{1 - e^{-2\tau_0}} \quad (1.21)$$

The energy gain for an on-crest particle is

$$\begin{aligned}\Delta W &= e \int_0^{L_s} E_a(z) dz = eE_0 L_s \\ &= e \sqrt{Z_s P_0 L_s (1 - e^{-2\tau_0})}\end{aligned}\quad (1.22)$$

The maximum ΔW is determined by a combination of Z_s and t_f .

1.2 Issues in optics design of RF electron linacs and beam transport systems

1.2.1 Space charge effect

The space charge effect has a big impact in the low energy part of a linac. Considering that the electrons in a bunch are moving in the same direction inside the linac, assuming the charges are distributed axisymmetrically and the charge density distribution function is $n(r)$, each electron is affected by the other electrons in the bunch and the force consists of two parts:

(1) Statistic electric force eE_r (calculation according to Coulomb's law):

$$F_1 = eE_r = \frac{e^2}{\epsilon_0 r} \int_0^r n(r) dr \quad (1.23)$$

(2) Magnetic force (Lorentz force):

$$F_2 = -\frac{e}{c} v \times B_\theta = -\frac{e^2 v^2 \mu_0}{cr} \int_0^r n(r) dr \quad (1.24)$$

where B_θ is the magnetic field generated by the moving electrons (Ampère's law).

Hence the total transverse space charge force (see Fig. 1.10) is:

$$F_{sc} = e(E_r - \frac{v}{c} B_\theta) = eE_r(1 - \beta^2) = eE_r/\gamma^2 \quad (1.25)$$

If $\beta < 1$, then $F_{sc} \neq 0$; else if $\beta = 1$, $F_{sc} = 0$.

The longitudinal space charge force will cause an additional beam energy spread and the transverse space charge will lead to a normalized emittance growth. To partially cure these effects, a higher extraction voltage of the electron gun is usually preferable.

In this work the accelerator program SAD [3] has been chosen to study the space charge effect in the low-energy part of a linac.

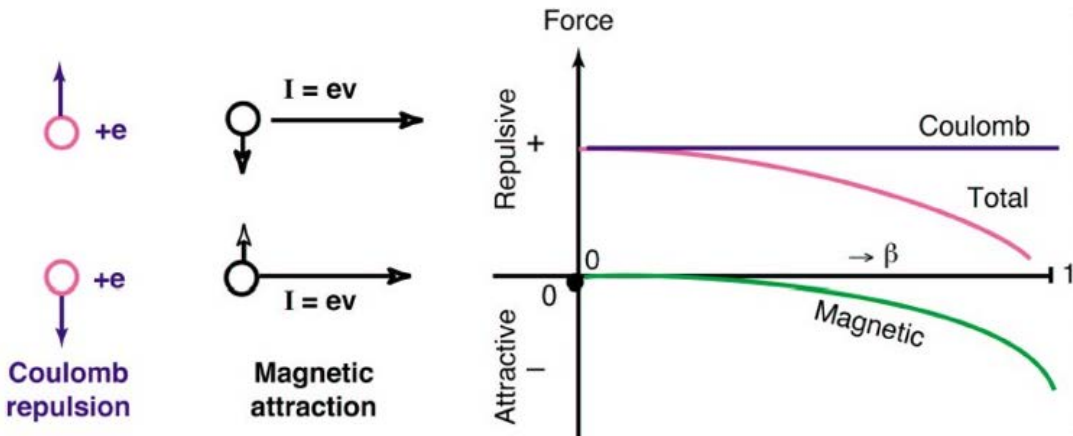


Fig. 1.10 Space charge force

1.2.2 Wakefields

EM fields are distributed around the moving charged particles. When the moving charged particles pass through a metal vacuum structure (discontinuous, smooth conductive beam pipes and non-ideal conductive pipes, etc.) of an accelerator component, they induce an EM field that decays with time, which is called wakefield. This process can be seen in Fig. 1.11. The wakefield in turn affects the beam, disturbing the beam motion, and further expanding the wakefield, leading to an instability of the beam, which we call collective instability.

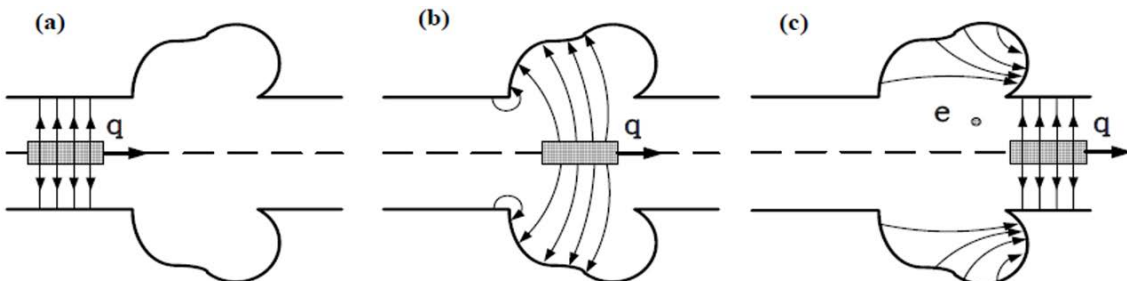


Fig. 1.11 Schematic diagram of wakefield generation. (a) Before the beam passes through the discontinuity of the vacuum chamber; (b) The beam is passing through the discontinuity; (c) After the beam passes through the discontinuity. "e" represents the test charge that follows the beam and moves at the same speed, and "q" represents the beam charge [113]

Two kinds of wakefields, namely single bunch (short-range) wakefield and multi-bunch (long-range) wakefield, are depicted in Fig. 1.12. In short-range wakefields, the EM fields induced by the head particles in a bunch will act on the tail particles in the same bunch

longitudinally and transversely, causing a beam head-tail instability. In long-range wakefields, it is the EM fields induced by the upstream bunch in a bunch train that act on the downstream bunches to cause multi-bunch instabilities, even beam-breakup instability (BBU).

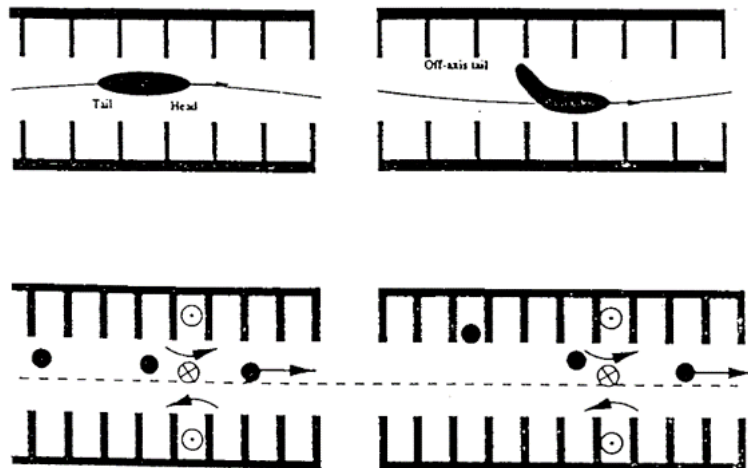


Fig. 1.12 Transverse wakefield effects. The upper figure represents single bunch effect and the lower figure represents the multi-bunch effect [112]

Single bunch longitudinal wakefield effect

A two-macroparticle model could be used to describe the single bunch wake effect. The energy variation due to the single bunch longitudinal wake [112, 111] for head and tail macro-particles (each having charge of $Ne/2$ and separated by a distance d) respectively are

$$\frac{dE_{head}}{dz} = -\frac{Ne^2}{4}W_{//}(0), \quad \frac{dE_{tail}}{dz} = -\frac{Ne^2}{4}W_{//}(0) - \frac{Ne^2}{2}W_{//}(d) \quad (1.26)$$

where $W_{//}$ is the longitudinal wakefield function. This equation can be used to estimate the averaged bunch energy loss (beam loading) in the accelerating structures and the energy difference between head and tail macro-particles leading to the additional beam energy spread.

To compensate the averaged bunch energy loss in the particular case of a linac RF structure, a little more RF power could be applied from the power source. In order to compensate the bunch energy spread, one can put the bunch center off the crest of the RF accelerating field, so the tail particles and head particles in the bunch respectively have higher and lower energy gain respectively.

Single bunch transverse wakefield effect

Using the two-macro-particle model, if the initial bunch offset x_0 at $z = 0$, then at $z = s$, the tail particle's further offset caused by the transverse wakefield function $W_{\perp}(d)$ of head particle is

$$\left\{ \frac{\Delta x}{x_0} \right\}_{max} = \frac{Ne^2 W_{\perp}(d)}{4kE} \times s \quad (1.27)$$

where k is the quadrupole focusing strength.

In a linac structure, the well-known BNS (Balakin-Novokhatsky-Smirnov) damping [19] can be employed to cure this effect. The principle is as follows: The accelerating phase of the bunch center is selected in the range of $0 < \varphi < \pi/2$ ($\varphi = 0$ is the phase crest), so that the tail particle in the bunch will gain less energy than the head particle. Since the focusing strength is inversely proportional to the beam energy, hence the tail particle will experience stronger focusing than the head particle in quadrupoles. The cost of using this scheme is a dilution of bunch energy spread. As we have seen from the formula (1.27), the single bunch transverse effect is inversely proportional to the bunch energy. Thus in the low energy part of the injector linac, one can employ the BNS damping scheme and then in the high energy part one can shift the accelerating phase of the bunch center to the normal range of $-\pi/2 < \varphi < 0$ so that the bunch energy spread can be damped soon after. Actually, BNS damping is not enough for the wakefield correction in most injector linacs, hence an orbit correction scheme may be adopted to cure the single bunch transverse wakefield effect, together with controlling the misalignment of the accelerating structures.

Multi-bunch longitudinal wakefield effect

For multi-bunch dynamics only the fundamental accelerating mode (beam loading) is important, for a constant gradient structure, the loaded accelerating gradient is

$$\frac{dE}{dz} = \frac{dE_0}{dz} - \frac{W_{//}(s)Q_b\tau}{1-e^{-2\tau}} \left\{ \frac{1-e^{-2\tau}}{2\tau} - e^{-2\tau} \right\} \quad (1.28)$$

where Q_b is the bunch charge, τ is the attenuation of the structure, $W_{//}(s)$ is the wake function at $z = s$.

To compensate the multi-bunch longitudinal wakefield effect, the simplest scheme is to ramp linearly the amplitude of the input RF accelerating field during the bunch train injection into the structure. For example, we could adjust the timing of the bunch train. If we let the first, the second and the third bunches enter the accelerating structures at 0.6 ns, 0.3 ns and 0 ns respectively, before the filling time of $0.8\mu\text{s}$, so that the input RF field in the structure is

ramped during the beam pulse and hence the most bunch to bunch energy variation in a short bunch may be compensated.

Multi-bunch transverse wakefield effects

BBU could be caused by the multi-bunch transverse wakefield, whose wake function $W_{\perp}(d)$ is dominated by one or a few resonators having large shunt-impedance $r_{\perp n}$ (the unit of $r_{\perp n}$: Ω/m):

$$W_{\perp}(d) = \sum_1^n \frac{r_{\perp n} \omega_n}{Q_n} e^{-\frac{\omega_n d}{2cQ_n}} \sin \left\{ \frac{\omega_n d}{c} \right\} \quad (1.29)$$

Controlling the misalignment of the accelerating structures and applying an orbit correction can be used to cure BBU effects.

A detailed analysis of the short-range wakefields for an accelerating structure with iris (see Fig. 1.5) will be made in the subsequent chapter of this work. The wakefield formulas are taken from reference [65] and the simulation code SAD is used to study the short-range wakefield effect.

1.2.3 Incoherent and coherent synchrotron radiation

Incoherent Synchrotron Radiation (ISR)

The EM radiation emitted from relativistic charged particles, especially electrons, as they are accelerated radially is called Synchrotron Radiation (SR). For a beam of N_e electrons or a circulating beam current $I = efN_e$, the total average radiation power [113] is

$$\langle P_{SR} \rangle = U_0 \frac{I}{e}$$

In more practical units, it can be expressed as

$$P_{SR}[kW] = \frac{88.5E^4 I[GeV \cdot A]}{\rho[m]} \quad (1.30)$$

where E is the electron beam energy, I is the beam current, and ρ is the bending radius of the dipoles. The total synchrotron radiation power scales like the fourth power of the beam energy and is inversely proportional to the bending radius.

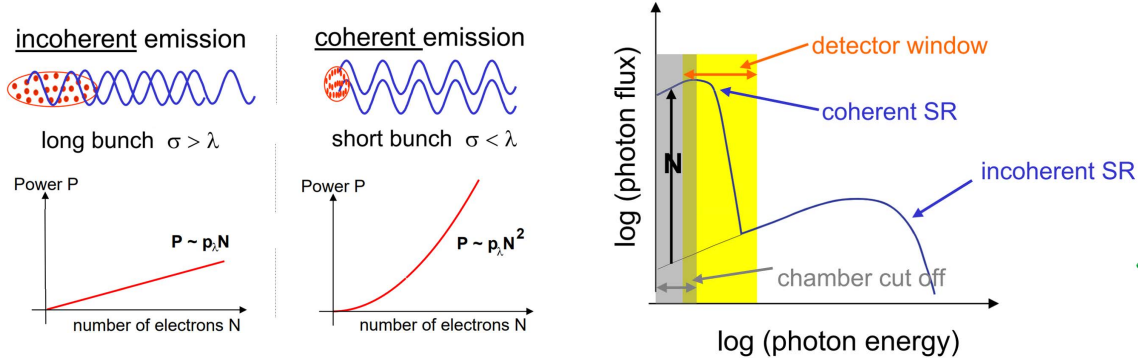


Fig. 1.13 Synchrotron radiation (ISR and CSR) flux spectral distribution [114]

Coherent Synchrotron Radiation (CSR)

CSR is the low-frequency component (typically up to the THz frequency range) of EM radiation emitted by ultra-relativistic particles in dipole magnets. The differences between ISR and CSR are shown in Fig. 1.13 [114]. The low-frequency part of the SR spectrum is amplified with regard to the high-frequency one, by the fact that electrons in the bunch are confined to a length scale of the order of, or shorter than, the radiation wavelength. This means that short electron bunches traversing a dipole with bending radius ρ can emit CSR at wavelengths longer than the bunch length. As a consequence, the electric field of radiation produced by individual electrons adds in phase. This gives rise to a total radiation intensity that is proportional to the number of electrons in the bunch squared. In contrast, at shorter wavelengths the radiation field adds incoherently, i.e., the total intensity goes linearly with the number of beam particles (ISR).

The total SR power emitted in the fully incoherent and fully coherent regime in a dipole magnet of bending radius ρ is, respectively [41]:

$$P_I = N \frac{e^2 c}{6\pi \epsilon} \frac{\gamma^4}{\rho^2}, \quad P_c = N P_I \quad (1.31)$$

where N is the particle number in the bunch. The total CSR power emitted by a Gaussian line-charge distribution moving along a dipole can be expressed as [83, 41]:

$$P_{CSR} \approx \frac{0.028c}{\epsilon_0} \frac{N^2 e^2}{\rho^{2/3} \sigma_z^{4/3}} \quad (1.32)$$

where σ_z is the RMS electron bunch length. It shows that CSR power is highest for shortest bunches. The CSR induces an average momentum loss and a momentum spread on the bunch. Beam optics techniques could be employed to suppress the CSR effect in case it causes serious beam energy loss [40].

One-dimensional (1-D) model for CSR with or without shielding [30] has been chosen to analyse the CSR effect in this work. The ISR and CSR effects in the bending areas of the beam transport systems have been studied using the accelerator simulation code PLACET [100] and the detailed results can be found in chapter 2.

1.2.4 Misalignments and corrections

In linacs, in order to better preserve the beam quality during acceleration, it is important to achieve a good alignment between all of its components, such as quadrupoles, RF cavities, Beam Position Monitors (BPMs), etc. There are several Beam-Based Alignment (BBA) techniques applied for the beam trajectory optimization and the corresponding steering magnets strength calculation, including the One-To-One (OTO) steering technique [105], the Dispersion-Free Steering (DFS) technique [94] and the Wakefield-Free Steering (WFS) technique [94, 72], etc. Among these techniques the most simple and straightforward one is the OTO steering, which steers the beam from quad center to center, and removes the betatron oscillation from quad focusing by pairing one corrector with the next downstream BPM. The OTO correction is mainly employed in this thesis.

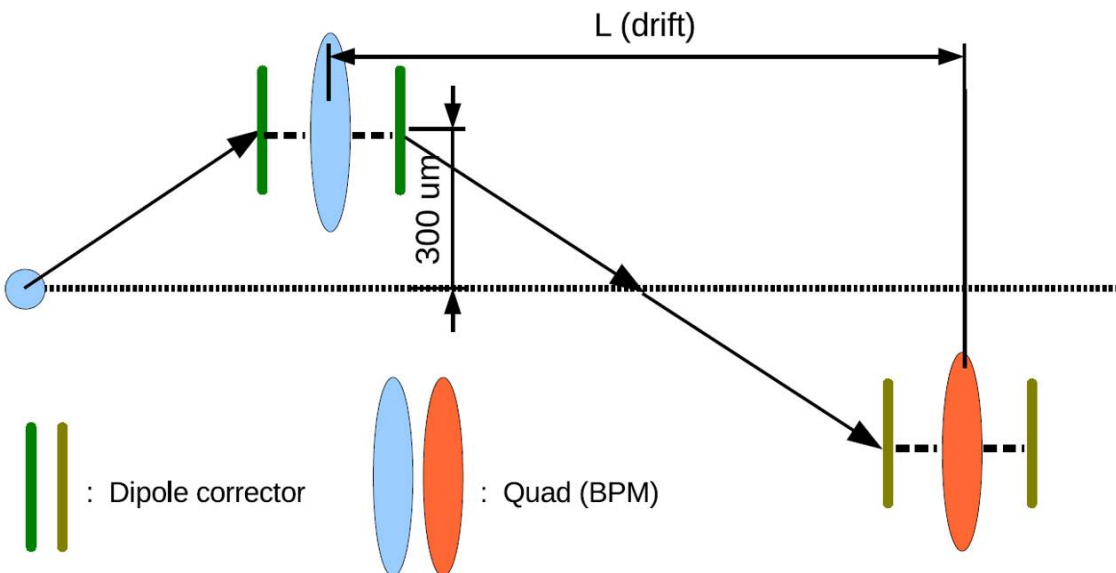


Fig. 1.14 Model for the analytical treatment of one to one correction [105]

We use the model as shown in Fig. 1.14 [105], initial longitudinal starting point is the middle of the drift in a FODO cell. The beam centroid is on the survey axis (treated as straight line here) at first. The original 6-D coordinates of the two particles are $(x_{00}, x'_{00}, y_{00}, y'_{00}, ct, 0)$ and $(x_{00}, x'_{00}, y_{00}, y'_{00}, ct, \delta_p)$. Assume after passing half cell (one quad) in the linac, the

difference of the transverse coordinates between two particles of different energy offsets in the bunch are $(\Delta x, \Delta x', \Delta y, \Delta y')$, and the coordinates of particle 1 are $(x_0, x'_0, y_0, y'_0, ct, 0)$, the coordinates of particle 2 are

$$x = x_0 + \Delta x, \quad x' = x'_0 + \Delta x', \quad y = y_0 + \Delta y, \quad y' = y'_0 + \Delta y', \quad ct, \quad \delta_p \quad (1.33)$$

Using the emittance formula $\varepsilon_y = \sqrt{\langle y^2 \rangle \langle y'^2 \rangle - \langle yy' \rangle^2}$, we can get the normalized emittance [105]:

$$(\gamma \varepsilon_y)^2 = \gamma^2 [(\sigma_y^2 + \langle \Delta y^2 \rangle) \cdot (\sigma_{y'}^2 - \langle \Delta y'^2 \rangle) - (\sigma_{yy'}^2 - \langle \Delta y \Delta y' \rangle)^2] \quad (1.34)$$

further get

$$\gamma \varepsilon_y = \gamma \varepsilon_{y0} \sqrt{1 + 2\Delta\gamma\varepsilon/\gamma\varepsilon_{y0}} \quad (1.35)$$

where

$$\Delta\gamma\varepsilon = \frac{\gamma}{2} \left(\frac{1 + \alpha^2}{\beta} \Delta y^2 + 2\alpha\Delta y\Delta y' + \beta\Delta y'^2 \right) \quad (1.36)$$

From Fig. 1.14, at the starting point, the beam gets a dipole kick which makes the beam center to travel through the next quadrupole center. The RMS normalized dipole corrector strength is $K_0 = 2\sigma_{quad}/L_{drift}$, where L_{drift} is the drift length between two quads, σ_{quad} is the RMS value of quadrupole offsets. After passing the corrector, the vertical divergences of particle 1 and particle 2 are respectively $\Delta y' = K_0$, $\Delta y'_1 = K_0(1 + \delta_p)$. The next corrector is used to cancel the kick from the first corrector and kick the beam to the second quadrupole center. At the first quadrupole, the coordinate y difference between particle 1 and 2 can be expanded into Taylor series [105]:

$$\Delta y = \frac{k_0 L}{1 + \delta_p} - k_0 L = k_0 L (-\delta_p + \delta_p^2 - \delta_p^3 + \dots) \quad (1.37)$$

where L is the length of quadrupole, and the divergence difference is

$$\Delta y' = K_1 \Delta y \quad (1.38)$$

with the equations above, we can get the new emittance after dispersive and chromatic growth in this small unit. With one unit containing two parts of two correctors and the next quadrupole (BPM), we can repeat this process along the linac and calculate the emittance. One thing to note: at the observatory point which is the exit of the quadrupole, the sign of α_y always is opposite to the sign of the normalized quadrupole strength K_1 . That means for vertical emittance, the cross term of Δy and $\Delta y'$ in formula 1.36 always cancels the contribution of the other two terms.

In the case of acceleration, the RMS energy spread will decrease as $\sigma_p E_0 / E$, and the formulas 1.36, 1.37 and 1.38 need to be updated. Here one unit is from the center of one quadrupole to the center of next quadrupole. The new formulas are as follows [?]:

$$\begin{aligned}\Delta y &= \frac{k_0 L}{1 + \delta_p} - k_0 L = k_0 L (-\delta_p + \delta_p^2 - \delta_p^3 + \dots) \\ \Delta y' &= K_1 \Delta y / 2 \\ \Delta \gamma \epsilon &= \frac{\gamma}{2} \left(\frac{1}{\beta} \Delta y^2 + \beta \Delta y'^2 \right) = \frac{\gamma}{2} \left(\frac{1}{\beta} + \frac{\beta K_1^2}{4} \right) \Delta y^2 \quad (\alpha = 0)\end{aligned}\tag{1.39}$$

The misalignments effect has also been taken into account in all the simulations of this work, assuming the elements in the linac are all misaligned according to a Gaussian distribution with standard deviation $\sigma_{pos} = 100 \mu\text{m}$. In such a situation, orbit steering technique [85, 49] simulated with SAD code and PLACET code has been performed to do the correction and the results are described in detail in chapters 2 and 3.

1.3 Applications of RF electron linacs

RF electron linacs are being applied in a wide energy range from several MeV to a possible TeV in many areas. Typically they can be divided into three categories according to their different purposes: (1) High-energy linacs can work as the injectors for HEP Lepton colliders or light sources, whose acceleration energy varying from hundreds of MeV to several GeV, even up to hundreds of GeV. (2) Medium-energy linacs with an energy range from 50 MeV to around 300 MeV are usually considered in R&D facilities or platforms for multidisciplinary studies of new accelerator technologies, novel clinical RT techniques, sub-atomic physics, astrophysics and so on. (3) Low-energy (several MeV \sim 30 MeV) linacs are the most commonly employed machines in medical (cancer therapy), industrial (material processing, sterilisation) and security (X-ray screening of cargo) applications of modern society. In this section a short summary of these interesting electron linacs' applications as well as the currently used RF technologies is given, to show the development of the modern linacs and present a prospect for the future exploitation.

1.3.1 Injector linacs for HEP Lepton Colliders

Particle physics recently has arrived at an important moment. The discovery of the 125 GeV Higgs boson at Large Hadron Collider (LHC) in 2012 completes the matrix of particles and interactions that has constituted the “Standard Model” for several decades. This model is a

consistent and predictive theory, which has so far proven successful at describing all phenomena accessible to collider experiments. On the other hand, several experimental facts require the extension of the Standard Model and explanations are needed for observations such as the domination of matter over antimatter, the evidence for dark matter and the non-zero neutrino masses. Theoretical issues that need to be addressed include the hierarchy problem, the neutrality of the Universe, the stability of the Higgs boson mass upon quantum corrections and the strong CP problem. The increasing interest in precision measurements of electroweak physics pushes high-luminosity and high-precision electron-positron collider studies. So far, CLIC (Compact Linear Collider) [12], ILC (International Linear Collider) [21], CEPC (Circular Electron Positron Collider) [59], FCC-ee (Future Circular electron-positron Collider) [36, 7] have been proposed as the possible future machines to explore the High Energy Physics (HEP) frontier.

No matter whether electron-positron linear or circular colliders, injector linacs are the essential components, which can provide electron and positron beams with desired energy, high charge density, low energy spread and short bunch length for the final collision of the highest possible luminosity in order to achieve high precision explorations and measurements for new physics.

FCC-ee

The FCC-ee [36, 7] is part of a more general study, known as FCC (Future Circular Collider), that comprises three different types of particle collisions: hadron (proton-proton) collisions FCC-hh, like in the LHC; the aforementioned electron-positron collisions FCC-ee, as in the former LEP; and proton-electron collisions FCC-he. The FCC project hosted by CERN (European Organization for Nuclear Research), is an international collaboration of more than 150 universities, research institutes and industrial partners from all over the world, to explore the feasibility of different particle collider scenarios with the aim of significantly increasing the energy and luminosity compared to existing colliders, in the search for new physics.

FCC-ee is a high-luminosity energy frontier electron-positron collider in a \sim 100 km tunnel at CERN, which can study the entire electroweak (EW) sector (Z and W bosons, Higgs boson, top quark) with centre-of-mass energies between 88 and 365 GeV. The schematic layout of FCC-ee baseline is shown in Fig. 1.15, in which the injector linac is located in the bottom left. In the FCC-ee injector baseline, a 6 GeV electron/positron linac is needed for the acceleration of about 3.2 nC (2.13×10^{10}) electrons and positrons per bunch at a repetition rate of 200 Hz [36]. Using the technologies already deployed at SLC [46], SuperKEKB [13], and other machines, normal conducting (NC) S-band (2.856 GHz) TW accelerating structures have been chosen as the basic acceleration unit, which could offer a high accelerating gradient of up to 25

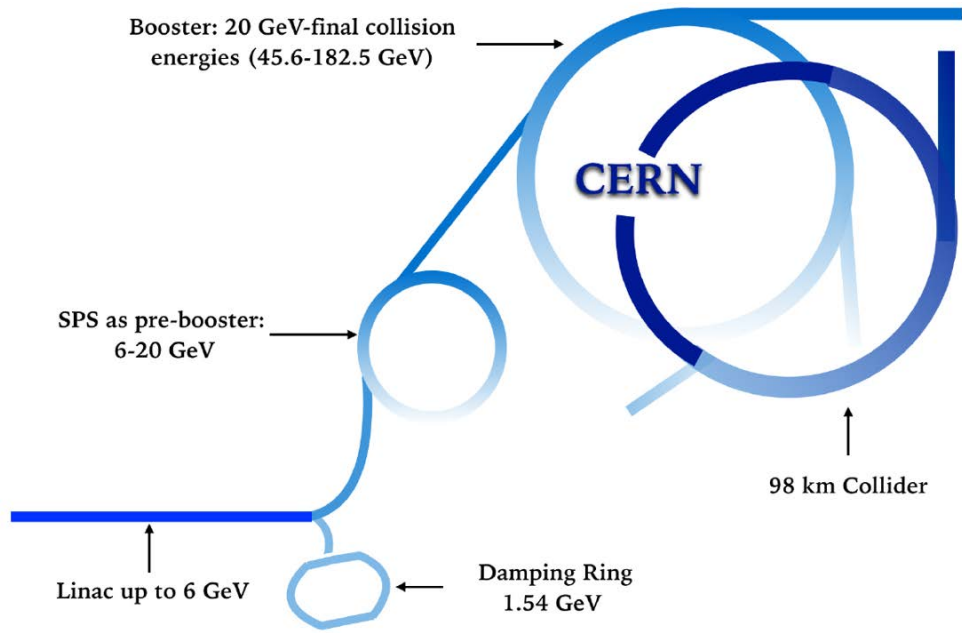


Fig. 1.15 Schematic layout of the FCC-ee complex [36]

MV/m. An alternative injector scheme for FCC-ee is the consideration of using a 20 GeV RF linac (a 6 GeV S-band linac + a 6-20 GeV C-band linac) to replace the baseline (6 GeV linac + 6-20 GeV pre-booster). An advantage is the accelerating gradient of C-band (5.7 GHz) linacs can reach to 50 MV/m [36], which could improve the robustness and flexibility of the injector. The specific design of the overall injector system for FCC-ee is one of the main focuses of this thesis, which is discussed in detail in chapter 2.

CEPC

The Circular Electron Positron Collider (CEPC) [59], a large international scientific project initiated and hosted by China, is located in a 100-km tunnel as shown in Fig. 1.16. CEPC is able to study the Z, the W, and the Higgs boson, with centre-of-mass energies from 90 to 250 GeV.

Three different proposed injector schemes [79] for CEPC can be seen in Fig. 1.17. The baseline scheme of CEPC injector is using NC S-band (2.860 GHz) linacs with an accelerating gradient of about 22 MV/m. The electron and positron beams with a charge of 3.3 nC per bunch are accelerated to 10 GeV and then injected into the booster ring. The second proposed scheme is like the FCC-ee alternative injector scheme mentioned above. A 20 GeV linac is employed using a combination of S-band (0-4 GeV) and C-band (4-20 GeV) linacs. The baseline scheme and the alternative second scheme can meet the requirements of CEPC injection. The third

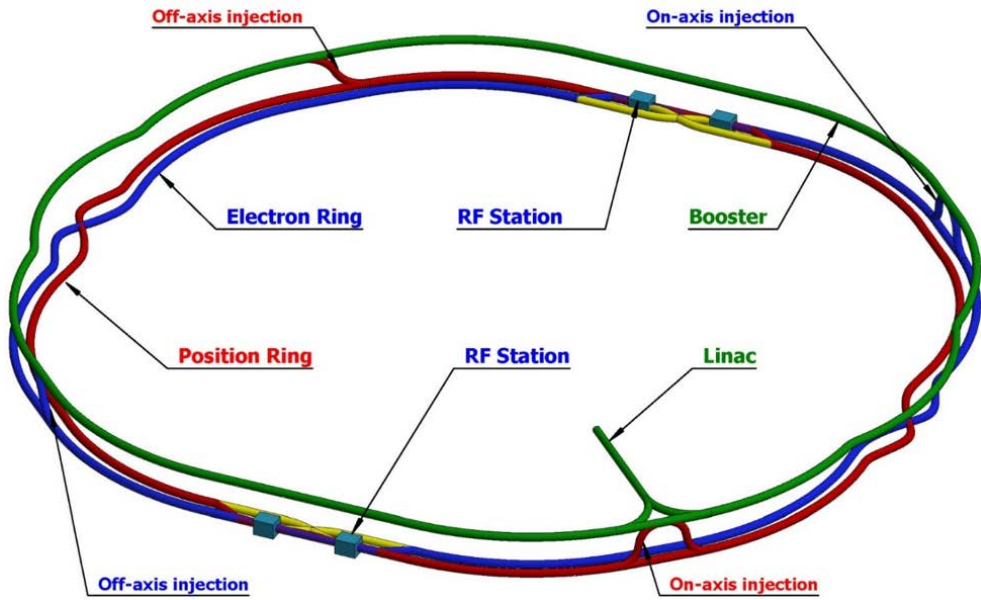


Fig. 1.16 Schematic layout of the CEPC complex [59]

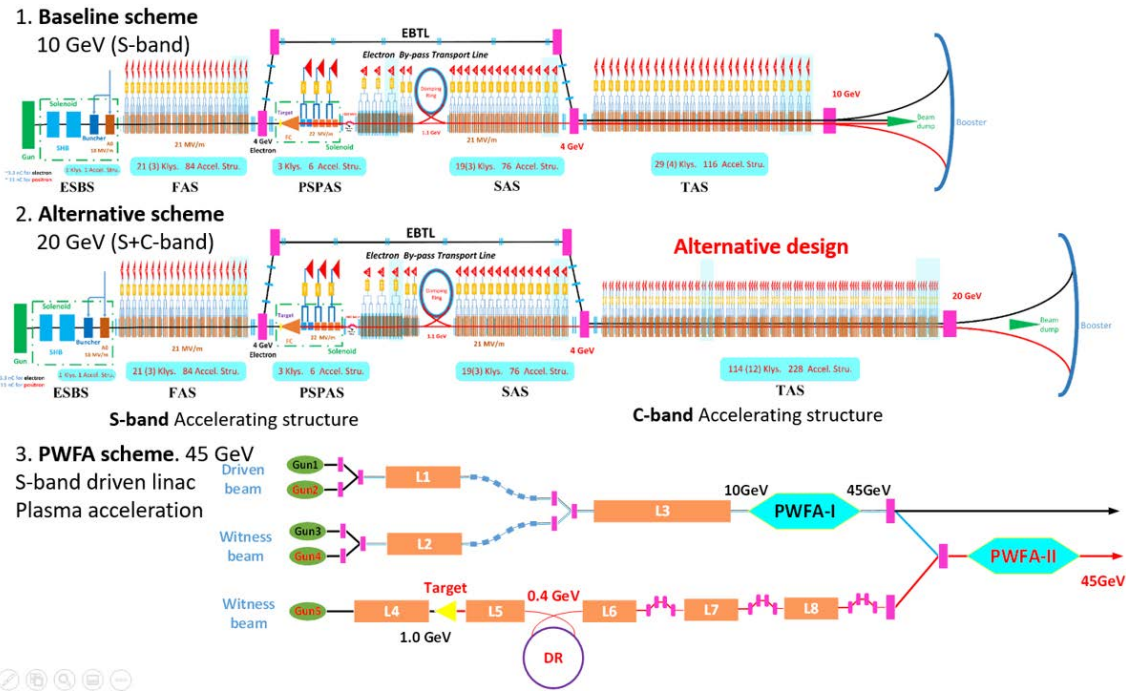


Fig. 1.17 Schematic layout of the CEPC injector [79]

scheme considers a beam-driven plasma wakefield acceleration (PWFA). It is a very challenging design for the acceleration of high charge beams with a short bunch length. The basic idea is

the passage of a relativistic (near light speed) electron bunch through a stationary plasma. The plasma is formed by ionizing a gas through field-ionization by the incoming driving electron bunch. This allows the production of meter-long, dense plasmas suitable for plasma wakefield acceleration, and greatly simplifies the experimental setup. The driving beam creates the plasma and drives a "wake" of charge. This effect produces a strong field that can accelerate the witness beam and the energy from the driven beam will be transferred to the witness beam.

ILC

The International Linear Collider (ILC) [21, 20] is a proposed high luminosity linear electron-positron collider hosted by Japan, focusing on the study of the Higgs boson with a centre-of-mass energy of 250 GeV (upgradable to 500 GeV, 1 TeV), based on L-band (1.3 GHz) superconducting radio-frequency (SCRF) accelerating technologies.

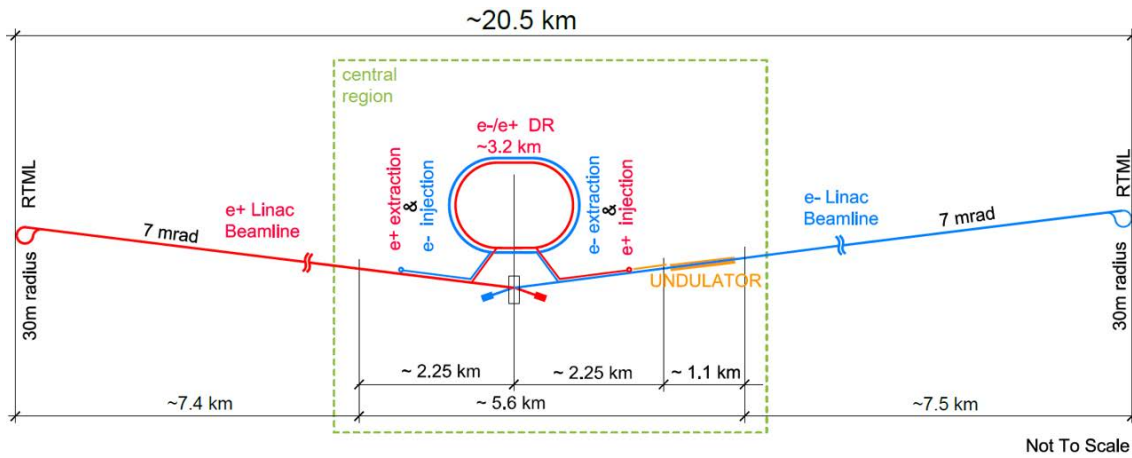


Fig. 1.18 Schematic layout of the ILC in the 250 GeV staged configuration [20]

The layout of ILC is shown in Fig. 1.18. The electron and positron sources are designed to produce 5 GeV beam pulses with a bunch charge that is 50 % higher than the designed 3.2 nC, in order to have sufficient reserve to compensate any unforeseen inefficiencies in the beam transport. The heart of the ILC accelerator consists of the two superconducting (SC) Main Linacs that accelerate both beams from 5 to 125 GeV with an accelerating gradient of 31.5 MV/m (35 MV/m improved to reduce cost) [20]. A new study result at JLab [56] of L-band (1.3 GHz) cavity shows a high gradient of 50 MV/m can be reached. Upgrade paths for ILC [58] using advanced accelerator technologies like PWFA to achieve high-gradient acceleration (>1 GV/m) are also being considered and investigated for the sake of costs and efficiency.

CLIC

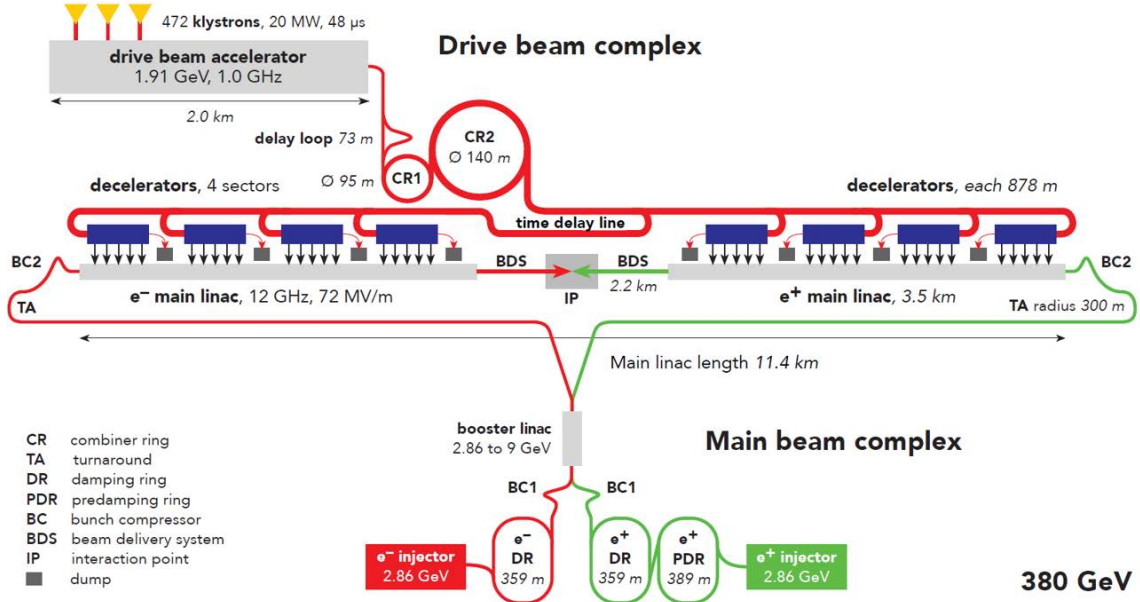


Fig. 1.19 Schematic layout of the CLIC complex at 380 GeV [97]

The Compact Linear Collider (CLIC) [12, 6] is a high-luminosity linear collider (like ILC) under development by the CLIC accelerator collaboration at CERN. CLIC uses a novel Two-Beam acceleration technique, with NC accelerating structures operating in the range of 70-100 MV/m. A comprehensive optimisation study of the CLIC accelerator complex was performed at collision energies of 380 GeV, 1.5 TeV and 3 TeV respectively, for a site length ranging from 11 to 50 km [33, 97]. The lowest centre-of-mass energy is set to 380 GeV for a better study of the Higgs boson and the top quark.

The schematic layout of CLIC at 380 GeV is shown in Fig. 1.19. The main-beam injector complex is a combination of several 2 GHz NC linacs to accelerate electron and positron beams up to 9 GeV with an accelerating gradient of about 20 MV/m [6]. The two Main Linacs (MLs), one for positrons and one for electrons, accelerate the beams from an initial energy of 9 GeV to the final energy of 190 GeV using NC accelerating structures with an RF frequency of 12 GHz (X-band) and a gradient of 72 MV/m (100 MV/m can be achieved) [97], which is chosen according to the optimisation of the total accelerator cost.

1.3.2 Multidisciplinary R&D facilities based on medium-energy RF electron linacs

CLEAR

The CLEAR (CERN Linear Electron Accelerator for Research, see Fig. 1.20) [27, 47] is an electron NC X-band linac located in the experimental area of the CLIC Test Facility 3 (CTF3) [37] at CERN, providing a testbed for new accelerator technologies and a versatile radiation source. The linac is capable of producing an electron beam with an energy 60-220 MeV, bunch charge 0.01-2 nC, relative energy spread < 0.2%, bunch length 200-1200 um, repetition rate 0.8-10 Hz, number of bunches 1-200 [102]. The beam line includes transport and focusing elements, an experimental area currently used to test CLIC two-beam modules, and a complete set of beam diagnostics, including spectrometers before and after the experimental area. A dedicated beam line for very high electron energy (VHEE) RT experiments is under study that could also be a test prototype for a larger clinical machine.



Fig. 1.20 The CLEAR facility for VHEE testing [27]

CLARA

The CLARA (Compact Linear Accelerator for Research and Applications) [31, 43, 78], as shown in Fig. 1.21, is a FEL test facility at Daresbury Laboratory, UK. The aim of CLARA is to experimentally demonstrate that sub-coherence length pulse generation with FELs is viable,

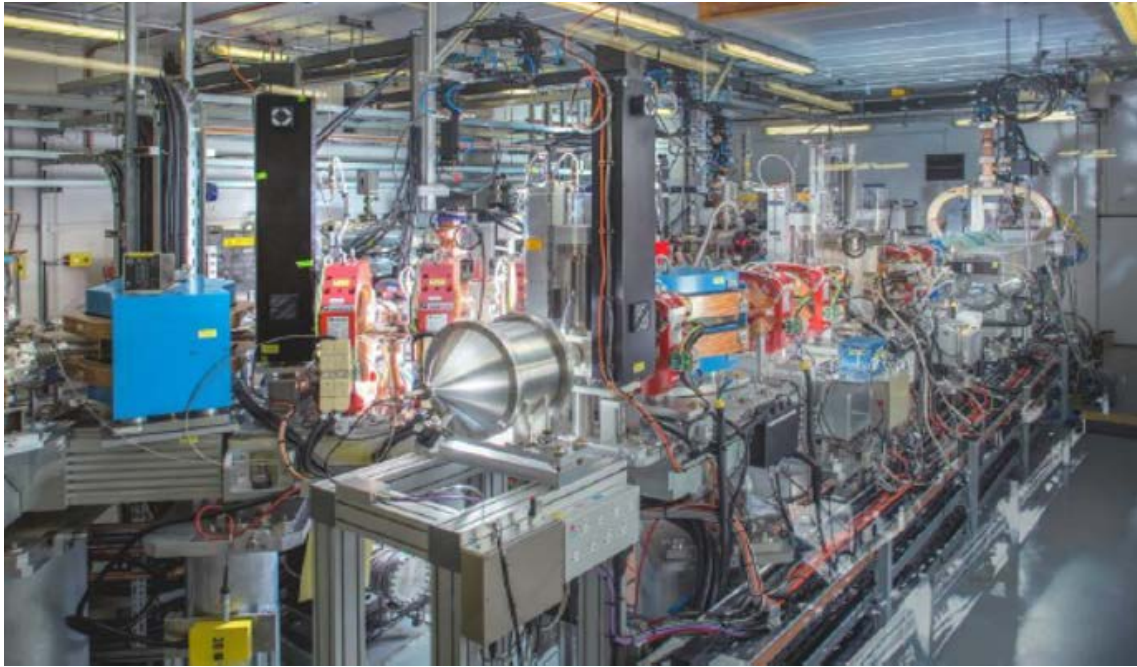


Fig. 1.21 The CLARA facility [78]

and to compare the various schemes being championed. CLARA Phase 1 is a NC S-band linac providing a high quality beam of energy up to 40 MeV with a repetition of 10 Hz and a bunch charge of 100 pC for FEL test and other novel concepts asked by academic and industrial users. CLARA Phase 2 will provide a high quality beam of energy up to 250 MeV for a possible multipurpose study including plasma accelerator research, Compton scattering study, clinical R&D study in VHEE RT, and etc. [31].

PRAE

Another potential medium-energy R&D facility - the Platform for Research and Applications with Electrons (PRAE) [39] has been proposed and studied at IJCLab, Orsay, which aims at creating a multidisciplinary R&D platform, joining various scientific communities involved in radiobiology, subatomic physics, instrumentation, particle accelerators, medical physics and clinical research around a high-performance S-band NCRF electron accelerator with beam energies up to 70 MeV (upgradable 140 MeV, even 300 MeV), in order to perform feasibility and radiobiological studies of novel promising RT techniques (like VHEE RT) as well as to provide the tools to develop a next generation of detectors used in many research areas such as medical imaging, subatomic and particle physics, etc. [50, 39]. The specific design of the linac

and two beam lines of PRAE as well as the beam-water interaction is the other main objective of this thesis, which is discussed in detail in chapter 3.

1.3.3 Low-energy RF electron linacs

RF electron linacs with an electron energy below 30 MeV play an important role in modern society.

They can work as RT machines to cure cancers, like X-ray therapy and electron therapy. X-rays are created by accelerating an electron beam to energies between 4 and 20 MeV with a linac, and impinging it on a heavy-metal target such as tungsten (W). The generated high-energy X-ray beam from this machine is then directed at the patient with the aid of collimation, so that the X-ray photons interact with the cancerous cells and disrupt molecular bonds, thus causing the cells to die. The electron beams themselves are sometimes also used in RT to treat skin cancers, as from current machines they do not penetrate very deeply; they are also used to directly treat surrounding tissues after tumour surgery (inter-operative radiation therapy, IORT) [5]. S-band linacs, which are a highly successful spin-off from high-energy and nuclear physics programs, are commonly used as the RT machines. Their compactness, efficiency and reliability have been key to their acceptance for clinical applications. A compact, low-cost electron medical linac is shown in left plot of Fig. 1.22.

They can be used in industrial applications, like sterilization (Fig. 1.22 right plot). At present only a limited number of radiation-sterilised products employ electron beam accelerators and the market share is still covered by gamma irradiators, but the situation is likely to change soon, due to the development of dual electron/X systems in which the electron beams are also used to create X-rays [5]. There are many emerging and exciting applications that need a higher beam power and efficiency to make them commercially viable. Some require very high power (MW class) and high energy (5 to 10 MeV) with high wall plug efficiencies [5]. Considering higher efficiency, more flexibility, less irradiation production cost per unit product and easier manipulation, more Rhodotrons[11] instead of linacs are used in the sterilization application recently.

They can also be applied in security checks (Fig. 1.23). X-ray transmission radiography is the established screening technique in security checks. It usually relies on an RF linac delivering an electron beam of several MeV energy. X-rays can be produced by bremsstrahlung, in which the electrons are decelerated by scattering inside a solid target. Such X-ray generators are typically a meter or so long, and are capable of delivering significant dose rates according to the penetration and regulation requirements for a particular transport method and objects to be scanned.



Fig. 1.22 Low-energy electron linac applications. Left: an electron medical linear accelerator (Photo: Varian Medical Systems) [108]; Right: Electron beam technology for sterilising medical products [5]

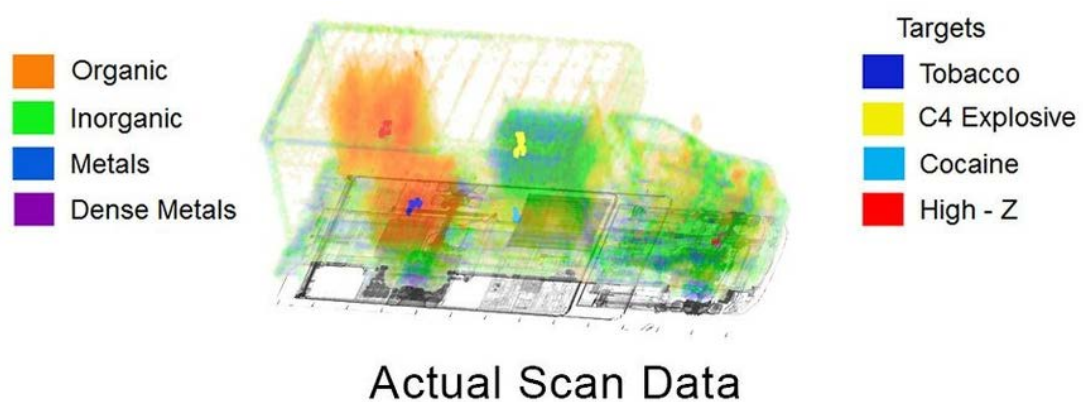


Fig. 1.23 X-ray data from Passport Systems scanning technology, which can detect a wide variety of materials (Photo from MIT News [2])

Chapter 2

Optics studies and optimizations for FCC-ee injector system

Since the discovery of Higgs boson at LHC [34, 35] in 2012, there is an increasing interest in precision measurements of EW physics including the properties of Higgs boson, which pushes high-luminosity and high-precision electron-positron collider studies. So far, CLIC [12], ILC [21], CEPC [59], FCC-ee [36] have been proposed as the possible future machines to explore the HEP frontier.

Large numbers of electrons and positrons are required in such large colliders. Electrons can be directly generated by photoelectric effect in RF or thermionic guns. While positrons are usually produced by bremsstrahlung and pair production in the process of electrons hitting a high Z (atomic number) positron target. The positron yield, which means how many positrons can be generated and captured when one electron is impinging on the target, is a crucial aspect in this process.

The positron schemes for past, current and future electron-positron colliders including SLC [32, 44, 46], LEP [24, 74], BEPC/BEPCII [89], KEKB/SuperKEKB [66, 116], CEPC [59, 79, 80] and FCC-ee [117], etc., are all based on such a positron source scheme as shown in Fig. 2.1 [44]: a high-intensity electron gun works as the feeding electron source for positron production by bremsstrahlung. The feeding electron beam is accelerated to a certain energy in a linear accelerator to hit the positron target made of high Z material (usually tungsten W). Afterwards, the positron beam, emerging from the target, gets captured and primarily accelerated in the capture system, and then extracted from a mixture of electrons, positrons and photons by a separator. Finally, another linac accelerates the extracted positron beam up to the injection energy of the positron damping ring (DR) for beam cooling. The performances of positron sources in different colliders are summarized in table 2.1.

Parameters	Colliders	SLC	LEP	SuperKEKB	CLIC	ILC	CEPC	FCC-ee baseline
e ⁻ beam energy @ target [GeV]	33	0.2	3.5	5/5 ³	126.5	4	4.46	
e ⁻ /bunch[10 ¹⁰]	3-5	0.5-30	6.25	0.52/0.44	2	6.25	4.2 (or 6.25) ⁴	
Bunch/pulse	1	1	2	352/312	1312	1	2	
Repetition rate [Hz]	120	100	50	50/50	5	100	200	
Target Scheme	γ production way for pair creation	bremssstrahlung	bremssstrahlung	Oriented Crystal (channeling)	helical undulator	bremssstrahlung	bremstrahlung \\\nOriented Crystal	
Target material	W74-Re26	W74-Re26	W	radiator (W) + converter (W74-Re26)	Ti	W	W74-Re26 \\\nradiator (W) + converter (W74-Re26)	
Target mobility	moving	fixed	fixed	fixed	moving	fixed	moving	
Capture system	AMD ¹	QWT ²	AMD	AMD	AMD	AMD	AMD	
Capture linac frequency [GHz]	2.856	2.999	2.856	1.999	1.3	2.860	1.999/2.856	
DR energy [GeV]	1.15	0.5	1.1	2.86	5	1.1	1.54	
e ⁺ yield @ injector exit	1.1	0.003	0.4	1	1.5	≥ 0.3	≥ 0.7	

Table 2.1 Positron production in different colliders

¹Adiabatic Matching Device²Quarter Wave Transformer³CLIC 380 GeV/ CLIC 3 TeV
⁴6.5 nC RF gun (or 10 nC thermionic gun)

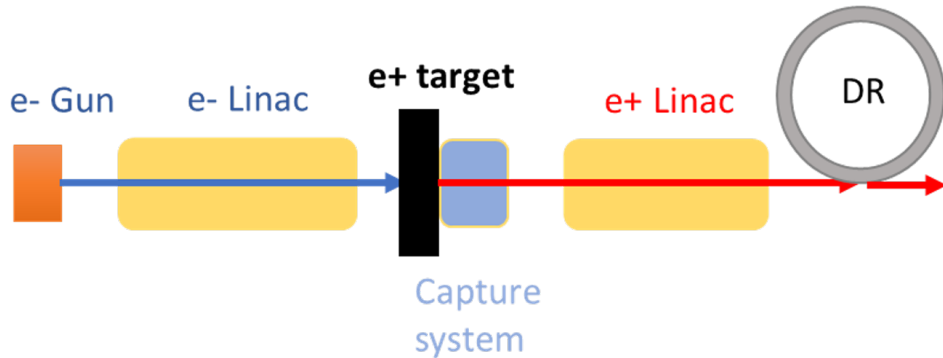


Fig. 2.1 The conventional positron production chain

In the case of FCC-ee, 2.13×10^{10} (3.2 nC, 3.5 nC has been selected for a margin) electrons and positrons per bunch are needed for the most demanding full filling of Z running mode (see Table 2.2). The baseline injection system for FCC-ee is based on the SuperKEKB positron production scheme [13]. In this scheme, electron and positron bunches are sharing the same linacs with a fixed target configuration and on-axis hole for electron beam passage. The main drawback of this scheme is the poor efficiency and flexibility. Recent experimental measurement gives a positron yield of $0.2 N_{e^+} / N_{e^-}$ against $0.4 N_{e^+} / N_{e^-}$ designed[64] (After the replacement of the new Flux Concentrator since 2020, the latest measured positron yield reaches $0.33 N_{e^+} / N_{e^-}$). It can be further improved after solving the discharge issues at dummy loads). The first objective of this work is to increase the efficiency and the flexibility of the positron production at FCC-ee injector.

Generally speaking, there are two ways to improve the positron yield in a positron source. One way is to optimize the overall design of the positron production chain, including electron gun, linacs and transfer lines, for avoiding excessive losses during the transport. The other way is the positron source (positron target + capture system) optimization for better positron yield. In this work, we will concentrate on the overall optimization of the positron production chain. A complementary study for positron source optimization is being made, and more details could be found in references [36, 117].

Considering the drawbacks of the current SuperKEKB injector scheme, in order to achieve a better performance and a higher positron yield, we proposed different bypass injection options to transfer electrons and positrons separately for a better transmission and the improved flexibility of the whole system.

The various schemes proposed are based on established technologies and different paths for electrons and positrons are used in order to improve the efficiency of the transport from the point of view of losses and cost.

2.1 Baseline injection scheme for FCC-ee

The schematic layout of the FCC-ee injector complex can be seen in Fig. 2.2, where the electron-positron injector linac is located in the bottom. The injector complex comprises two electron sources (6.5 nC RF gun and 10 nC thermionic gun), an electron/positron linac (for energies up to 6 GeV), a pre-booster synchrotron ring (PBR; In the current baseline, the Super Proton Synchrotron works as the PBR), accelerating beams from 6 to 20 GeV, and a full energy booster synchrotron ring (BR), integrated in the collider tunnel.

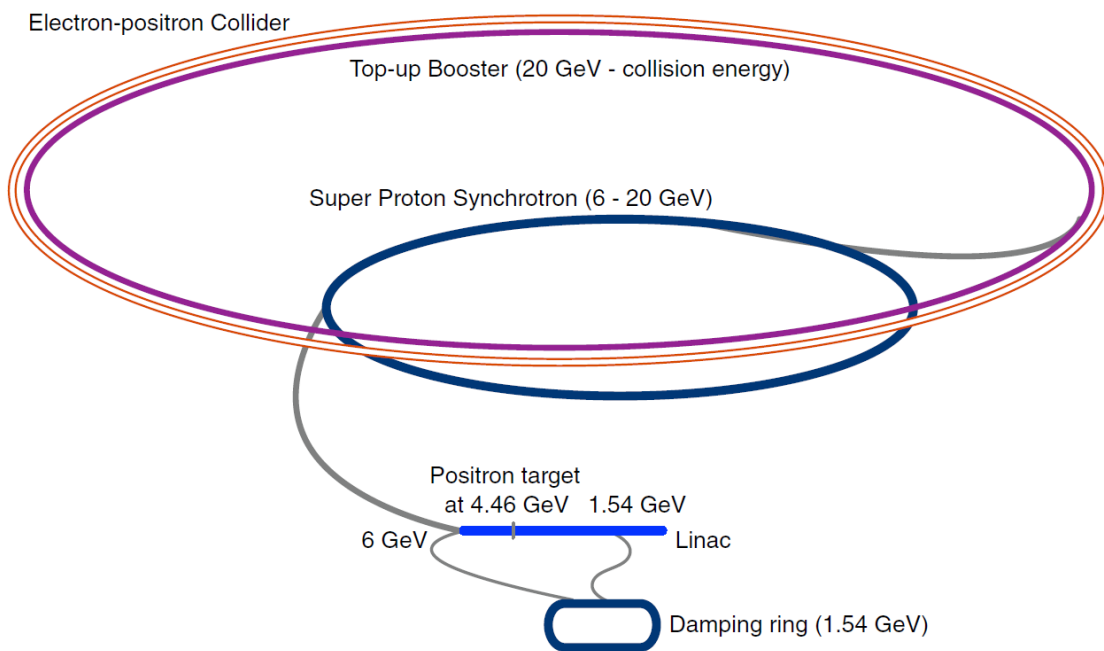


Fig. 2.2 Schematic layout of the FCC-ee injector complex

Table 2.2 contains a list of parameters for the injection schemes of the different collider energies and filling modes (top-up or full filling) for FCC-ee [36, 88]. The baseline parameters are established assuming a SuperKEKB-like linac [13] (S-band 2.856 GHz RF system) with 1 or 2 bunches per pulse and a repetition rate of 100 or 200 Hz. The most demanding full filling of Z running mode requires a linac bunch intensity of 2.13×10^{10} particles for both species.

The baseline selection for FCC-ee is inspired by the SuperKEKB injector, whose layout can be seen in Fig. 2.3 (green color for electron beam, pink color for positron beam). Two electron beams generated from the two guns (RF gun and thermionic gun) will go through the same linacs (noted as A, B, C, 1, 2, 3, 4 and 5) and the same transfer line (J-Arc) before injection into the downstream booster ring. The first electron beam emitted from the RF gun gains about 7 GeV energy in the injector, while the second electron beam with high intensity

Parameter (unit)	Z		W		H		$t\bar{t}$	
Beam energy (GeV)	45.6		80		120		182.5	
Type of filling	full	top-up	full	top-up	full	top-up	full	top-up
Linac bunches/pulse	2		1					
Linac repetition rate (Hz)	200		100					
Linac RF frequency (GHz)	2.856							
Bunch population (10^{10})	2.13	1.06	0.94	0.56	0.94	0.56	1.38	0.83
No. of linac injections	594/595		1000		328		48	
PBR bunch spacing (ns)	15/17.5/20		22.5		67.5		450	
No. of PBR cycles	14		2		1			
No. of PBR bunches	1188/1190		1000		393		50	
PBR cycle time (s)	3.3		5.4		3.6		0.8	
PBR duty factor	0.76		0.49		0.23		0.05	
No. of BR/collider bunches	16640		2000		328		48	
BR cycle time (s)	47.9		13		6.9		5.7	
No. of BR cycles	10	1	10	1	10	1	20	1
No. of injections/collider bucket	10	1	10	1	10	1	20	1
Total No. of bunches	16640		2000		328		48	
Filling time (both species) (s)	958.8	95.9	520	26	277.2	13.9	227.7	11.4
Injected bunch population (10^{10})	2.13	1.06	1.44	1.44	1.13	1.13	1.38	0.83

Table 2.2 FCC-ee injector parameters [88]

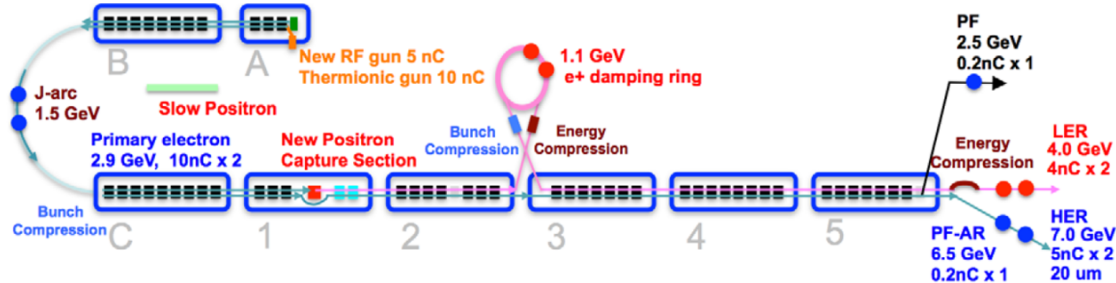


Fig. 2.3 The SuperKEKB injector linac [67]

from the thermionic gun is accelerated to the energy of 3.5 GeV to hit the positron target (the red box after the section 1 linac) to produce positrons. Afterwards, the created positrons get captured in the capture section, and gain a primary energy of 1.1 GeV in linac 2 before injection into the following 1.1 GeV positron damping ring. When the positron beam comes out of the damping ring, it will be further accelerated in the downstream linacs 3, 4 and 5. As mentioned above, in this scheme, electron and positron bunches are sharing the same linacs (linacs 2, 3, 4 and 5) with a fixed target configuration and on-axis hole (Fig. 2.4) for electron beam passage. The main drawbacks of this scheme are the poor positron production efficiency and the system

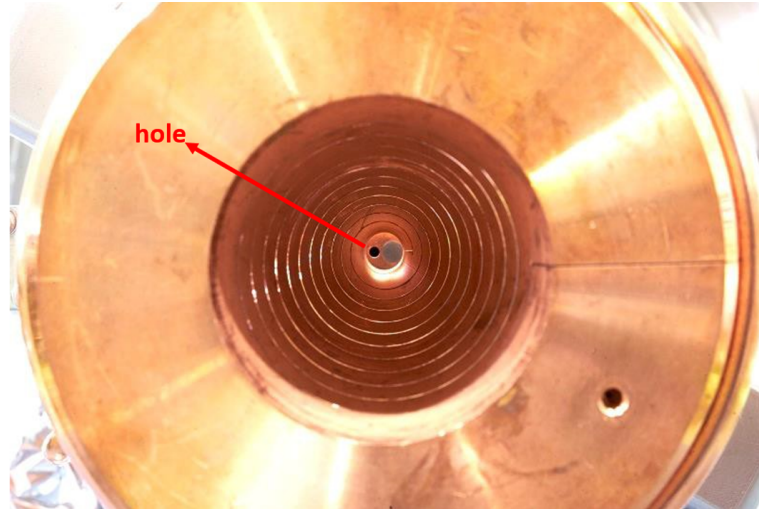


Fig. 2.4 The SuperKEKB positron target [116]

flexibility. Recent experimental measurement gives us a positron yield of $0.33 N_{e^+}/N_{e^-}$ against $0.4 N_{e^+}/N_{e^-}$ designed at the exit of the injector linac when a 3.5 GeV, 10 nC electron beam works as incident electrons. In addition, the positron target is fixed in the direct beam line for both particles, which is not possible to make the movement of the target that could increase the positron yield production.

The optics and phase space of an ideal beam before and after the target areas of the SuperKEKB injector can be seen from Fig. 2.5 and 2.6 [14]. The first electron beam before positron target will pass through the hole on the target, which is in the longitudinal central axis. The center of the flux concentrator and the positron target is respectively 2 mm, 3.5 mm horizontally deviated from the hole, as is shown in Fig. 2.5. And the second electron beam will hit the target for positron generation. A short summary of the design parameters for the area near the positron target is summarized in the Fig. 2.7.

The details of the FCC-ee injector linac baseline are shown in Fig. 2.8 (green color for electrons, red color for positrons and blue color for incident electrons to produce positrons). This 6 GeV accelerator composed of section 1, section 2 and section 3 linacs accelerates both species (electrons and positrons) to obtain an intensity of 2.13×10^{10} particles per bunch in the Pre-Booster Ring (PBR). The first low emittance electron beam (green color beam) is generated from the 6.5 nC RF gun and directly accelerated in the 6 GeV electron linac for the next injection. While the positron beam is produced from a 10 nC electron beam (blue color beam, emitted from the 10 nC thermionic gun) at the energy of 4.46 GeV. After passing through the target, the produced positrons get captured in the capture system (AMD + Capture linac)

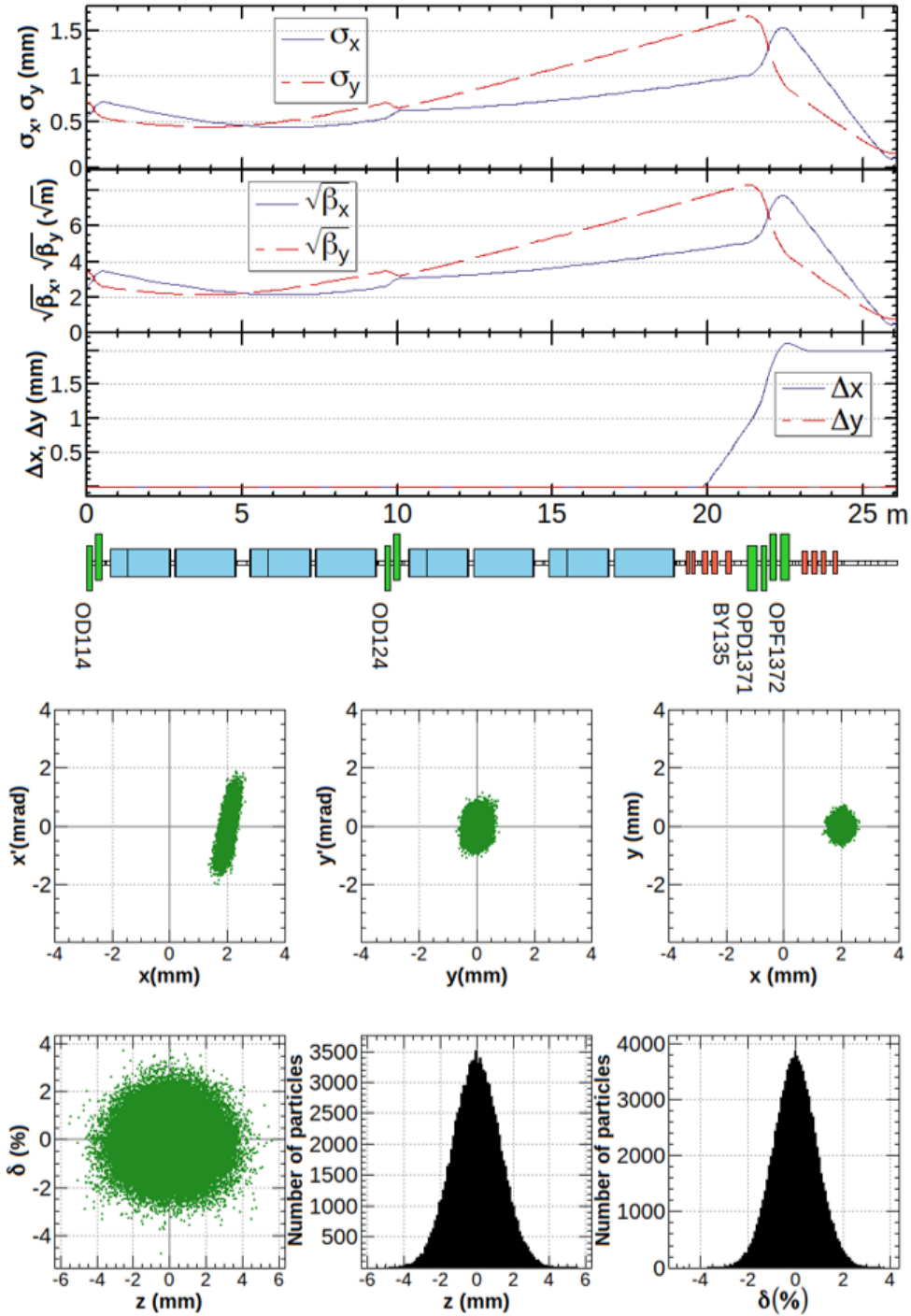


Fig. 2.5 Beam sizes, orbits and phase space plots before the positron target for the SuperKEKB injector calculated with SAD (for electron beam not serving for positron production). Top: transverse betatron function, beam envelope and the position deviation; Bottom: six dimensional phase space of ideal beam

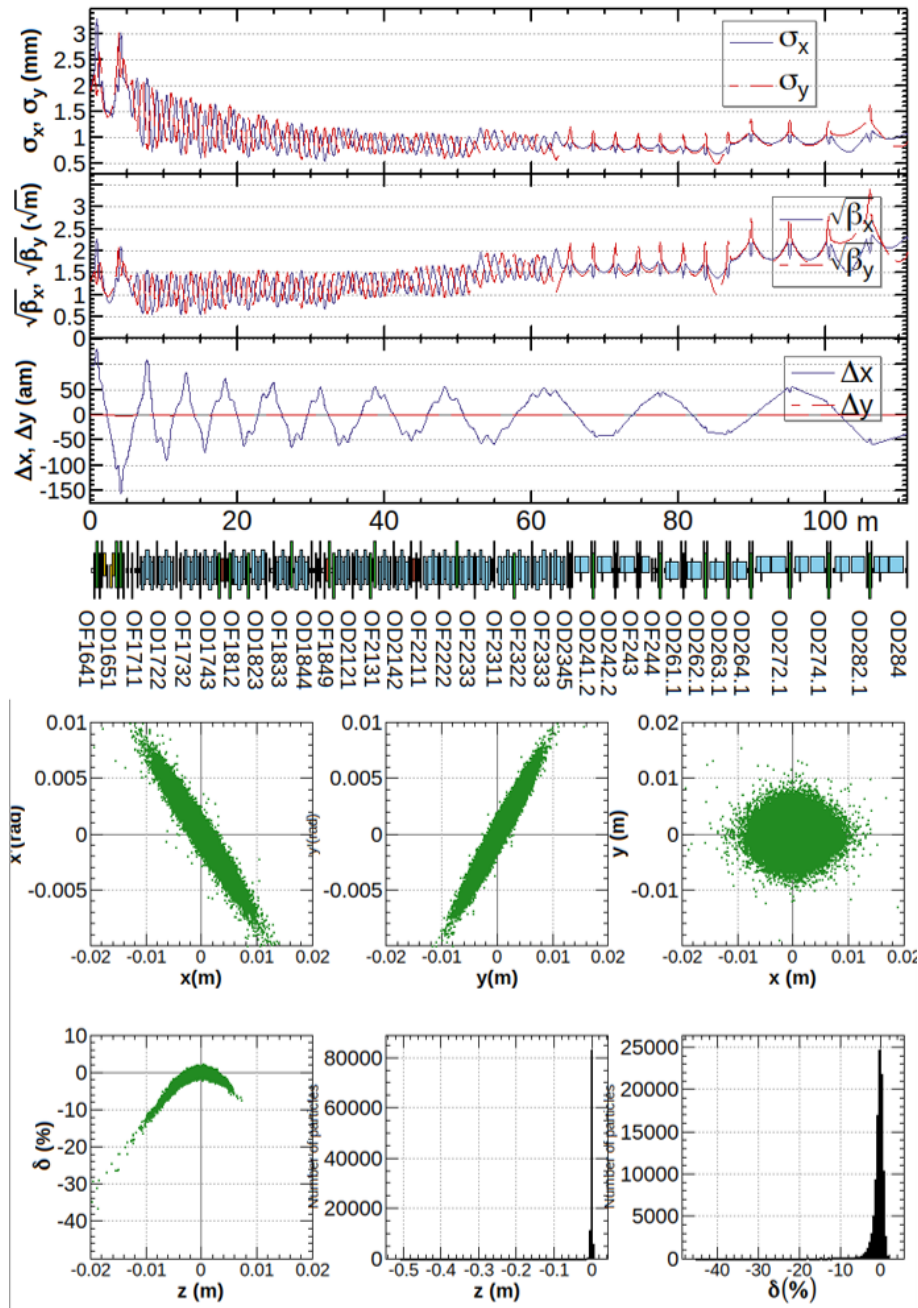


Fig. 2.6 Beam sizes, orbits and phase space plots of the produced positron beam after the positron target for the SuperKEKB injector calculated with SAD. Top: transverse betatron function, beam envelope and the position deviation; Bottom: six dimensional phase space of ideal beam

and first accelerated in section 3 linac, to be transferred back to the positron damping ring (DR), injected into the section 2 and section 3 linac, and then into the pre-booster ring (PBR).

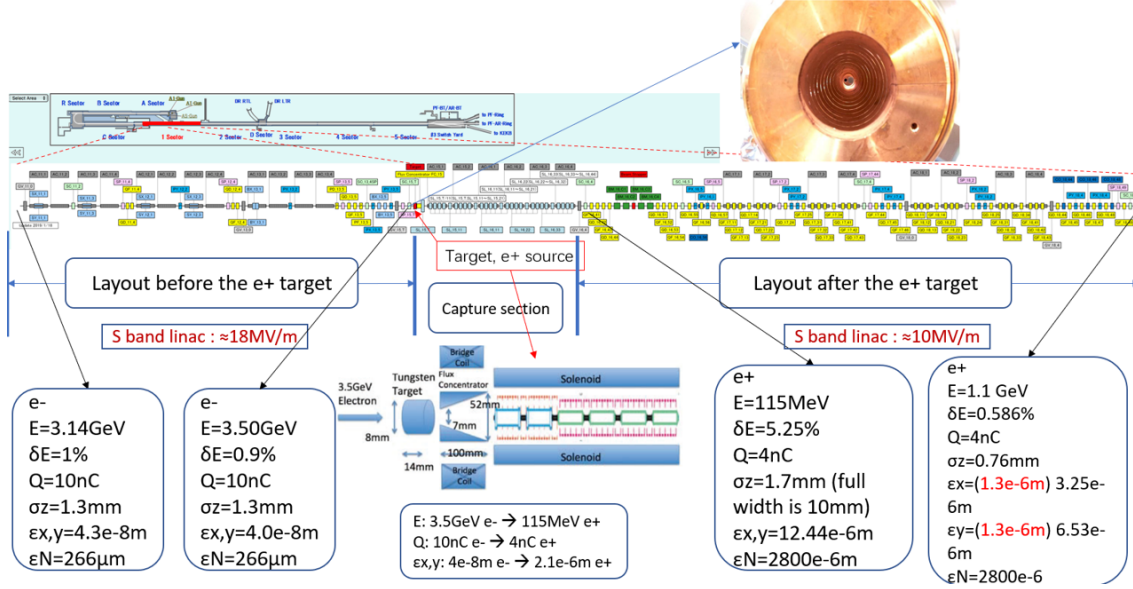


Fig. 2.7 Parameters of the electron/positron beam before/after the positron target in SuperKEKB

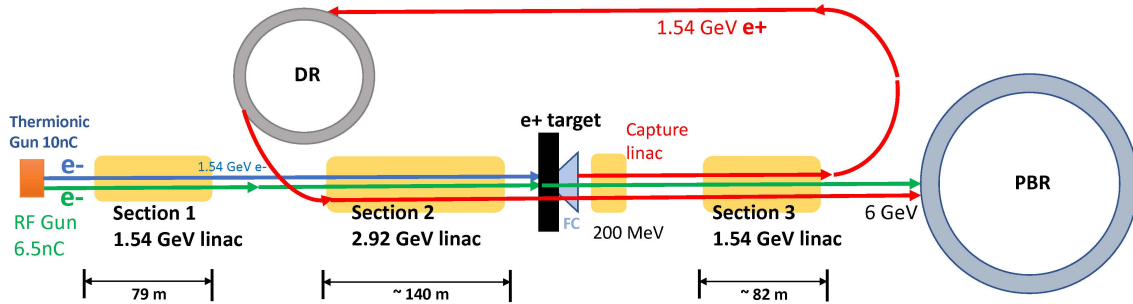


Fig. 2.8 The FCC-ee injector linac baseline

The design of the 6 GeV electron linac is originally split into two parts in the CDR of FCC-ee [36, 86]: (1) 1.54 GeV linac (section 1 linac); (2) 1.54-6 GeV linac (section 2 linac + section 3 linac). The optics of the two linacs are respectively shown in Fig. 2.9 and Fig. 2.10. In the baseline, the position of the positron damping ring is located near linac 1 and linac 2, because the electron beam could also be deflected by a bending magnet towards the damping ring (DR) for cooling before delivering into the collider. The DR is capable of curing beam emittance dilution due to misalignments and space charge from the upstream linacs and transfer lines. The design parameters of the two linacs are also shortly summarized in the Table 2.3 and 2.4.

Some preliminary studies about the positron production efficiency has been made for the baseline scheme in references [36, 86]. From these studies and based on the SuperKEKB

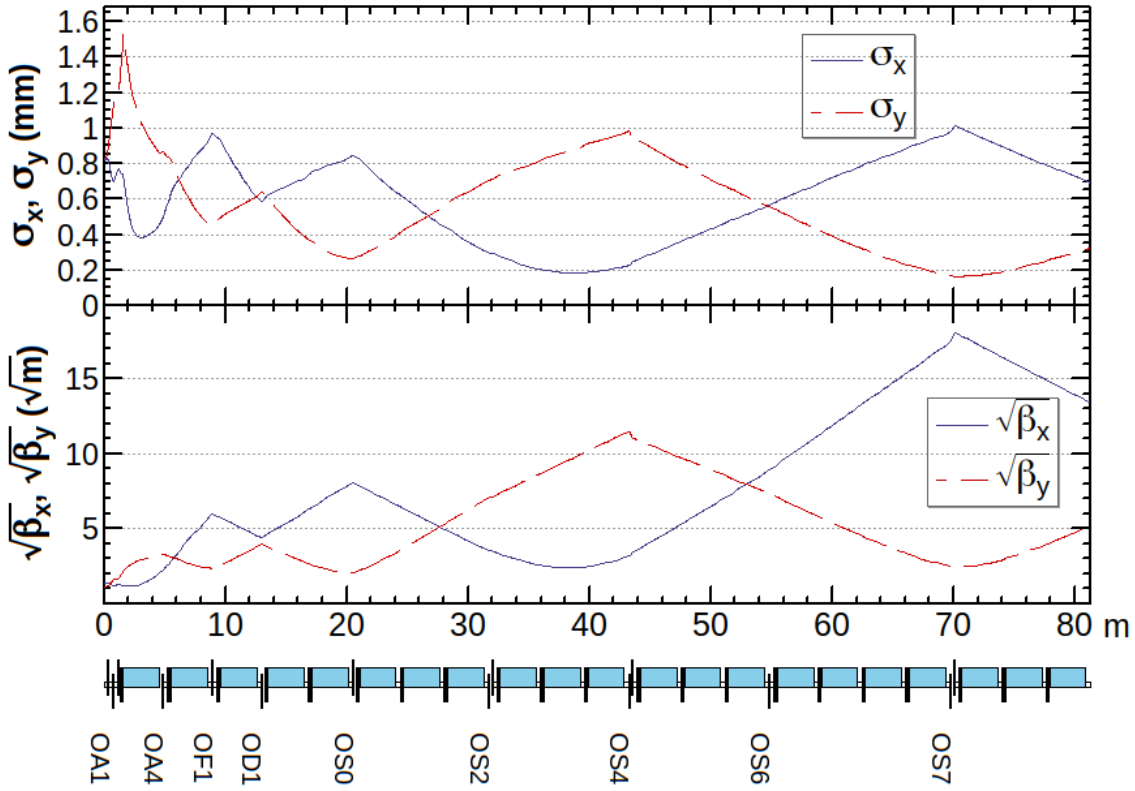


Fig. 2.9 The 1.54 GeV (section 1) electron linac design in the FCC-ee injector system baseline calculated with SAD code [86]

Parameter (unit)	Value
Length (m)	79.1
No. of cavities, quadrupoles	21, 14
RF Frequency (GHz)	2.856
Accelerating gradient (MV/m)	25
Injected emittance (h/v, μm)	0.35/0.5
Average extracted emittance (h/v, nm)	6.4/5.0
Transmission for 3.2 nC	100 %

Table 2.3 Parameters of the 1.54 GeV (section 1) linac

results, we could conclude that similar poor positron production rates are envisaged. In order to improve these results, three novel injection schemes using bypass option and then separated paths for electrons and positrons are proposed in this work. Their schematic layouts are respectively shown in Fig. 2.18, 2.44 and 2.54. The main objective of the new proposed designs is to increase the positron production rate by optimizing the beam transport to avoid as much as possible the losses.

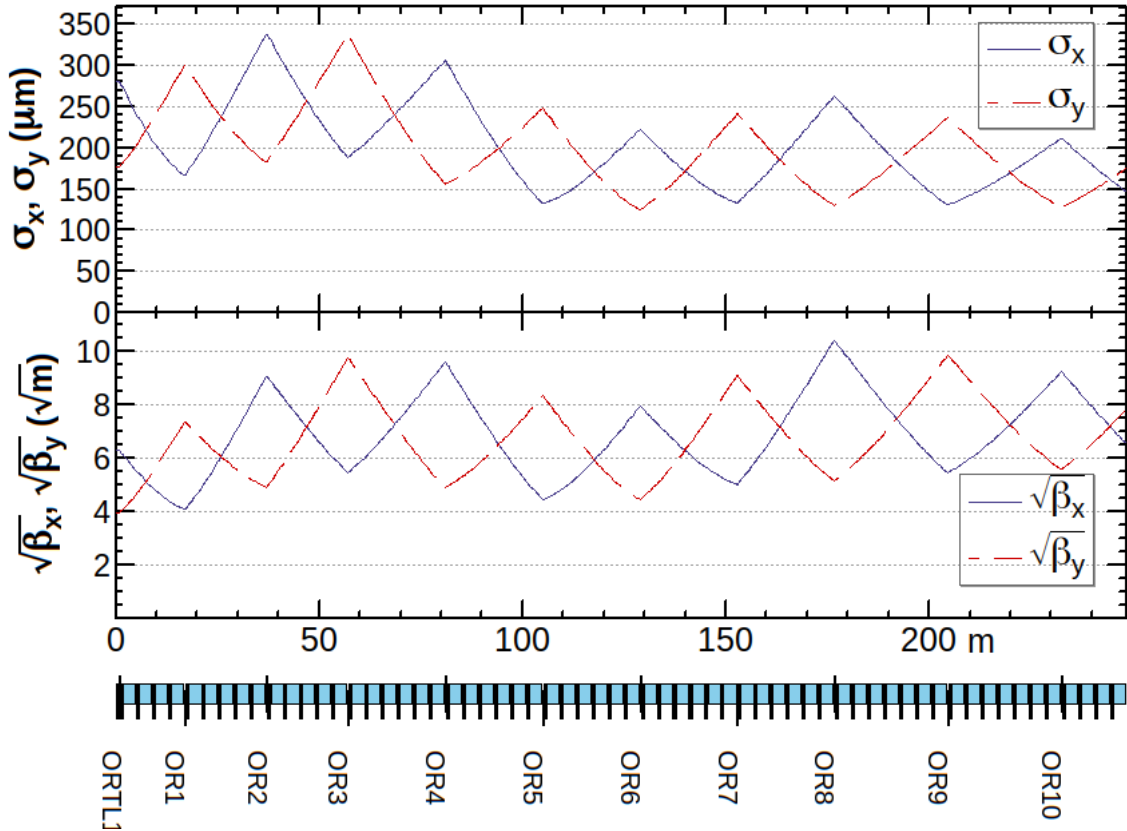


Fig. 2.10 The 1.54-6 GeV (section 2 + section 3) electron linac design calculated by SAD [86]

Parameter (unit)	Value
Length (m)	221.9
Injection-extraction energy	1.54GeV - 6 GeV
RF Frequency (GHz)	2.856
Accelerating gradient (MV/m)	25
Injected emittance (h/v, nm)	1.9/0.4
Average extracted emittance (h/v, nm)	1.1/0.4
Transmission for 3.2 nC	100 %

Table 2.4 Parameters of the 1.54-6 GeV (section 2 + section 3) linac

The optics design and start-to-end tracking simulation for beam production, acceleration and transport from the feeding electron source to the positron damping ring of the three schemes including the positron system (positron production chain) and the electron system (electron injection chain) are going to be described in detail in this chapter [18].

2.2 Electron source and positron production

2.2.1 Electron sources

The electron source for the FCC-ee injector system is required to provide two intense beams (two bunches per pulse for each beam) for injecting into the PBR according to the demand of the FCC-ee different operations. One electron source, the RF gun, provides the required injected low-emittance electron beam, while the other is used to produce the positrons. The second electron source may be a thermionic gun that could provide large numbers of electrons for the positron production. Due to the high demand of the Z running mode of FCC-ee, each of the electron and positron bunches must at least result in 2.13×10^{10} particles being transferred into the PBR.

6.5 nC RF gun

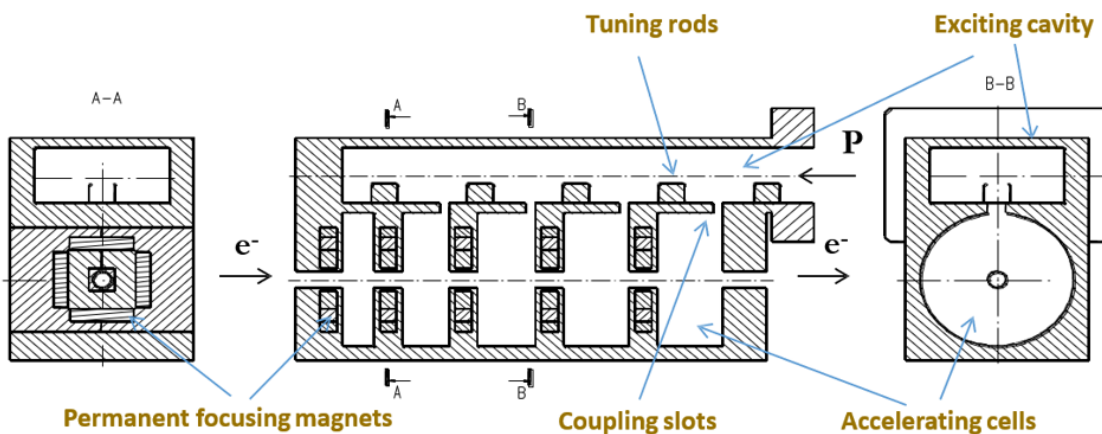


Fig. 2.11 Schematic drawing of the S-band RF gun with parallel coupling accelerating structures of the FCC-ee baseline injector system [36]

The RF gun of the FCC-ee baseline injector system has a normalized transverse emittance of around $10 \mu\text{m}$, and could provide 6.5 nC of charge at the energy of 11 MeV. The charge is intentionally high to allow for a high charge injection for the initial fill of the collider at startup. From Fig. 2.11, we can see that the RF gun is based on a parallel coupled accelerating structure [16, 118] and has permanent magnets integrated in the irises to reduce the beam size and limit emittance dilution so as to provide low emittance electron beam for the injection. This design of the RF gun allows considering the cavities as independent elements, thus, the length and field amplitude can be tuned separately for each cavity. IrCe alloy [68, 99] will be chosen as the photocathode because this material could bring many benefits in providing

Parameter	Value
Initial geometrical emittance	$0.6 \mu\text{m}$
Total charge	6.5 nC
Bunch length ¹	1.5 mm
Injection kinetic energy	11 MeV
Energy spread ²	0.6 %

Table 2.5 Main parameters of the 6.5 nC RF gun [15]

acceptable lifetime with high charge extraction at high repetition rate which helps the injection of 2 electron bunches (each bunch at most has 6.5 nC charge) per pulse at a high pulse repetition rate of 200 Hz. A prototype of the RF gun has been produced at Budker Institute of Nuclear Physics (BINP) in Russia [15] and some output parameters of the gun are presented in Table 2.5.

10 nC thermionic gun

A high current thermionic gun inspired by the SuperKEKB one [14, 67, 87] has been selected as a backup considering the high demand of the positron yield for FCC-ee. In the pre-injector area, an electron beam pulse of 1 ns from the 200-kV thermionic gun with a Barium-impregnated tungsten cathode is compressed to a single-bunched beam of 10 ps (FWHM) by an RF bunching section with two sub-harmonic bunchers (SHBs) of 114 MHz and 571 MHz, an S-band pre-buncher (PB) and a buncher. The sketch layout of the pre-injector is described below in Fig. 2.12. Table 2.6 summarizes the main parameters of the 10 nC thermionic gun.

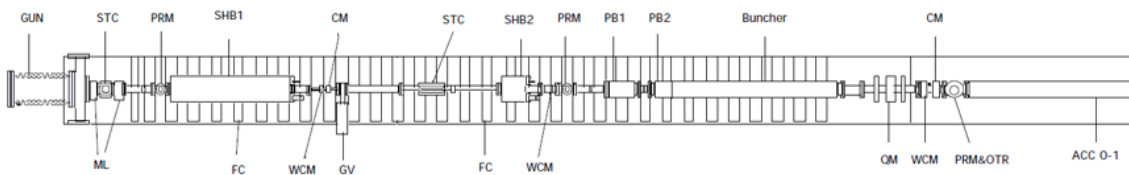


Fig. 2.12 Sketch layout of the 10 nC thermionic gun and pre-injector system for FCC-ee baseline inspired by the SuperKEKB injector. Others are beam monitors (screen monitor: PRM, and current monitor: WCM) and components of the beam transport system (magnetic lens: ML, focusing coil: FC, and quadrupole magnet: QM) [87]

¹It will be shortened to 1 mm via a bunch compressor before the electron beam being injected into the linac

²It will be transformed to 1 % due to the impact of bunch compressor

³After the buncher system

Parameter	Value
Initial geometrical emittance	$3.1 \mu\text{m}$
Total charge	10 nC
Bunch length ³	1.3 mm
Injection kinetic energy	15 MeV
Energy spread	5.2 %

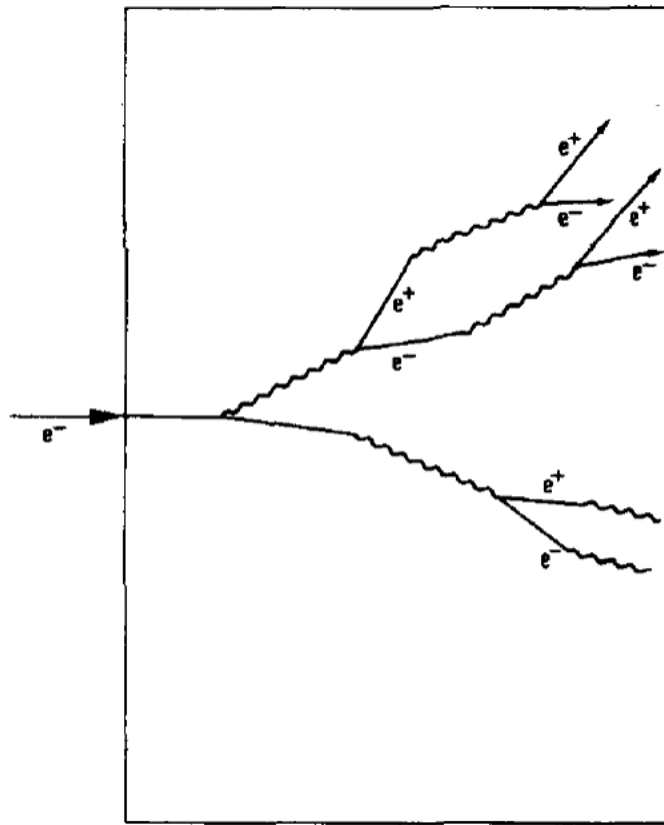
Table 2.6 Main parameters of the 10 nC thermionic gun [14]

2.2.2 Positron production

In order to get the high-luminosity goal in the different operation modes of the FCC-ee, the positron source is required to produce sufficient numbers of positrons to saturate the intensity capability of the linac. Since the positrons will share the same linac with electrons after coming out of the DR before injection into the PBR, the positron system is required to deliver at least one positron into the damping ring for each electron incident on the positron target. This means, when 3.5 nC electrons (2.13×10^{10}) impinge on the target, the same number (2.13×10^{10}) positrons are required to be delivered into the DR (the most crucial injection requirement for FCC-ee is 2.13×10^{10} particles per bunch), which means the positron yield is $1 N_{e^+}/N_{e^-}$ (conversion efficiency is 100 %). Of course, if we use 6.5 nC incident electron beam, at least $0.5 N_{e^+}/N_{e^-}$ positron yield (50 % conversion efficiency) needs to be guaranteed; $0.35 N_{e^+}/N_{e^-}$ positron yield (35 % conversion efficiency) should be accomplished in the case of 10 nC incident electron beam.

Generally speaking, positrons can be created by pair production or by nuclear beta decay. Both approaches could be used as positron sources but pair production is more common for accelerator applications, usually because it has the desired time structure and high phase space density. A positron system consists of an incident beam hitting a target, followed by focusing devices to collect the positrons and an accelerator to provide the required energy (Fig. 2.1).

Electrons from guns and accelerated at a certain energy will lose energy when traversing a target by radiation and collision. The energy lost by collision is used in atom excitation and ionization leading to secondary electron emission and is hence essentially dissipated. This mainly contributes to heating effect in the target. The energy lost by bremsstrahlung radiation is distributed among the secondary photons whose energy can reach the energy of the primary electrons. The created photons interact with the nucleus, and in a weaker manner with the peripheral electrons, to generate subsequent electron-positron pair (pair production process). The Compton effect could also occur by elastic collision of the photons with electrons. The electron-positron pair radiates photons and are then transformed into other pairs, the energy of regenerated electron-positron pairs decreasing at each step. Such a process is called a cascade



(a) Sketch of the electron generated cascade shower [93]

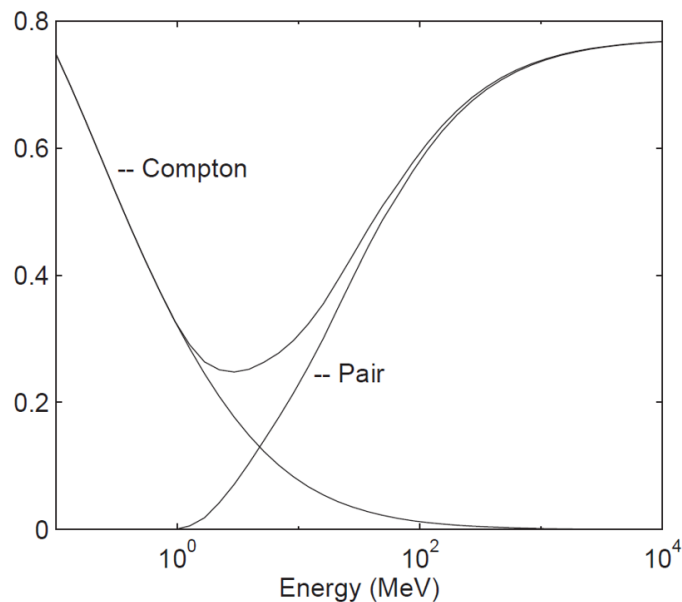
(b) Probability per X_0 (radiation length) of e^+e^- pairs and Compton scattering vs incident photon energy [28]

Fig. 2.13 Positron production process

shower, and the diagram can be seen in Fig. 2.13(a) [93]. Electromagnetic showers can be initiated by high energy electrons as well as by high energy photons.

Fig. 2.13(b) [28, 98] shows the cross section (probability) change of pair production and Compton scattering at different incident photon energy. It could be concluded from the figures that the pair production cross section is rapidly rising from threshold, becoming nearly constant at incident photon energies larger than a few hundred MeV.

The techniques for photon creation (pair production) dedicated to positron production also include oriented crystals (channeling radiation) [17] (now is used in the CLIC study [62, 120]), helical undulator radiation (now is the baseline for ILC [42, 55]), etc., apart from the bremsstrahlung radiation (conventional way). In some cases, in order to enhance the positron production and limit the peak energy deposition density (PEDD) on the target, an oriented crystal is applied in the target. The characteristics of the electron-photon showers initiated by 2 to 10 GeV electrons aligned along the $\langle 111 \rangle$ -axis of tungsten crystals are compared with those for the amorphous tungsten.

In the case of the FCC-ee injection scheme, as in CLIC two types of positron targets are being considered:

1. **Conventional** amorphous target using a thick tungsten alloy (W74-Re26) material, where the positrons are produced by bremsstrahlung;
2. **Hybrid** target composed of a radiator (crystal W) and a converter (amorphous, W74-Re26), in which an oriented crystal (channeling radiation) is located in the positron production path.

The schematic drawing of the two types of positron targets is presented in Fig. 2.14.

The positron production system of most of the electron-positron colliders are based on the conventional target scheme. In such a system, a high-intensity incident electron beam hits an amorphous tungsten target to produce positrons; after the target a focusing device (usually using an AMD (Fig. 2.15 and Table 2.7) - Adiabatic Matching Device, see reference [29] for details) is used to collect the positrons and then an accelerator provides the positrons with the required energy. The specific performances of some positron sources for past, current and future colliders could be found in Table 2.1. The main limitation of the conventional scheme is the high heat load in the target and the peak energy deposition density (PEDD). This limitation can be overcome in the second option which uses a hybrid target in a two-stage process.

As depicted in the top plot of Fig. 2.14, the hybrid positron target is composed of a photon radiator made of thin crystal target (pure W) with an enhanced photon yield due to channeling radiation and a thicker amorphous target (W alloy) for pair production. The advantage of the hybrid scheme is the possibility to use thinner targets to reduce the energy

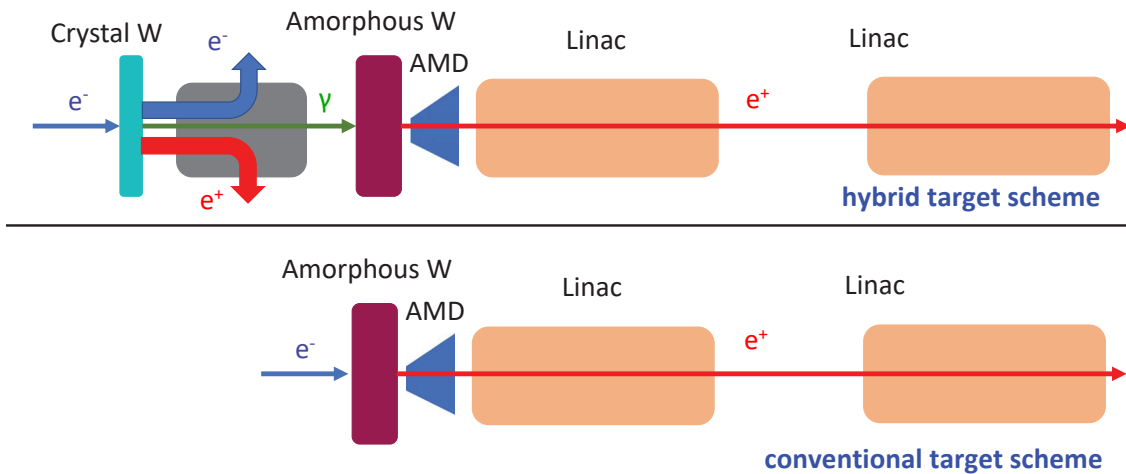


Fig. 2.14 Two different positron systems considered for positron production in the FCC-ee injector system. Top: hybrid target scheme; bottom: conventional target scheme

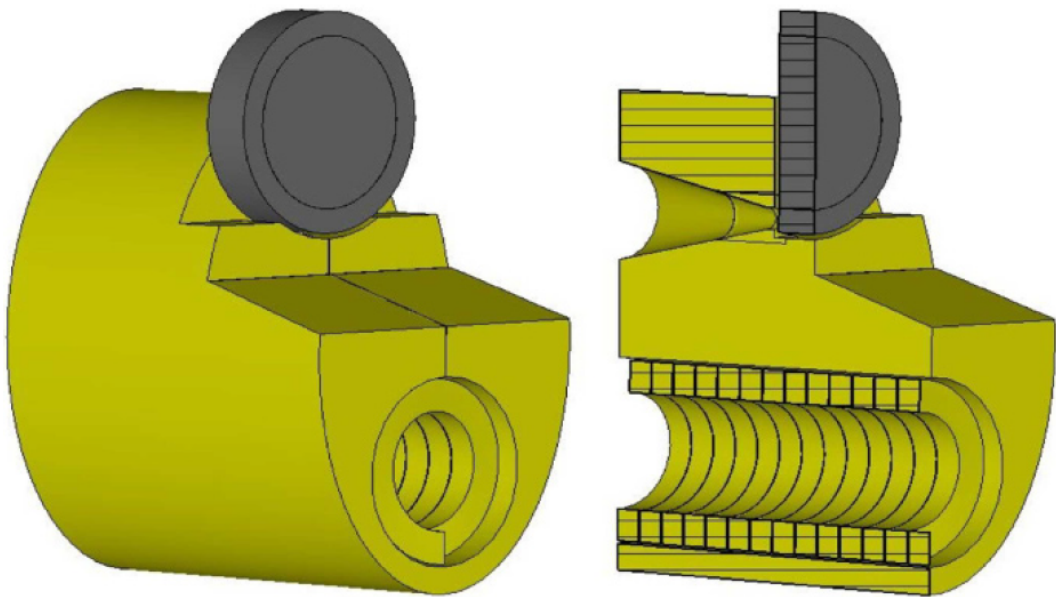


Fig. 2.15 Model of the flux concentrator at the FCC-ee positron source [36]

deposition in the target. It also allows sweeping out undesired particles in front of the final converter target. An incident electron beam impinges on a crystal tungsten target to produce photons via the channelling process; the photons will go straight to the downstream amorphous tungsten target while the simultaneously generated charged particles are bent away, reducing the deposited energy. The channelling effect [17] enhances the photon yield compared to a pure bremsstrahlung process. The W target thickness and the distance between the two targets

Parameter (unit)	Value
Target diameter (mm)	90
Target thickness (mm)	15.8
Gap between target and FC (mm)	2
Grooving gap between target side face and FC body (mm)	2
Elliptical cylinder size (mm)	120×180
Total length (mm)	140
Conical part length (mm)	70
Min cone diameter (mm)	8
Maximum cone diameter (mm)	44
Cone angle (deg.)	25
Cylindrical hole diameter (mm)	70
Coil turns (-)	13
Current profile pulse length (μ s)	25
Peak field (T)	7
Peak transverse field (mT)	135 – 157
Gap between coil turns (mm)	0.4
Gap between coil and FC body (mm)	1
Turns size	$9.6 \times 14\text{mm}$

Table 2.7 Flux concentrator (FC) parameters for the FCC-ee injection system [36]

needs to be carefully optimized for maximum positron production (see references [38, 62, 120] for the gradually optimized results of CLIC positron source). The produced positrons with large transverse divergence and energy spread could also be captured by an AMD with a flux concentrator (FC) same as that used in the conventional scheme. Fig. 2.15 shows the proposed FC model at FCC-ee positron source and its key parameters are listed in Table 2.7.

A complete description and simulation of the performances of the two targets for the FCC-ee injector system is beyond the scope of this work (a short summary of the preliminary results will be concluded in Section 2.4) and could be found in references [8, 9, 52].

2.3 Linacs in the FCC-ee injector system

As sketched in Fig. 2.8, different Normal Conducting (NC) linacs (section 1, section 2 and section 3) are used to accelerate either the electrons or the positrons. These linacs are made of S-Band (2.856 GHz) periodic High-Gradient (HG) accelerating structures, whose parameters are presented in Table 2.8. Fig. 2.16 shows the normal S-band periodic accelerating structures used in BEPCII [73].

Parameter (unit)	Value
Frequency (GHz)	2.856
Length (m)	2.97
Cavity mode	$2\pi/3$
Aperture diameter (mm)	20
Unloaded cavity gradient (MV/m)	25

Table 2.8 Normal conducting S-band accelerating structures parameters for the FCC-ee injector system



Fig. 2.16 Normal conducting S-band periodic accelerating structures in BEPCII [73]

In the three new schemes of FCC-ee injector linac proposed in this work, we still keep using NC S-band periodic accelerating structures as basic acceleration units for electrons and

Parameter (unit)	Value
Frequency (GHz)	2.856
Length (m)	2
Aperture diameter (mm)	30
Unloaded cavity gradient (MV/m)	10

Table 2.9 Large aperture S-band accelerating structures parameters

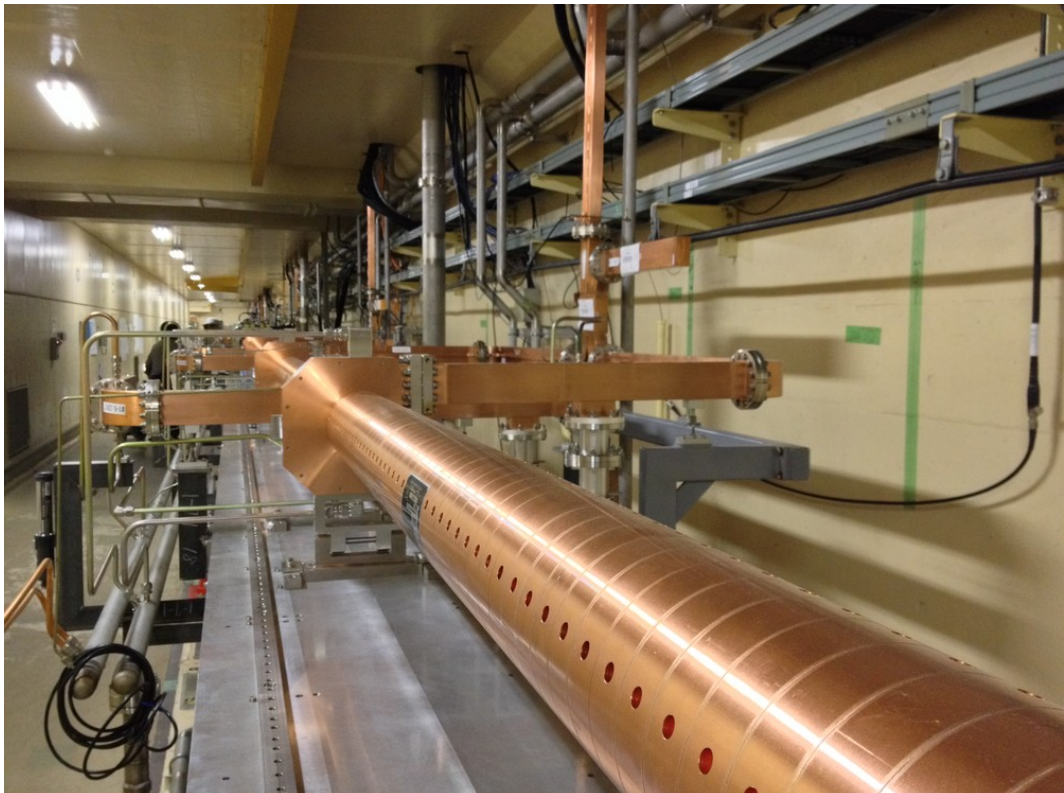


Fig. 2.17 Large aperture S-band (LAS) accelerating structure in SuperKEKB [106]

positrons. However, in the new injector linac schemes, we have proposed the use of "Large aperture S-band" (LAS) HG structures as in SuperKEKB [77] in the 1.54 GeV positron linac design (section 3 linac in Fig. 2.8), which is used to accelerate the positron beam just coming from the capture system, in order to capture the maximum number of positrons for a better positron yield. The physical aperture of the structures is 30 mm in diameter, 10 mm larger than the ones used in other section linacs. The main parameters and a photo of the LAS accelerating structures at SuperKEKB are respectively, shown in Table 2.9 and Fig. 2.17 [106].

2.4 New injection schemes for FCC-ee injector linac

In order to improve the positron production of FCC-ee, as stated before we have proposed three different injection schemes, where we have tried to optimize the transport, minimizing the losses and the cost. In the following I will describe in detail these options.

The overall injector system is composed of two parts:

1. The electron system (electron injection chain);
2. The positron system (positron production chain).

For doing these studies we have made use of state of the art simulation tools described in chapter [1.2](#) and appendix [A](#).

The 6.5 nC RF gun and the 10 nC thermionic gun, whose parameters can be found in Table [2.5](#) and Table [2.6](#) have been respectively used as feeding electron sources for the positron production. Performance comparisons between the two feeding electron sources also have been made and presented.

For the optics design of the electron system, the simulation tool - SAD [\[3\]](#) has been used to perform the study. Also, start-to-end tracking simulation from the RF gun to the end of the 6 GeV electron linac is presented.

In the design of the positron system, the 4.46 GeV e^- linac, first part of the whole positron system, has been designed keeping using SAD code as in the baseline. This is the starting point of the whole positron system. For the design of the downstream bypass structures and the after-positron-target parts including an electron/positron separator, a 1.54 GeV linac dedicated for positrons acceleration and a turnaround loop, MADX code [\[1\]](#) is used for the beam optics design and PLACET code [\[100\]](#) for the beam tracking study. 100,000 macro particles per bunch have been tracked taking into account the impact of the wakefields and the CSR. The short-range wakefields formulas used for simulation could be found in reference [\[65, 119\]](#). Meanwhile, the output results of the different positron sources we have used in this work can be referred to [\[117\]](#), where FOT code [\[115\]](#) has been used to simulate the channeling process in the crystal of the hybrid target and Geant4 [\[48\]](#) is applied for the simulation of the standard EM processes in the both targets.

2.4.1 Dogleg scheme

The dogleg scheme design is shown in Fig. [2.18](#), whose design idea is inspired by the SLC injector [\[46\]](#). As in the case of the baseline, we use two guns as electron sources. One low emittance electron beam from the RF gun will be straightly accelerated by section 1, section

2 and section 3 linacs to 6 GeV and then be transferred into the PBR. The other electron beam from the second feeding source (can be RF gun or thermionic gun) is used for positron production, which shares section 1 and section 2 linacs with the first electron beam to 4.46 GeV, and then will be bypassed in the dogleg structure to hit the positron target to generate positrons. Afterwards, the produced positrons could be captured in an Adiabatic Matching Device (AMD) with a Flux Concentrator (FC) and get primary acceleration to about 200 MeV in the capture linac with solenoidal focusing. After the capture system, to get pure positrons, a separator chicane is inserted to separate the mixture of positrons and secondary electrons from the target. Next, the positron beam will gain 1.54 GeV energy in section 4 linac before being transferred back to the damping ring (DR) via the turnaround loop. Finally, after the beam cooling in the DR, the 1.54 GeV positron beam gains another 4.46 GeV through section 2 and section 3 linacs to 6 GeV before entering the PBR. The difference between the baseline and the dogleg scheme is that in the dogleg scheme, we need a supplementary linac (section 4 linac) dedicated to the positron acceleration, which leads to the increase of the cost.

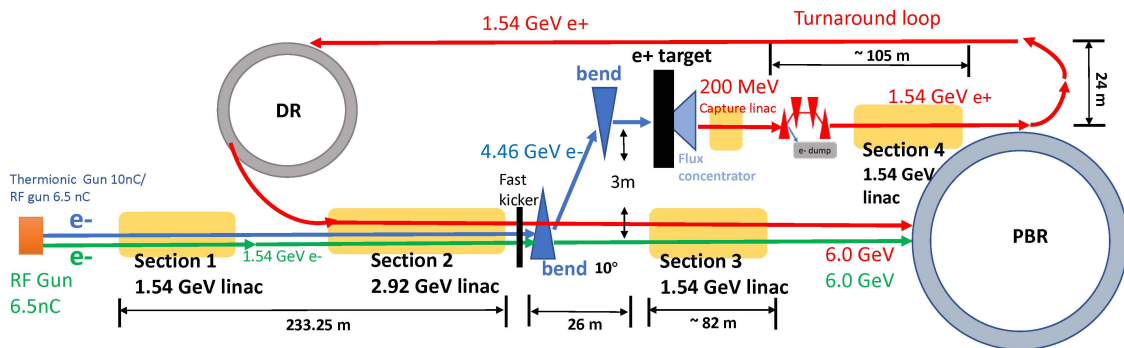


Fig. 2.18 Dogleg scheme for the FCC-ee injector linac

The overall layout as well as positron system of SLC is depicted in Figures 2.19 and 2.20 [44, 32]. The main differences between the FCC-ee dogleg injection system and the SLC injection complex are the energy of the incident electron beam dedicated to positrons production and the turnaround loop for transferring positrons back to the DR. In SLC positron system (Fig. 2.19), the incident electron beam energy at the positron target is 33 GeV, larger than that of our design (4.46 GeV); the beam intensity is limited to values from about 3×10^{10} to 5×10^{10} per bunch considering the thermal effect (heat stress), a little less than that of FCC-ee dogleg scheme (4.2×10^{10} or 6.25×10^{10}); and the turnaround loop consisting of two 90° bends is just used for the transport of 200 MeV positrons, while in the case of FCC-ee dogleg scheme, the transfer line is composed of six 30° 2-meter-long dipoles for the transmission of 1.54 GeV positron beam.

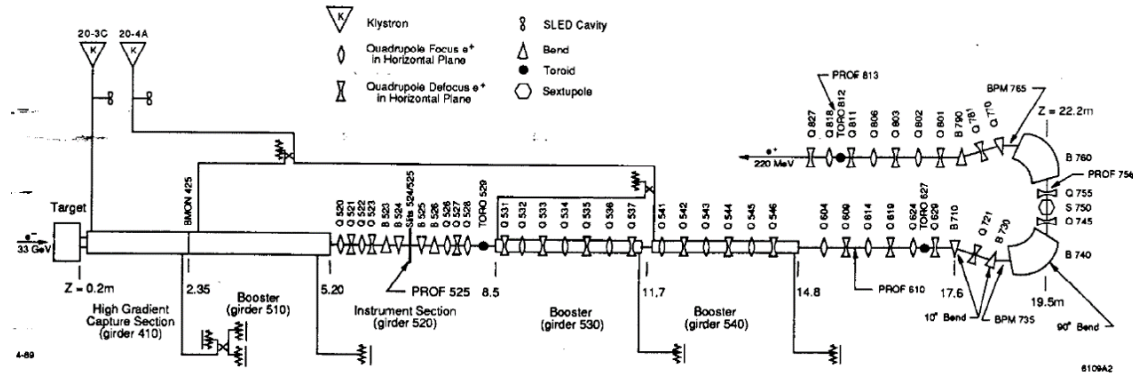


Fig. 2.19 The SLC positron system [32]

For the sake of clarity, the overall dogleg scheme shown in Fig. 2.18 has been depicted into two parts: one part is the electron system (electron injection chain, see Fig. 2.21) and the other is the positron system (positron production chain, Fig. 2.24).

Electron injection chain for the dogleg scheme

As depicted in Fig. 2.21, the electron injection chain is composed of an RF gun, and three NC S-band linacs (section 1, section 2 and section 3).

The optics design and tracking simulation starting at the output of the RF gun and finishing at the entrance of the PBR, have been calculated with SAD. For doing such a tracking we have taken into account the wakefield effect of the accelerating structures (AS). The results of the design optics and the phase space are shown in Fig. 2.22 and 2.23 respectively, whose transverse geometric emittance ($\epsilon_{x,y}$) is 1.2 nm. The total length of the electron injection chain is around 320 meters. 3.5 nC charge of electrons has been simulated and 100 % transmission efficiency can be guaranteed in the end of the section 3 linac without considering the misalignments of elements. The main performances are summarized in Table 2.10.

Parameter (unit)	Value
Length (m)	317.65
Accelerating gradient (MV/m)	~ 20
Electron energy (GeV)	6.17
Injected emittance (h/v)	0.6 μ m
Average extracted emittance (h/v)	1.2 nm
Transmission efficiency (3.5 nC)	100 %

Table 2.10 Main performance parameters for the 6 GeV electron injection chain in the dogleg scheme

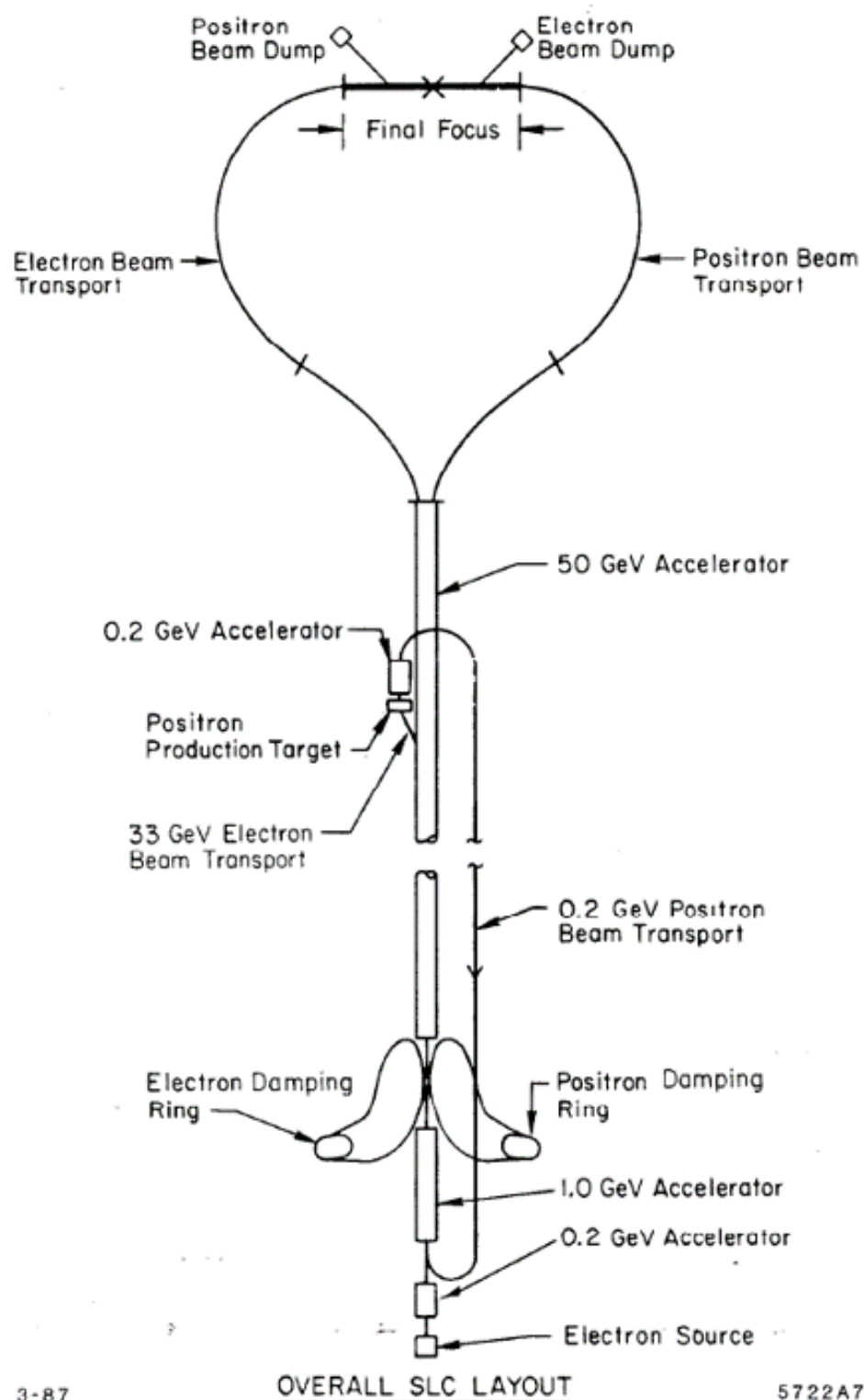


Fig. 2.20 Overall SLC layout [46]

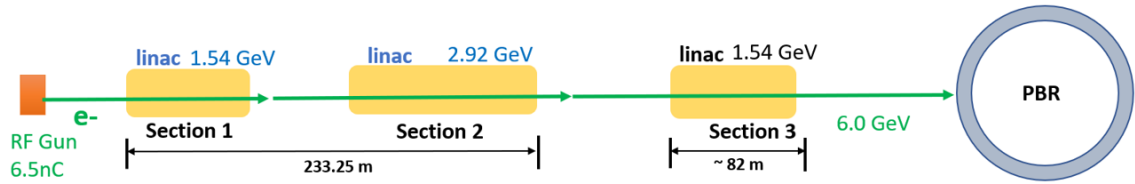


Fig. 2.21 The electron injection chain of the dogleg scheme for the FCC-ee injector system

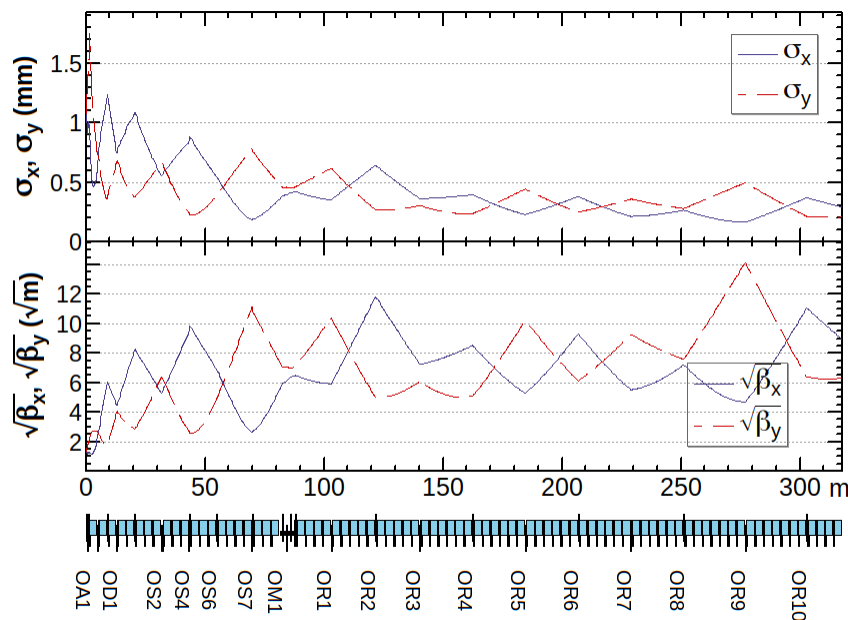


Fig. 2.22 Beam optics of the 6 GeV electron linac for the dogleg scheme calculated with SAD

Positron production chain in the dogleg scheme

The positron production chain (Fig. 2.24) consists of an RF gun / a thermionic gun, a 4.46 GeV electron linac (section 1 + section 2), a dogleg bypass, a positron target with a capture system, an electron/positron separator, a 1.54 GeV (section 4) positron linac and a turnaround loop to transfer positrons to the damping ring.

The 4.46 GeV electron linac The 4.46 GeV electron linac needs to be flexible enough to accelerate both the electron beams with different emittance and energy spread. We have calculated using the optics of the 4.46 GeV electron feeding linac (section 1 + section 2) for the two feeding electron sources. The optics design has been made with SAD and the results are shown in Fig. 2.25, along with the beam envelope evolution. In this linac, electron beam will be accelerated to the energy of about 4.46 GeV making use of 2.856 GHz NC S-band accelerating

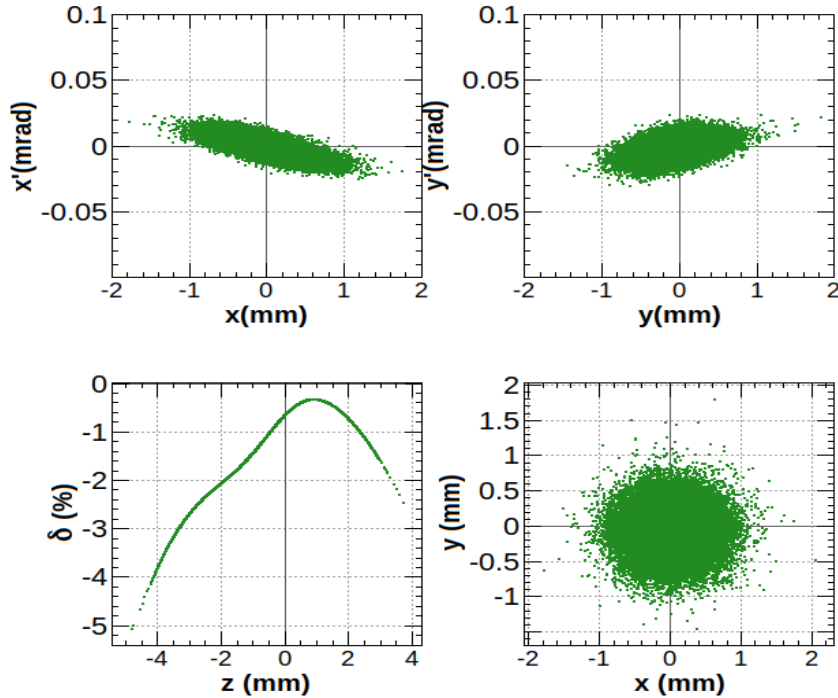


Fig. 2.23 Phase space of 3.5 nC electron beam at the end of the 6 GeV electron linac for the dogleg scheme calculated with SAD

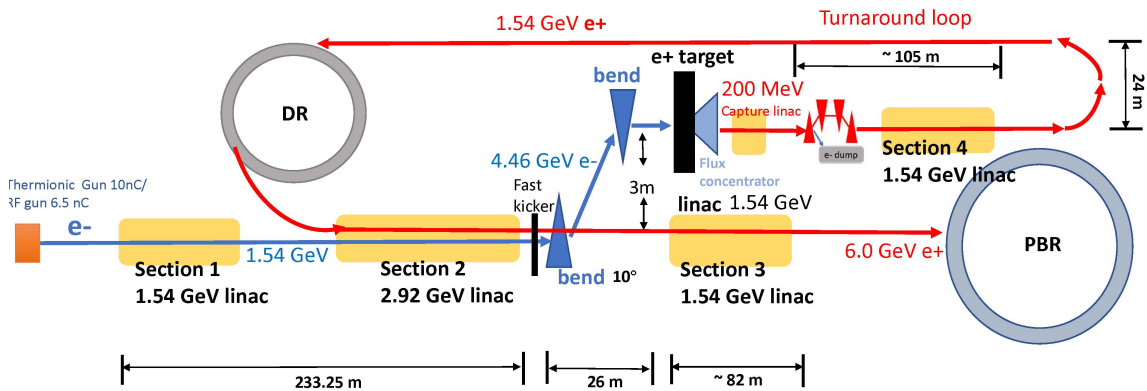


Fig. 2.24 The positron production chain of dogleg scheme

structures of 3 m length each one, the accelerating gradient is 25 MV/m and the aperture radius is 10 mm. The total length of this (section 1 + section 2) linac is around 233 meters. Normal conducting quadrupoles are used as the focusing system with a maximum magnetic field of around 1.8 T. The corresponding phase spaces and beam distributions calculated with SAD for the two feeding electron sources (6.5 nC RF gun and 10 nC thermionic gun) at the end of the 4.46 GeV electron linac are shown in Fig. 2.26.

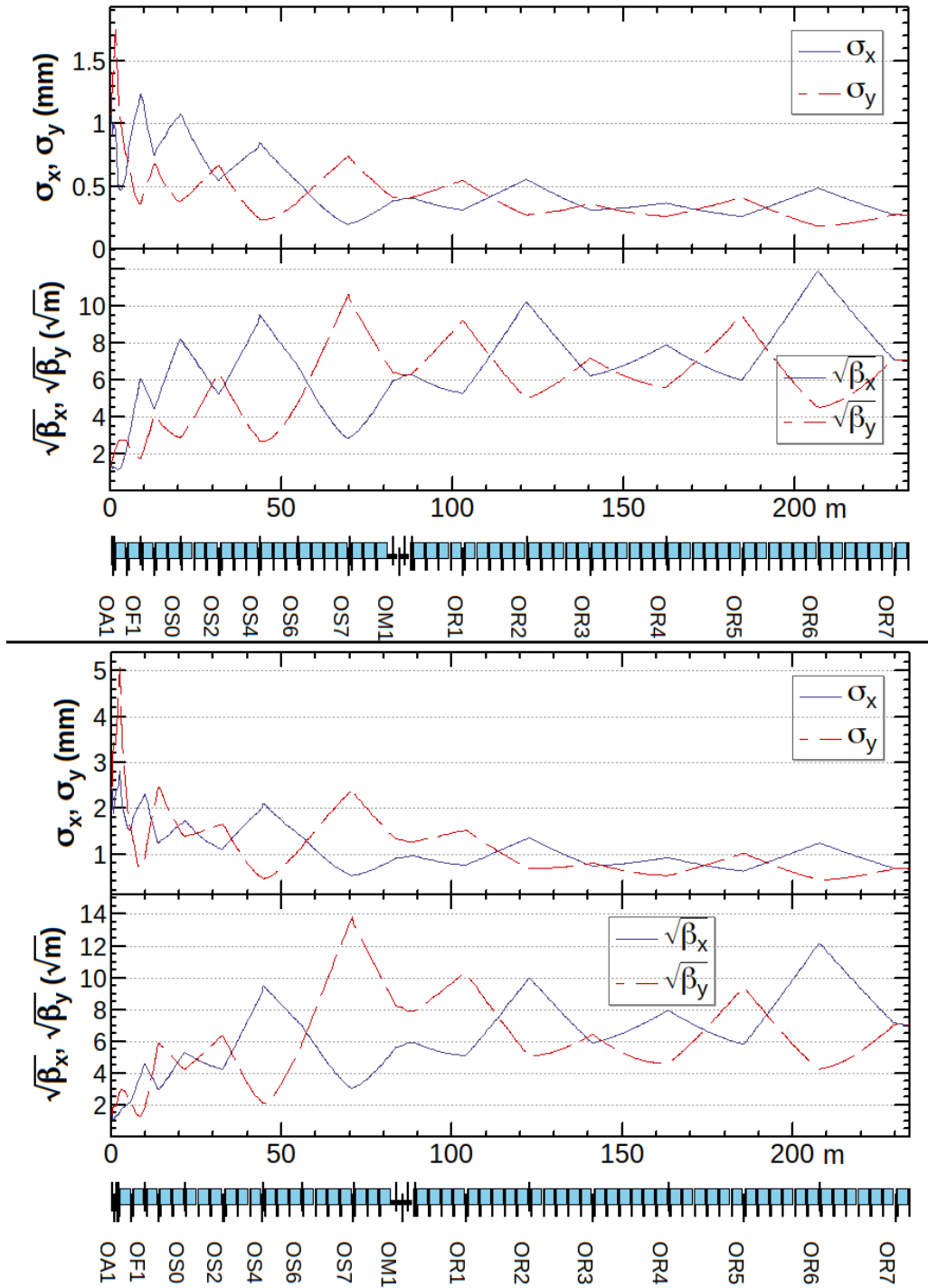


Fig. 2.25 Optics design of the 4.46 GeV electron linac in the dogleg scheme. Top: The 4.46 GeV electron injector linac twiss function with the 6.5 nC RF feeding electron source calculated by SAD; Bottom: The 4.46 GeV electron injector linac twiss function with the 10 nC thermionic electron feeding source calculated by SAD

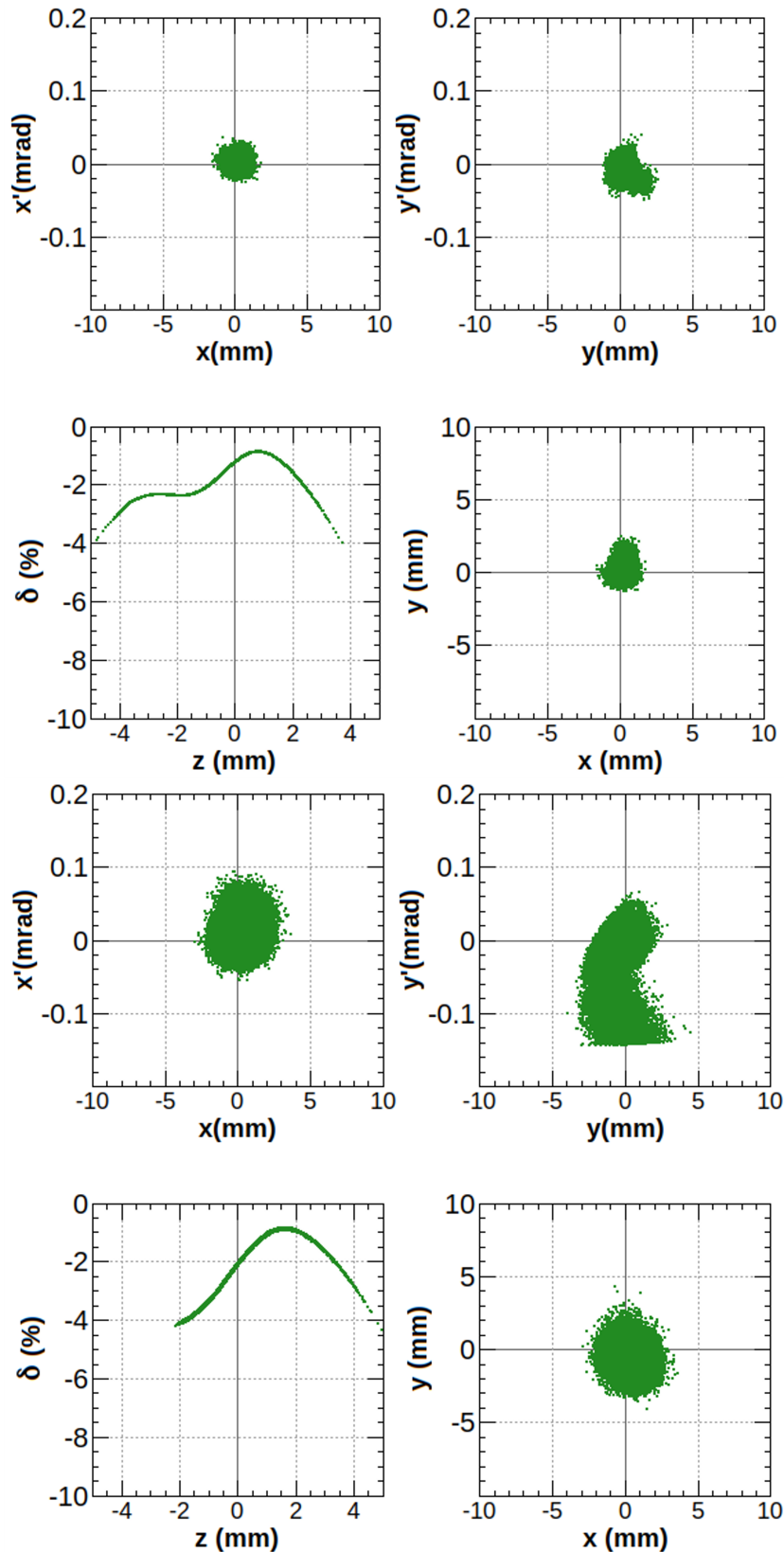
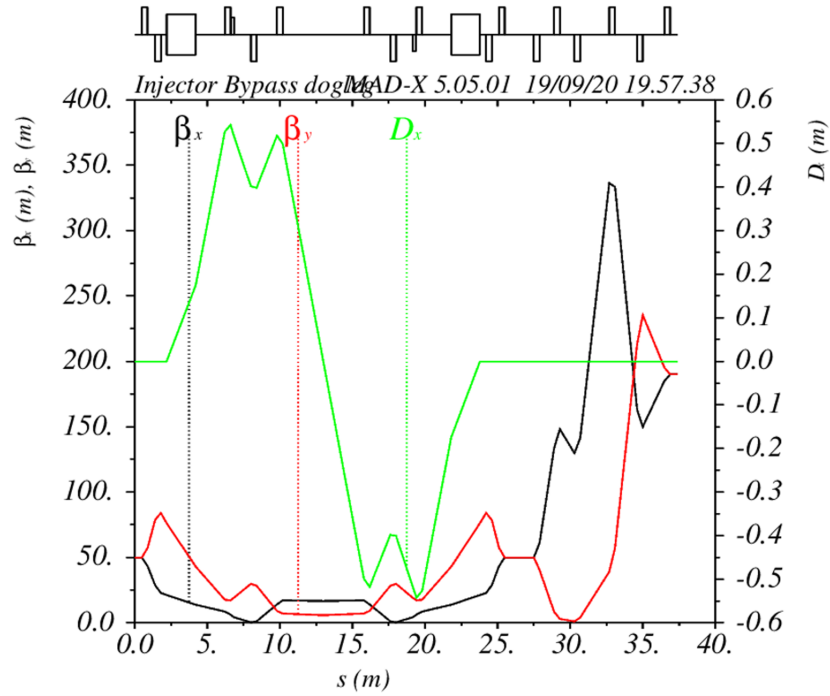


Fig. 2.26 Phase space at the 4.46 GeV electron linac exit in the dogleg scheme. Top: Phase space at the 4.46 GeV electron linac exit using the 6.5 nC RF feeding electron source calculated by SAD; Bottom: Phase space at the 4.46 GeV electron linac exit using the 10 nC thermionic gun calculated by SAD

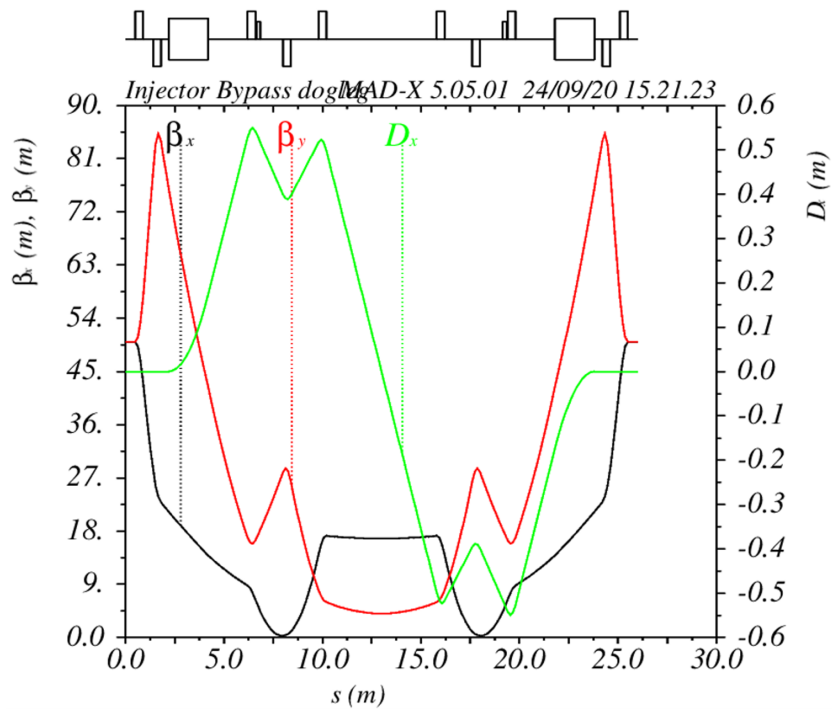
In the case of using a thermionic gun, we will obtain a higher intensity beam but its beam size and its energy spread are larger compared to those of an electron beam from an RF gun, therefore, its beam size near the low-energy end of the linac will exceed the aperture radius (10 mm) under the effect of the transverse wakefield, which causes about 10 % \sim 15 % beam loss in the current design of the 4.46 GeV linac. This could be observed in the vertical phase space $y-y'$ of right plot of Fig. 2.26. Meanwhile, in such a case, we set RF phase of all cavities to -94° (-90° is the RF phase crest) for an off-crest acceleration to decrease the energy spread between beam head and tail given the effect of longitudinal wakefield, but this will of course slightly cut down the energy gain from 4.42 GeV to 4.4 GeV correspondingly. Wakefields have less impact on the electron beam from RF gun, which can guarantee 100 % transmission without considering misalignments. The geometric transverse emittance for thermionic electron beam at the end of the linac is $\epsilon_{x,y} = 14/31$ nm, respectively 1.5 times and 3 times larger compared to the ideal emittance $\epsilon_{x,y} = 9.2$ nm. To be compared with the RF gun beams, the emittance values $\epsilon_{x,y} = 1.9/2.7$ nm, are horizontally 1.3 times and vertically 1.8 times of the ideal value $\epsilon_{x,y} = 1.5$ nm.

The dogleg bypass The electron beam will be bypassed in the deviated dogleg beam line when it comes out of the 4.46 GeV electron linac. The horizontal distance between the straight line and the deviated line is 3 m to provide enough space for proper shielding of the positron target area. The dogleg bypass is a symmetric structure constituted by two 2-meter-long 10° dipoles, with several quadrupoles for betatron manipulation and dispersion correction. Different bending angles (15°, 20°) and distances between the two lines (1 m, 2 m, 2.5 m) have been studied taking account of leaving enough shielding space for the positron source. Finally 10° bending angle and 3 meter-long distance was chosen. The design results calculated with MADX are shown in Fig. 2.27(a) and 2.27(b).

A pair of sextupoles are placed in the largest/smallest dispersion area for the correction of chromaticity. The values of sextupole strength k_2 are $\pm 14.75 \text{ m}^{-3}$ in the case of 6.5 nC RF gun, while for the 10 nC thermionic gun, sextupoles are not so necessary to be used after considering the collective effects. The optics designs for both feeding electron beams are shown in Fig. 2.27(a) and 2.27(b). The electron beam sizes $\sigma_{x,y}$ are constrained to be around 1 mm before positron production to avoid much high thermal effect on the positron target. Notice that in the situation of incident electron beam fed by the RF gun, two triplet of quadrupoles placed after the dogleg structure help to increase the beam size. The total length of the dogleg structure is 26 m.

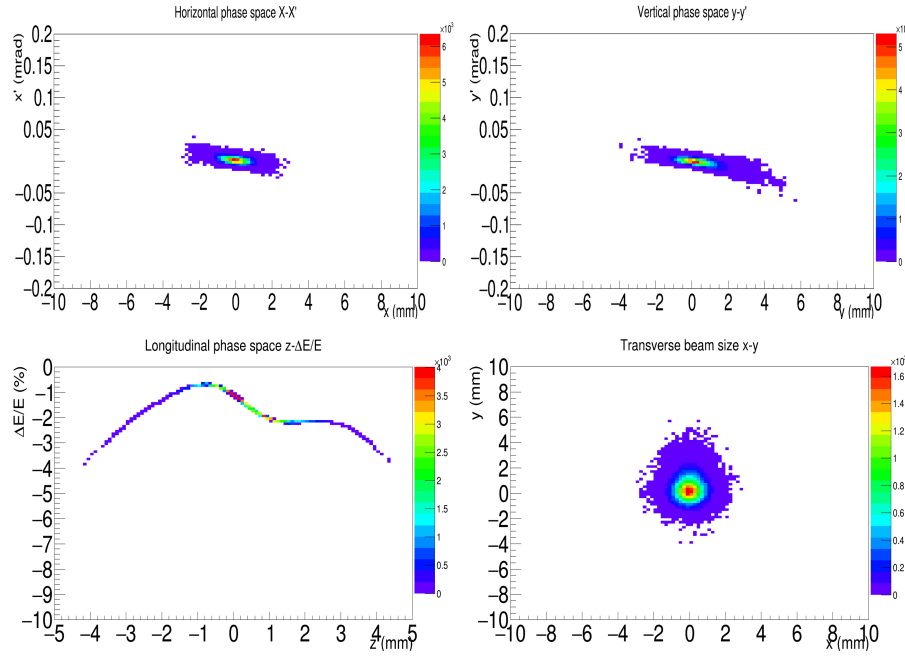


(a) The dogleg bypass design with the 6.5 nC RF feeding electron source

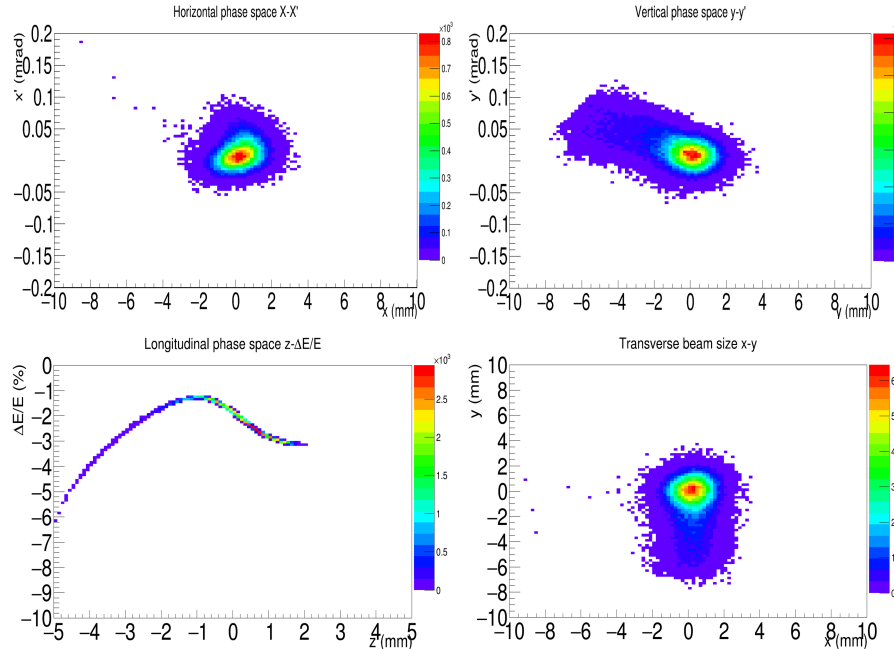


(b) The dogleg bypass design with the 10 nC thermionic electron feeding source

Fig. 2.27 Optics design of the dogleg bypass in the dogleg scheme calculated with MADX



(a) Phase space at the dogleg bypass exit using the 6.5 nC RF feeding electron source calculated by PLACET



(b) Phase space at the dogleg bypass exit using the 10 nC thermionic feeding electron source calculated by PLACET

Fig. 2.28 Phase spaces before the positron target in the dogleg scheme (bunch head are in opposite directions in longitudinal phase for SAD and PLACET)

The beam distribution of the 4.46 GeV electron linac output (Fig. 2.26) is used as the input of the dogleg bypass. The final corresponding outputs of the two electron beams in the dogleg bypass exit are shown in Fig. 2.28(a) and 2.28(b) respectively.

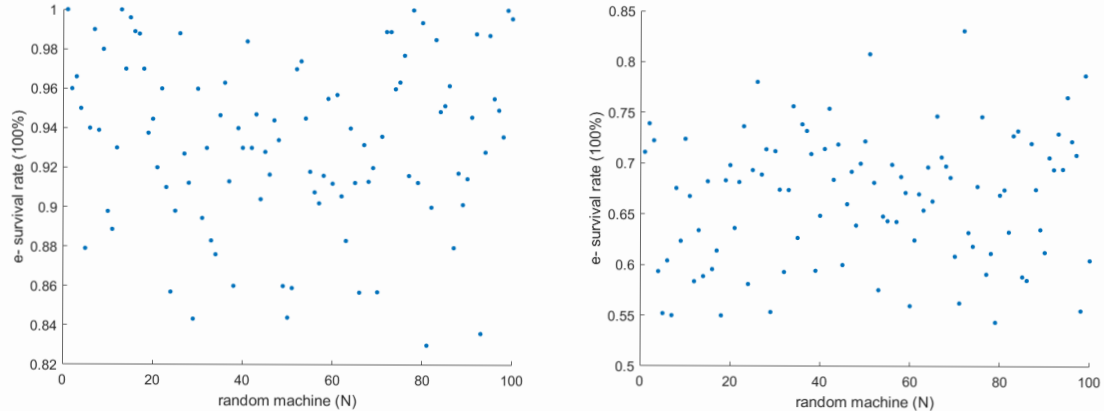
Note that beam head is set in the left ($z < 0$) in PLACET code simulation, while in SAD code it's in the right ($z > 0$). And this explains why the longitudinal phase spaces in Fig. 2.26 are in the opposite direction in z axis of those in Fig. 2.28(a) and 2.28(b) in our simulation.

As mentioned in the optics design of bypass above, the final beam size $\sigma_{x,y}$ is constrained to be around 1 mm. Although the transverse beam size $x-y$ in Fig. 2.28(b) looks a little weird (due to the collective effects of transverse wake fields and small aperture of linac), the largest y is still smaller than 10 mm, which is the aperture radius of the accelerating structure. Fig. 2.28(a) $x-y$ sizes are smaller than those in Fig. 2.28(b), but still they are around 1 mm.

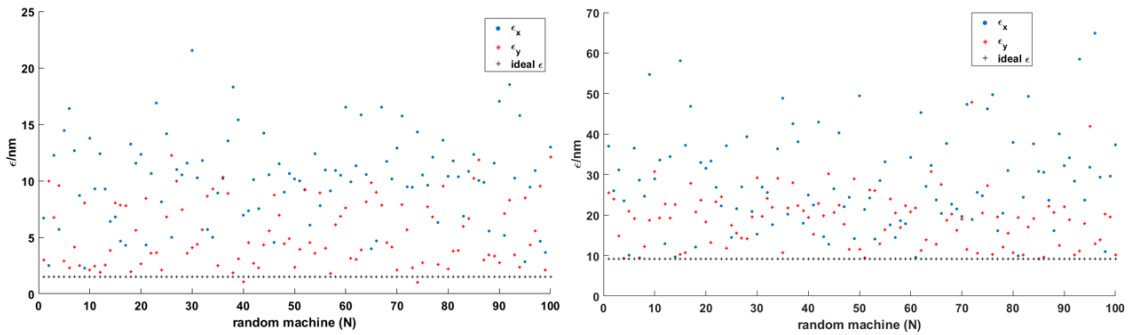
For the RF gun, 100 % of the 6.5 nC (4.06×10^{10}) electrons per bunch could be used to impinge on the positron target for positron production in ideal condition. The impact of misalignments as described in Table 2.11 also has been considered. The simulation process is as follows: the horizontal and vertical positions of initial injection beam, RF cavities and magnets are all misaligned according to a Gaussian distribution with standard deviation $\sigma_{pos} = 100 \mu\text{m}$, as listed in Table 2.11; the RMS misalignments of BPMs are set to be $30 \mu\text{m}$ to perform a better orbit steering (see reference [85] for details); each simulation is a Monte Carlo simulation with 100 different random configurations, which are named machines here. From the left plot of Fig. 2.29(a), at least 82 % (5.33 nC, 3.33×10^{10}) electrons can still survive at the dogleg exit after orbit steering correction within 100 random machines' simulation in RF gun case. For the simulation with thermionic gun, about 8.5 nC (5.31×10^{10} , 85 % of 10 nC) electrons could survive before hitting the positron target in ideal condition. However, only more than 5.5 nC (3.44×10^{10} , 55 % of 10 nC). This can be improved by the new lattice design and beam matching at the very beginning of the 4.46 GeV linac, as well as the use of more orbit steering techniques, like dispersion free steering and wakefield free steering, etc.) electrons per bunch can be used for positron production when considering the misalignments of optical elements, which can be seen from the right plot of Fig. 2.29(a).

Error type	Value [μm]
Injection beam offsets (h/v)	100
Cavity misalignments (h/v)	100
Quadrupole misalignments (h/v)	100
BPM misalignments (h/v) w.r.t cavities	30

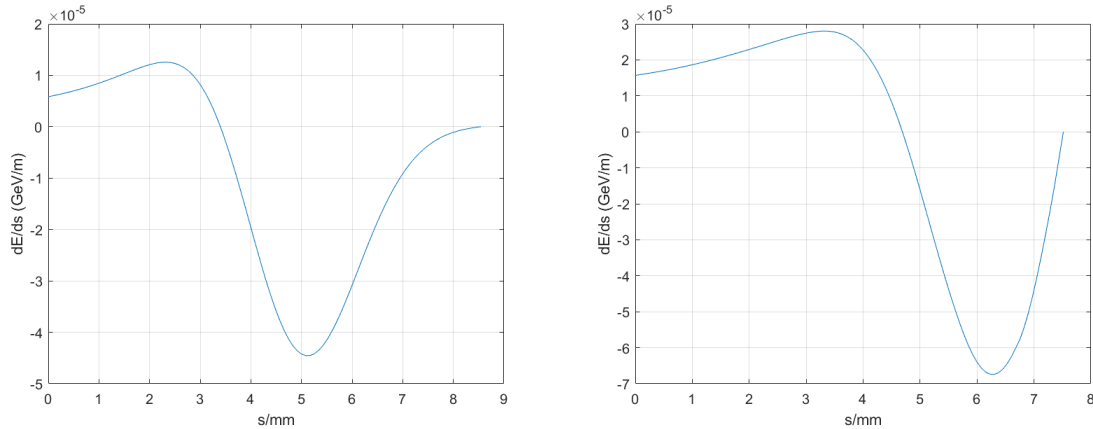
Table 2.11 Misalignments for the before-target elements in the dogleg scheme of the FCC-ee injector linac



(a) Left: 100 random machines with the RF gun feeding source; Right: 100 random machines with the thermionic gun feeding source;



(b) Left: The emittance change of the 100 random machines with the RF gun feeding source; Right: The emittance change of the 100 random machines with the thermionic gun feeding source



(c) Left: The dipole CSR study with the RF gun feeding source; Right: The dipole CSR study with the thermionic gun feeding source

Fig. 2.29 Misalignments impact study and CSR study before the positron target in the dogleg scheme

The emittance change of the 100 random machines also has been studied and its result is shown in Fig. 2.29(b). The maximum values of the transverse emittance for the two guns are around 23 nm / 64 nm, separately 15 times / 7 times as large as the ideal $\varepsilon_{x,y} = 1.5 \text{ nm} / 9.2 \text{ nm}$. A more complete and accurate simulation on the imperfection correction remains to be studied further in the future.

The CSR effect has also been taken into account, and the simulation results when the electron beam passes through the dogleg dipoles is shown in Fig. 2.29(c). The x-coordinate is the electron beam bunch length, and the y-coordinate is the beam energy change (unit: 10^{-5} GeV/m) along the bunch length. There is almost no energy change along the bunch length considering the beam energy of 4.36 GeV, which shows CSR has no influence on the electron beam distribution.

A summary of the performances of the two feeding electron beams before the positron target can be seen in Table 2.12.

feeding e ⁻ source	parameters	before e ⁺ target
6.5 nC RF gun	E [GeV]	4.39
	$\Delta E/E$	0.5%
	beam intensity [nC/bunch)]	$5.4 (N_{e^-} : 3.38 \times 10^{10})$
	$\varepsilon_{N_{x,y}} [\mu\text{m}]$	$15.7/22.7^1$ (ideal value: 13)
	$\sigma_{x,y} [\text{mm}]$	$0.5 \sim 1$
	$\sigma_{x',y'} [\mu\text{rad}]$	5
	$\sigma_z [\text{mm}]$	0.94
transmission efficiency		> 82 %
10 nC thermionic gun	E [GeV]	4.36
	$\Delta E/E$	0.69%
	beam intensity [nC/bunch)]	$8.44 (N_{e^-} : 5.28 \times 10^{10})$
	$\varepsilon_{N_{x,y}} [\mu\text{m}]$	$124/250^1$ (ideal value: 80)
	$\sigma_{x,y} [\text{mm}]$	~ 1
	$\sigma_{x',y'} [\mu\text{rad}]$	20
	$\sigma_z [\text{mm}]$	0.97
transmission efficiency		> 55 %

Table 2.12 Performances of the two feeding electron beams before the positron target in the dogleg scheme from tracking simulation with SAD code and PLACET code

The positron source The electron beam coming out of the dogleg bypass will hit the positron target for positron production. The generated positrons will be collected in the capture system for later acceleration. Detailed information could be found in reference [117]. The two electron

¹Collective effects in consideration

sources described before - the RF gun and the thermionic gun have been simulated in this part and show almost no difference.

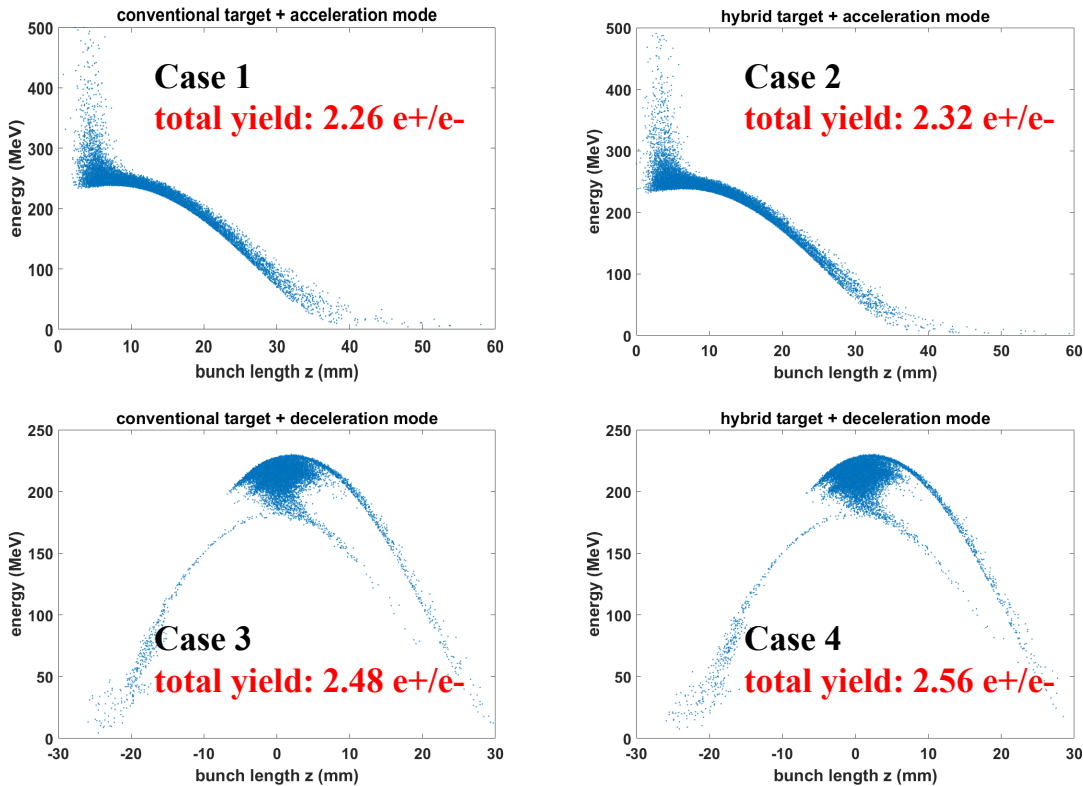


Fig. 2.30 Positron source: Longitudinal phase space for different cases of positron production in the end of capture linac

Two kinds of positron targets have been simulated: the conventional target (a thick amorphous tungsten target) and the hybrid target (a crystal + an amorphous tungsten target). After the positron generation, an AMD is used to match the positron beam (with very large transverse divergence and energy spread) to the acceptance of the capture linac. In the downstream capture linac, positrons will be accelerated approximately to about 200 MeV. Two operation modes, accelerating mode and decelerating mode in the first RF structure of the capture linac, also have been studied in order to find the best option for a good positron yield potentially. The specific study results of the output positron beam distribution of the capture system for different cases are shown in Fig. 2.30 (The simulated number of incident macro-electrons is ten thousand).

It is obvious to find that there is a large tail in the distribution of the acceleration mode (case 1, 2) in the first RF structure of the capture linac which causes a very long bunch length. While in the deceleration mode (case 3, 4), most of the particles well accumulate in high energy area (about 200 MeV), which is not only easier to fit into the acceptance of the DR, but also

helps to boost the positron yield. At the same time, there's almost no big difference in positron yield comparing the hybrid target with the conventional target, but the hybrid target will cost more than the conventional one.

After comparing the results for the two types of positron targets (the conventional target and the hybrid target) and the two operation modes (the accelerating mode and the decelerating mode) in the first RF structure of the capture linac, taking the cost and positron yield into consideration, the case of conventional target with the deceleration mode (case 3) is chosen for our preliminary study of the positron production, whose details are shown in Fig. 2.31. In this case, the total positron yield is about $2.48 N_{e^+}/N_{e^-}$ at the end of the 200 MeV capture linac, and the effective yield is about $2.28 N_{e^+}/N_{e^-}$ as shown in the red box of Fig. 2.31 (only considering the high energy area at around 200 MeV). We assume that about 5.5 nC (3.44×10^{10}) electron particles of the 10 nC electron beam can survive before impinging on the positron target. Then about 12.5 nC (7.8×10^{10}) positron particles per bunch could be obtained after capture system without considering wakefields and misalignments of accelerator components.

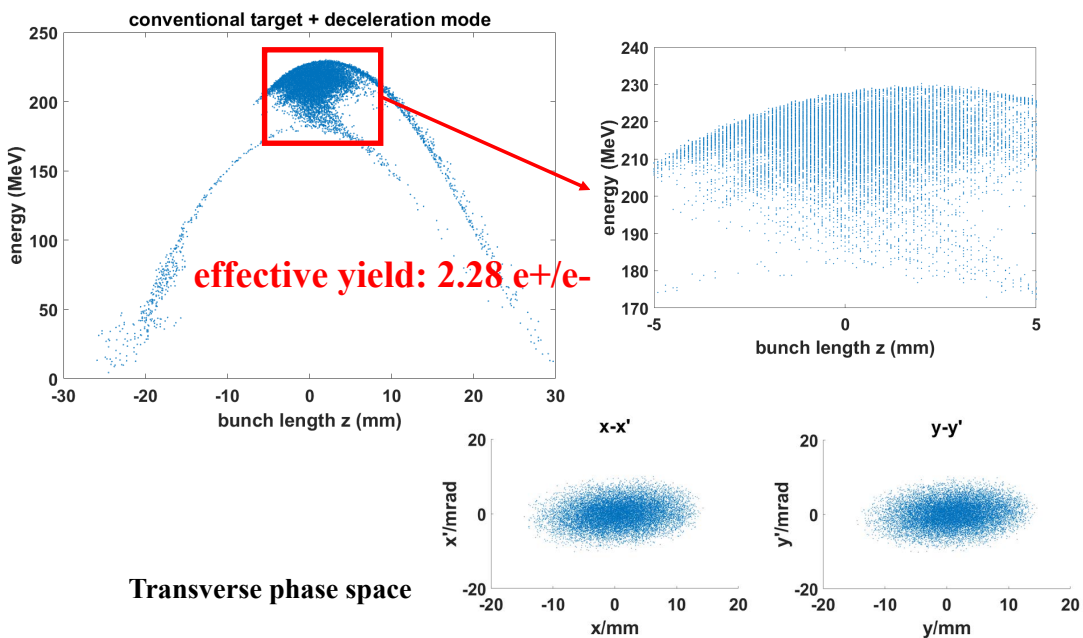


Fig. 2.31 Positron source: Phase space of case 3 at the end of the positron capture linac

The electron/positron separator In fact, apart from positrons, the beam coming out of the 200 MeV capture linac also contains photons and secondary electrons generated by initial positron production process. To get pure positrons after the capture system, a separator chicane is located between the 200 MeV capture linac and the main 1.54 GeV positron linac to separate

the mixture of positrons and secondary electrons. The design idea follows the electron/positron separator of SuperKEKB (see Fig. 2.32) [66]. The secondary electrons are absorbed by a 60 mm thick tungsten-copper alloy (W 70 % + Cu 30 %) block. A positron stopper block is set on the other side of the separator.

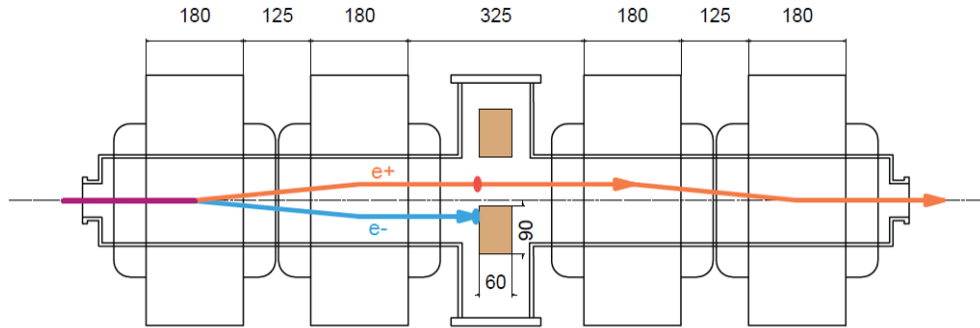


Fig. 2.32 The electron/positron separator chicane of SuperKEKB [66]

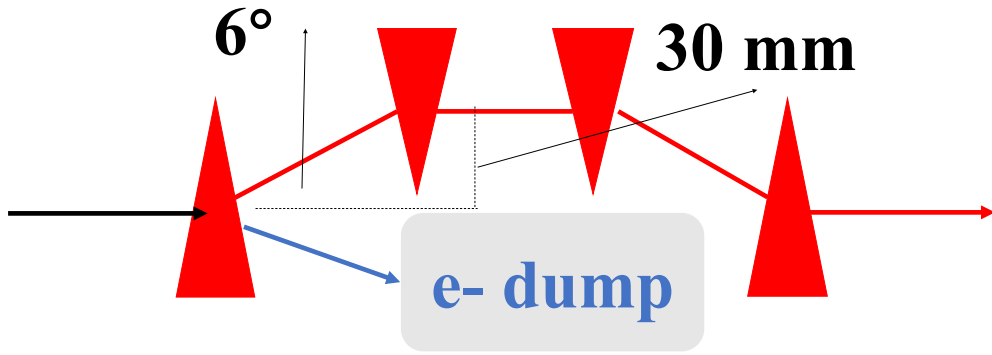


Fig. 2.33 The schematic layout of the electron/positron separator chicane for FCC-ee positron system

Fig. 2.33 shows the sketch of our design in FCC-ee, where the electron beam and positron beam will be deflected 6° off the longitudinal axis in symmetric directions. In the middle of the chicane, positron beam passes 30 mm aside from the beam line axis to ensure no interactions with separated electron beam. The optics design calculated with MADX is shown in Fig. 2.34. Fig. 2.35 shows the phase space of the positron beam tracking result at the end of the separator chicane. Its energy is 214.7 MeV with an energy spread of 3.75 %. The total simulated positron charge is 12.5 nC and the positron bunch length is around 1.9 mm. The transverse beam size is

$\sigma_{x,y} = 4.5$ mm and the calculated geometric transverse emittance is $\epsilon_{x,y} = 13.9 \mu\text{m}$ ($\epsilon_{N,x,y} = 5.87$ mm). The total length of the separator chicane is 5.35 m.

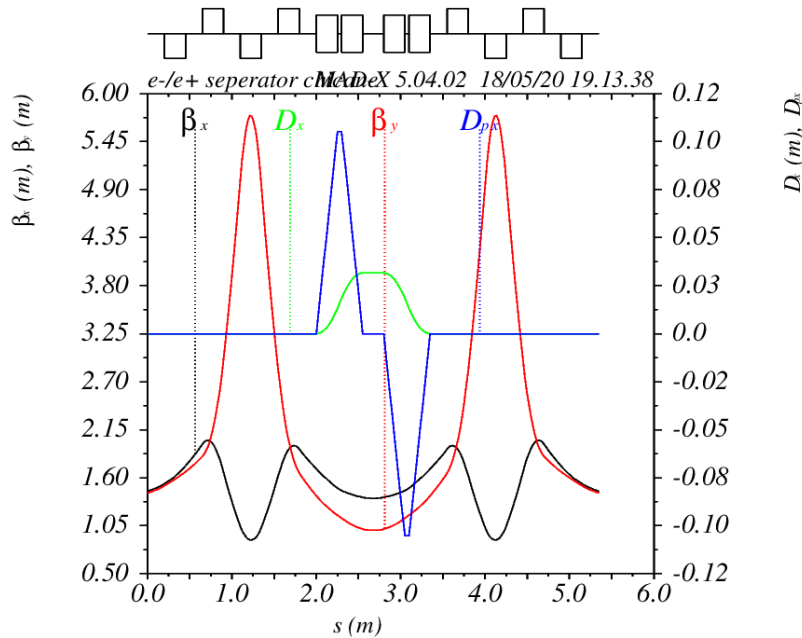


Fig. 2.34 Optics of the electron/positron separator chicane calculated with MADX

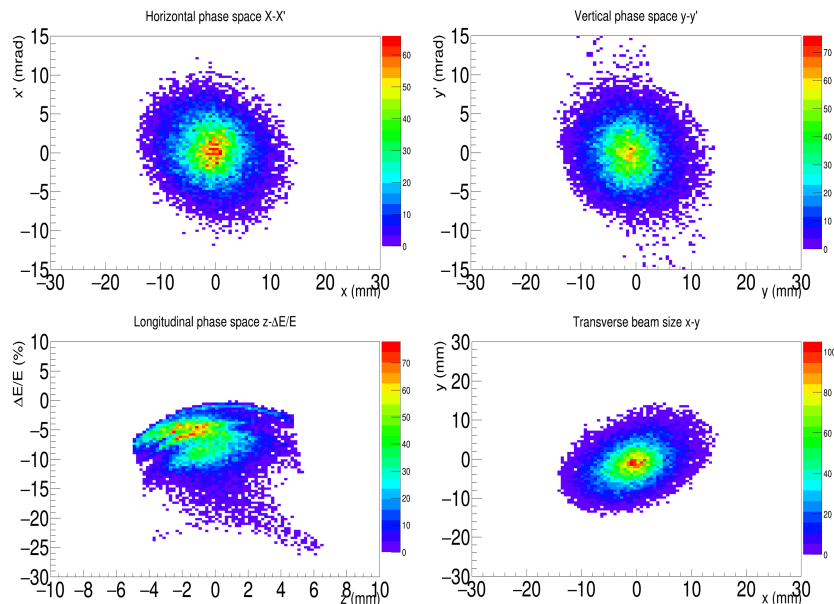


Fig. 2.35 Phase space at the end of the electron/positron separator chicane calculated with PLACET

The 1.54 GeV positron linac Using a Gaussian distribution, about 99.7 % of the values lie within three standard deviations ($\pm 3\sigma$) of its mean value. As a result, the aperture radius R_A of the accelerating structure in the 1.54 GeV positron linac at least needs to be 3 times larger than the positron beam size $\sigma_{x,y}$ (see equation 2.1) for a full transmission.

$$R_A \geq 3\sigma_{x,y} = 3\sqrt{\beta\varepsilon} \quad (2.1)$$

$$\beta_{max,x,y} = \left\{ \frac{R_A}{3} \right\}^2 / (\varepsilon_{N,x,y}/\gamma) \quad (2.2)$$

We can get the maximum β value change along the linac using equation 2.2. Forty periodic accelerating structures are used for positron beam acceleration to about 1.54 GeV. The first 12 accelerating structures use "Large aperture S-band" structures (LAS) (Fig. 2.17) [77] with a length of 2 m, an aperture radius of 15 mm and an accelerating gradient of 10 MV/m for a better acceptance as much as possible. The left 28 are normal 2.856 GHz S-band structures whose length is 2 m, aperture radius is 10 mm and acceleration gradient is set 20 MV/m. The specifications of the two accelerating structures are presented in table 2.13. The magnetic field B of quadrupoles is also well limited below 2 T for NC magnets with an aperture radius of 0.1 m.

Items	LAS	NC S-band
Frequency [GHz]	2.856	2.856
Active accelerating length [m]	2	2
Aperture diameter (2a) [mm]	30	20
Accelerating gradient [MV/m]	10	20

Table 2.13 Main parameters of the two accelerating structures used in the 1.54 GeV (section 4) positron linac for the dogleg scheme

FODO lattice has been chosen for the 1.54 GeV linac optics design. Three different FODO subsections have been designed, whose focus-and-defocus-quad distance (FODO 1: 0.3 m; FODO 2: 0.5 m; FODO 3: 0.8 m) increases gradually. The detailed parameters are listed in Table 2.14. Fig. 2.36 shows the schematic diagram of the three FODO lattices. 130 quadrupoles are used in the design, including 8 quadrupoles for matching between different subsections. Some quadrupoles in the three FODO cells are overlapped on the accelerating structures in our design in order to accept as many positrons as possible.

The lattice design is presented in Fig. 2.37. The total length of the linac is 99.9 m. Fig. 2.38 shows the positron beam energy change along the linac. The simulated parameters of the 1.54 GeV positron linac are listed in Table 2.15. Fig. 2.39 shows the phase space of the positron

Subsection	L_Q [m]	k [m^{-2}]	β_{max} [m]	L_{cell} [m]	N_{cell}	E_{input} [GeV]	E_{output} [GeV]	Linac structure
1	0.3	± 8.20	2	1.2	36	0.214	0.694	12 LAS + 6 NC
2	0.4	± 4.69	3	1.8	17	0.694	1.254	14 NC
3	0.4	± 3.22	4	2.4	8	1.254	1.564	8 NC

Table 2.14 Parameters of the three different FODO cells for the 1.54 GeV (section 4) positron linac design in the dogleg scheme

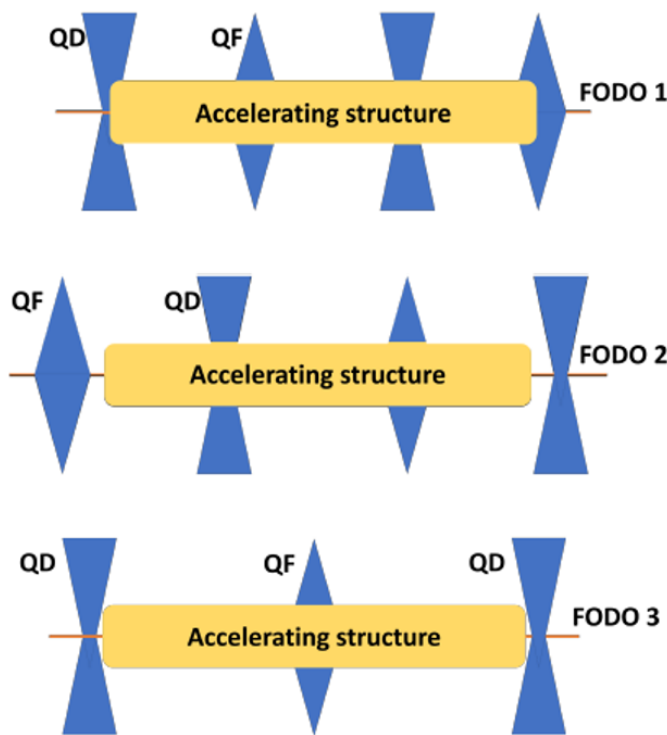


Fig. 2.36 Schematic drawing of the three FODO lattices in the 1.54 GeV (section 4) positron linac design for the dogleg scheme

Parameter (unit)	Value
Length (m)	99.9
Electron energy (GeV)	1.56
Injected emittance (h/v)	$13.9 \mu\text{m}$
Average extracted emittance (h/v)	$\sim 2 \mu\text{m}$
Normalized emittance (h/v)	$\sim 6 \text{ mm}$

Table 2.15 Main parameters of the 1.54 GeV (section 4) positron linac in the dogleg scheme

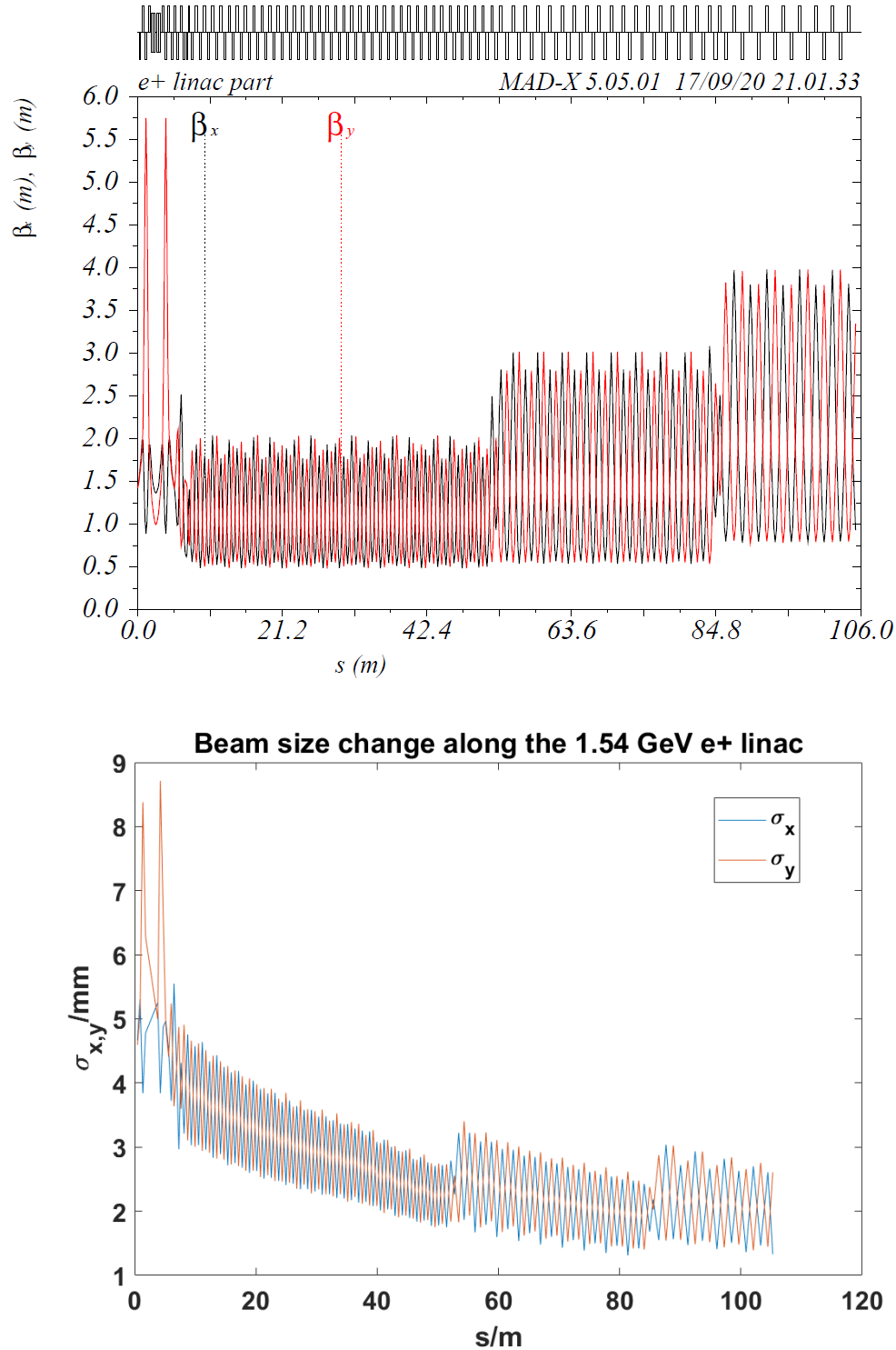


Fig. 2.37 Optics of the 1.54 GeV (section 4) positron linac in the dogleg scheme calculated with MADX. Top: betatron function; Bottom: beam envelope

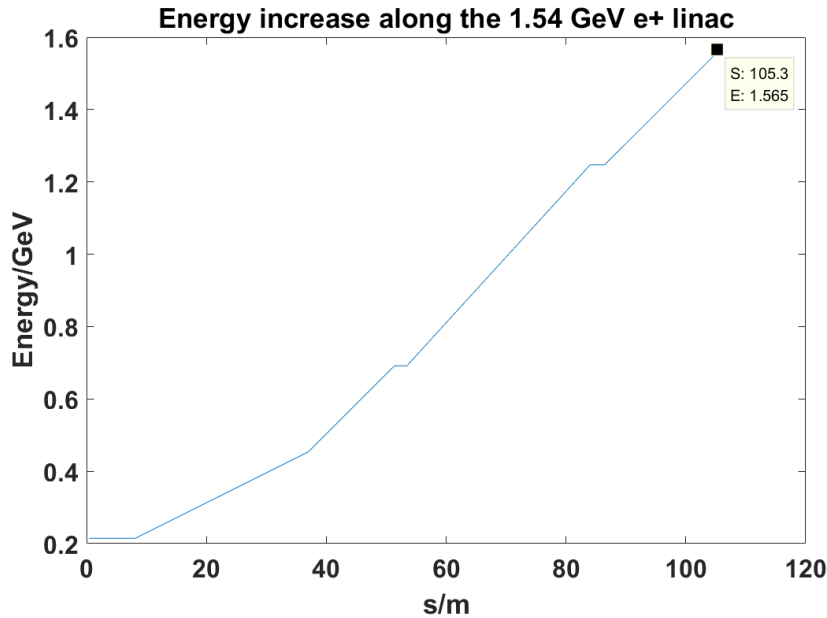


Fig. 2.38 The positron beam energy change along the 1.54 GeV (section 4) positron linac in the dogleg scheme

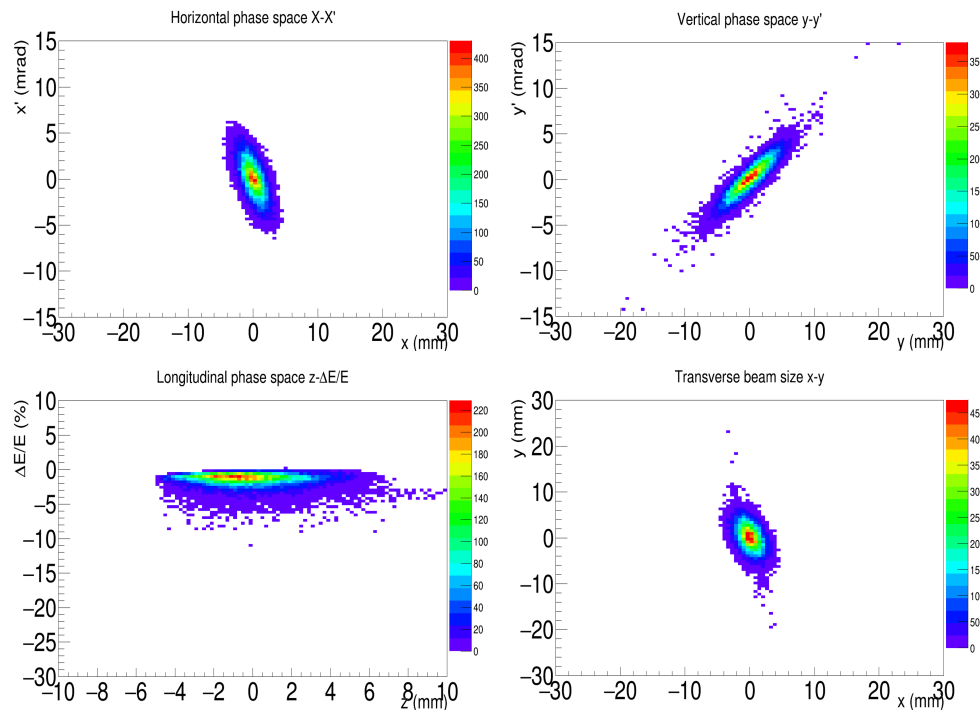


Fig. 2.39 Phase space at the end of the 1.54 GeV (section 4) positron linac in the dogleg scheme calculated with PLACET

beam tracking result at the end of the 1.54 GeV positron linac, whose normalized transverse emittance is $\epsilon_{N,x,y} \approx 6$ mm.

The turnaround loop A turnaround loop (arc structure) has been designed to transfer the 1.54 GeV positron beam back into the DR for beam cooling. This is the final step of the whole design of the dogleg scheme positron system. The 1.54 GeV positron beam with very high emittance needs to be cooled in the DR to meet the requirement of injection into the PBR. Given that the DR also can be used for low emittance electron beam cooling besides for positron beam, we locate it near the section 1 (1.54 GeV electron) linac. Therefore, a turnaround loop is necessary to turn around the positron beam out of the section 4 (1.54 GeV positron) linac.

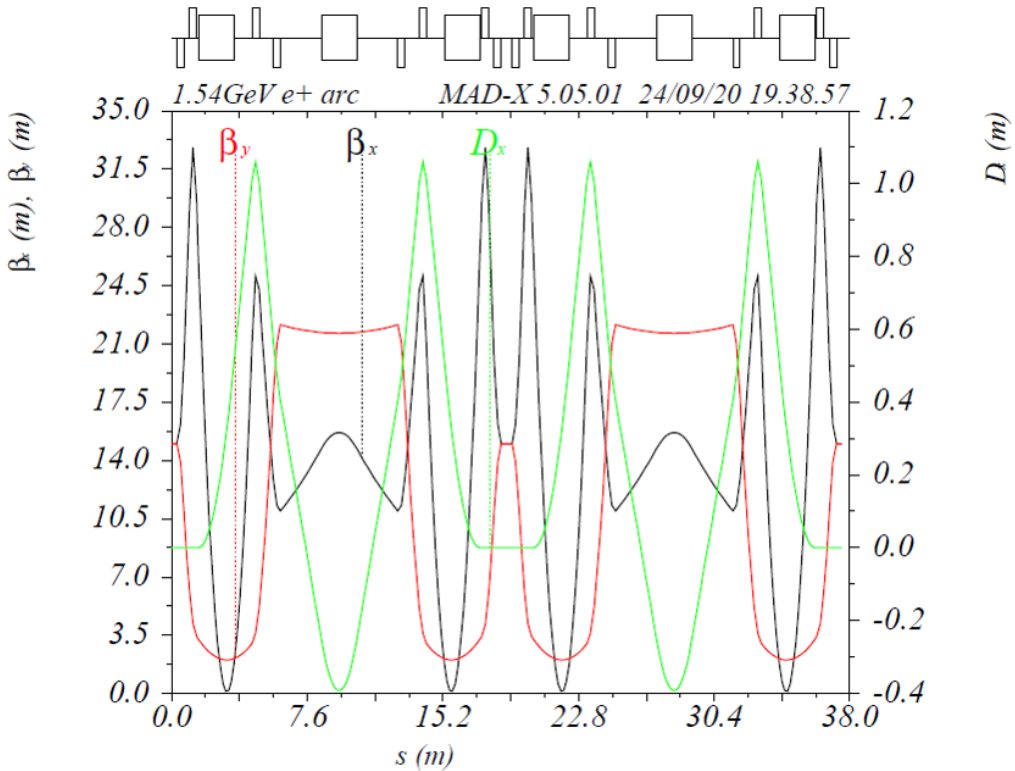


Fig. 2.40 Optics of the turnaround loop in the dogleg scheme

In our design, the turnaround arc is composed of two TBA (triple bend achromat) cells, shown in Fig. 2.40, which is inspired by the CLIC Central Arc [12]. The reason why we use TBA structure here is that the first-order transfer matrix value R_{56} (determining the relation between bunch length and energy spread $\delta E/E$) can be easily controlled in longitudinal distribution. The TBA arc has been used to avoid bunch lengthening ($R_{56}=0$, see Fig. 2.41). Quadrupoles are used for betatron manipulation and dispersion correction, and four pairs of

sextupoles are used to limit the second-order transfer matrix values T_{166} and T_{266} to 0 with the k_2 values of $\pm 10 \text{ m}^{-3}$. The total length of the arc is 44.25 m (the horizontal distance between the 1.54 GeV positron linac and the exit of the turnaround arc is around 24 m).

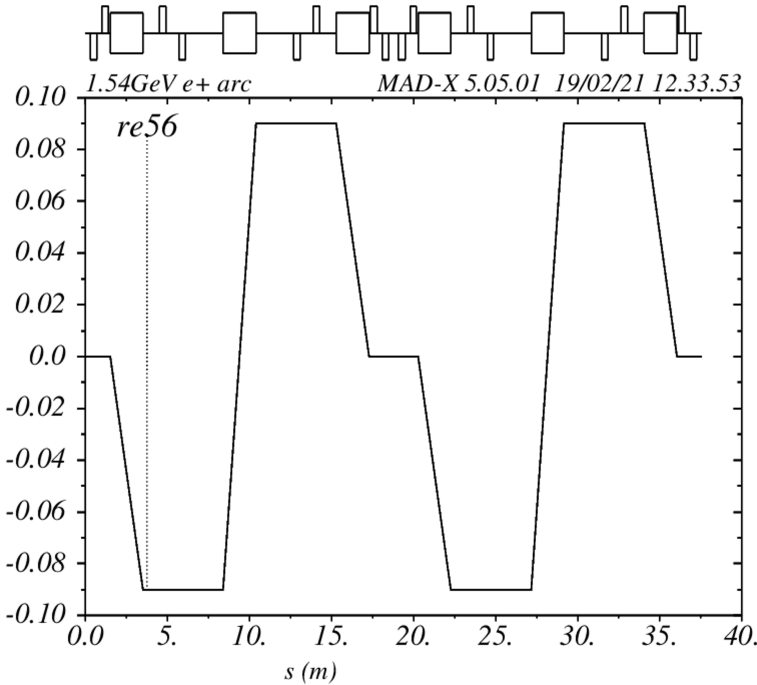


Fig. 2.41 R_{56} change along the turnaround loop

The start-to-end optics design after positron target from the separator chicane to the turnaround loop arc is presented in Fig. 2.42. The total length of this area is 152.8 m.

The beam distribution before the DR can be seen from Fig. 2.43, with a normalized emittance $\varepsilon_{Nx,y}$ of 7.12 mm, geometric transverse emittance $\varepsilon_{x,y}$ of 2.325 μm , energy spread $\Delta E/E$ of 1%, and bunch length σ_z of about 2.2 mm. According to the FCC-ee CDR [36], the transverse emittance acceptance of the DR is 22.4 μm , the energy acceptance is $\pm 7.8\%$ and the longitudinal acceptance is 14.7 mm, which leaves a large margin in view of our tracking simulation.

The final accepted positron bunch intensity is about 7.8×10^{10} before the DR without considering positron linac wakefields and misalignments, which can meet the demand of 2.13×10^{10} positron particles per bunch. The final positron yield before the DR is about $7.8 \times 10^{10}/6.25 \times 10^{10} = 1.2 N_{e^+}/N_{e^-}$. Realistic bunch intensity will be studied in future with the experiments of test facilities for the positron production.

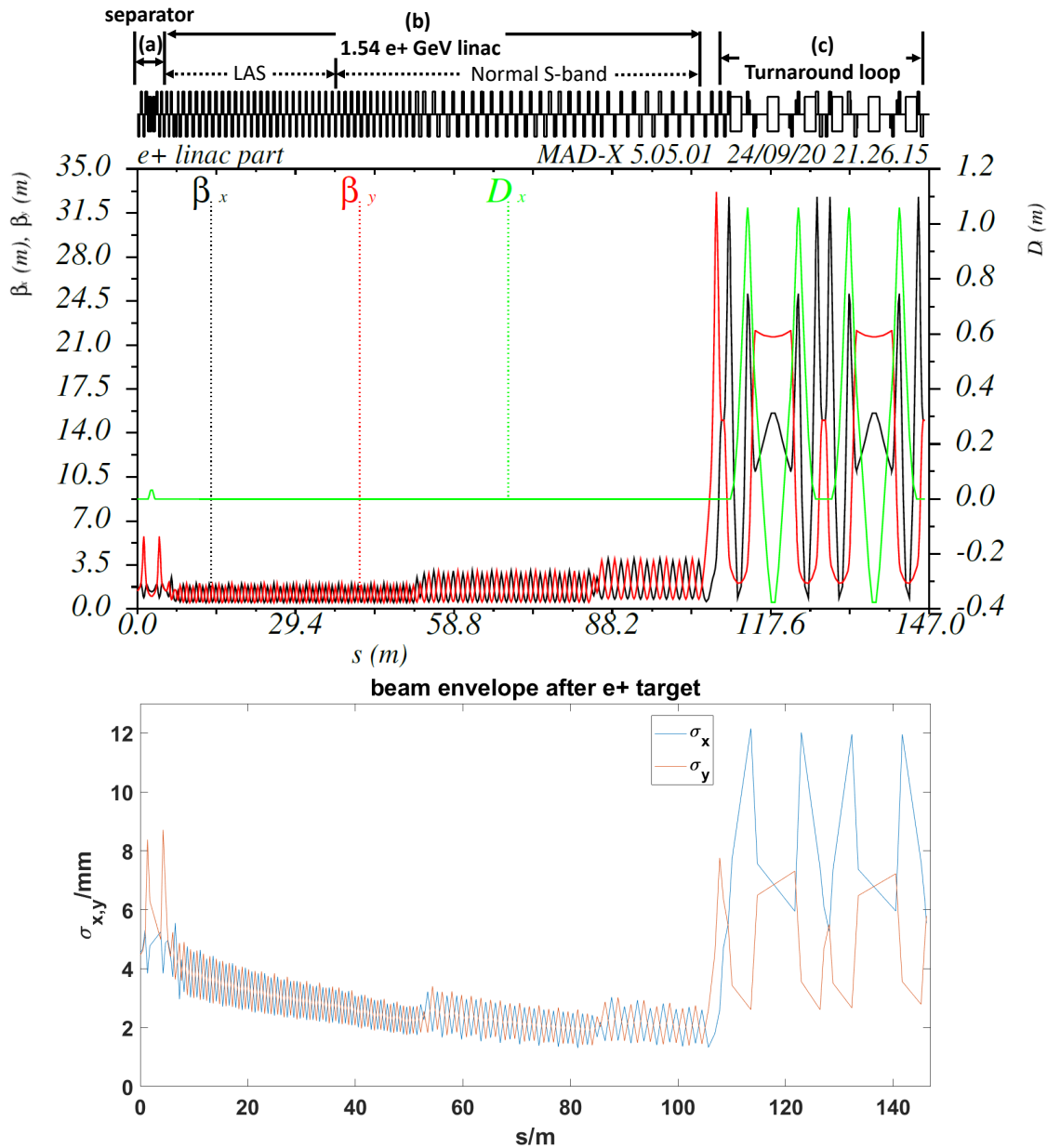


Fig. 2.42 Optics design after the positron target in the dogleg scheme calculated with MADX and PLACET: Top plot: betatron function; Bottom plot: beam envelope evolution (This is the 10 nC thermionic feeding e^- gun case; the result is similar for the 6.5 nC RF feeding e^- gun)

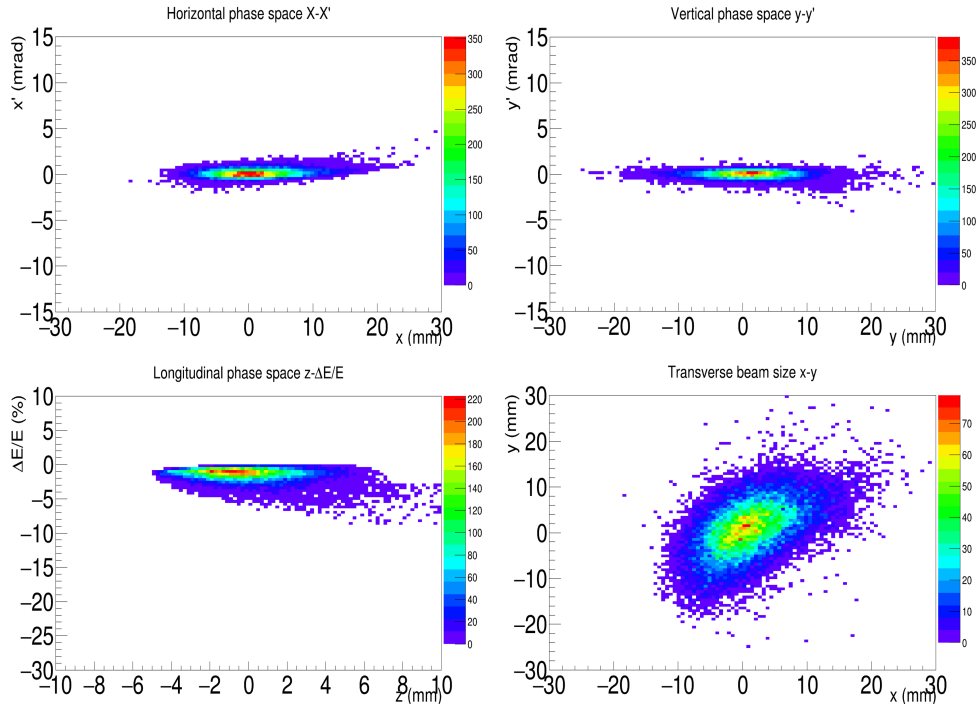


Fig. 2.43 Phase space at the end of the turnaround loop in the dogleg scheme

2.4.2 Chicane scheme

The chicane scheme design is shown in Fig. 2.44: the electron beam not serving for positron production is first accelerated in the 4.46 GeV linac (section 1, 2); and then bypassed by a chicane structure; finally gain another 1.54 GeV energy in section 4 linac before injection into PBR. The electron beam serving for positron production makes its way in the straight line. After the created positrons get captured, they will follow the same path before the DR as what the positrons undergo in the dogleg scheme. When the positrons come out of the DR, they will go through the section 2 linac, the second chicane bypass and the section 4 linac to PBR. One advantage of this scheme is that we do not need a supplementary linac (section 3) as in the Dogleg scheme.

There are some similarities between this scheme and the CEPC linac baseline scheme (see Fig. 2.45) [79]. Both schemes use a chicane bypass for the transport of the low emittance electron beam which is not serving for positron production, the positron targets are all located in the direct line, and the positron beams are all produced by an incident electron beam of around 4 GeV energy. However, an advantage of our chicane scheme is that section 2 and section 4 linacs will be reused for positron acceleration, which is not the case for the CEPC scheme.

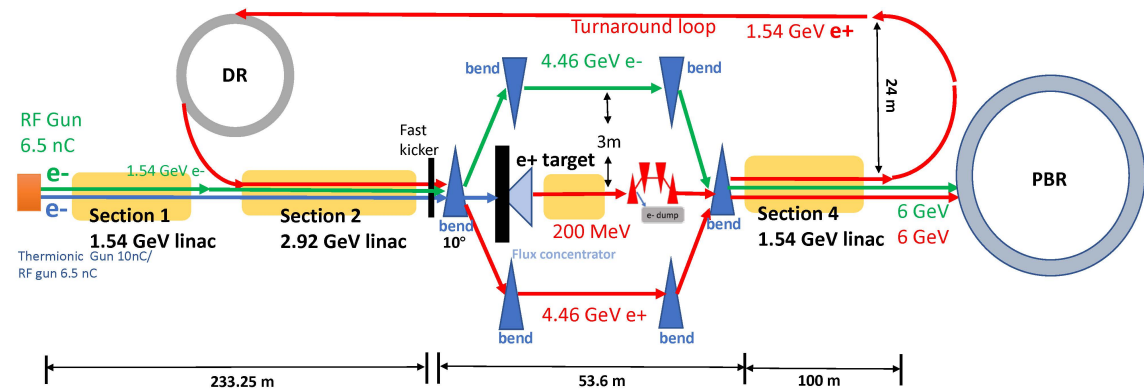


Fig. 2.44 The Chicane scheme for the FCC-ee injector linac

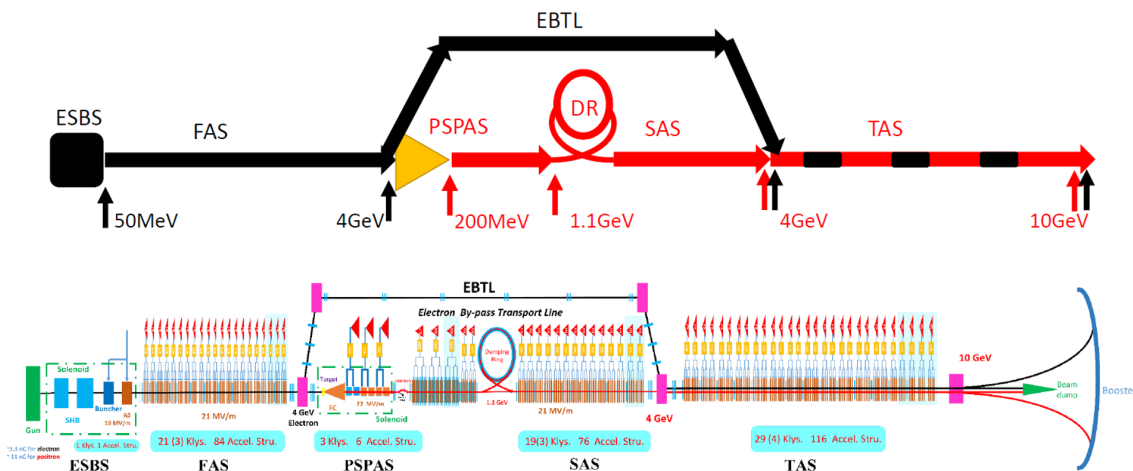


Fig. 2.45 The CEPC injector system and details of the positron production on the top (black color: electron beams; red color: positron beams) [79]

The two parts of the chicane scheme (Fig. 2.44) are shown in Fig. 2.46 (electron injection chain) and Fig. 2.53 (positron production chain). In the chicane scheme, the electron beam serving for positron production makes its way in the straight line. It directly impinges on positron target for positron production when coming out of the 4.46 GeV electron linac (section 1 linac + section 2 linac). The 3.5 nC low emittance electron beam not serving for positron production will go through the chicane bypass.

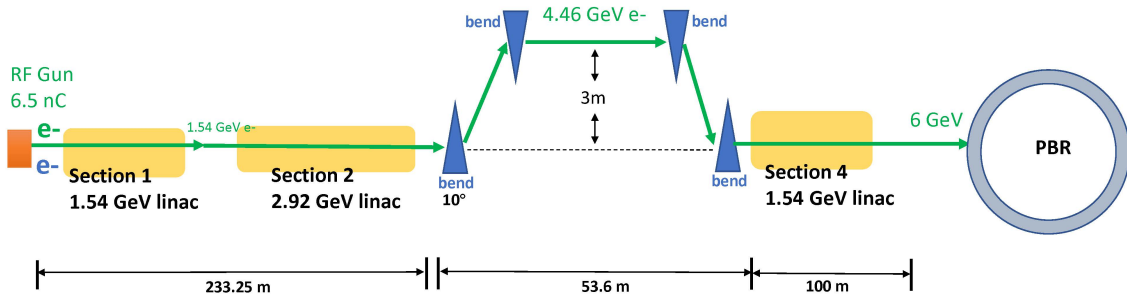


Fig. 2.46 The electron injection chain of the chicane scheme for the FCC-ee injector system

Electron injection chain in the chicane scheme

As shown in Fig. 2.46, the electron injection chain is composed of an RF gun, a 4.46 GeV electron S-band linac (section 1 + section 2), a chicane bypass and a 1.54 GeV electron/positron linac (section 4).

The 4.46 GeV linac The optics design of the 4.46 GeV linac and the tracking simulation with wakefields effect of 3.5 nC electron beam at the end of the linac calculated with SAD code are respectively shown in Fig. 2.47 and 2.48.

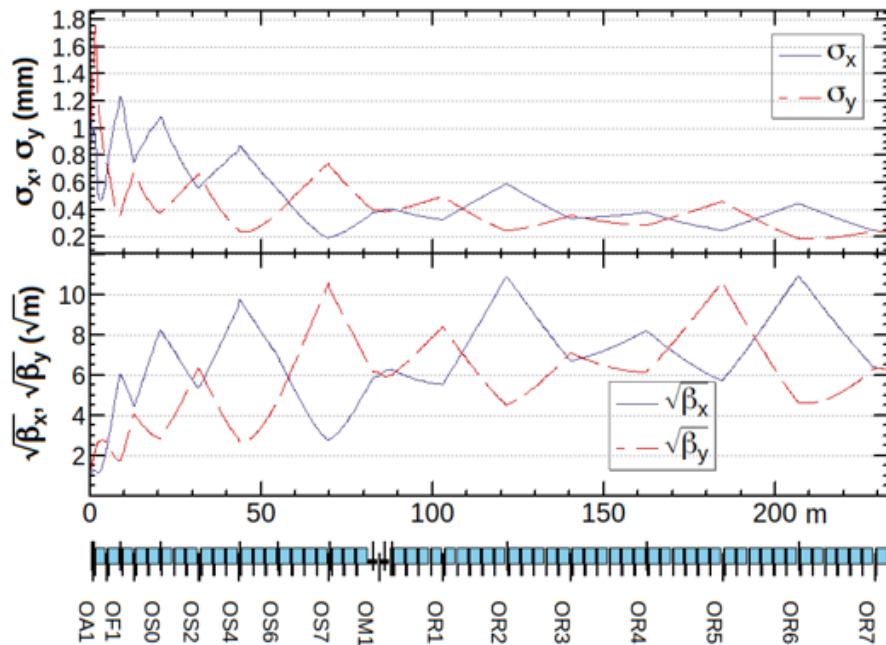


Fig. 2.47 Optics design of the 4.46 GeV electron linac in the chicane scheme calculated with SAD

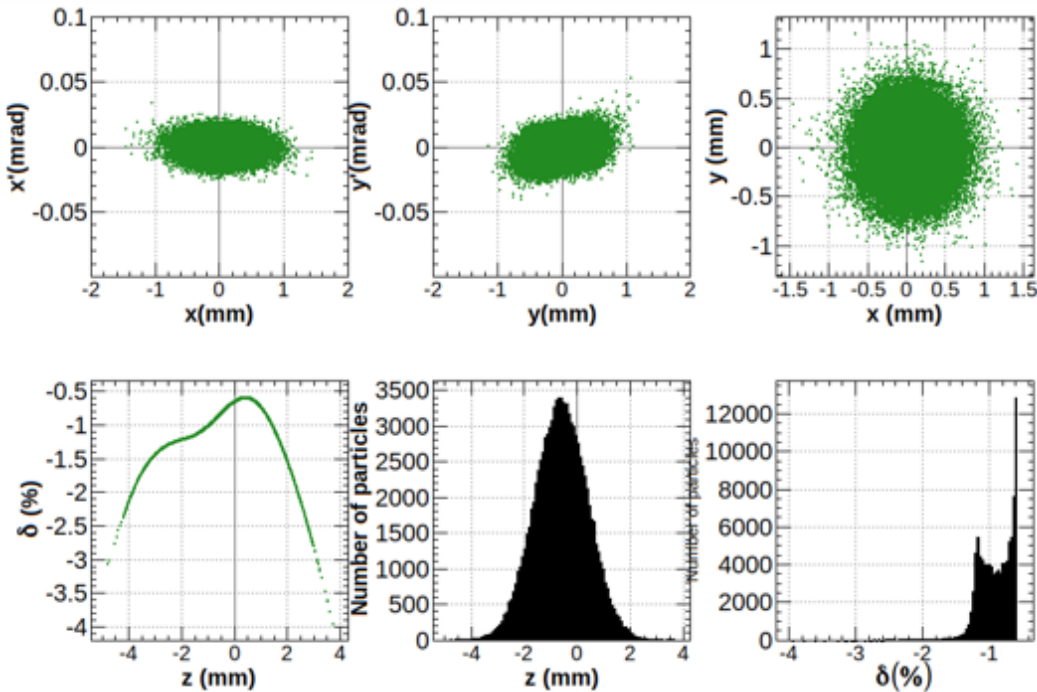


Fig. 2.48 Phase space of 3.5 nC electron beam at the end of the 4.46 GeV electron linac in the chicane scheme calculated with SAD

The chicane bypass The 3.5 nC electron beam will move in the downstream chicane bypass when it comes out of the 4.46 GeV electron linac. The optics design calculated with MADX can be seen in Fig. 2.49. The horizontal distance between the middle of the chicane bypass and the straight positron production line is kept 3 m for positron target shielding. The chicane is a symmetric structure constituted by four 2-meter-long 10° dipoles. Two pairs of sextupoles are used for chromaticity correction. Fig. 2.50 shows the phase space calculated with PLACET of the 3.5 nC electron beam at the exit of the chicane bypass. The total length of the chicane is 53.6 m.

The CSR study making use of PLACET code also has been performed in the dipoles of the chicane bypass and shows no impact on the beam distribution. The simulation result can be found in Fig. 2.51.

The 1.54 GeV electron/positron linac The optics design of the 1.54 GeV electron/positron linac calculated with MADX is the same as depicted in Fig. 2.37, and the phase space of the 3.5 nC electron beam before injection into the PBR calculated with PLACET considering wakefields effect is presented in Fig. 2.52.

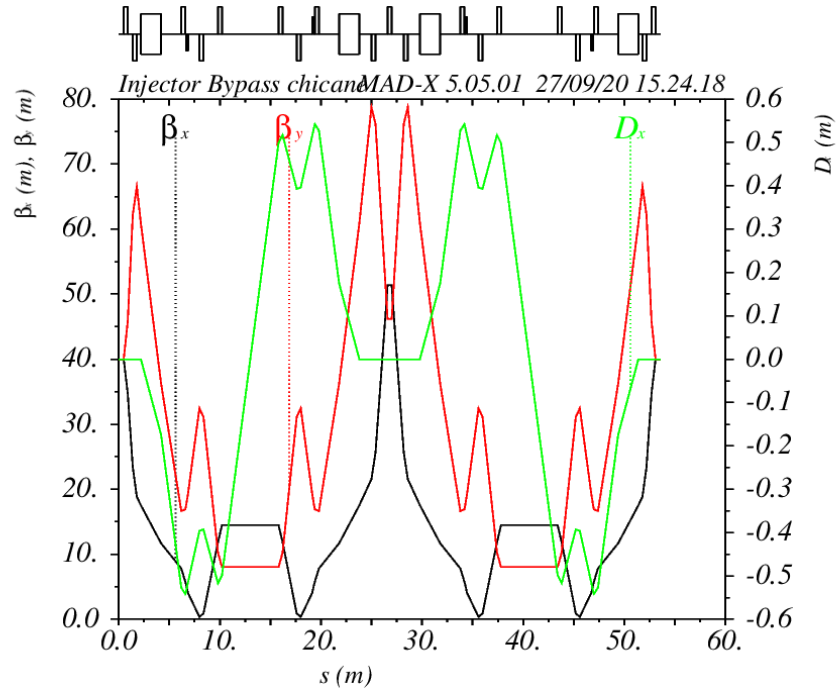


Fig. 2.49 Optics design of the chicane bypass in the chicane scheme calculated with MADX

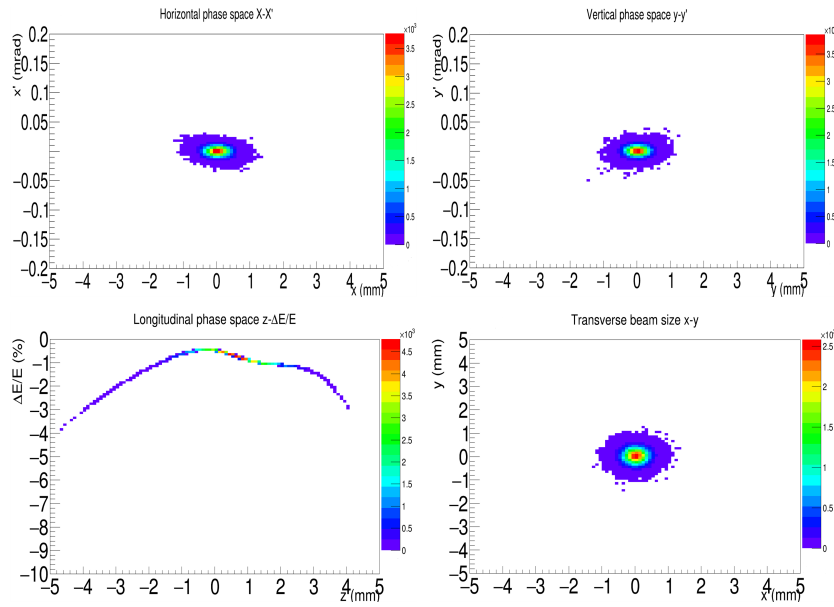


Fig. 2.50 Phase space of the 4.46 GeV 3.5 nC electron beam at the chicane bypass exit calculated by PLACET

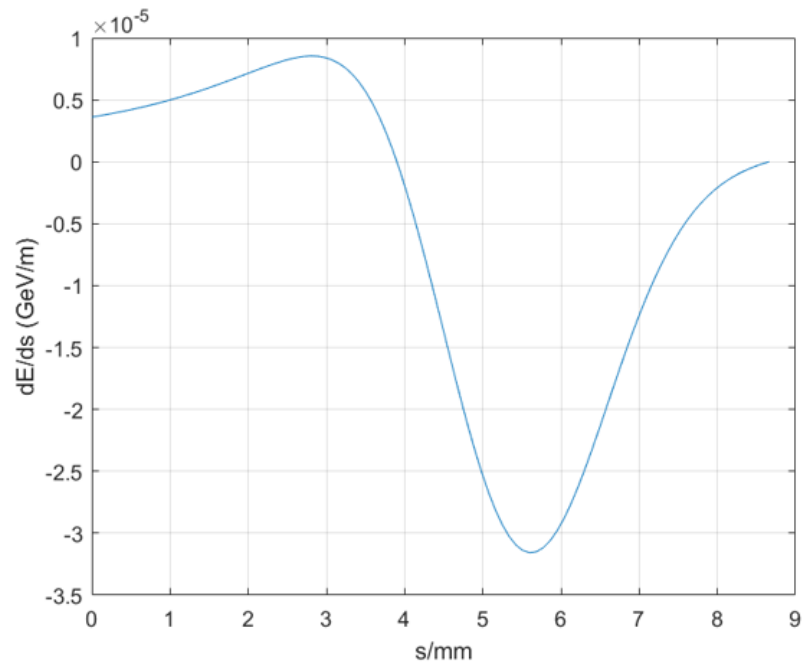


Fig. 2.51 The CSR study of the chicane bypass calculated with PLACET

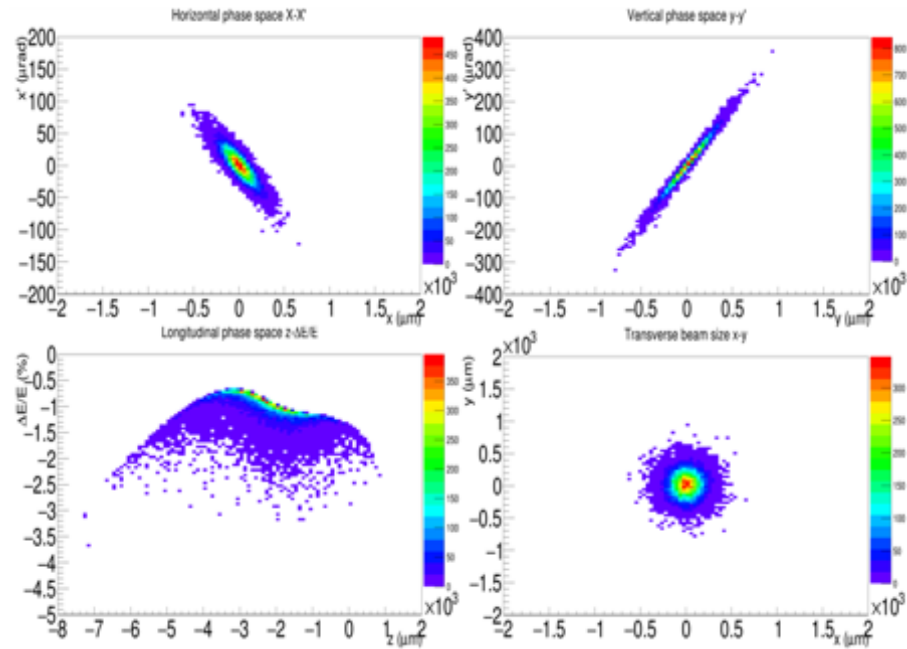


Fig. 2.52 Phase space of 3.5 nC electron beam before injection into the PBR calculated by PLACET

Positron production chain in the chicane scheme

The positron production chain (Fig. 2.53) consists of an RF gun / a thermionic gun, a 4.46 GeV electron linac (section 1 + section 2), a positron target with a capture system, an electron/positron separator, a 1.54 GeV (section 4) positron linac and a turnaround loop to transfer positrons to the damping ring.

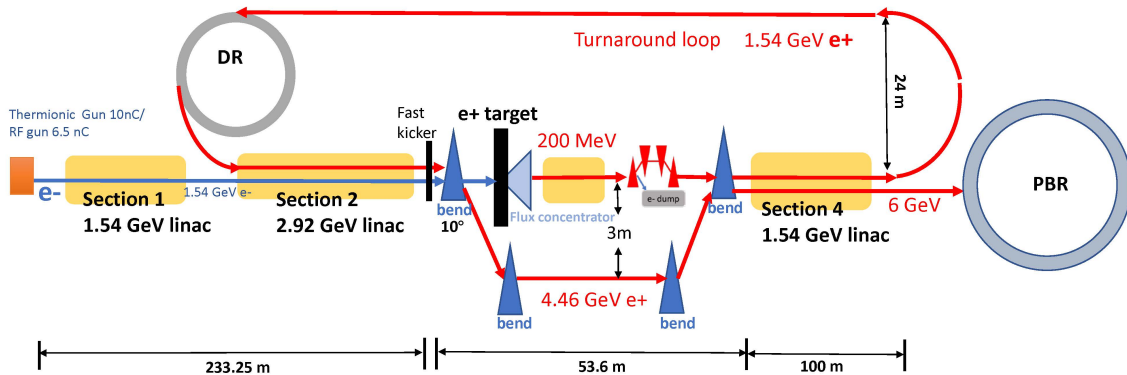


Fig. 2.53 Positron production chain of chicane scheme

The optics design calculated with SAD code for the two feeding electron sources in the 4.46 GeV electron linac is the same as shown in Fig. 2.25. Meanwhile, the positron source keeps the same scheme as in the dogleg scheme. The optics design for the part after positron target for the chicane scheme of the FCC-ee injector is presented as in Fig. 2.42 of the dogleg scheme, and for the corresponding beam distribution we could also refer to Fig. 2.35, Fig. 2.39 and Fig. 2.43.

In the case of the chicane scheme, when the positrons come out of the DR, they will be accelerated again in the section 2 (2.92 GeV) linac, and then be bypassed in the second chicane structure. This structure design is consistent with the one used in the electron system, whose specific structure information is shown in Fig. 2.47. In the next step, section 4 (1.54 GeV) linac will be reused for the final acceleration of the 4.46 GeV positron beam coming from the second chicane to the energy of 6 GeV.

2.4.3 Arc scheme

The arc scheme shown in Fig. 2.54 is quite similar to the dogleg scheme. The first low emittance electron beam will follow a similar path as in the dogleg scheme to the PBR. However, we use an arc to turn around the second electron beam for the positron production at the energy of 4.46 GeV, which has simpler structures than the dogleg scheme. This arc is constituted by six 30° dipoles like the design of the turnaround loop in the dogleg scheme, but longer dipoles of 4 m

length are used. When the positrons are produced, they will follow the same path as in the case of the dogleg scheme, but the advantage in this case is that the turnaround loop is not needed anymore. Notice that in this case the higher energy of the beam in the arc (4.46 GeV instead of 1.56 GeV) could be a concern.

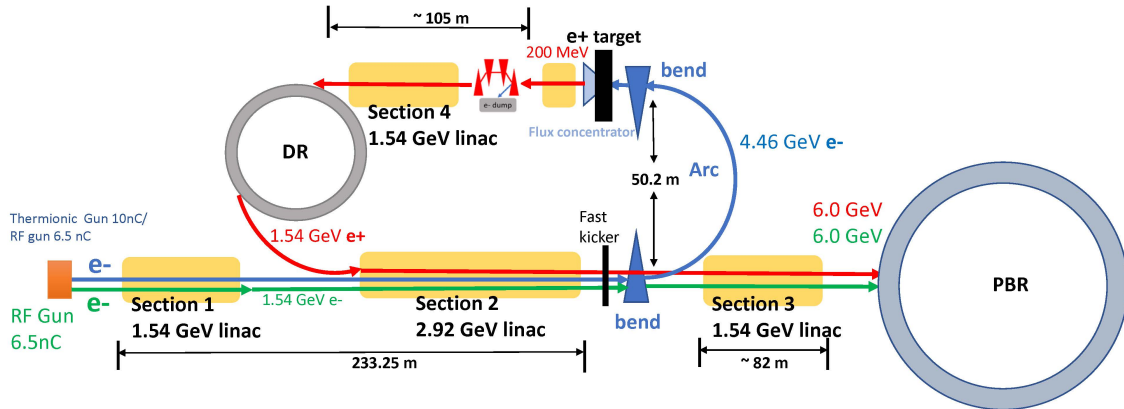


Fig. 2.54 Arc scheme for FCC-ee injector linac

The arc scheme injector linac could be divided into two parts: the electron system (Fig. 2.55) and the positron system (Fig. 2.56).

Electron injection chain in the arc scheme

The electron injection chain is exactly the same the dogleg scheme. The details could be found in chapter 2.4.1.

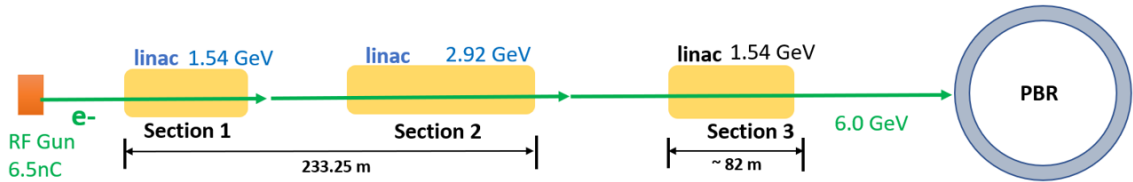


Fig. 2.55 The electron injection chain of arc scheme

Positron production chain in the arc scheme

There are two parts of the positron production chain as presented in Fig. 2.56. One is the part before the positron target, and the other one is the after-target part. The former is made up of a 4.46 GeV electron linac and a turnaround arc structure, and the latter consists of a positron source (positron target + capture system), a separator chicane and a 1.54 GeV positron linac.

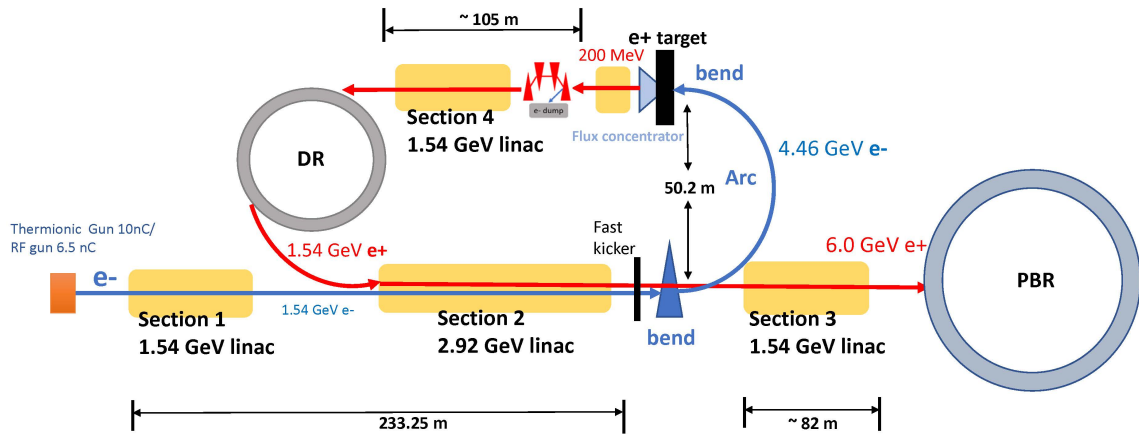


Fig. 2.56 The positron injection chain of arc scheme

Before-target section The part before positron target in the arc scheme consists of a 4.46 GeV electron linac and a turnaround arc. The optics calculated with SAD is shown in Fig. 2.57. For the arc structure, a double TBA has been used as in the 1.54 GeV positron turnaround loop in dogleg scheme and chicane scheme. It is made of six dipoles, in which each dipole has an angle of 30° and a length of 4 m. The whole system is achromatic and isochronous, however, considering the transverse emittance increase caused by wakefields, we leave a small value to R_{56} (first order transport matrix value) for the arc structure working as a bunch compressor to compress the bunch length, which can be seen in the longitudinal phase space calculations in Fig. 2.58. The simulation is done with SAD using 10 nC electron gun, and it has similar design as the one of the 6.5 nC RF electron gun case. The total length of the part before positron target is 313.45 m, and the arc structure is 79.2 m long (the horizontal distance between the 4.46 GeV electron linac and the positron target is about 50 m).

After-target section Detailed information of the optics and tracking simulation for the after-target part in arc scheme are shown in Fig. 2.37 (without considering the 1.54 GeV turnaround loop for positrons transmission), Fig. 2.35 and Fig. 2.39.

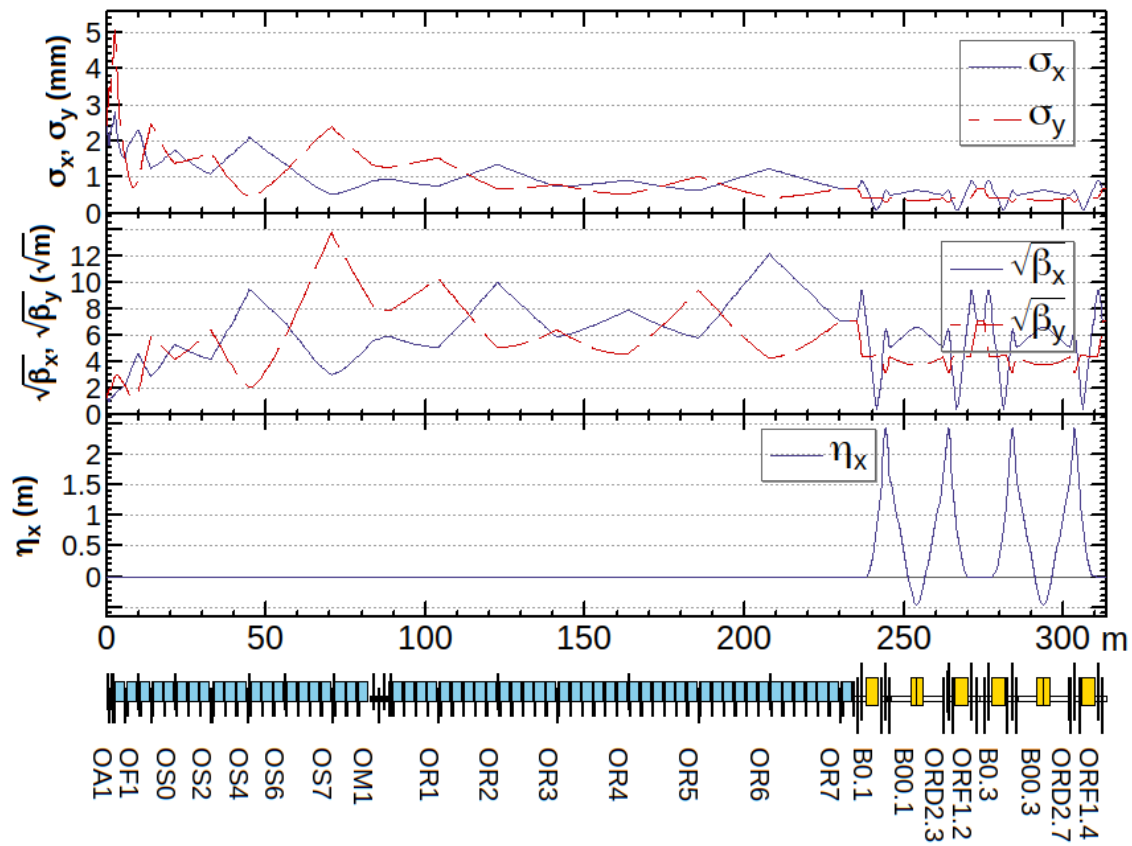


Fig. 2.57 Optics design of the before-target part in the arc scheme using the 10 nC thermionic electron gun calculated by SAD

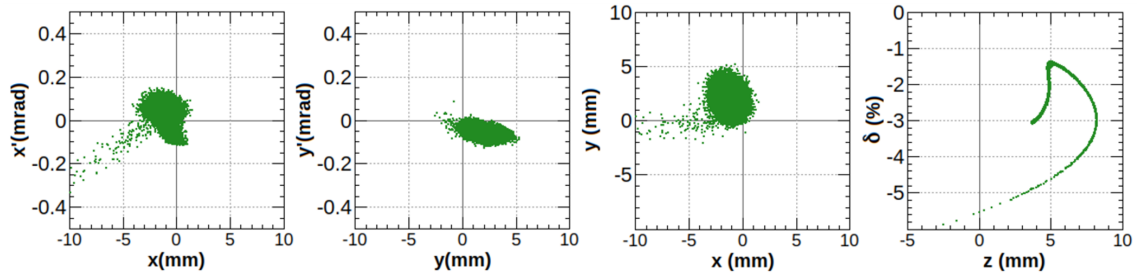


Fig. 2.58 Phase space of electron beam at the arc bypass exit using the 10 nC thermionic gun in the arc scheme calculated by SAD

2.4.4 Comparisons and conclusions

Table 2.16 summarizes the different schemes proposed for the FCC-ee injector complex including the baseline.

The **dogleg scheme** has the simplest bypass structure among the three cases, but an additional 1.54 GeV linac and a turnaround loop for 1.54 GeV positron beam is needed. In the case of the **chicane scheme** the supplementary 1.54 linac is not needed, but a double-chicane structure system more complex than the dogleg bypass is required. The **arc scheme** remains a simple solution even if the arc is longer than the turnaround loop options and the energy is higher that could cause some issues related to the SR. Meanwhile, an additional 1.54 GeV linac is also required in this scheme as in the dogleg scheme. The main objective of this chapter is to increase the positron yield and its value before the DR could reach $1.2 N_{e^+}/N_{e^-}$ in comparison to the $0.7 N_{e^+}/N_{e^-}$ design value of the baseline in simulations of all the three new schemes proposed if using a 10 nC thermionic electron gun as the feeding electron source.

Furthermore, even in some of the cases (the dogleg scheme and the arc scheme) we need a supplementary linac, this could give us more flexibility in the design possibilities of design for such a large complex machine. Further studies using multi-bunches in a linac pulse instead of the current 2 bunches per pulse (see Table 2.1) is being considered, including beam loading, multi-bunch beam breakup, and etc.. In future studies, another option that could be studied to maximize the positron yield is a further exploration of the target itself, including the use of hybrid targets in combination with superconducting solenoids in the Adiabatic Matching Devices. Other options and configurations including higher energies incident electron beams for the positron production are also being considered in the FCC-ee injector collaboration. In this sense, possible optimizations from the point of view of the cost of the dogleg scheme and the arc scheme in which the use of the section 4 linac could be avoided, are sketched in Fig. 2.59. The detailed study is beyond the scope of this PhD work but could be an interesting option to be considered in the future.

In conclusion, this work is a first step in the optimization of the FCC-ee injector system from the point of view of the efficiency of the transport and optics design. The various schemes proposed are based on established technologies and different paths for electrons and positrons are used in order to improve the efficiency of the transport taking account of losses and costs.

Schemes	Before e ⁺ target	After e ⁺ target	Supplementary linac	e ⁺ yield @ DR
Baseline (section 1 + section 2)	4.46 GeV e ⁻ linac (section 1 + section 2)	1.54 GeV e ⁺ linac (section 3)	1.54 GeV e ⁺ turnaround loop	≥ 0.7
Dogleg (section 1 + section 2)	4.46 GeV e ⁻ linac (26 m) (2 B, 10 Q, 2 S) ¹	1.54 GeV e ⁺ linac (section 4)	1.54 GeV e ⁺ turnaround loop (44.25 m) (6 B, 16 Q, 8 S)	1.54 GeV e ⁻ /e ⁺ linac (section 3) (10 nC targeted e ⁻)
Chicane (section 1 + section 2)	4.46 GeV e ⁻ linac (53.6 m) (6 B, 34 Q, 8 S)	1.54 GeV e ⁺ linac (section 4)	1.54 GeV e ⁺ turnaround loop (44.25 m) (6 B, 16 Q, 8 S)	1.54 GeV e ⁻ /e ⁺ linac (section 3) (10 nC targeted e ⁻)
Arc (section 1 + section 2)	4.46 GeV e ⁻ linac (79.2 m) (6 B, 20 Q, 8 S)	1.54 GeV e ⁺ linac (section 4)	1.54 GeV e ⁻ /e ⁺ linac (section 3)	1.54 GeV e ⁻ /e ⁺ linac (section 3) (10 nC targeted e ⁻)

Table 2.16 Summaries of the three new schemes injector linac as well as the baseline

¹B - bend, Q - quadrupole, S - sextupole

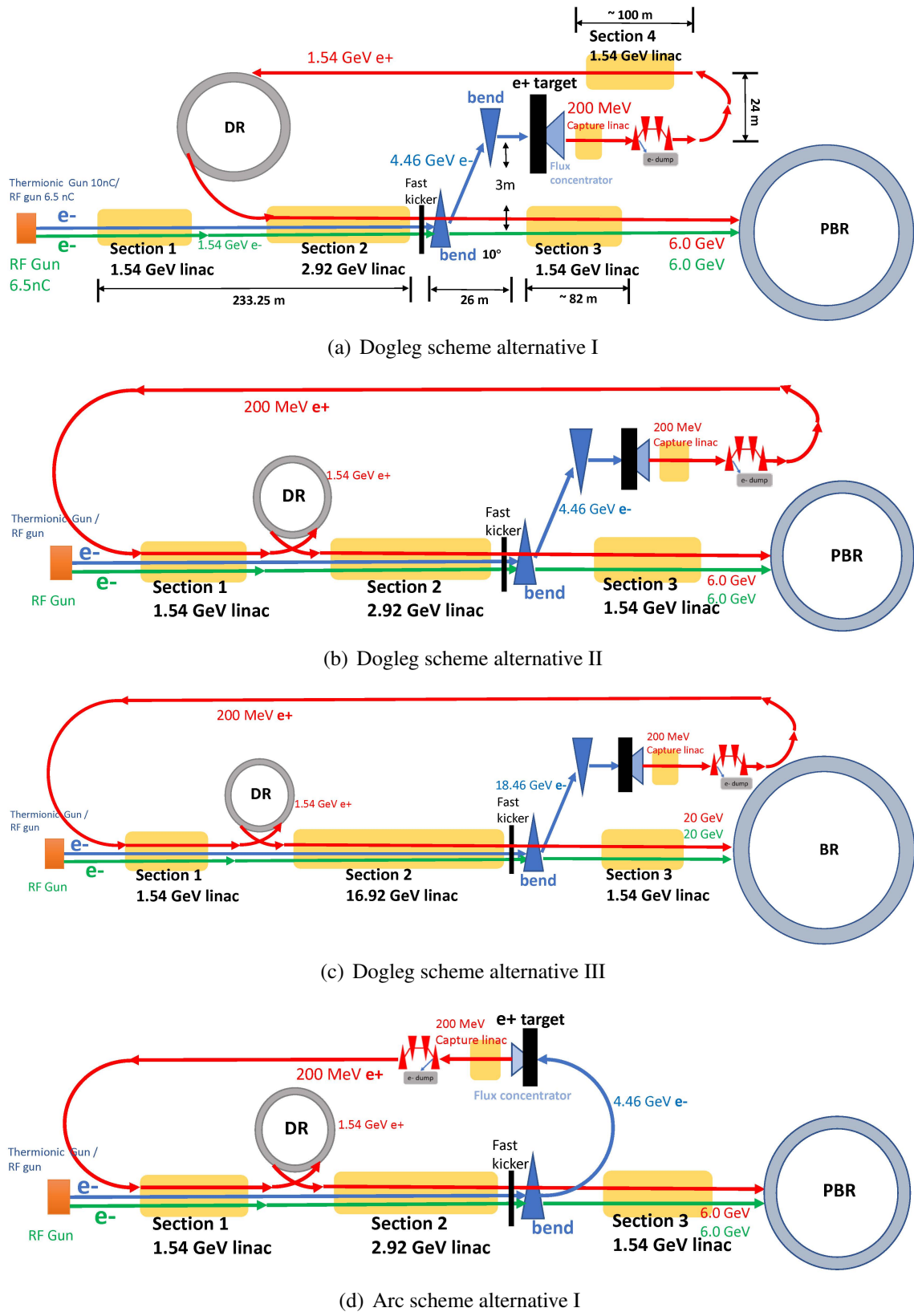


Fig. 2.59 Potential recommended modified schemes

Chapter 3

Optics design for the linac and the beam lines of a multidisciplinary R&D platform PRAE

The Platform for Research and Applications with Electrons (PRAE) [75, 39] is a multipurpose R&D facility gathering subatomic physics, instrumentation, radiobiology and clinical research around a high-performance 50 Hz pulsed accelerator delivering a pulsed electron beam to two beam lines in the energy range of 50–70 MeV in the first stage (Phase A, see Fig. 3.2), and upgradable to 140 MeV in the second stage (Phase B, see Fig. 3.3), which was planned to be built in Orsay, France (the infrastructure is presented in Fig. 3.1). The idea of such a platform arose from a joint venture of researchers and engineers from three nearby laboratories, namely *Imagerie et Modélisation en Neurobiologie et Cancérologie* (IMNC), *Institut de physique nucléaire d'Orsay* (IPNO) and *Laboratoire de l'accélérateur linéaire* (LAL), which have already in 2020 merged into the new *Laboratoire de Physique des 2 Infinis Irène Joliot-Curie* (IJCLab).

The 50 to 140 MeV electron energy range will be suitable to perform a series of new promising feasibility and radiobiological studies of less destructive radiotherapy treatments relying on space fractionated sub-millimetric pencil beams and other novel techniques. In the field of subatomic physics, they are aiming at a significant contribution to the worldwide effort of understanding the puzzle of the proton charge radius [22]. The ProRad (Proton-Radius) experiment will investigate electron proton elastic scattering to accurately measure the proton electric form factor in an unexplored ultra-low four-momentum squared range. Additionally, a fully equipped instrumentation platform will provide the tools to develop a next generation of detectors used in many research areas such as medical imaging, subatomic and particle physics, spatial technology, and astrophysics. As mentioned before, the electron beam will be delivered

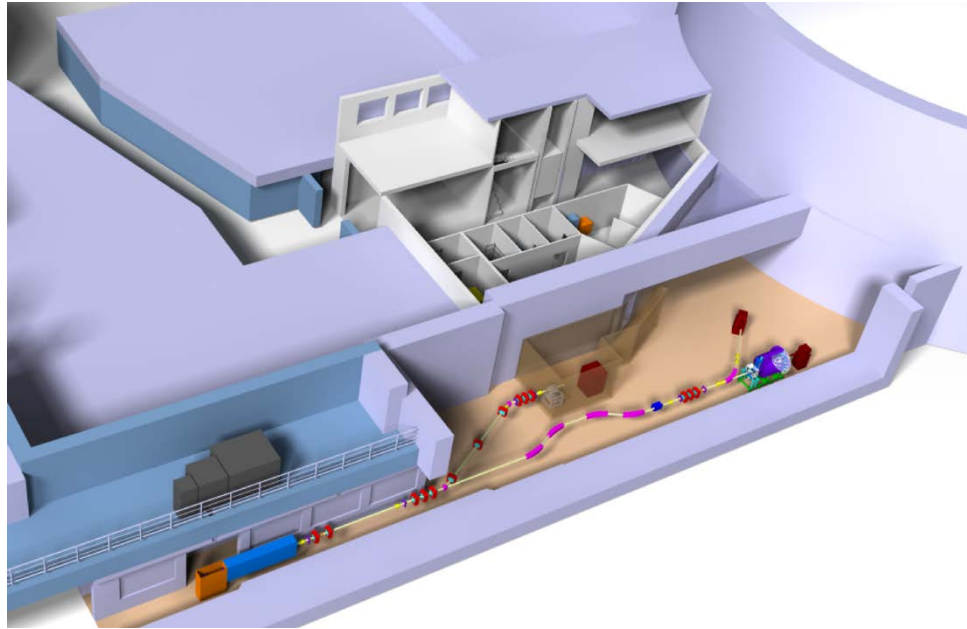


Fig. 3.1 Infrastructure and implantation of the PRAE accelerator

to one of the two beam lines, each of them being designed to fulfill specific research and applications projects. The highest energy electron beam will be used to perform pre-clinical studies in radiotherapy as well as be fully instrumented to test and optimize detectors whereas the second one will be dedicated to nuclear physics (proton-radius) experiments.

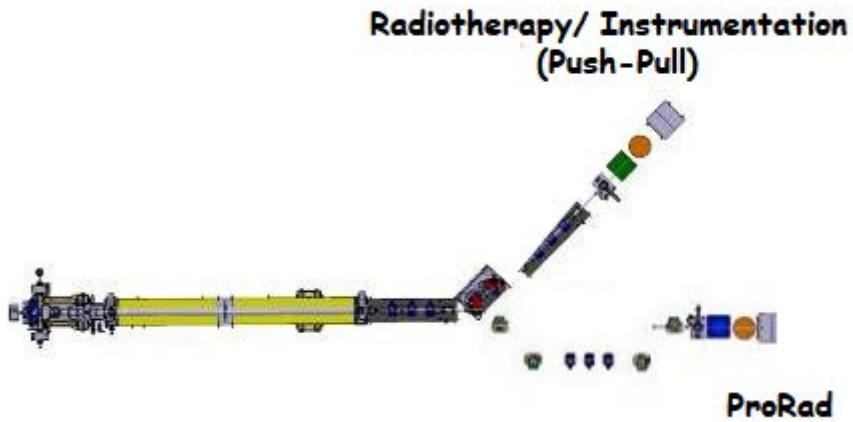


Fig. 3.2 PRAE phase A

The PRAE accelerator phase A will consist of 2 nC electron bunches produced in an RF gun at 50 Hz, post-accelerated by a S-band linac to 50-70 MeV and injected into a direct beam line



Fig. 3.3 PRAE phase B

plus one deviated line as shown in the Fig. 3.2. The beam lines optics has to be as flexible as possible to cope with the different kinds of beam characteristics (beam size, energy, dispersion, current...) and operation modes depending on the applications. The studies of the different optics options and implementation of these two lines are the main tasks of this project. More specifically, the deviated beam line dedicated to radiotherapy application will have a scanning dipole at its end, and it will also be equipped with a spectrometer for the instrumentation use. The Subatomic Physics line will have a dedicated section (collimator) for reducing the energy spread and for performing a precise energy measurement.

There exists a significant potential for innovation in the instrumentation and control techniques needed to master the extreme beam conditions required by some of the experiments and applications. With respect to beam measurement and control, BPMs for the monitoring of the position, a beam size monitor and an intensity monitor will be used. Taking into account the characteristics of the beam, the necessities of the different experiments, and mainly the very broad intensity range (2 nC - 10 pC), the technology choice and the location optimization of the BPMs also needs to be well considered. The beam size measurement has to be also studied and optimized in different locations, after the linac in the diagnostic section and at the end of the direct line. Different conventional technologies are available (OTRs, YAG screen), a possible novel option to be studied could be the use of Micro Strip Metal Foil Monitors (MMD) profile monitoring technique. The beam current will be measured after the linac, where an Intensity Current Transformer (ICT) could be a suitable option.

Moreover, another important aspect of development and innovation is the conceptual design and realization of the stations where the irradiation will be delivered. In the case of the radiotherapy research, the use of spot-scanned electron High-energy Grid Radiation Therapy (eHGRT) may for example open the way for a totally new approach in radiotherapy. Other applications, for instance in space research, are of a pioneering nature because the devices to be tested are not usually probed with primary electron beams, thus opening up an entirely new range of procedures, for studies with hitherto unexplored energies. The detailed physical design for the whole project is presented in the next sections of this chapter.

3.1 The linac simulation

The PRAE accelerator is a high performance electron accelerator consisting of a photo-injector, an accelerating section (linac) and two beam lines. A photo-injector using current technology laser will extract the electrons from the photocathode of an RF gun. To obtain a high electron charge per bunch, a metallic magnesium photocathode will be used with a laser pulse energy of a few tens of μJ at a wavelength of 260 nm. The RF gun is made of 2.5 copper cells, magnetically coupled to a waveguide. Small emittance is obtained by coupling the photocathode with an accelerating field of 80 MV/m, representing an RF power of 5 MW in a 3 μs pulse. An instrumented section for beam characterization immediately follows. The PRAE acceleration section is a 3.5 m long High-Gradient (HG) RF S-band (3 GHz) TW structure, constituting a compact machine [50, 110]. The final HG structure will provide an energy gain of around 65 MeV for an input peak power of 40 MW. The design performance of the PRAE beam at the end of the accelerating section is summarized in Table 3.1. The accelerating section is followed by a 3.5 m drift that will host a second accelerating structure in the second stage - Phase B. The main beam line separates further into one direct line and one deviated line. The direct line comprises an energy compression system consisting of a magnetic D-type chicane, involving a movable horizontal collimator for reducing the beam energy spread to the value of the order of 10^{-4} required for the ProRad experiment. The deviated line comprises several magnetic elements to cope with the different beams scenarios: electron focusing, Grid mini-beam modality, FLASH beam modality and so on.

3.1.1 The RF gun

Since a low emittance electron beam is required, a photo-injector has been chosen as the electron source. Risks minimization guides towards the construction of a gun similar to the one

Parameter (unit)	Value
Energy (MeV)	50 - 70 (140)
RF frequency (GHz)	3
Normalized emittance (mm · mrad)	3 - 10
Energy spread (%)	< 0.2
Repetition rate (Hz)	50
Bunch charge (nC)	0.00005 - 2
Bunch number (/pulse)	1
Bunch length (ps)	< 10

Table 3.1 Design performances of the beam at the end of the accelerating section in PRAE

constructed for the CLIC Test Facility (CTF3) at CERN [26, 37] and running successfully since then. This technology is also used for the ThomX project now under commissioning [109].

The photo-injector consists of a normal conducting RF gun, a drive laser and two focusing solenoids, whose 3D design is shown in Fig. 3.4. To obtain high electron charge per bunch, we will use a metallic magnesium photocathode, which can deliver more than 1 nC with a laser pulse energy of a few tens of μ J s at a wavelength of 260 nm. The S-band gun is made of 2.5 copper cells, magnetically coupled to a waveguide. To get 1 nC with an emittance lower than 5 mm · mrad, an accelerating field of 80 MV/m is required, which means an RF power of 5 MW in a 3 μ s pulse. The electron beam energy at the exit of the gun will be of the order of 5 MeV. The RF gun characteristics are listed in Table 3.2.

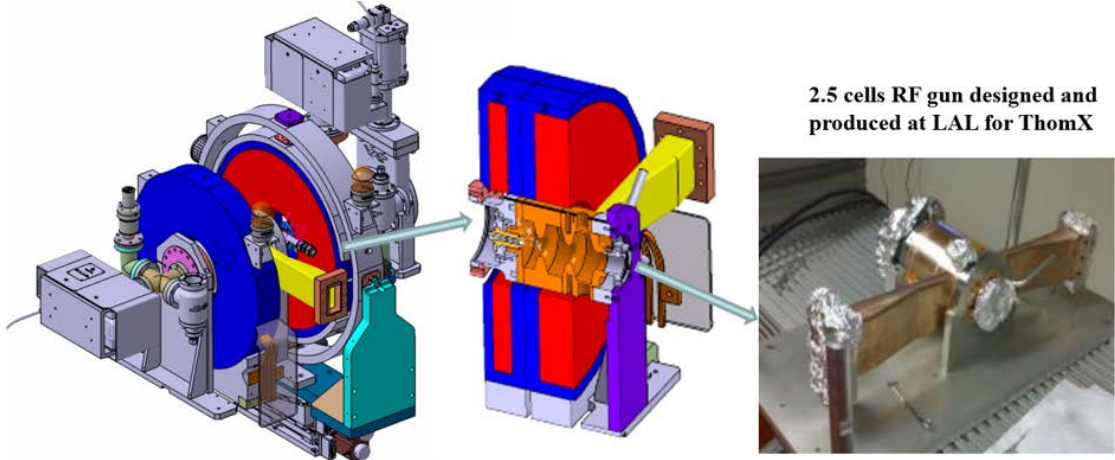


Fig. 3.4 PRAE RF gun 3D design with solenoids [110]

The study of the laser spot size and its effect on emittance and particle losses has been performed with ASTRA [53], and the detailed result can be found in reference [110]. A total bunch charge of 1nC and 2 ps laser pulse duration are found as the optimal one, with RMS

Parameter (unit)	Value
Charge per bunch (nC)	1
Length (m)	0.125
Energy gain (MeV)	~5
Peak accelerating field (MV/m)	80
RF input power (MW)	5
Laser wavelength (nm)	266
Laser pulse duration (ps)	2

Table 3.2 The RF gun characteristics of PRAE

beam size $\sigma_{x,y} = 0.5$ mm and normalized transverse emittance $\varepsilon_{N,x,y} \approx 5.3$ mm·mrad, supposing a Gaussian distribution. The particle loss is kept to an acceptable value of 5%.

The solenoid configuration used in the RF gun also has been simulated for a better output. The magnetic field generated on the photocathode is maximum close to the photocathode and has a waist at the exit of the RF gun. Changing the distance between the two solenoids could optimize the slope of the magnetic field profile (Fig. 3.5). The mechanical constraints give us a limited range of 23 cm. The optimizations have been done between 0 cm and 23 cm, and the length of 23 cm gives a minimum emittance of 5.85 mm·mrad with the solenoid magnetic field of 0.254 T. The detailed information can be found in reference [110].

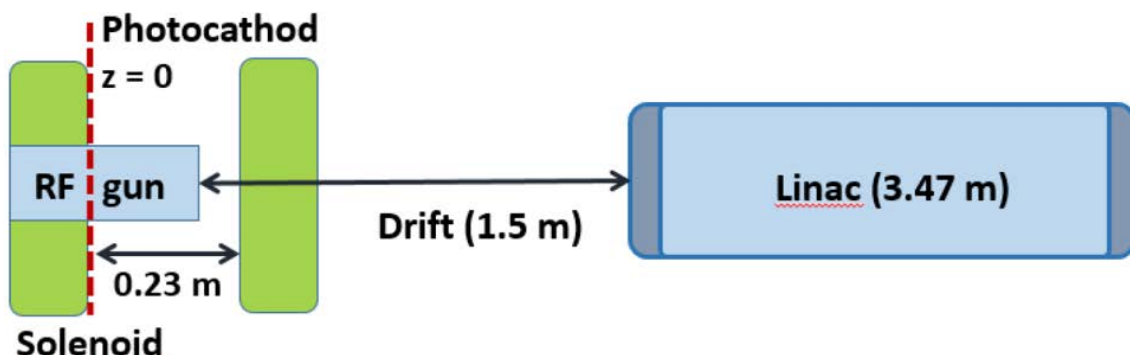


Fig. 3.5 Schematic drawing of the PRAE injector

3.1.2 The linac section

The PRAE acceleration section is a 3.47 m long HG S-band structure, in order to make the machine more compact. This section is located after the RF gun. It is a travelling wave (TW), quasi-constant gradient structure and will operate at 3 GHz frequency (30 °C in vacuum) in the $2\pi/3$ mode. The choice of a single cell shape derives from an optimization aiming to maximize RF efficiency and minimize surface fields and modified Poynting vector at very

high accelerating gradients. Such gradients can be achieved using shape optimized elliptical irises, quasi-symmetrical type coupler, and specialized fabrication procedures developed for HG structures [45]. Before the construction of the final HG structure, constant impedance (CI) prototypes with a reduced number of cells has been realized, in order to verify the validity of the manufacturing procedures and all technical choices. The final HG structure will provide an energy gain of 65 MeV for an input peak power of 22 MW with a RF flat top pulse length of 3 μ s and a repetition rate of 50 Hz. The RF design consists of 97-cells (95 regular cells + 2 coupling cells) as shown in Fig. 3.6. The calculations have been carried out with HFSS and CST [63, 103]. The design parameters of the SLAC-type TW S-band accelerating structures (a prototype made in Research Instruments [95] is shown in Fig. 3.7) are summarized in Table 3.3.

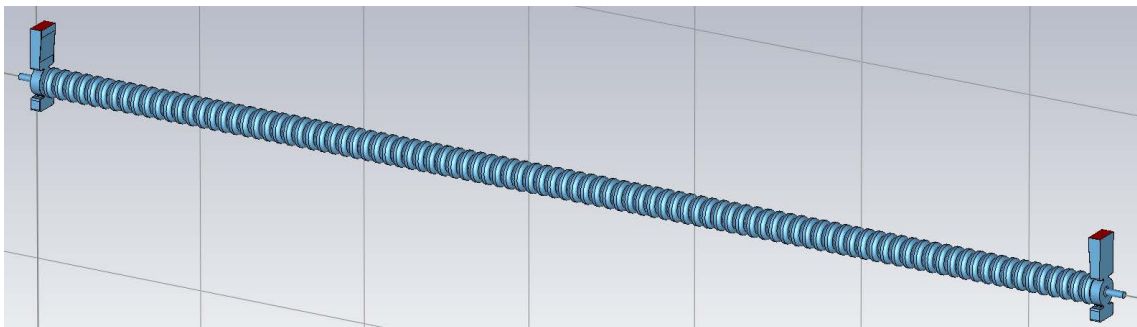


Fig. 3.6 PRAE HG accelerating structure 3D design calculated with CST [110]

Parameter (unit)	Value
Length (m)	3.5
Number of couplers + Cells	1+95+1
Type	constant gradient
Phase advance	$2\pi/3$
Frequency (MHz)	2998.95 @ 30°
Pulse width (μ s)	3
Repetition rate (Hz)	50
Maximum input power (MW)	40
Maximum average power (kW)	5
Guaranteed unloaded energy gain (MeV)	> 65

Table 3.3 A SLAC-type TW S-Band accelerating structure parameters

These specifications lead us to choose a klystron producing 35 MW in a 4.5 μ s pulse. To feed the klystron, a modulator is needed that provides high voltage pulses of typically 240 kV, through a high voltage transformer soaking in an oil tank. The two technologies, which can be



Fig. 3.7 A SLAC-type TW S-band periodic accelerating structure made by RI [95]

used for this component, are commercially available. Between the RF gun and the acceleration section there is an instrumented beam line. This beam line section is optimized in order to accommodate the eventual necessity of a focusing quadrupole doublet.

The beam dynamics along the acceleration section is calculated with ASTRA and RF-Track [71]. A total of 97 cells have been tracked in a simplified model without input and output couplers, substituted by drifts, considering the effects of space charge. The accelerating gradient is about 21 MV/m, and the required RF power is about 30 MW. The normalized transverse emittance and the beam size along the PRAE injector line calculated with ASTRA are plotted in Fig. 3.8 and 3.9. The phase space of the beam at the linac end calculated with RF-Track is shown in Fig. 3.10. The geometric transverse emittance and the beam size ($\sigma_{x,y}$) at the exit of the linac ($s \approx 5$ m) calculated with RF-Track code are around 0.05 mm·mrad and 0.7 mm. The parameters of the beam at the end of the linac section are summarized in Table 3.4.

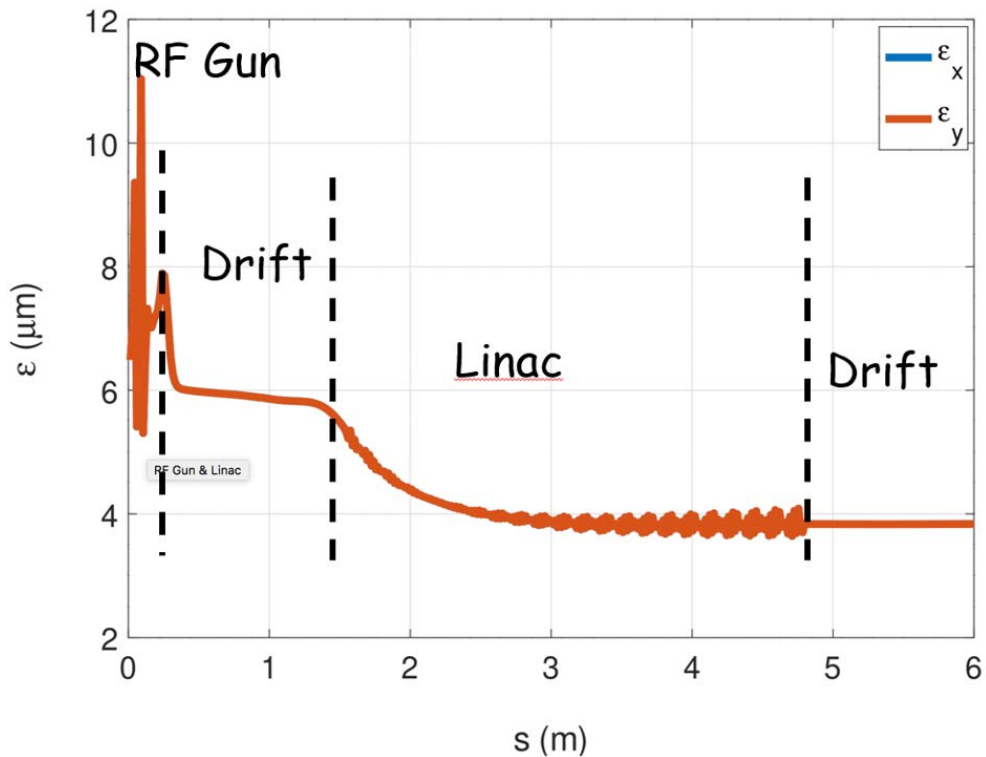


Fig. 3.8 Normalized transverse emittances along the PRAE injector calculated with ASTRA (black vertical dashed lines indicate the boundary between each segment; the blue one corresponding ε_x is the same as the orange one (ε_y))

Parameter (unit)	Value
Energy (MeV)	~ 70
Energy spread (%)	0.28
Geometric $\varepsilon_{x,y}$ (mm·mrad)	0.05
$\sigma_{x,y}$ (mm)	~ 0.7
Beam loss (%)	5

Table 3.4 Beam parameters at the exit of the PRAE injector

3.2 Two beam lines simulation

As mentioned above, there are three applications in the PRAE project implemented in the two beam lines. One beam line is dedicated for the applications of Radiotherapy (RT) and instrumentation (the VHEE Radiobiology beam line), and the other one is used for the subatomic physics study of proton radius puzzle (the ProRad beam line). The sketch of phase A of PRAE is shown in Fig. 3.11. The optics designs of the two beam lines are done with MADX.

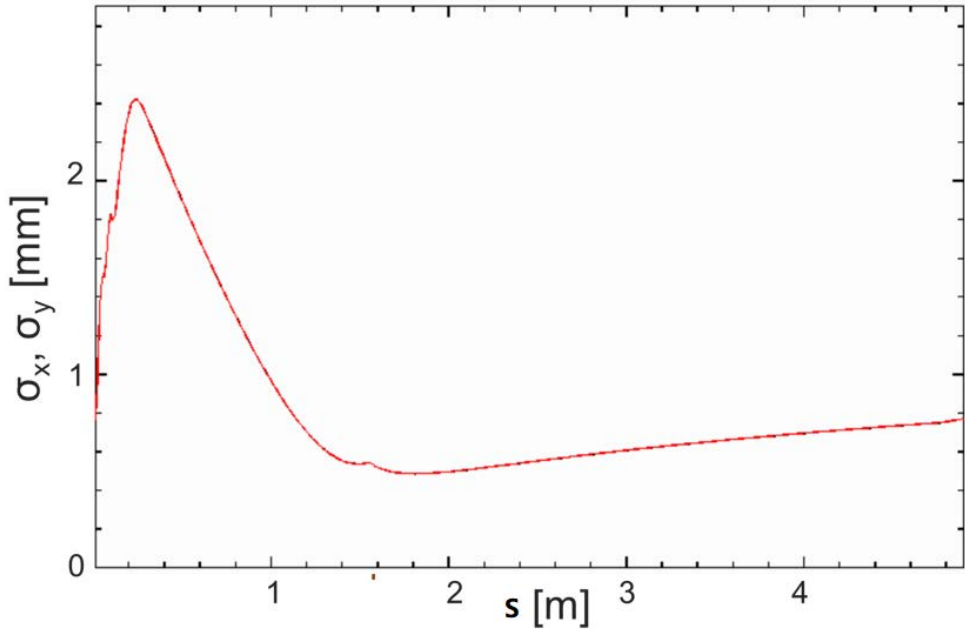


Fig. 3.9 Beam size along the PRAE injector calculated with ASTRA [110]

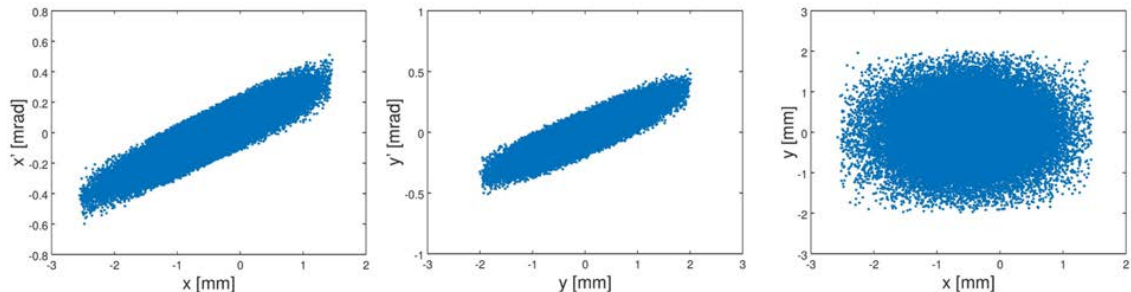


Fig. 3.10 Transverse phase space at the end of the PRAE injector calculated with RF-Track [110]

The tracking simulation of 10,000 Gaussian distribution macro particles have been performed with PLACET.

3.2.1 The VHEE Radiobiology beam line

Currently most widely used RT modality is the conventional linear accelerator delivering 6-10 MV photon beams and, in a small proportion, 3-25 MeV electron beams. Higher photon energies (eg. up to 25 MV) have been in use for deep clinical targets, but their application is being reduced in particular for the associated neutron production and for an increased interest

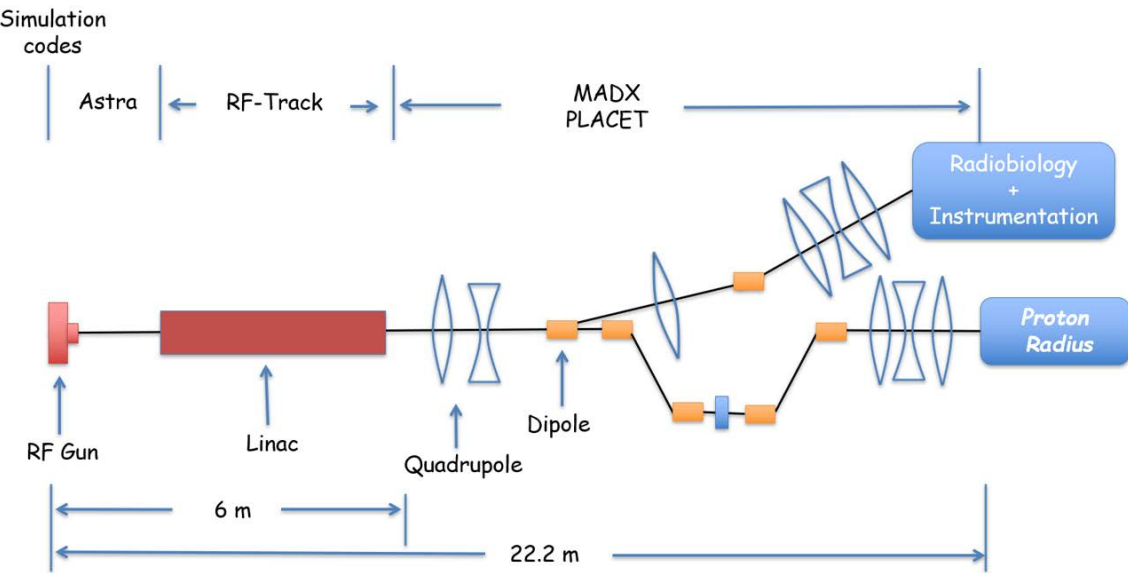


Fig. 3.11 Sketch of PRAE phase A

in short low-energy linacs delivering full rotational techniques with sharp lateral penumbra. Currently, there is a growing interest by the biomedical community in Very High Energy Electron (VHEE) beams ranging from 50 to 300 MeV [101, 104]. Increasing the energy above 70 MeV shows the following advantages: (1) the penetration becomes deeper and the transverse penumbra sharper thus allowing a more precise treatment of deeper tumors; (2) the small diameter VHEE beams can be scanned avoiding mechanical solutions such as the multi-leaf collimator; (3) a rather smaller sensitivity to tissue heterogeneity can be achieved with VHEE beams under certain conditions [69]; (4) VHEE accelerators may be constructed at significantly lower cost than current proton facilities. The VHEE could be of particular interest for treating deep, large or small tumors with several distinct beam entrances within the same radiotherapy session, performing better than current photon-based treatments in terms of doses delivered to surrounding healthy tissues [101]. This would allow to treat patients with VHEE beam directly or with innovative ways of dose delivery, with an increase of the normal tissue tolerance like Grid therapy mini-beams [76] or ultra-high dose rates FLASH beam [51], in a more convenient manner with VHEE compared to conventional photon beams.

The layout of the PRAE platform, comprising an RF-gun, a linac section and two beam lines with the corresponding experimental setups: the sub-atomic physics experiment in the direct line and the instrumentation and radiobiology platform sharing the deviated line, is shown in Fig. 3.12. The cyan box represents the injector linac. A downstream quadrupole doublet is used to focus the electron beam. A drift space of about 4 meters is left for a second HG linac which can boost the electron energy to 140 MeV in future. A quadrupole triplet

is used to confine the beam as well as to measure the beam emittance. After the triplet, a dogleg structure with two 30° dipoles (pink boxes) are used to deviate the beam following the building constraints and providing a separated area for the radiobiology experiments. Between the dipoles three quadrupoles are used to match the dispersion and betatron function. Finally, another quadrupole triplet is used to achieve the beam requirements for the Grid mini-beams and FLASH modalities.

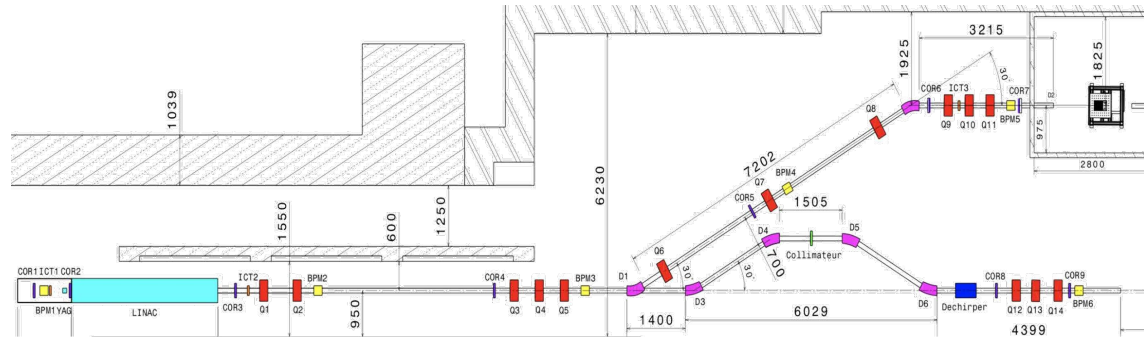


Fig. 3.12 Mechanical drawing of the PRAE platform

The radiobiology beam line has been designed with a large flexibility to achieve the beam requirements of the Grid mini-beams and FLASH:

1. Grid mini-beam: transverse beam sizes of less than $700 \mu\text{m}$ with low beam divergence [91, 92].
2. FLASH: transverse beam sizes of around 10 mm with a dose of 10 Gy with beam on time 100 ms (5 bunches at 50 Hz), i.e. 100 Gy/s [82].

In the following, the Grid mini-beam with three different energies (70, 140 and 300 MeV) and the FLASH beam of 70 MeV energy are illustrated [61]. For each energy, we first use the MADX program to match the beam line in order to provide proper beam properties. Then the simulated beam from the RF gun and linac will be tracked along the beam line by the program PLACET. The phase space at the end of the beam line are shown for each case. Geant4 [48] is used to simulate the transport of the electron beam in air and the interaction between the beam and biological water samples.

The Grid mini-beam

70 MeV Grid beam Fig. 3.13 shows the optics of the Radiobiology beam line for 70 MeV Grid beam, and the beam envelope along the beam line is constrained to be less than 2 mm.

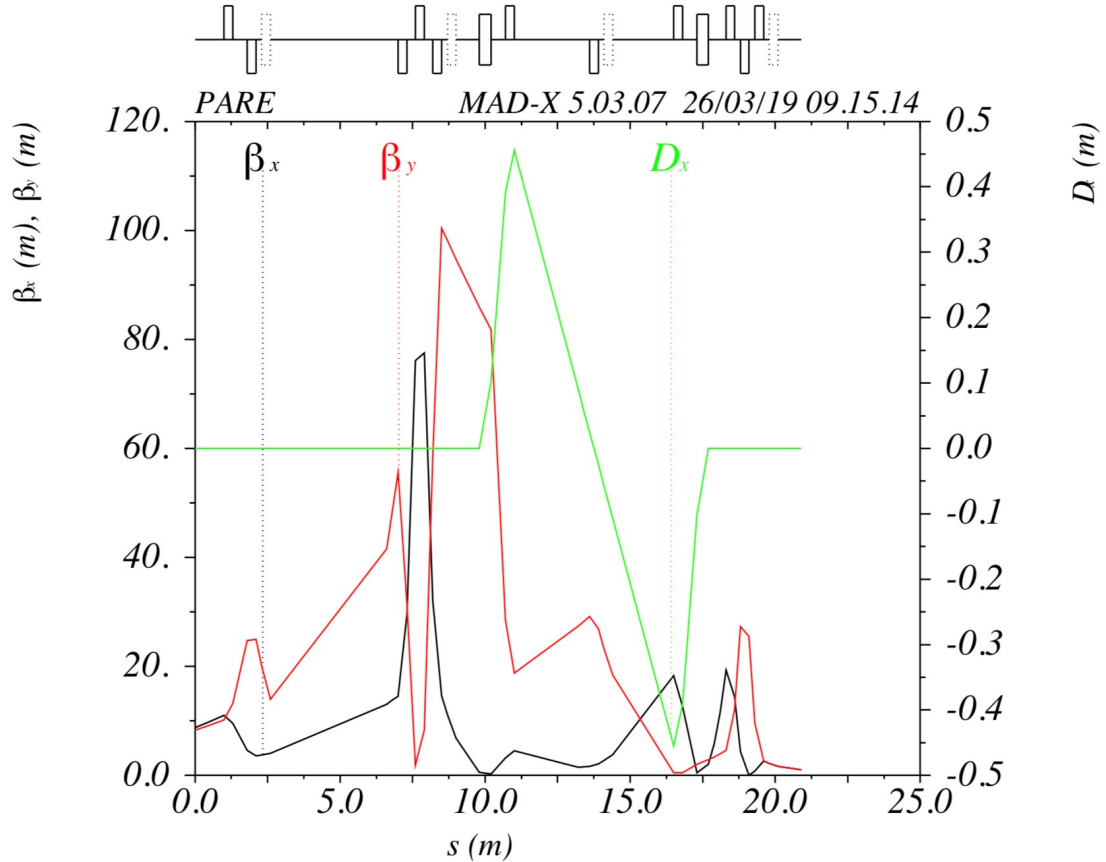


Fig. 3.13 Beam optics design of the Radiobiology beam line for the 70 MeV Grid mini-beam calculated with MADX

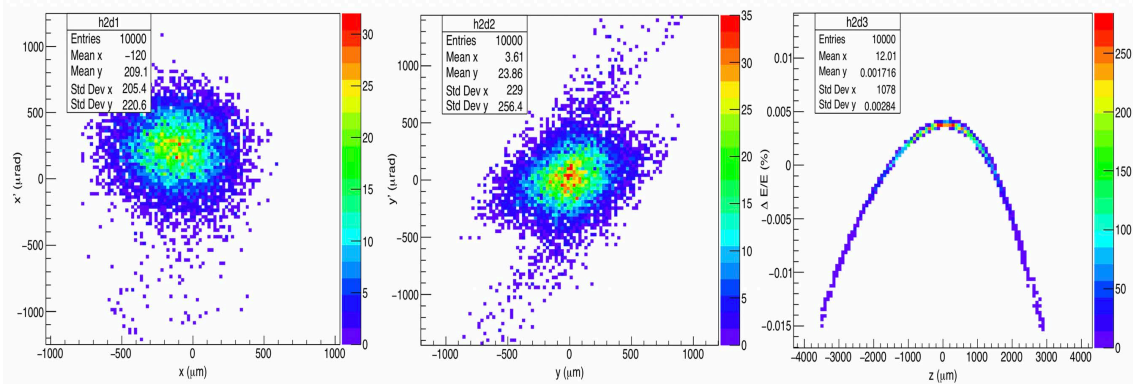


Fig. 3.14 Phase space at the end of the Radiobiology beam line for the 70 MeV Grid mini-beam calculated with PLACET

The phase space at the end of the radiobiology beam line is shown in Fig. 3.14. The beam sizes at the end of the beam line are $\sigma_x = 207 \mu\text{m}$ and $\sigma_y = 240 \mu\text{m}$.

The sketch of the Grid mini-beam experiment is depicted in Fig. 3.15. The simulation results of the interactions of the beam with 10 cm of air and 30 cm of water are shown in Fig. 3.16.

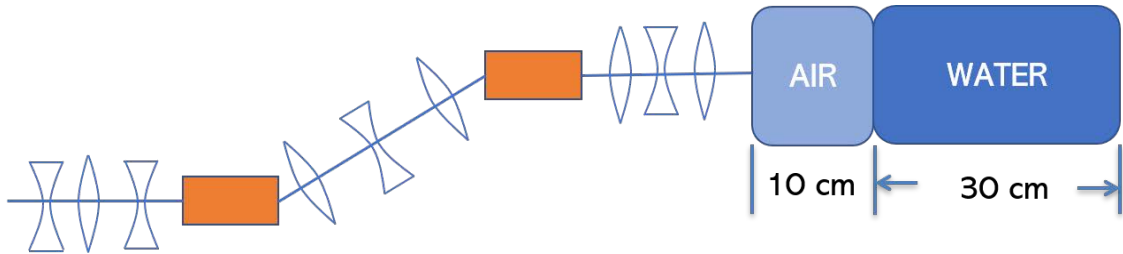


Fig. 3.15 Sketch of the Grid mini-beam experiment

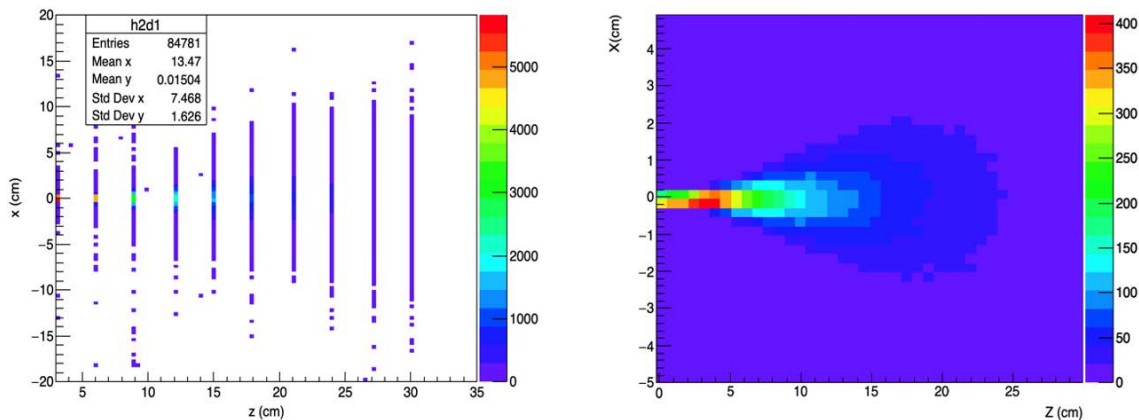
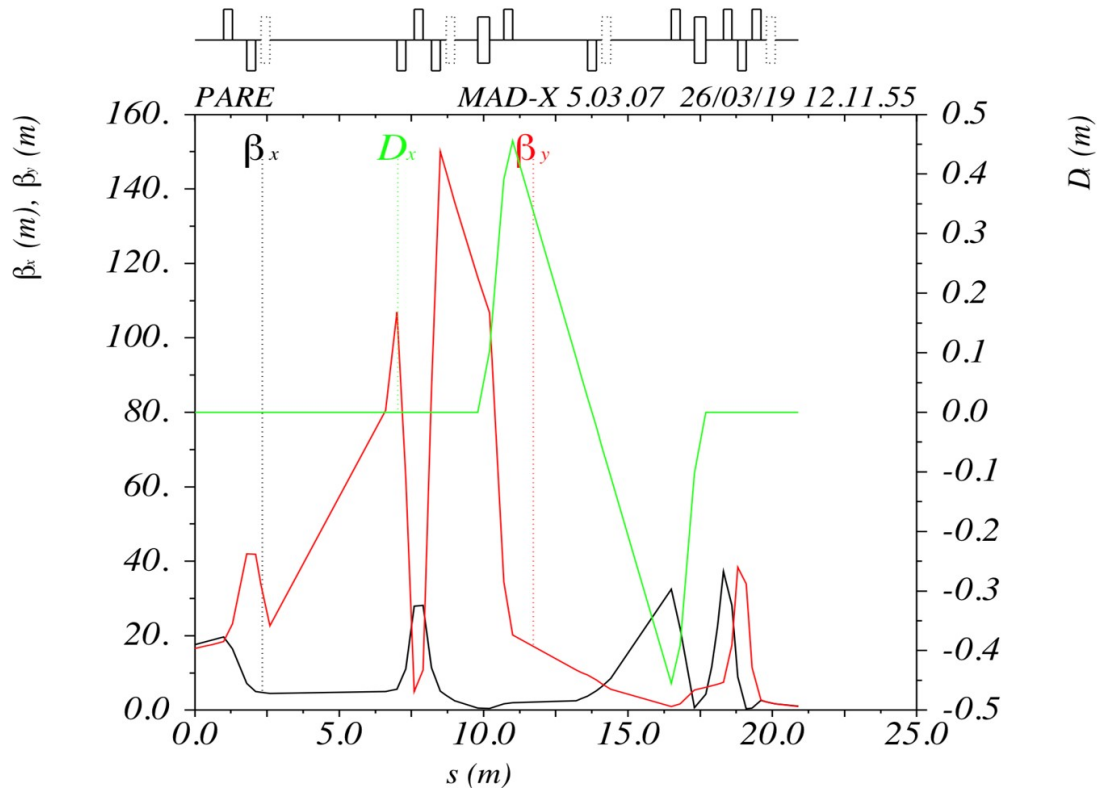


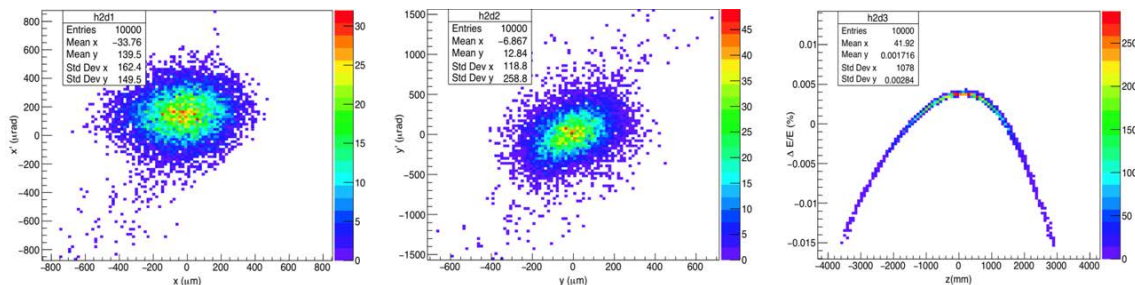
Fig. 3.16 Horizontal beam profile along the longitudinal direction (left plot) and energy deposition on the x-z plane (right plot) in the 30-cm-length water box for 70 MeV Grid mini-beam calculated with Geant4

The beam in the air gap of 10 cm will not diverge greatly because it reaches the beam waist ($\alpha_{x,y} = 0$) at the exit of vacuum beam pipe. The beam sizes after the air box are $\sigma_x = 250 \mu\text{m}$, $\sigma_y = 290 \mu\text{m}$. When the 70 MeV beam enters the water, it will interact strongly: the energy will be reduced and the beam size will be enlarged. The beam sizes become $\sigma_{x,y} = 5.5 \text{ mm}$ after traversing 9 cm of water. At 15 cm in water, they become $\sigma_x = 17.3 \text{ mm}$, $\sigma_y = 17.4 \text{ mm}$.

140 MeV and 300 MeV Grid beams Similar optics have been calculated for the 140 MeV and 300 MeV beam energies, whose designs calculated with MADX are respectively presented

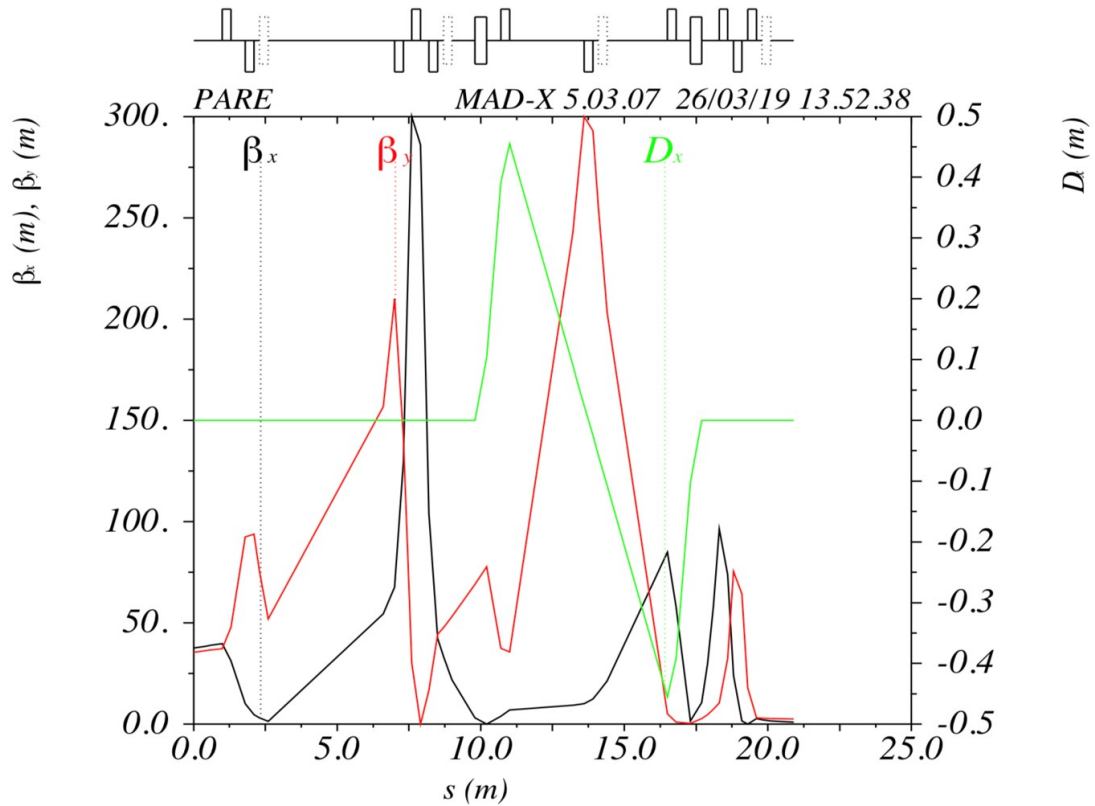


(a) Beam optics design of the Radiobiology beam line for the 140 MeV Grid mini-beam calculated with MADX

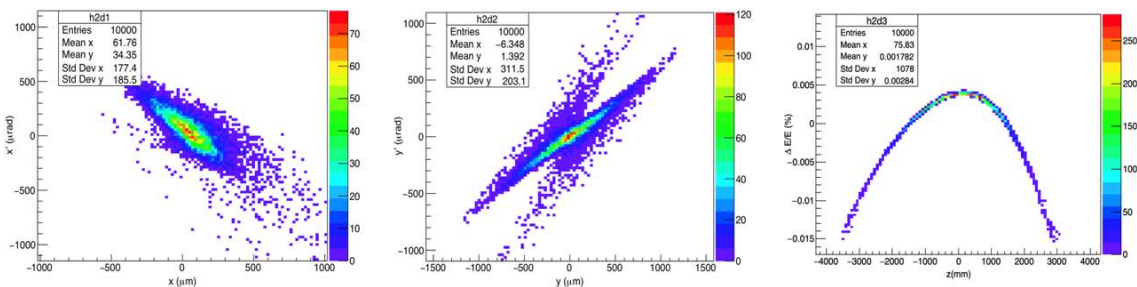


(b) Phase space at the end of the Radiobiology beam line for the 140 MeV Grid mini-beam calculated with PLACET

Fig. 3.17 Beam optics and phase space at the end of the Radiobiology beam line, for 140 MeV Grid mini-beam

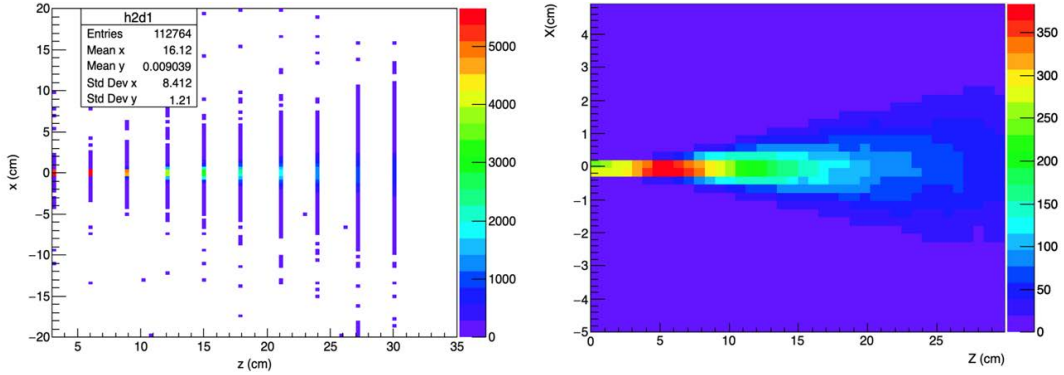


(a) Beam optics design of the Radiobiology beam line for the 300 MeV Grid mini-beam calculated with MADX

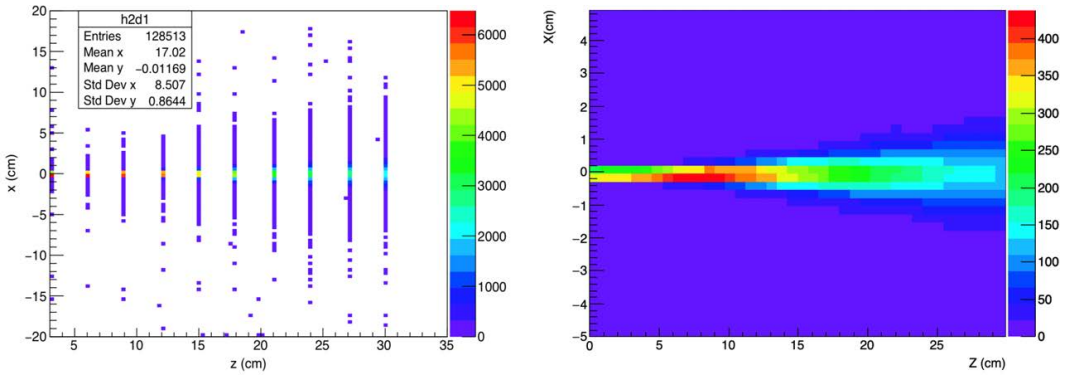


(b) Phase space at the end of the Radiobiology beam line for the 300 MeV Grid mini-beam calculated with PLACET

Fig. 3.18 Beam optics and phase space at the end of the Radiobiology beam line, for 300 MeV Grid mini-beam



(a) Horizontal beam profile along the longitudinal direction (left plot) and energy deposition on the x-z plane (right plot) in the 30-cm-length water box for 140 MeV Grid mini-beam simulated with Geant4



(b) Horizontal beam profile along the longitudinal direction (left plot) and energy deposition on the x-z plane (right plot) in the 30-cm-length water box for 300 MeV Grid mini-beam simulated with Geant4

Fig. 3.19 Beam-water interaction simulation in Grid mini-beam experiment calculated with Geant4

in Fig. 3.17(a) and 3.18(a). Fig. 3.17(b) and 3.18(b) show the corresponding phase spaces calculated with PLACET at the end of the beam lines for 140 MeV beam and 300 MeV beam. The beam sizes after the air box are $\sigma_x=200, 340 \mu\text{m}$ and $\sigma_y=170, 330 \mu\text{m}$ respectively for 140 and 300 MeV. The simulation results of the beam-water interactions similar to that of the 70 MeV energy case for 140 MeV and 300 MeV beams are individually shown in Fig. 3.19(a) and 3.19(b). For 140 MeV beam, the maximum dose deposition is at around 19 cm (projection onto the longitudinal axis). The beam sizes become $\sigma_x=3.3 \text{ mm}$, $\sigma_y=3.3 \text{ mm}$ after traversing 9 cm of water. At 15 cm in water, they become $\sigma_x=7.5 \text{ mm}$, $\sigma_y=7.6 \text{ mm}$. We could observe that the most intensive energy deposition region shifts a little to the depth compared to the 70 MeV beam. At the same time, the region of energy deposition becomes larger. In the 300 MeV case, the beam sizes become $\sigma_x=2.0 \text{ mm}$, $\sigma_y=2.0 \text{ mm}$ after 9 cm of water. At 15cm in water, they become $\sigma_x=4.1 \text{ mm}$, $\sigma_y=5.2 \text{ mm}$. We could observe that at this energy the most intensive

energy deposition region shifts deeper compared to the 140 MeV beam. The divergence of the 300 MeV beam at 30 cm water depth is well limited.

The FLASH beam

In order to obtain the $10 \text{ mm} \times 10 \text{ mm}$ transverse beam size, we will utilize the dispersion caused by the dipoles in the dogleg structure. Two methods are used to generate the FLASH beam. For the first method in the horizontal plane, we leave the dispersion uncorrected, but in the vertical plane, there is no dispersion generated for a beam without coupling. So the quadrupole in the middle of dogleg is changed to a skew quadrupole, which can couple the horizontal dispersion to the vertical plane. The second method just uses normal quadrupoles to set a large $\beta_{x,y}$ at the end of the beam line to create large transverse beam sizes as required. The beam optics designs for the two methods are shown in Fig. 3.20(a) and 3.20(b). In a similar way as in the Grid mini-beam, Geant4 has been used to simulate the interaction of the beam with air and water. In the FLASH case, an air box of 1 meter and water box of 30 cm are used (see Fig. 3.21). The results for a 70 MeV beam are shown in Fig. 3.22(a) and 3.22(b). In Method 1, after 1 meter of air, the beam will not diverge because the beam is tuned to have a small divergence. The beam sizes after the air box are $\sigma_x=11.4 \text{ mm}$ and $\sigma_y=12.0 \text{ mm}$. When the beam enters the water, it will diverge quickly. The maximum dose deposition location is the same as for the 70 MeV Grid mini-beam, i.e. around 10 cm. The beam sizes become $\sigma_x=13.6 \text{ mm}$ and $\sigma_y=14.0 \text{ mm}$ after 9 cm of water. At 15 cm in water, they become $\sigma_x=18.2 \text{ mm}$ and $\sigma_y=18.4 \text{ mm}$. The most intensive energy deposition region is located at the beginning of the water. The region of energy deposition in the water becomes larger when the beam further interact with water. For Method 2, the beam will diverge a lot due to large divergence at the end of the beam line. The beam size after the air box are $\sigma_x=20.3 \text{ mm}$ and $\sigma_y=17.3 \text{ mm}$. When the beam enters the water, it will not diverge as quickly as the Grid mini-beam case because of its relative large beam size. The dose profile is the same as that of the Method 1. The beam sizes become $\sigma_x=21.4 \text{ mm}$ and $\sigma_y=17.6 \text{ mm}$ after 9 cm of water. After 15 cm of water, they become $\sigma_x=24.6 \text{ mm}$ and $\sigma_y=21.6 \text{ mm}$. The large beam also gives a high dose in a relatively large region while the energy being mainly deposited in the area below 15cm in depth.

A summary of the beam performances in the beam-water interactions for the two radiobiology experiments is listed in Table 3.5.

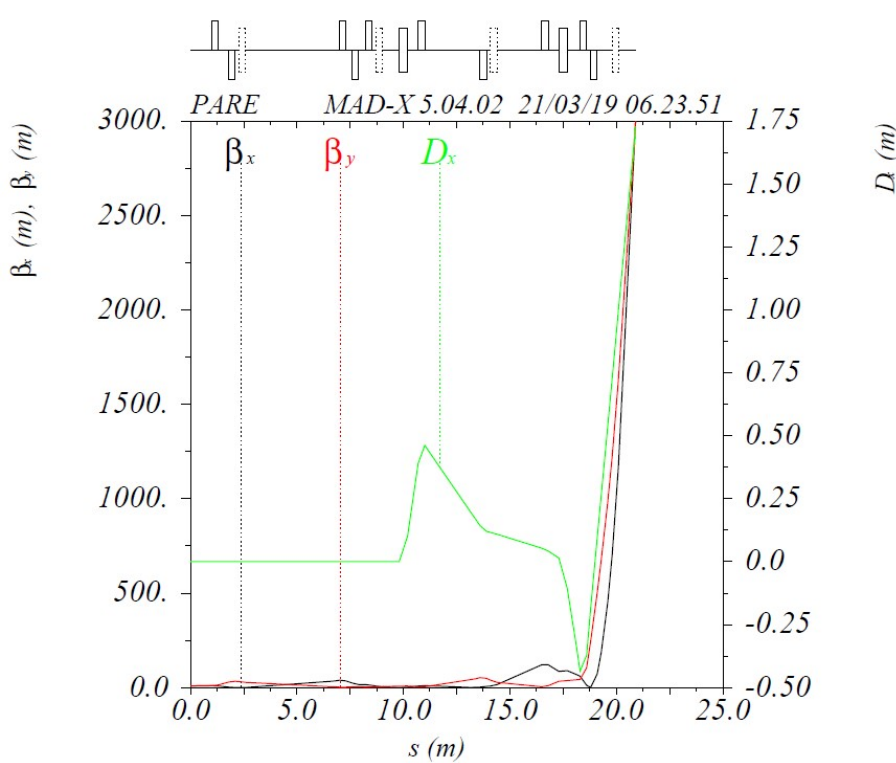
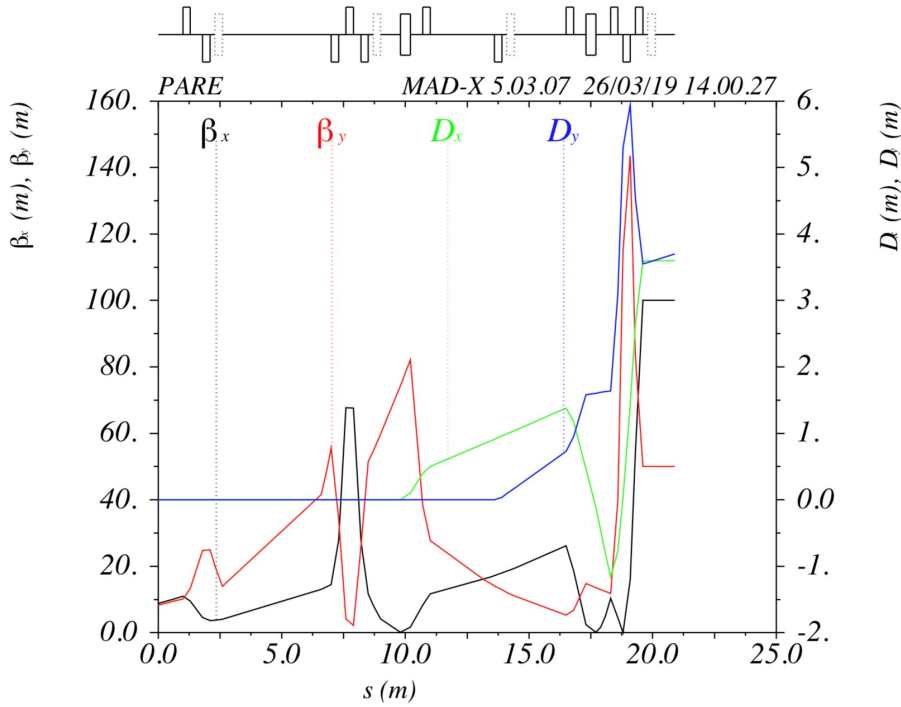


Fig. 3.20 Optics designs for the FLASH beam in the Radiobiology beam line using Method 1 (top) and Method 2 (bottom)

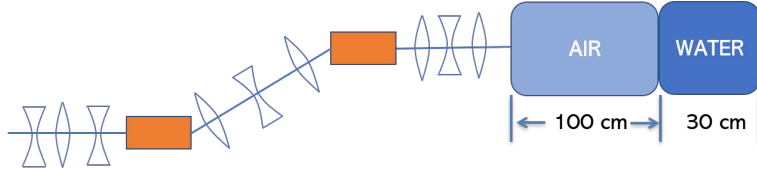
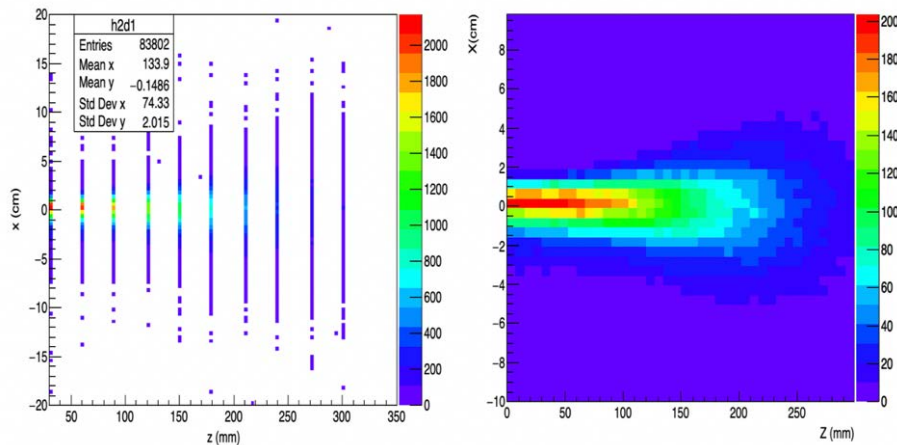
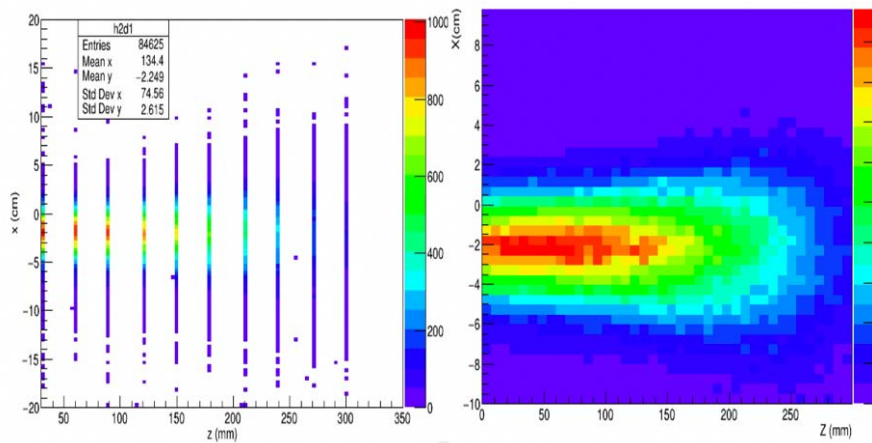


Fig. 3.21 Sketch of the FLASH beam experiment



(a) Method 1: Horizontal beam profile along the longitudinal direction (left plot) and energy deposition on the x-z plane (right plot) in the 30-cm-length water box for 70 MeV FLASH beam simulated with Geant4



(b) Method 2: Horizontal beam profile along the longitudinal direction (left plot) and energy deposition on the x-z plane (right plot) in the 30-cm-length water box for 70 MeV FLASH beam simulated with Geant4

Fig. 3.22 Beam-water interaction simulation in FLASH beam experiment calculated with Geant4

Beam (E)	Vacuum ($\sigma_{x,y}$ unit: mm)	Air ($\sigma_{x,y}$ unit: mm)	Water (@9 cm) ($\sigma_{x,y}$ unit: mm)	Water (@15 cm) ($\sigma_{x,y}$ unit: mm)	Water (@30 cm) ($\sigma_{x,y}$ unit: mm)
mini 70 MeV	0.21/0.24	0.25/0.29	5.5/5.5	17.3/17.4	35.9/36.6
mini 140 MeV	0.17/0.14	0.20/0.17	3.3/3.3	7.5/7.6	20.8/21.2
mini 300 MeV	0.32/0.31	0.34/0.33	2.0/2.0/	4.1/5.2	11.8/11.7
FLASH 70 MeV (Method 1)	9.9/10.3	11.4/12.0	13.6/14.0	18.2/18.4	37.3/37.0
FLASH 70 MeV (Method 2)	12.55/10.91	20.3/17.3	21.4/17.6	24.6/21.5	40.5/38.6

Table 3.5 Beam performances in interactions with different materials for the Grid mini-beam and the FLASH beam experiments in the VHEE Radiobiology beam line

3.2.2 The ProRad beam line

The proton is one of the most fundamental particles that had been discovered in the universe, and the exact knowledge of its radius is very important. The proton radius measured using the Lamb shift of muonic hydrogen is 0.84184 ± 0.00067 fm [84]. However, the electron scattering experiments gives a result of 0.879 ± 0.008 fm [23]. The discrepancy between these two methods is larger than 5 standard deviations, which is known as proton charge radius puzzle. A large number of possible explanations ranging from inaccurate extraction of the proton radius up to genuine physics effects and Physics Beyond the Standard Model have been proposed to explain this striking discrepancy. However, the existing world data set is not enough in order to provide a consensus.

The Proton-Radius (ProRad) measurement is the other important application of PRAE, which requires an extremely low energy spread (5×10^{-4}) and low divergence with beam energies of 30, 50 and 70 MeV. The beam line design and simulation for the ProRad calculated with MADX and PLACET are presented here. Meanwhile, the tolerance for magnets misalignments is studied and the beam-based alignment technique is used to improve this tolerance [49].

The sketch of the ProRad is shown in Fig. 3.23. The ProRad experiment at PRAE aims at collecting high accuracy data (1%) about the proton electric form factor $G_E(Q^2)$ in the unexplored four-momentum Q^2 range 10^{-5} - 10^{-4} (GeV/c²)². This will give requirements for the electron beam like: beam energies are 30, 50 & 70 MeV; bunch charge is between 10-100 pC; energy spread is less than 5×10^{-4} ; beam size is 20-30 μm in one direction and 100-200 μm in another direction; the divergence is smaller than 50 μrad .

To get such a low energy spread, an energy compressor system (ECS) is needed. The principle of a chicane-structure ECS is described in Fig. 3.24. The beam head is located in the negative z direction. When the beam passes through the chicane structure and a downstream RF section, the energy spread $\frac{\Delta E}{E}$ could be reduced according to the linear approximation calculation (a symplectic matrix) of the transport matrix (see equations 3.1-3.5, Z_0 is the initial

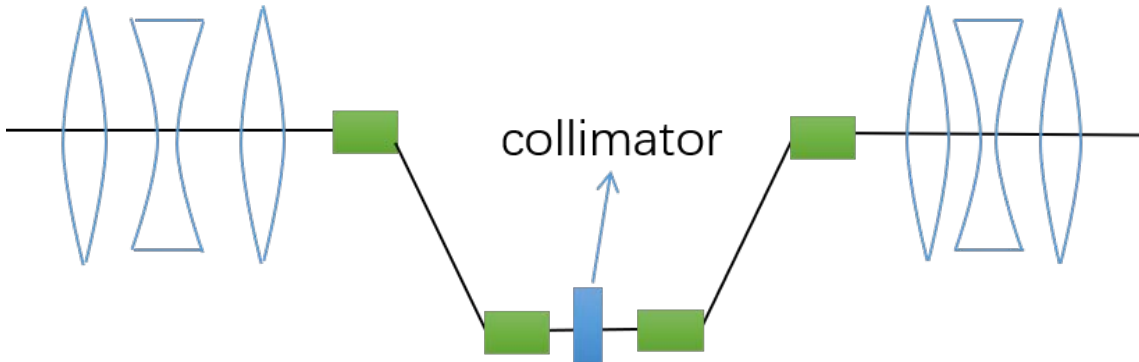


Fig. 3.23 Sketch of the ProRad beam line

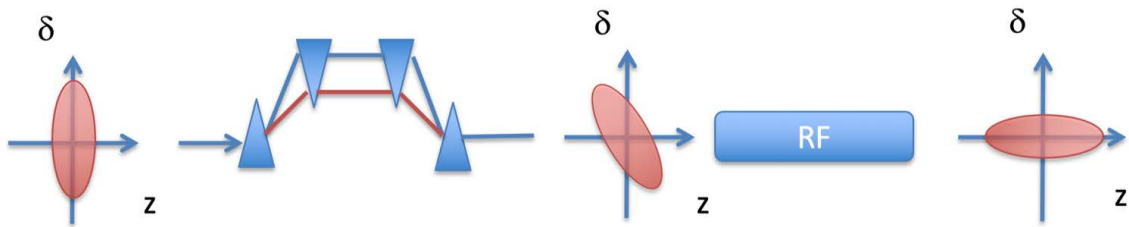


Fig. 3.24 Sketch of Energy Compressor System (ECS)

bunch length, Z_1 is the final bunch length, $(\frac{\Delta E}{E})_0$ is the initial energy spread, $(\frac{\Delta E}{E})_1$ is the final energy spread) at the cost of an increase of the bunch length Z after the ECS longitudinal phase-space rotation [28].

$$\begin{bmatrix} Z_1 \\ (\frac{\Delta E}{E})_1 \end{bmatrix} = \begin{bmatrix} 1 & 0 \\ R_{65} & 1 \end{bmatrix} \begin{bmatrix} 1 & R_{56} \\ 0 & 1 \end{bmatrix} \begin{bmatrix} Z_0 \\ (\frac{\Delta E}{E})_0 \end{bmatrix}, \quad (3.1)$$

$$M_{chicane} = \begin{bmatrix} 1 & R_{56} \\ 0 & 1 \end{bmatrix}, \quad (3.2)$$

$$M_{RF} = \begin{bmatrix} 1 & 0 \\ R_{65} & 1 \end{bmatrix}, \quad (3.3)$$

$$Z_1 = Z_0 + R_{56} \cdot (\frac{\Delta E}{E})_0, \quad (3.4)$$

$$(\frac{\Delta E}{E})_1 = Z_0 R_{65} + (R_{56} R_{65} + 1) \cdot (\frac{\Delta E}{E})_0 \quad (3.5)$$

However, this ECS needs to introduce a supplementary RF section, which will increase the project budget. To simplify the design process, a collimator was chosen to remove the electrons whose energies are far away from the average bunch energy. The PRAE can delivery electron bunches with charge up to 1 nC, while the ProRad experiment only demands a bunch charge of 10-100 pC. So the particle losses due to the collimation is not a problem. The collimator is put between the second and the third dipole magnet of the chicane structure (Fig. 3.23). The angle of the dipoles in the chicane is chosen as 30 degrees which is the same as the deviated angle of the dogleg structure for the VHEE Radiobiology beam line.

The beam line design The optics design of the ProRad beam line (Fig. 3.12) calculated with MADX is presented in Fig. 3.25. The transverse beam size at the end of the beam line needs to be $200 \mu\text{m}$ and the beam should reach the beam waist to give less divergence. And the betatron function along the beam line is required to be smaller than 100 m in order to adapt the beam pipe with a radius of 2 cm. The horizontal beam size at the middle of chicane structure is about 4 mm due to dispersion. PLACET is used to track the beam coming from the upstream linac until the end of beam line without considering the effect of the collimator. The phase space of the beam at the end of the ProRad beam line is shown in Fig. 3.26.

The collimator A 1-meter-long collimator with half aperture of 2 mm in the horizontal plane is put in the middle of the chicane structure to reduce the energy spread. The effects of using a collimator or not in the ProRad beam line are shown in Fig. 3.27. It can be seen that the particles with relative low energies are removed by the collimator. About 48% of particles can pass through the collimator and the energy spread for these survived particles is 4.2×10^{-4} .

The transverse beam position distributions before and after the collimation are shown in Fig. 3.28. It can be seen that after the collimation, the transverse position distributions still remain a quasi Gaussian distribution. The central positions are located near $-200 \mu\text{m}$ and $70 \mu\text{m}$ for x and y plane, respectively. These offsets are coming from the initial beam and can be corrected with some dipole correctors.

The misalignments study The above simulations for the ProRad beam line are based on ideal machines. Here we consider the misalignment tolerance for all the elements in the beam line: the dipole magnets, the quadrupoles and the collimator. The misalignments include the position offsets, the angle offsets and the rotation errors, which are presented in Table 3.6. In the following simulation, we will simulate 100 machines with random misalignment errors of Gaussian distribution.

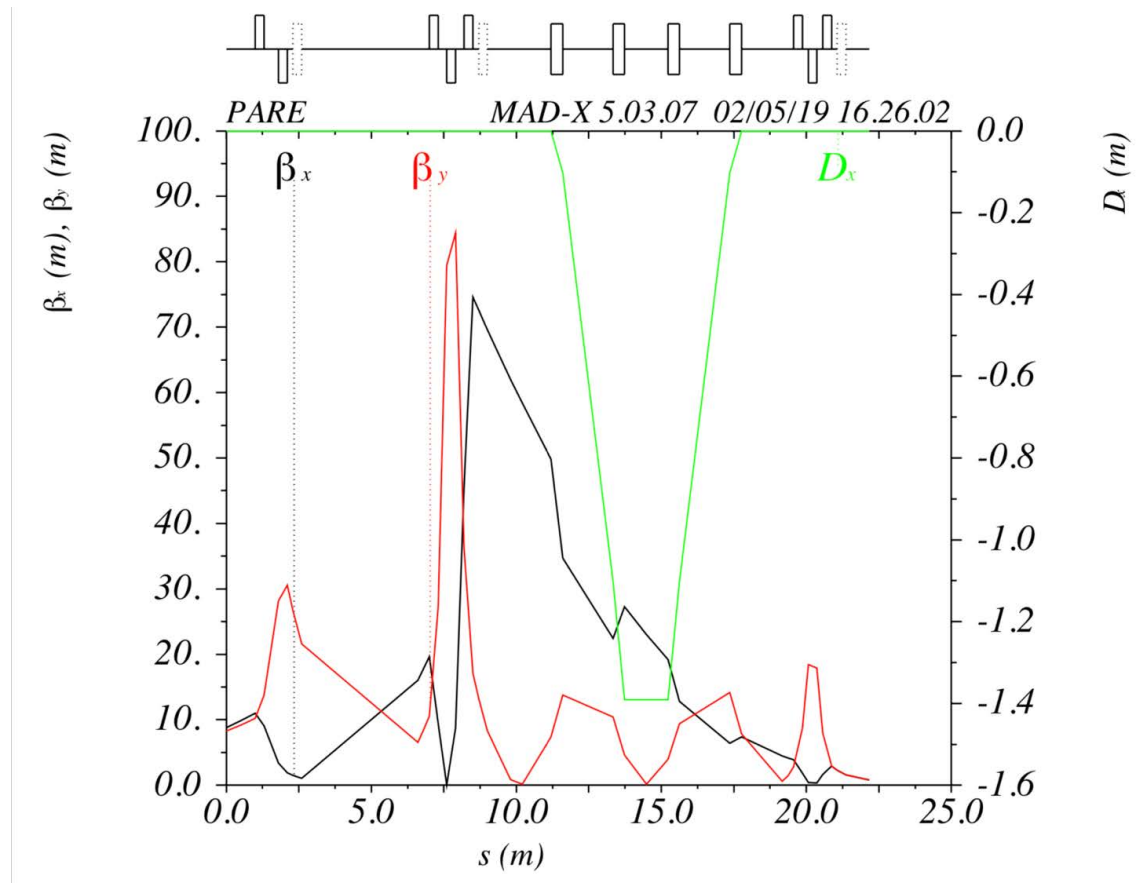


Fig. 3.25 Optics design for the ProRad beam line of PRAE calculated with MADX

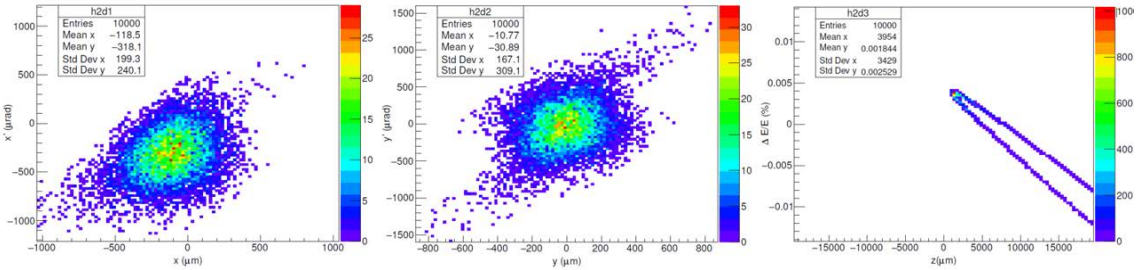


Fig. 3.26 Phase space at the end of the ProRad beam line of PRAE calculated with PLACET

The mechanical alignment technology can help to align the element error to the level of 100 μm and 100 μrad . In such an imperfection level, if we require that the percentage of surviving particles is larger than 20%, there will be only 45% of the 100 simulated machines whose beam energy spread is smaller than 5×10^{-4} . This means that we must use the BBA technique to correct the beam line during the machine operation. The distributions of the energy spread and

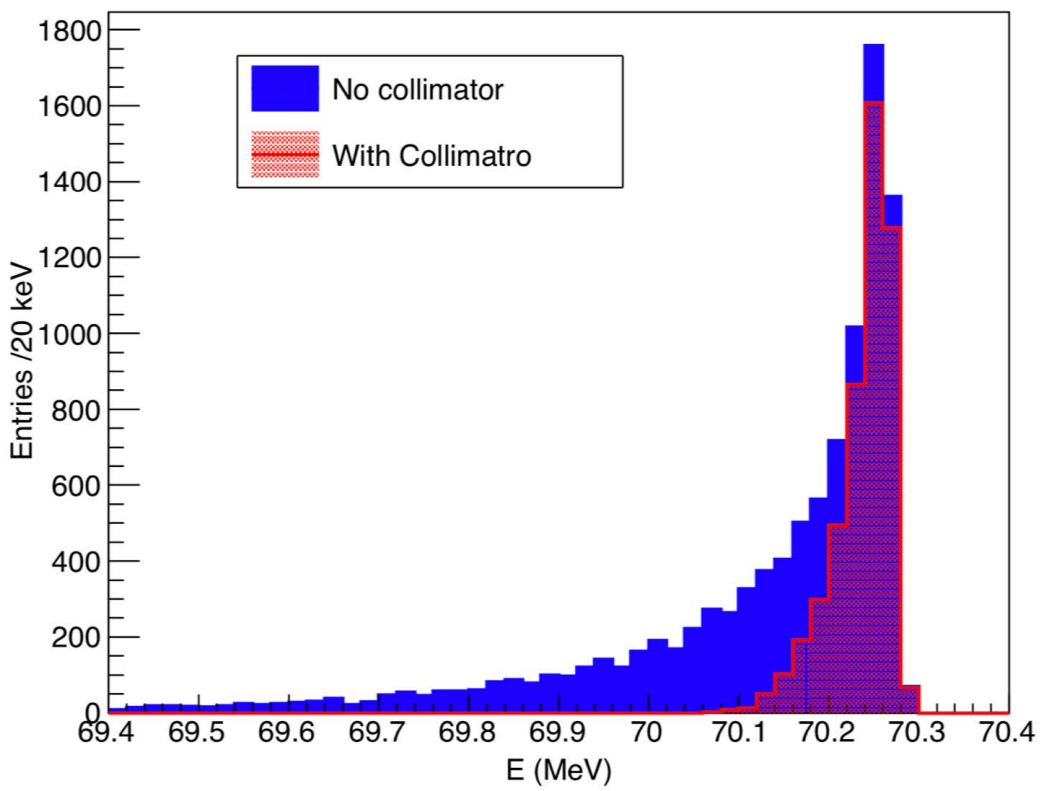


Fig. 3.27 The comparison of the beam energy distribution in the ProRad beam line between with and without collimator

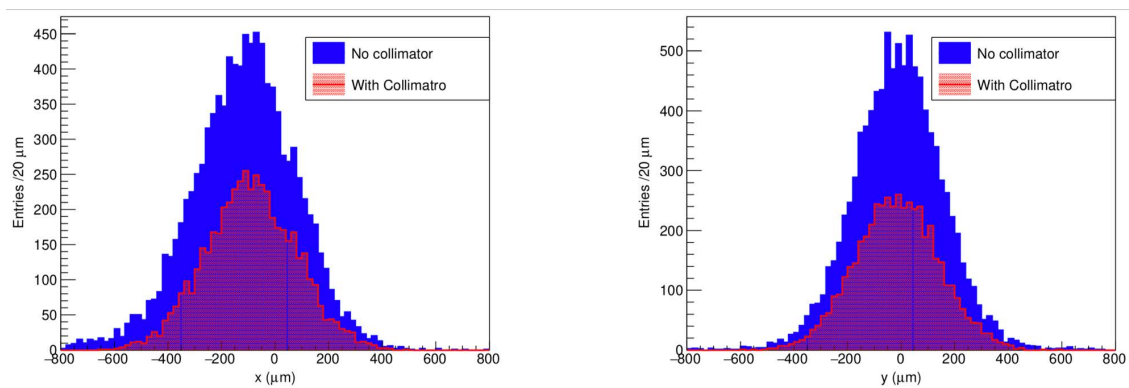


Fig. 3.28 The comparison of transverse distribution in the ProRad beam line between with and without collimator. Left: the horizontal beam size (x) distribution; Right: the vertical beam size (y)

the surviving particles for the 100 simulated machines of the ProRad beam line are shown in Fig. 3.29.

The misalignment tolerance is obtained by reducing the imperfection level. It is found that when the imperfection level decreases from 100 μm and 100 μrad to 20 μm and 20 μrad , the result that 93% of the machines with energy spread less than 5×10^{-4} and particle percentage larger than 20% can be obtained.

Error type	Value
position offsets (h/v)	100 μm
angle offsets (h/v)	100 μrad
rotation offsets (h/v)	100 μrad

Table 3.6 Misalignments for elements (bends, quads and the collimator) in the ProRad beam line of PRAE

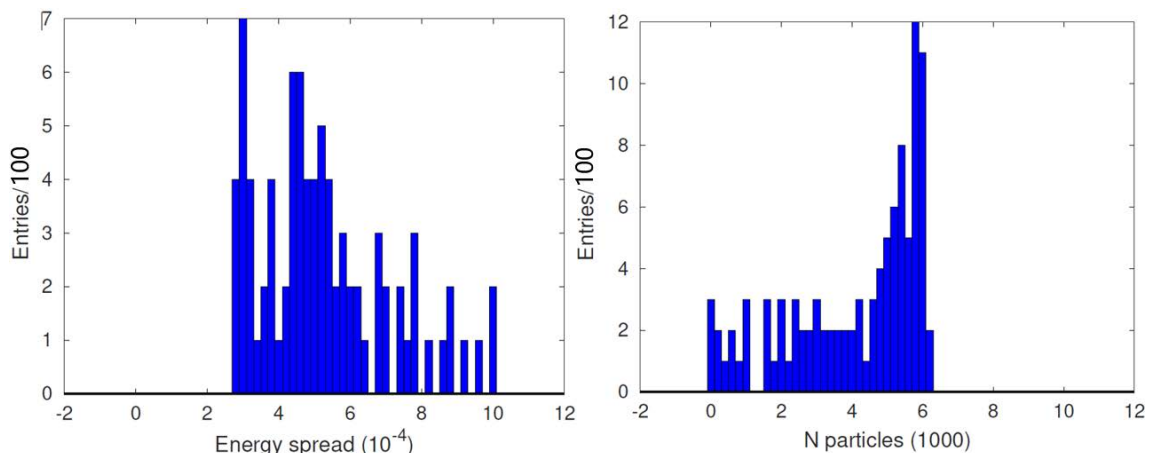


Fig. 3.29 The beam distributions for 100 machines of the ProRad beam line with the element imperfection level of 100 μm and 100 μrad . Left: the energy spread distribution for machines with surviving particle percentage larger than 20%; Right: the number of surviving particle distribution of the 100 machines (initial particle: 10,000)

In order to improve the tolerance level, four BPMs and three dipole correctors are placed along the ProRad beam line in order to correct the errors due to the misalignments. The one-to-one correction algorithm [105] is used to perform the steering by pairing one corrector with the next downstream BPM to improve the trajectory. This is a simple and fast algorithm which is often used first to correct the misalignments. The equation (3.6) [60] is used to get the strengths of the dipole correctors for the 1-to-1 correction.

$$\theta = \min \left\{ \| \Delta u - R\theta \|_2^2 + \alpha^2 \| \theta \|_2^2 \right\} \quad (3.6)$$

Here, θ is the strength of the dipole correctors. $\Delta u = u - u_0$ represent the beam position difference recorded by BPMs between misalignment machine and ideal machine. R is the response matrix between the dipole correctors and the BPMs. α is a free parameter which is used to avoid a large fluctuation of corrector strength.

With the help of the correction, the tolerance for the quadrupole offsets can be increased to $500 \mu\text{m}$ and $500 \mu\text{rad}$, which are easily reached using the state-to-art alignment techniques. The distributions of the surviving particles and the energy spreads after the correction for the 100 simulated machines of the ProRad beam line are shown in Fig. 3.30.

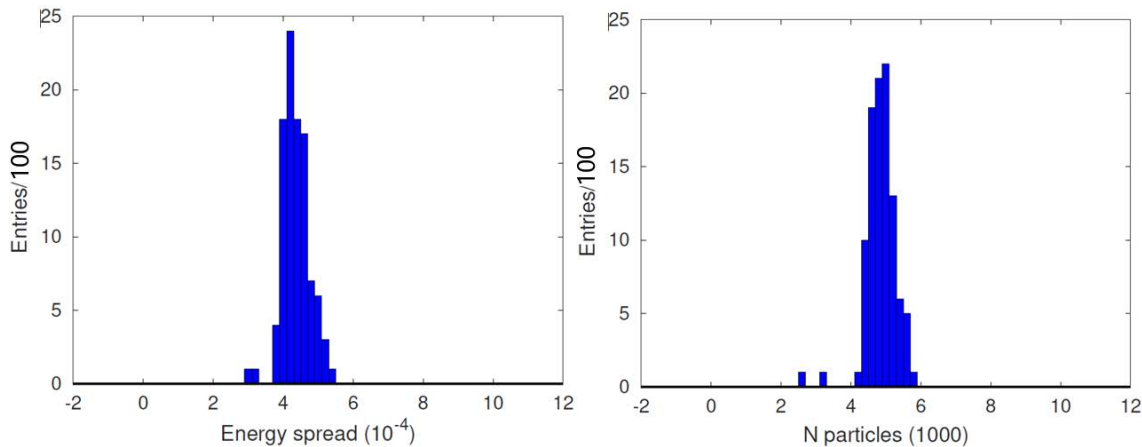


Fig. 3.30 The machine distributions for the imperfection of $500 \mu\text{m}$ and $500 \mu\text{rad}$ for the 100 simulated machines of the ProRad beam line after the one-to-one beam-based alignment correction

3.3 Conclusion

The overall detailed physical design of the multidisciplinary facility PRAE has been presented in this chapter, including applications for radiotherapy and nuclear experiments.

VHEE as a novel RT technique is being investigated, and is showing very promising simulation results and preliminary experimental results. Here two new ways of dose delivery to mitigate the RT effects in healthy cells are being considered: the spatial fractionation treatment with Grid mini-beams and the FLASH ultrahigh dose rate delivery treatment. Beam optics design and performance simulations to create a radiobiology experiment with Grid mini-beams and FLASH beam modalities in the same beam line are completed. Meanwhile, the beam line design for the proton radius experiment has been finished as well. A chicane structure with

a collimator is applied taking account of the requirement of an extremely low beam energy spread of 5×10^{-4} .

The design results of PRAE are encouraging and more in-depth technical feasibility studies could be done in the future to demonstrate experimentally innovative radiotherapy modalities, high quality instrumentation tests and more accurate proton radius measurements.

Chapter 4

Summary and Conclusions

RF electron linacs are a key component in many applications including HEP colliders, medium-energy electron beam based R&D facilities as well as industrial and medical areas, which have greatly promoted the development of different disciplines over the past half century.

The injector system optimization for FCC-ee as well as the application for an electron platform PRAE is studied and presented in this thesis as detailed as possible. A mature technology employing normal conducting S-band accelerating structures has been chosen to accomplish the electron beam acceleration study in an energy range from 50 MeV to 6 GeV and shows a promising result.

4.1 FCC-ee injector system

The final extremely high collision luminosity of FCC-ee demands a stable, high-efficient, cost-effective injector system, which can provide electron and positron beams with required high energy, charge, and low emittance. In the FCC-ee baseline, a 6 GeV S-band linac and a 6-20 GeV Pre-Booster Ring function as the injector. The 6 GeV linac system will hold the electron and positron beams with a bunch charge of about 3.5 nC (2.13×10^{10}) in the same S-band accelerating sections, which could cause the degradation of the final particle numbers injected into the 6-20 GeV Pre-Booster Ring. The acceleration and injection of electrons is easy to be performed in the 6 GeV linac. What we care most is the positron yield of the whole system. Three different improved injection schemes for FCC-ee have been studied using bypass structures to transport and accelerate electrons and positrons separately in different paths in the 6 GeV linac system for a better particle generation and transmission (mainly on positrons). A dedicated large-aperture S-band linac has been chosen to capture and accelerate as many positrons as possible when they are produced from the positron target. Start-to-end optics design and tracking simulation have been finished for the 6 GeV electron-positron linac system.

The positron yield before the damping ring is what we care about most, and the result could reach $1.2 N_{e^+}/N_{e^-}$ in our simulations, greater than the proposed goal value of $0.7 N_{e^+}/N_{e^-}$ in FCC-ee CDR. All the designs are based on established technologies, which have been proven to be reliable and effective in SLC, SuperKEKB and other past and existing machines.

Considering such a large complex machine, more potential injection schemes are welcomed. Besides the three optimized options, an alternative choice that a 6 GeV S-band linac + a 6-20 GeV C-band linac working as the injector takes the place of the 6 GeV linac + 6-20 GeV Pre-Booster Ring (SPS) is also being considered. Although in this case the beam transmission efficiency may be improved, the cost will be higher (a new 6-20 GeV C-band linac is needed), while the existing SPS can work as the Pre-Booster Ring in the baseline design. Two bunches per pulse with a repetition of 200 Hz are chosen as the current injection schedule. Further studies using multi-bunches in a pulse is being considered for a high efficiency. In addition, the beam instabilities and beam loss caused by the effects of beam loading, multi-bunch beam breakup, and etc. could be a concern and should be taken into account carefully.

4.2 The PRAE platform

The electron application platform PRAE was planned to be constructed as a multi-purpose tool for the study in radiotherapy, sub-atomic physics and new instrumentation technologies. The overall physical designs from the RF electron source, 70 MeV S-band linac to the two downstream beam lines have been finished and meet the design requirement of different users. My contribution to this work is the design and optimization of the two beam lines and the beam-water interaction simulations. One main application of this platform is the new RT techniques exploration using VHEE beams for the tumor treatment. And the other application is the study of the proton radius, which asks for a very low energy spread of 5×10^{-4} . The design shows a promising performance in simulations, and it is easy to be realized technically.

References

- [1] Methodical Accelerator Design (MAD-X). <http://mad.web.cern.ch/mad/>.
- [2] <https://news.mit.edu/2016/startup-improved-nuclear-threat-detection-0622>.
- [3] Strategic Accelerator Design (SAD). <http://acc-physics.kek.jp/SAD/>.
- [4] Comparison of Standing and Travelling Wave Operations for a Positron Pre-Accelerator in the TESLA Linear Collider. 2000.
- [5] Applications of Particle Accelerators in Europe. Technical Report CERN-ACC-2020-0008, CERN, Geneva, Jun 2017. URL <http://cds.cern.ch/record/2716155>.
- [6] The Compact Linear Collider (CLIC) - Project Implementation Plan. 4/2018, 12 2018. doi: 10.23731/CYRM-2018-004.
- [7] 2020 Update of the European Strategy for Particle Physics (Brochure). Technical Report CERN-ESU-015, Geneva, 2020.
- [8] 1st FCC-France workshop. Design of FCC-ee positron system, November 2019. <https://indico.in2p3.fr/event/19693/contributions/76085>.
- [9] 2nd FCC-France workshop. Optimized positron production in FCC-ee, January 2021. <https://indico.in2p3.fr/event/23012/contributions/89978/attachments/61983/84688/chaikovska-fcc-france.pdf>.
- [10] Milton Abramowitz, Irene A Stegun, and Robert H Romer. Handbook of mathematical functions with formulas, graphs, and mathematical tables, 1988.
- [11] M Abs, J M Capdevila, T Delvigne, F Genin, Y Jongen, and A Nguyen. RHODOTRON Accelerators for Industrial Electron-Beam Processing: A Progress Report. 1996. URL <http://cds.cern.ch/record/865095>.
- [12] M. Aicheler and European Organization for Nuclear Research. *A Multi-TeV Linear Collider Based on CLIC Technology: CLIC Conceptual Design Report*. CERN (Series). CERN, 2012. ISBN 9789290833796.
- [13] Kazunori Akai, Kazuro Furukawa, Haruyo Koiso, et al. SuperKEKB collider. *Nuclear Instruments and Methods in Physics Research Section A: Accelerators, Spectrometers, Detectors and Associated Equipment*, 907:188–199, 2018.
- [14] Mitsuo Akemoto et al. The KEKB injector linac. *PTEP*, 2013:03A002, 2013. doi: 10.1093/ptep/ptt011.

- [15] A.M. Barnyakov et al. RF gun based on parallel coupled accelerating structure for high charge and low emittance (report). <https://indico.cern.ch/event/655723>.
- [16] A.V. Andrianov, A.M. Barnyakov, A.E. Levichev, M.V. Maltseva, D.A. Nikiforov, and S.L. Samoylov. Development and low power test of the parallel coupled accelerating structure. *Journal of Instrumentation*, 11(06):P06007–P06007, jun 2016. doi: 10.1088/1748-0221/11/06/p06007. URL <https://doi.org/10.1088/1748-0221/11/06/p06007>.
- [17] X. Artru, R. Chehab, M. Chevallier, and V. Strakhovenko. Advantages of axially aligned crystals used in positron production at future linear colliders. *Phys. Rev. ST Accel. Beams*, 6:091003, Sep 2003. doi: 10.1103/PhysRevSTAB.6.091003. URL <https://link.aps.org/doi/10.1103/PhysRevSTAB.6.091003>.
- [18] B. Bai. Alternatives injection design for FCC-ee injector linac (to be published). <https://indico.ihep.ac.cn/event/11444/session/0/contribution/103>.
- [19] V. E. Balakin, A. V. Novokhatsky, and V. P. Smirnov. VLEPP: TRANSVERSE BEAM DYNAMICS. *Conf. Proc. C*, 830811:119–120, 1983.
- [20] Philip Bambade and et al. The International Linear Collider: A Global Project. 3 2019. doi: 10.2172/1527401. URL <https://www.osti.gov/biblio/1527401>.
- [21] Ties Behnke, James E Brau, Brian Foster, Juan Fuster, Mike Harrison, James McEwan Paterson, Michael Peskin, Marcel Stanitzki, Nicholas Walker, and Hitoshi Yamamoto. The international linear collider technical design report-volume 1: Executive summary. *arXiv preprint arXiv:1306.6327*, 2013.
- [22] Bernauer, Jan, C., Pohl, and Randolph. The Proton Radius Problem. *Scientific American*, 2014.
- [23] Jan C Bernauer. Measurement of the elastic electron-proton cross section and separation of the electric and magnetic form factor in the Qsup 2 range from 0.004 to 1 (GeV/c)², Sep 2010.
- [24] Bossart, R., Delahaye, J.P., Godot, J.C., Madsen, J.H.B., Pearce, P., Riche, A., Rinolfi, L. The LEP Injector Linac (LA-12004-C). United States, 1991.
- [25] Leon Brillouin. Wave propagation in periodic structures: electric filters and crystal lattices. 1953.
- [26] J. Brossard, M. Desmons, B. M. Mercier, C. P. Prevost, and R. Roux. Construction of the probe beam photo-injector of CTF3. *Conf. Proc. C*, 060626:828–830, 2006.
- [27] M Brugger, R Corsini, T Lefevre, B Salvant, S Stapnes, W Wuensch, M Petrarca, S Reiche, C Welsch, E Adli, and P N Burrows. The CLEAR facility at CERN. Technical report, 2016. URL <https://cds.cern.ch/record/2311397>.
- [28] Alexander Wu Chao, Karl Hubert Mess, et al. *Handbook of accelerator physics and engineering*. World scientific, 2013.
- [29] R. Chehab, G. Le Meur, B. Mouton, and M. Renard. An Adiabatic Matching Device for the Orsay Linear Positron Accelerator. *IEEE Transactions on Nuclear Science*, 30(4):2850–2852, 1983. doi: 10.1109/TNS.1983.4332976.

- [30] Christopher, Mayes, Georg, and Hoffstaetter. Exact 1D model for coherent synchrotron radiation with shielding and bunch compression. *Physical Review Accelerators & Beams*, 2009.
- [31] J. A. Clarke and et al. The conceptual design of clara, a novel fel test facility for ultra-short pulse generation. *Proceedings of Ipac*, 2013.
- [32] J. E. Clendenin. High-yield positron systems for linear colliders. In *Proceedings of the 1989 IEEE Particle Accelerator Conference, . 'Accelerator Science and Technology*, pages 1107–1111 vol.2, 1989. doi: 10.1109/PAC.1989.73367.
- [33] CLIC and CLICdp collaborations. *Updated baseline for a staged Compact Linear Collider*. CERN Yellow Reports: Monographs. CERN, Geneva, Aug 2016. doi: 10.5170/CERN-2016-004. URL <http://cds.cern.ch/record/2210892>. Comments: 57 pages, 27 figures, 12 tables.
- [34] ATLAS collaboration. Observation of a new particle in the search for the Standard Model Higgs boson with the ATLAS detector at the LHC. *Physics Letters B*, 716(1):1–29, 2012. ISSN 0370-2693. doi: <https://doi.org/10.1016/j.physletb.2012.08.020>. URL <https://www.sciencedirect.com/science/article/pii/S037026931200857X>.
- [35] CMS collaboration. Observation of a new boson at a mass of 125 GeV with the CMS experiment at the LHC. *Physics Letters B*, 716(1):30–61, 2012. ISSN 0370-2693. doi: <https://doi.org/10.1016/j.physletb.2012.08.021>. URL <https://www.sciencedirect.com/science/article/pii/S0370269312008581>.
- [36] FCC collaboration et al. FCC-ee: The Lepton Collider: Future Circular Collider Conceptual Design Report Volume 2. *European Physical Journal: Special Topics*, 228(2):261–623, 2019.
- [37] CTF3. <https://section-mpc.web.cern.ch/content/ctf3>.
- [38] O Dadoun, I Chaikovska, R Chehab, F Poirier, L Rinolfi, V Strakhovenko, A Variola, and A Vivoli. Study of an hybrid positron source using channeling for CLIC. Technical Report CLIC-Note-808, CERN, Geneva, Sep 2009. URL <http://cds.cern.ch/record/1248436>.
- [39] R. Delorme, D. Marchand, and C. Vallerand. The PRAE Multidisciplinary Project. *Nuclear Physics News*, 29(1):32–35, 2019. doi: 10.1080/10619127.2019.1571833. URL <https://doi.org/10.1080/10619127.2019.1571833>.
- [40] S. Di Mitri, M. Cornacchia, and S. Spampinati. Cancellation of coherent Synchrotron Radiation kicks with optics balance. *Phys. Rev. Lett.*, 110(1):014801, 2013. doi: 10.1103/PhysRevLett.110.014801.
- [41] Simone Di Mitri. Coherent Synchrotron Radiation and Microbunching Instability. *CERN Yellow Rep. School Proc.*, 1:381, 2018. doi: 10.23730/CYRSP-2018-001.381.
- [42] Felix Dietrich, Gudrid Moortgat-Pick, Sabine Riemann, Peter Sievers, and Andriy Ushakov. Status of the undulator-based ILC positron source. In *International Workshop on Future Linear Colliders*, 2 2019.

- [43] David Dunning et al. Start-to-End Simulations of the CLARA FEL Test Facility. In *9th International Particle Accelerator Conference*, 6 2018. doi: 10.18429/JACoW-IPAC2018-THPMK060.
- [44] Stanley D. Ecklund. THE STANFORD LINEAR COLLIDER POSITRON SOURCE. In *1987 Workshop on Intense Positron Beams*, 10 1987.
- [45] MOHAMED EL KHALDI and LUCA GAROLFI. RF DESIGN OF A HIGH GRADIENT S-BAND TRAVELLING WAVE ACCELERATING STRUCTURE FOR THOMX LINAC. In *IPAC'15, the sixth International Particle Accelerator Conference*, Richmond, United States, May 2015. URL <http://hal.in2p3.fr/in2p3-01206183>.
- [46] Roger Erickson. SLC Design Handbook. Technical report, Stanford Linear Accelerator Center, 2004.
- [47] D. Gamba et al. The CLEAR user facility at CERN. *Nuclear Instruments and Methods in Physics Research Section A: Accelerators, Spectrometers, Detectors and Associated Equipment*, 909:480–483, 2018. ISSN 0168-9002. doi: <https://doi.org/10.1016/j.nima.2017.11.080>. URL <https://www.sciencedirect.com/science/article/pii/S0168900217313311>. 3rd European Advanced Accelerator Concepts workshop (EAAC2017).
- [48] S. Agostinelli et al. Geant4—a simulation toolkit. *Nuclear Instruments and Methods in Physics Research Section A: Accelerators, Spectrometers, Detectors and Associated Equipment*, 506(3):250–303, 2003. ISSN 0168-9002. doi: [https://doi.org/10.1016/S0168-9002\(03\)01368-8](https://doi.org/10.1016/S0168-9002(03)01368-8). URL <https://www.sciencedirect.com/science/article/pii/S0168900203013688>.
- [49] Angeles Faus-Golfe, Bowen Bai, Patricia Duchesne, Yanliang Han, Denis Marchand, Cynthia Vallerand, and Eric Voutier. The PRORAD Beam Line Design for PRAE. In *10th International Particle Accelerator Conference*, page THPMP003, Melbourne, Australia, May 2019. doi: 10.18429/JACoW-IPAC2019-THPMP003. URL <https://hal.archives-ouvertes.fr/hal-02290778>.
- [50] Angeles Faus-Golfe et al. First Optics Design and Beam Performance Simulation of PRAE: Platform for Research and Applications With Electrons at Orsay. In *8th International Particle Accelerator Conference*, page THPVA079, 2017. doi: 10.18429/JACoW-IPAC2017-THPVA079.
- [51] V. Favaudon, L. Caplier, V. Monceau, F. Pouzoulet, M. Sayarath, C. Fouillade, M. F. Poupon, I. Brito, P. Hupe, and J. and Bourhis. Ultrahigh dose-rate FLASH irradiation increases the differential response between normal and tumor tissue in mice. *Science Translational Medicine*, 6(245):245ra93, 2014.
- [52] FCC-ee positron source collaboration. Physics design of the positron target and capture system - meeting # 01, July 2020. <https://indico.cern.ch/event/938292/overview>.
- [53] Klaus Floettmann. ASTRA. <https://www.desy.de/~mpyflo/>.
- [54] Gaston Floquet. Sur les équations différentielles linéaires à coefficients périodiques. In *Annales scientifiques de l’École normale supérieure*, volume 12, pages 47–88, 1883.

- [55] G. Moortgat-Pick, S. Riemann, P. Sievers, A. Ushakov. Undulator e+ source summary. AWLC 2020. <https://agenda.linearcollider.org/event/8622/sessions/5078/#20201021>.
- [56] Rongli Geng. First Step Entering Territory of 50 MV/m in 9-Cell LSF Cavity. AWLC 2020. <https://agenda.linearcollider.org/event/8622/contributions/46628/>.
- [57] Frank Gerigk. Cavity types. *arXiv preprint arXiv:1111.4897*, 2011.
- [58] Spencer Gessner. Advanced accelerator upgrade paths for the ILC. AWLC 2020. <https://agenda.linearcollider.org/event/8622/contributions/46642/>.
- [59] CEPC Study Group et al. CEPC conceptual design report: Volume 1-accelerator. *arXiv preprint arXiv:1809.00285*, 2018.
- [60] Y. Han, A. Latina, L. Ma, and D. Schulte. Static beam-based alignment for the Ring-To-Main-Linac of the Compact Linear Collider. *Journal of Instrumentation*, 12(06):P06010–P06010, jun 2017. doi: 10.1088/1748-0221/12/06/p06010. URL <https://doi.org/10.1088/1748-0221/12/06/p06010>.
- [61] Y. Han, A. Faus Golfe, C. Vallerand, B. Bai, P. Duchesne, Y. Prezado, R. Delorme, P. Poortmans, V. Favaudon, C. Fouillade, F. Pouzoulet, and M. Dosanjh. Optics Design and Beam Dynamics simulation for a VHEE Radiobiology beam line at PRAE accelerator. In *Journal of Physics Conference Series*, volume 1350 of *Journal of Physics Conference Series*, page 012200, November 2019. doi: 10.1088/1742-6596/1350/1/012200.
- [62] Y.L. Han, C. Bayar, A. Latina, S. Doebert, D. Schulte, and L.L. Ma. Optimization of the CLIC positron source using a start-to-end simulation approach involving multiple simulation codes. *Nuclear Instruments and Methods in Physics Research Section A: Accelerators, Spectrometers, Detectors and Associated Equipment*, 928:83–88, 2019. ISSN 0168-9002. doi: <https://doi.org/10.1016/j.nima.2019.03.044>. URL <https://www.sciencedirect.com/science/article/pii/S0168900219303523>.
- [63] HFSS. <http://www.ansoft.com/products/hf/hfss/>.
- [64] Naoko Iida et al. Commissioning of Positron Damping Ring and the Beam Transport for SuperKEKB. In *62nd ICFA Advanced Beam Dynamics Workshop on High Luminosity Circular e+e- Colliders*, page TUPAB07, 2019. doi: 10.18429/JACoW-eeFACT2018-TUPAB07.
- [65] K. Yokoya. "Short-Range Wake Formulas for Infinite Periodic Pill-Box" (unpublished), 1998.
- [66] Takuya Kamitani, Mitsuo Akemoto, Dai Arakawa, Yoshio Arakida, Atsushi Enomoto, Shigeki Fukuda, Yoshihiro Funakoshi, Kazuro Furukawa, Toshiyasu Higo, Hiroyuki Honma, et al. SuperKEKB positron source construction status. In *5th Int. Particle Accelerator Conf.(IPAC'14), Dresden, Germany, June 15-20, 2014*, pages 579–581. JACOW, Geneva, Switzerland, 2014.
- [67] Takuya Kamitani et al. Injector Linac Upgrade for SuperKEKB. In *25th International Linear Accelerator Conference*, page MOP011, 2011.

- [68] G I Kuznetsov. IrCe cathodes for EBIS. *Journal of Physics: Conference Series*, 2:35–41, jan 2004. doi: 10.1088/1742-6596/2/1/005. URL <https://doi.org/10.1088/1742-6596/2/1/005>.
- [69] Agnese Lagzda, Deepa Angal-Kalinin, James Jones, Roger Jones, Karen Kirkby, and W. Farabolini. Relative Insensitivity to Inhomogeneities on Very High Energy Electron Dose Distributions. In *8th International Particle Accelerator Conference*, page THPVA139, 2017. doi: 10.18429/JACoW-IPAC2017-THPVA139.
- [70] P. M. Lapostolle and A. L. Septier. *LINEAR ACCELERATORS*. North-Holland Publishing Company, 1970.
- [71] Andrea Latina. RF-Track: Beam tracking in field maps including space-charge effects, features and benchmarks. page MOPRC016. 4 p, 2017. doi: 10.18429/JACoW-LINAC2016-MOPRC016. URL <http://cds.cern.ch/record/2304522>.
- [72] Andrea Latina, Erik Adli, Nuria Fuster-Martínez, Juergen Pfingstner, Daniel Schulte, and Jochem Snuverink. Tests of Wakefield-Free Steering at ATF2. In *6th International Particle Accelerator Conference*, 6 2015. doi: 10.18429/JACoW-IPAC2015-MOPJE059.
- [73] JIE LIU. BEPCII linac S-band accelerating structure. 2008. <http://ir.ihep.ac.cn/handle/311005/220586>.
- [74] J H B Madsen. LEP injector linacs 1989. Technical Report CERN-PS-89-56-LP, CERN, Geneva, Sep 1989. URL <http://cds.cern.ch/record/2742719>.
- [75] Marchand, Dominique. A new platform for research and applications with electrons: the PRAE project. *EPJ Web Conf.*, 138:01012, 2017. doi: 10.1051/epjconf/201713801012. URL <https://doi.org/10.1051/epjconf/201713801012>.
- [76] I. Martínez-Rovira, G. Fois, and Y. Prezado. Dosimetric evaluation of new approaches in GRID therapy using nonconventional radiation sources. *Medical Physics*, 42(2), 2015.
- [77] Shuji Matsumoto, Toshiyasu Higo, Kazuhisa Kakihara, Takuya Kamitani, and Madoka Tanaka. Large-aperture Travelling-wave Accelerator Structure for Positron Capture of SuperKEKB Injector Linac. In *5th International Particle Accelerator Conference*, page THPRI047, 7 2014. doi: 10.18429/JACoW-IPAC2014-THPRI047.
- [78] Peter McIntosh et al. The VELA and CLARA Test Facilities at Daresbury Laboratory. In *28th International Linear Accelerator Conference*, 5 2017. doi: 10.18429/JACoW-LINAC2016-TH3A03.
- [79] C. Meng. CEPC Linac. <https://indico.ihep.ac.cn/event/11444/session/0/contribution/96>.
- [80] Cai Meng, Yunlong Chi, Xiaoping Li, Guoxi Pei, Shilun Pei, Dou Wang, and Jingru Zhang. CEPC Linac Design and Beam Dynamics. In *8th International Particle Accelerator Conference*, page TUPAB008, 2017. doi: 10.18429/JACoW-IPAC2017-TUPAB008.
- [81] Roger H Miller. Comparison of standing-wave and traveling-wave structures. Technical report, Stanford Linear Accelerator Center, 1986.

- [82] P. Montay-Gruel, K. Petersson, M. Jaccard, G. Boivin, J. F. Germond, B. Petit, R. Doenlen, V. Favaudon, F. Bochud, and C. Bailat. Irradiation in a flash: Unique sparing of memory in mice after whole brain irradiation with dose rates above 100 Gy/s. *Radiotherapy & Oncology*, 2017.
- [83] J. B. Murphy, S. Krinsky, and R. L. Gluckstern. Longitudinal wake field for an electron moving on a circular orbit. *Part. Accel.*, 57:9–64, 1997.
- [84] T. Nebel, C. Schwob, J. D. Santos, S. Dhawan, and J. Veloso. The size of the proton. *Nature*, 2010.
- [85] S Ogur, T Charles, K Oide, Y Papaphilippou, L Rinolfi, F Zimmermann, E V Ozcan, K Furukawa, N Iida, T Kamitani, F Miyahara, A Barnyakov, A Levichev, P Martyshkin, D Nikiforov, I Chaikovska, R Chehab, and S M Polozov. Layout and performance of the FCC-ee pre-injector chain. *Journal of Physics: Conference Series*, 1067:022011, sep 2018. doi: 10.1088/1742-6596/1067/2/022011.
- [86] Salim Ogur. *Linac and Damping Ring Designs of the Future Circular e^+e^- Collider of CERN*. PhD thesis, Bogazici U., 2019.
- [87] Satoshi Ohsawa, Jae-Young Choi, Yujiro Ogawa, Atsushi Enomoto, Takuya Kamitani, Hitoshi Kobayashi, and Isamu Sato. Preinjector of the KEK 2.5-GeV linac and high current single bunch acceleration. *Conf. Proc. C*, 9608262:815–817, 1996.
- [88] Yannis Papaphilippou. Consolidated FCC-ee filling scheme. https://indico.cern.ch/event/915196/contributions/3847973/attachments/2034724/3406307/FCCEe_injector_parameters_2020_05_08.pdf.
- [89] G. X. Pei, Y. L. Sun, J. T. Liu, Y. L. Chi, and N. Z. Liu. BEPC II positron source. *High Energy Physics and Nuclear Physics -Beijing-*, 30(1):66–70, 2006.
- [90] Poynting and H. J. On the Transfer of Energy in the Electromagnetic Field. *Phil Trans*, 175:343–361, 1884.
- [91] Yolanda Prezado, Sukhena Sarun, Silvia Gil, Pierre Deman, Audrey Bouchet, and Geraldine Le Duc. Increase of lifespan for glioma-bearing rats by using minibeam radiation therapy. *Journal of Synchrotron Radiation*, 19(1):60–65, Jan 2012. doi: 10.1107/S0909049511047042. URL <https://doi.org/10.1107/S0909049511047042>.
- [92] Yolanda Prezado, Pierre Deman, Pascale Varlet, Gregory Jouvion, Silvia Gil, Céline Le ClecH, Hélène Bernard, Géraldine Le Duc, and Sukhena Sarun. Tolerance to Dose Escalation in Minibeam Radiation Therapy Applied to Normal Rat Brain: Long-Term Clinical, Radiological and Histopathological Analysis. *Radiation Research*, 184(3):314–321, 2015.
- [93] R. Chehab. Positron sources. In Turner, S. (Ed.). CAS CERN accelerator school: 5 general accelerator physics course Vol 2 Proceedings, (p. 537). European Organization for Nuclear Research (CERN), January 1994.

- [94] T.O. Raubenheimer and R.D. Ruth. A dispersion-free trajectory correction technique for linear colliders. *Nuclear Instruments and Methods in Physics Research Section A: Accelerators, Spectrometers, Detectors and Associated Equipment*, 302(2):191–208, 1991. ISSN 0168-9002. doi: [https://doi.org/10.1016/0168-9002\(91\)90403-D](https://doi.org/10.1016/0168-9002(91)90403-D). URL <https://www.sciencedirect.com/science/article/pii/016890029190403D>.
- [95] Research Instruments (RI). <https://research-instruments.de/>.
- [96] Kenneth Franklin Riley, Michael Paul Hobson, Stephen John Bence, and Mike Hobson. *Mathematical methods for physics and engineering: a comprehensive guide*. Cambridge university press, 2002.
- [97] A. Robson, P. N. Burrows, N. Catalan Lasheras, L. Linssen, M. Petric, D. Schulte, E. Sicking, S. Stapnes, and W. Wuensch. The Compact Linear e^+e^- Collider (CLIC): Accelerator and Detector, 2018.
- [98] Bruno Benedetto Rossi. *High-energy particles*. Prentice-Hall physics series. Prentice-Hall, New York, NY, 1952. URL <https://cds.cern.ch/record/99081>.
- [99] D. Satoh, T. Shibuya, N. Hayashizaki, R. Zhang, X. Zhou, T. Natsui, and M. Yoshida. Research and development of iridium cerium photocathode for SuperKEKB injector linac. *Energy Procedia*, 131:326 – 333, 2017. ISSN 1876-6102. doi: <https://doi.org/10.1016/j.egypro.2017.09.430>. URL <http://www.sciencedirect.com/science/article/pii/S1876610217345319>.
- [100] Schulte, D. PLACET: A program to simulate drive beams. In *7th European Particle Accelerator Conference (EPAC 2000)*, pages 1402–1404, 7 2000.
- [101] Emil Schüler, Kjell Eriksson, Elin Hynning, Steven Hancock, Susan Hiniker, Magdalena Bazalova-Carter, Tony Wong, Quynh-Thu Le, Billy Loo, and Peter Maxim. Very high-energy electron (VHEE) beams in radiation therapy; Treatment plan comparison between VHEE, VMAT, and PPBS. *Medical Physics*, 44, 03 2017. doi: 10.1002/mp.12233.
- [102] Kyrre et al. Sjobak. Status of the CLEAR electron beam user facility at CERN. (CERN-ACC-2019-084):MOPTS054. 4 p, 2019. doi: 10.18429/JACoW-IPAC2019-MOPTS054. URL <https://cds.cern.ch/record/2695092>.
- [103] CST Microwave studio. <https://www.cst.com/>.
- [104] Anna Subiel, Vadim Moskvin, Gregor Welsh, S. Cipiccia, D Reboredo, P Evans, Mike Partridge, Colleen Desrosiers, Maria Pia Anania, Alessandro Cianchi, Andrea Mostacci, Enrica Chiadroni, D. Giovenale, Fabio Villa, Riccardo Pompili, Massimo Ferrario, M Belleveglia, Giampiero Di Pirro, G Gatti, and Dino Jaroszynski. Dosimetry of very high energy electrons (VHEE) for radiotherapy applications: Using radiochromic film measurements and Monte Carlo simulations. *Physics in Medicine and Biology*, 59:5811, 09 2014. doi: 10.1088/0031-9155/59/19/5811.
- [105] Yipeng Sun, Chris Adolphsen, and /SLAC. Linac Alignment Algorithm: Analysis on 1-to-1 Steering. 8 2011. doi: 10.2172/1022483. URL <https://www.osti.gov/biblio/1022483>.
- [106] SuperKEKB injector photo. <https://www-linac.kek.jp/linacphoto/>.

- [107] Georgi P Tolstov. *Fourier series*. Courier Corporation, 2012.
- [108] Varian Medical Systems. <https://www.iaea.org/newscenter/news/iaea-receives-medical-linear-accelerator-under-partnership-from-manufacturer>.
- [109] A. Variola, J. Haissinski, A. Loulergue, Fabian Zomer, and et al. ThomX Technical Design Report. 01 2014.
- [110] Anna Vnuchenko, Christelle Bruni, Mohamed El Khaldi, Angeles Faus-Golfe, Andrea Latina, Pierre Lepercq, and Cynthia Vallerand. Start-to-End Beam Dynamics Simulations for PRAE. In *9th International Particle Accelerator Conference*, page MOPML044, 2018. doi: 10.18429/JACoW-IPAC2018-MOPML044.
- [111] Shu-Hong Wang. Rf Electron Linac and Microtron. In *Accelerator Physics, Technology and Applications*, pages 256–290, February 2004. doi: 10.1142/9789812702807_0011.
- [112] Wangler and P. Thomas. Principles of RF linear accelerators. Wiley,, 10.1002/9783527618408:1–34, 1998.
- [113] Helmut Wiedemann. *Particle Accelerator Physics*. Springer International Publishing, 2015. doi: 10.1007/978-3-319-18317-6. URL <https://doi.org/10.1007%2F978-3-319-18317-6>.
- [114] G. Wuestefeld. Short Bunches in Electron Storage Rings and Coherent Synchrotron Radiation. *Conf. Proc. C*, 0806233:MOZAG02, 2008.
- [115] Artru Xavier. A simulation code for channeling radiation by ultrarelativistic electrons or positrons. *Nuclear Inst & Methods in Physics Research B*, 48(1-4):278–282, 1990.
- [116] Y. Enomoto. Status and challenges of the SuperKEKB positron source. <https://indico.cern.ch/event/938292>.
- [117] Y. Han. "FCC-ee positron source" (to be published). <https://indico.cern.ch/event/938292/contributions/3942250/>.
- [118] Y.D. Chernousov et al. Accelerating structure with parallel connection (report). <https://patents.google.com/patent/RU2605949C1/en>.
- [119] K. Yokoya and K. L. F. Bane. The Longitudinal high frequency impedance of a periodic accelerating structure. In *IEEE Particle Accelerator Conference (PAC 99)*, pages 1725–1727, 4 1999.
- [120] Yongke Zhao, Andrea Latina, Steffen Doeberl, Daniel Schulte, and Lianliang Ma. Optimisation of the CLIC positron source at the 1.5 TeV and 3 TeV stages. Technical Report CERN-ACC-2020-0026. CLIC-Note-1165, CERN, Geneva, Sep 2020. URL <https://cds.cern.ch/record/2735292>.

Appendix A

Different accelerator simulation programs

A.1 SAD

SAD (Strategic Accelerator Design) [3], developed at KEK, is a computer program complex for accelerator design, whose functions include beam optics matching, particle tracking simulation, nonlinear analysis and so on.

The optics design of the baseline injector scheme of FCC-ee has originally been done using SAD, and we keep using it in the electron linac design of the three optimized injector schemes.

SAD has many advantages. We can conclude everything that we care in just one *.sad* file, like beam matching, beam tracking, wakefield study, misalignment study and so on. Meanwhile, the command execution is very convenient and fast. The simulation results are also relatively intuitive and easy to be handled. A trivial disadvantage is that the calculation of higher-order transport matrices is not included in the source code and extra packages could be installed when considering higher-order effects (of course, this is not mandatory).

A.2 MAD-X

MAD-X [1], whose full name is Methodical Accelerator Design - X, is project developed at CERN, dedicated to the computational simulation and design in the field of beam dynamics and particle accelerators.

We mainly use MAD-X to do the optics design in beam transport systems in this work. As many kinds of magnets (dipoles, quadrupoles and sextupoles) have been applied in several different electron beam lines, it is easier to get the transport matrices (whatever first-order or second-order matrix values) using MAD-X. Although MAD-X can use its PTC module [1] to do the tracking simulation for beams with given initial conditions, we have chosen PLACET,

a more powerful tracking simulation code, to cooperate with MADX to finish the physical designs of linacs and transport systems in this work.

A.3 PLACET

PLACET (Program for Linear Accelerator Correction and Efficiency Tests) [100] is a code that simulates the dynamics of a beam in the main accelerating or decelerating part of a linac in the presence of wakefields.

PLACET is a powerful accelerator design code with many functions. It not only can do the beam matching and tracking simulation, but also have the ability to simulate collective effects, like CSR, wakefields, etc.. In this thesis, a combination of MADX and PLACET has been chosen to do the optics design and beam tracking respectively.

The three programs can be converted among each other and the simulation results obtained by them have good uniformity, which ensure the reliability of our design in this work.

Titre : Optimisations des injecteurs linacs pour FCC-ee et applications pour PRAE**Mots clés :** Accélérateur physique, FCC-ee, PRAE projet, Conception optique de faisceau, Simulation de suivi de faisceau, Rendement en positons

Résumé : Au cours des dernières années, il y a eu un développement intense d'accélérateurs d'électrons linéaires conduit par différentes communautés comme la communauté X-FEL, la communauté des collisionneurs linéaires de la physique des hautes énergies (HEP): ILC et CLIC ainsi que la communauté des collisionneurs circulaires HEP: FCC- ee et CEPC. En outre, il existe également de nombreuses autres applications de la science médicale à l'industrie qui utiliseront un tel linac comme accélérateurs principaux. Dans toutes ces études, un e-linac à haut rendement avec des énergies de 10 à 1000 MeV est nécessaire comme conducteur ou injecteur. Même si la technologie linac pour faire face aux performances recherchées est très connue, un important effort de R&D sur des solutions plus compactes, plus simples, plus rentables, efficaces, robustes et fiables est en cours.

Dans ce cadre, cette thèse optimisera le linac et ses lignes de transfert associées dans deux cas:

- (1) L'injecteur linac pour FCC-ee (Future Electron-Positron Circular Collider), en particulier le positron.
- (2) Le linac pour les applications dites projet PRAE (Platform for Research and Application with Electrons).

Le Future Circular Collider (FCC) hébergé par le CERN, est une collaboration internationale visant à explorer la faisabilité de différents scénarios de collisionneurs de particules dans le but d'augmenter considérablement l'énergie et la luminosité par rapport aux collisionneurs existants, dans la recherche d'une nouvelle physique. L'objectif principal de cette thèse est de réaliser la conception et l'optimisation de bout en bout pour la production de faisceaux, l'accélération et le transport de la source d'électrons d'alimentation à l'anneau d'amortissement de positons ainsi que d'augmenter l'efficacité et la flexibilité de la production de positons (le rendement en positons doit être supérieur à 0,7) pour l'injecteur linac FCC-ee. Une étude complémentaire pour l'optimisation de la cible positron utilisant une cible conventionnelle ou une

cible hybride est également brièvement résumée. Compte tenu des inconvénients du schéma d'injecteur SuperKEKB actuel, trois nouveaux modèles de schémas de dérivation différents ont été finis pour transférer les particules d'électrons et de positrons séparément pour une meilleure transmission et une flexibilité améliorée de l'ensemble du système, ce qui pourrait finalement nous donner un rendement en positons d'environ 1,2 e+/e- à l'anneau d'amortissement e + dans les simulations théoriques. En conclusion, ce travail est une première étape dans l'optimisation du système d'injecteur FCC-ee du point de vue de l'efficacité du transport et de la conception optique. Les différents schémas proposés sont basés sur des technologies établies et différents chemins pour les électrons et les positrons sont utilisés afin d'améliorer l'efficacité du transport du point de vue des pertes et du coût.

Dans la deuxième partie de cette thèse, la conception d'une plateforme d'application de radiobiologie et de physique nucléaire PRAE (Platform for Research and Application with Electrons) linac basée sur un faisceau d'électrons pulsé de haute qualité d'énergie jusqu'à 70 MeV en phase 1 et 140 MeV en phase 2 a été réalisé. 2 paquets d'électrons nC dans l'accélérateur PRAE phase 1 sont produits dans un canon RF à une fréquence de 50 Hz, post-accelérés par un linac en bande S à 50-70 MeV et injectés dans la ligne directe du faisceau plus une ligne déviée. La conception optique des lignes de faisceau doit être aussi flexible que possible pour faire face à différents types de caractéristiques de faisceau et modes de fonctionnement en fonction de l'application. L'étude des différentes options optiques et la mise en œuvre de ces deux lignes de faisceau ainsi que l'interaction faisceau-eau pour les études précliniques pour le cas des expériences de radiobiologie ont également été réalisées et présentées dans cette thèse.

Title : Injector linac optimizations for FCC-ee and applications for PRAE

Keywords : Accelerator physics, FCC-ee, PRAE project, Beam optics design, Beam tracking simulation, Positron yield

Abstract : In the last years there has been intense linear electron-accelerator development driven by different communities as the X-FEL community, the High Energy Physics (HEP) linear-collider community: ILC and CLIC as well as HEP circular-collider community: FCC-ee and CEPC. Furthermore, there are also many other applications from medical science to industry that will use such a linac as main accelerators. In all these studies, a high-efficient e-linac with energies from 10 to 1000 MeV is needed as driver or injector. Even if the linac technology to cope with the performances needed is very well known, an important R&D effort on more compact, simpler, cost-effective, efficient, robust and reliable designs is in progress.

In this frame, this thesis will optimize the linac and its associated transfer lines in two cases: (1) The injector linac for FCC-ee (Future electron-positron Circular Collider), in particular the positron one. (2) The linac for an application known as PRAE project (Platform for Research and Application with Electrons).

The Future Circular Collider (FCC) hosted by CERN, is an international collaboration to explore the feasibility of different particle collider scenarios with the aim of significantly increasing the energy and luminosity compared to existing colliders, in the search for new physics. In the case of the Future Circular electron-positron Collider (FCC-ee), 2.13×10^{10} (3.2 nC) electron and positron particles per bunch are needed for the most demanding full filling of Z running mode in the conceptual design report (CDR). The baseline selection for FCC-ee injector linac is based on the SuperKEKB one, which gives us a positron yield of 0.2 e+/e- against 0.4 e+/e- design in recent experiment. The main objective of this thesis is to perform the start-to-end design and optimization for beam production, acceleration and transport from the feeding electron source to the positron damping ring as well as to increase the efficiency and the flexibility of the positron production (the positron yield needs to be larger than 0.7) for FCC-ee injector linac. A complementary study for positron target optimisation using conventional target or hybrid

target is also shortly summarized. Considered the drawbacks of the current SuperKEKB injector scheme, three new different bypass scheme designs have been finished to transfer electron and positron particles separately for a better transmission and improved flexibility of the whole system, which finally could give us a positron yield of around 1.2 e+/e- at the positron damping ring in theoretical simulations. In conclusion, this work is a first step in the optimization of the FCC-ee injector system from the point of view of the efficiency of the transport and optics design. The various schemes proposed are based on established technologies and different paths for electrons and positrons are used in order to improve the efficiency of the transport from the point of view of losses and cost.

In the second part of this thesis, the design for a radiobiology and nuclear physics application linac platform PRAE(Platform for Research and Application with Electrons) based on a high-quality pulsed electron beam of energy up to 70 MeV in phase 1 and 140 MeV in phase 2 has been realized. 2 nC electron bunches in the PRAE accelerator phase 1 are produced in a RF gun at 50 Hz frequency, post-accelerated by a S-band linac to 50-70 MeV and injected into the direct beam line plus a deviated line. The optics design of the beam lines has to be as flexible as possible to cope with different kinds of beam characteristics (beam size, energy, dispersion, current...) and operation modes depending on the application. The study of the different optics options and the implementation of these two beam lines as well as the beam-water interaction for pre-clinical studies for the case of the radiobiology experiments has also been done and presented in this thesis.